

Cooling and Slowing Towards a Lithium MOT for High Precision Laser Spectroscopy

Dissertation
zur Erlangung des Grades
„Doktor der Naturwissenschaften“
am Fachbereich Physik, Mathematik und Informatik
der Johannes Gutenberg-Universität
in Mainz

Marcel Willig

geb. in Frankenthal
Mainz, den 13.05.2025

-
1. Gutachter: Prof. Dr. Randolph Pohl
 2. Gutachter: Univ.-Prof. Dr. Frank Maas
 3. Gutachter: Prof. Dr. Marc Vanderhaeghen
 4. Gutachter: Prof. Dr. Hans-Joachim Elmers

Datum der mündlichen Prüfung: 13.05.2025

Zusammenfassung

Lithium ist das dritte Element im Periodensystem und das leichteste Alkalimetall und das einzige, das stabile fermionische und bosonische Isotope besitzt. Es ist simpel genug um *ab initio* beschrieben zu werden, aber so komplex, dass viele physikalische Effekte für eine korrekte Beschreibung berücksichtigt werden müssen. Die D-Linien, also die Übergänge vom Grundzustand $2S_{1/2}$ zu den ersten angeregten Zuständen $2P_{1/2}$ und $2P_{3/2}$, werden beeinflusst von der Zusammensetzung und Größe des Kern und seiner Polarisierbarkeit, der Abschirmung des Kerns durch die Elektronen der 1S-Schale, Quanteninterferenz und weitere Effekte. Das macht Lithium zum perfekten Testobjekt um Theorien der Kern- und Atomphysik zu untersuchen. Hochpräzise Laserspektroskopie soll das Mittel der Wahl für diese Untersuchung sein.

Um Lithium spektroskopieren zu können, muss es zuerst erhitzt und in die Gasphase gebracht werden. Aufgrund der dafür nötigen Temperaturen sind die gemessenen Spektren allerdings stark durch den relativistischen Dopplereffekt beeinflusst. Messungen sind durchaus möglich, aber höhere Präzision benötigt niedrigere Temperaturen. Diese Arbeit präsentiert die Ergebnisse des Aufbaus einer magneto-optischen Falle zum Fangen und Kühlen von ${}^6\text{Li}$ -Atomen ($N = 10(1) \cdot 10^9$) sowie ihren zugehörigen Zeeman-Slower. Sowohl die dafür notwendigen Lasersysteme als auch die einzelnen Komponenten des Aufbaus werden ausführlich erläutert und analysiert.

Abstract

Lithium is the third element on the periodic table and the lightest alkali metal and the only one that has stable fermionic and bosonic isotopes. It is simple enough to be described *ab initio* but so complex that many physical effects have to be taken into account for a correct description. The D lines, i.e. the transitions from the groundstate $2S_{1/2}$ to the first excited states $2P_{1/2}$ and $2P_{3/2}$, are influenced by the composition and size of the nucleus and its polarizability, the shielding of the nucleus by the electrons of the 1S shell, quantum interference and more effects. This makes lithium the perfect test object to examine theories of nuclear and atom physics. High precision laser spectroscopy shall be the method of choice for this examination.

To perform spectroscopy on lithium, it first has to be heated and brought into the gas phase. Due to the therefor required temperatures, the measured spectra are strongly influenced by the relativistic Doppler effect. Measurements are absolutely possible but higher precision demands lower temperatures. This thesis presents the results of the installation of a magneto-optical trap for capturing and cooling of ${}^6\text{Li}$ atoms ($N = 10(1) \cdot 10^9$) as well as its dedicated Zeeman slower. Both the necessary laser systems and the setup's components are thoroughly explained and analyzed.

Contents

List of Figures	iii
List of Tables	vi
1. Introduction	1
2. The Laser Setups	4
2.1. Home-built External Cavity Diode Laser	4
2.1.1. Laser Diode Theory	5
2.1.2. The Real Laser Diode: Collimation	9
2.1.3. The Real Laser Diode: P-I-Curve	12
2.1.4. The Real Laser Diode: Frequency Tuning via Temperature . . .	13
2.1.5. The Real Laser Diode: Frequency Tuning via Current	17
2.1.6. External Cavity Diode Laser Setup	21
2.1.7. Doppler-Free Saturated Absorption Spectroscopy	24
2.1.8. Tapered Amplifier	31
2.2. Commercial ECDL	38
2.2.1. Li D Lines	42
2.2.2. Eliminating the Doppler Background	50
2.2.3. Frequency Calibration Procedure	53
2.2.4. Laser Locking	56
3. The Zeeman Slower	62
3.1. Hot Atomic Beams	62
3.2. The Zeeman Effect on the Lithium D Lines	68
3.3. The Setup	78
3.4. Slowing – Simulation Algorithm	80
3.5. Slowing – Velocity Measurement	83
3.6. Slowing – Comparing Simulation Results and Measurement	87
4. The Magneto-Optical Trap	95
4.1. General Setup	96
4.2. Trapping Beams	99
4.3. A Filled Trap	104
4.4. Loading and Unloading the MOT	109
4.4.1. The Loading Curve	113
4.4.2. The Loss Curve	115
4.5. MOT Temperature	117
4.5.1. The Problem with the ${}^6\text{Li}$ MOT	122
5. Conclusion and Outlook	127
5.1. Potential Improvements	128
5.2. Offspring Projects	130
5.3. Final Words	131
Bibliography	134
A. Appendix: Diodes	145

B. Appendix: The Fabry-Pérot Cavity	149
C. Appendix: Optical Elements	152
C.1. Beam Splitter	152
C.2. Retarder Plates	153
C.3. Optical Isolator	155
D. Appendix: MOT Laser Polarization and Jones Calculus	157
E. Appendix: ${}^6\text{Li } 2P_{3/2}$ excited state	160
F. Appendix: Generating Random Velocities	167

List of Figures

2.1. Recombination processes in LEDs	5
2.2. Light Amplification in a Laser Diode	6
2.3. p-n junction laser diode	7
2.4. Double heterojunction laser diode	8
2.5. Laser diode collimation and profile	10
2.6. Parameters of beam profile fit	11
2.7. Beam profile widths	12
2.8. P-I curve of laser diode	13
2.9. Frequency vs Temperature of laser diode	15
2.10. Laser frequency vs diode current	18
2.11. Amplification factors of a model diode	20
2.12. Photograph of the ECDL setup	21
2.13. P-I-curves of laser diode and ECDL	23
2.14. Mode hop-free ECDL scan	24
2.15. Stylized absorption spectroscopy setup and signal	26
2.16. DFSAS setup and signal	27
2.17. Velocity distribution for ${}^7\text{Li}$ at 300°C	27
2.18. DFSAS Spectrum of the ${}^7\text{Li}$ D_2 line	28
2.19. Λ -crossover resonance configuration	29
2.20. V-crossover resonance configuration	30
2.21. Tapered Amplifier Schematics	31
2.22. Photograph of the tapered amplifier setup	32
2.23. Schematic of laser setup including tapered amplifier	33
2.24. Tapered Amplifier output power vs applied current	34
2.25. Tapered amplifier output power vs seed beam polarization	35
2.26. Tapered amplifier output power vs applied current (Temperature comparison)	36
2.27. Tapered amplifier output power vs applied current (Seed power comparison)	37
2.28. Tapered amplifier output power saturation	38
2.29. Photograph of the insides of the Toptica TApr0	39
2.30. TApr0 scan range demonstration	39
2.31. TApr0 scan over lithium resonances	40
2.32. TApr0 free-running frequency over time	41
2.33. Allan Deviation of TApr0	42
2.34. ${}^6\text{Li}$ and ${}^7\text{Li}$ level scheme	44
2.35. ${}^6\text{Li}$ D_1 line DFSAS spectrum	45
2.36. ${}^6\text{Li}$ D_2 line and ${}^7\text{Li}$ D_1 line DFSAS spectrum	47
2.37. Second-order crossover resonance level scheme	48
2.38. ${}^7\text{Li}$ D_2 line DFSAS spectrum	49
2.39. DFSAS setup with chopper and lock-in amplifier	50
2.40. Schematic depiction of an arbitrary signal with multiple frequencies	51
2.41. Schematic of lock-in amplifier working principle	52
2.42. Comparison DFSAS vs regular transmission spectrum	52
2.43. Lock-in amplified ${}^6\text{Li}$ D_2 and ${}^7\text{Li}$ D_1 DFSAS spectrum	53
2.44. ${}^6\text{Li}$ D_2 and ${}^7\text{Li}$ D_1 DFSAS spectrum with fit (vs time)	55
2.45. ${}^6\text{Li}$ D_2 and ${}^7\text{Li}$ D_1 DFSAS spectrum with fit (vs frequency)	56

2.46.	Schematic of frequency stabilization setup	58
2.47.	Modulated DFSAS and error signal vs laser frequency	59
2.48.	Locked DFSAS and error signal vs time	60
3.1.	Schematic view of Hot Atomic Beam experimental setup	63
3.2.	Top view of hot beam spectroscopy setup	64
3.3.	Measured Fluorescence of a hot ${}^6\text{Li}$ atom beam	66
3.4.	Fitted temperature vs assumed angle between atom beam and laser beam	67
3.5.	Zeeman shifts of ${}^6\text{Li}$ $2S_{1/2}$ ground states	74
3.6.	Zeeman shifts of ${}^6\text{Li}$ $2P_{3/2}$ excited states	75
3.7.	Strength of allowed transitions driven by σ^+ light	77
3.8.	Magnetic field of a Zeeman slower	79
3.9.	Experimental Zeeman slower setup	80
3.10.	Determining the excited state by generating a random number	82
3.11.	Fluorescence signal of an unslowed and a slowed atom beam	84
3.12.	Fluorescence peak of slowed ${}^6\text{Li}$ atom beam around 446 799 803 MHz	86
3.13.	Fluorescence comparison: hot atom beam vs simulation	88
3.14.	Fluorescence comparison: slowed atom beam vs simulation	89
3.15.	Velocity vs position of atoms in the slower simulation	90
3.16.	Fluorescence comparison: slowed atom beam vs simulation (including slow atoms)	91
3.17.	Velocity distribution of simulated ${}^6\text{Li}$ atoms after slowing	92
3.18.	Difference in atoms within in a certain velocity class for the simulated unslowed and the slowed beams	93
4.1.	Level scheme of a simple atom in a 1D-MOT	95
4.2.	Magnetic quadrupole field within the MOT chamber	97
4.3.	Zoom in on MOT magnetic field center	98
4.4.	Simplified MOT laser setup	99
4.5.	Setup to turn one single-frequency laser beam into three separate two-frequency beams	102
4.6.	Schematic depiction of an acousto-optic modulator	103
4.7.	Comparison: AOM on vs AOM off	103
4.8.	Picture of the AOM crystal with and without applied RF signal	104
4.9.	Photograph of the ${}^6\text{Li}$ 3D-MOT	105
4.10.	Top view of setup to measure MOT fluorescence	107
4.11.	Top view of setup to measure MOT loading and unloading	110
4.12.	Exemplary image of MOT fluorescence recorded by CCD camera	111
4.13.	Two-dimensional Gaussian fit of MOT measurement by CCD camera	112
4.14.	Data and fit of cumulative exposure for MOT loading	114
4.15.	Corrected data and fit of cumulative exposure for MOT unloading vs time	116
4.16.	Exemplary measurement triplet of rubidium MOT transmission mea- sured by CCD camera	118
4.17.	Zoom-in on MOT region of exemplary rubidium MOT + Fit	120
4.18.	Expansion of an exemplary thermal ${}^{87}\text{Rb}$ cloud in a vacuum over time	121
4.19.	Picture of setup used to test shutdown process of magnetic field	123
4.20.	Measurement of delayed decline in magnetic field strength of proto- type coil in brass housing	124
4.21.	${}^6\text{Li}$ MOT cloud expansion and magnetic field difference vs time	125

5.1. Measurement of delayed decline in magnetic field strength of proto- type coil in plastic housing	129
5.2. Velocity distribution of ${}^6\text{Li}$ atom beam generated by a 2D-MOT setup	131
A.1. Excerpt of the periodic table	145
A.2. p-n junction	146
A.3. Relation between current and voltage applied to a p-n junction	147
B.1. Phase shift in a Fabry-Pérot cavity	149
B.2. Simulated Fabry-Pérot cavity transmitted intensity	151
C.1. 50/50 and polarizing beam splitter cubes	152
C.2. Quarter-wave plate and half-wave plate	153
C.3. Optical Isolator	155
E.1. Strength of allowed transitions driven by σ^+ light	163
E.2. Strength of allowed transitions driven by σ^+ light (Zoomed In)	164
E.3. Strength of allowed transitions driven by π light	164
E.4. Strength of allowed transitions driven by π light (Zoomed In)	165
E.5. Strength of allowed transitions driven by σ^- light	165
E.6. Strength of allowed transitions driven by σ^- light (Zoomed In)	166
F.1. Exemplary value generation using the acceptance-rejection method .	168
F.2. CDF for modified Maxwell-Boltzman velocity distribution	169

List of Tables

2.1.	Characteristics of HL6756MG laser diode	9
2.2.	Parameters of Temperature vs Frequency fit of laser diode	15
2.3.	Parameters of Laser mode fit of laser diode	18
2.4.	Chosen tapered amplifier parameters	34
2.5.	${}^6\text{Li}$ D_1 line frequencies	45
2.6.	${}^6\text{Li}$ D_2 line frequencies	46
2.7.	${}^7\text{Li}$ D_1 line frequencies	46
2.8.	${}^7\text{Li}$ D_2 line frequencies	49
3.1.	Resonance frequencies of ${}^6\text{Li}$ D2-lines	65
3.2.	Values of exemplary hot atomic beam fit	67
3.3.	Hyperfine structure constants for lowest ${}^6\text{Li}$ states	69
3.4.	Numbering for ${}^6\text{Li}$ states $2S_{1/2}$ and $2P_{3/2}$	70
3.6.	Zeeman shift eigenvalues of the ${}^6\text{Li}$ -ground states	72
3.7.	$2P_{3/2}$ eigenstates of ${}^6\text{Li}$ with corresponding $ F, m_F\rangle$ states	73
3.8.	Allowed transitions from ${}^6\text{Li}$ $2S_{1/2}$ to $2P_{3/2}$ depending on light polarization	76
3.9.	Fit parameters of slowed beam fluorescence	85
4.1.	Dipole-allowed σ^+ -transitions from the ${}^6\text{Li}$ $F_{\text{gs}} = 3/2$ ground state . .	100
4.2.	Dipole-allowed σ^- -transitions from the ${}^6\text{Li}$ $ F_{\text{gs}} = 3/2, m_F = 3/2\rangle$ ground state	100
4.3.	Two-dimensional Gaussian fit parameters for MOT measurement by CCD camera	113
4.4.	Fit parameters for MOT loading curve	115
4.5.	Fit parameters for MOT unloading curve	116
4.6.	Parameters of optical density fit	120
4.7.	Fit parameters of hot rubidium cloud expansion	121
C.1.	Special light polarizations and their corresponding polarization vectors	154
D.1.	Special light polarizations and their corresponding Jones vectors . . .	157
D.2.	Polarization shifting optical elements and their corresponding Jones matrices	158
E.1.	Reminder: $2P_{3/2}$ eigenstates of ${}^6\text{Li}$ with corresponding $ F, m_F\rangle$ states	163
F.1.	Prominent PDFs and their respective CDFs' inverse function	170

1. Introduction

One question that is often asked regarding fundamental research is: “Why?”

And besides sheer curiosity, the answer often is: “We don’t know. Yet.”

When Charles Babbage, Luigi Federico Menabrea, and Ada Lovelace thought about the *analytical engine* and the first ideas of hard- and software, they probably didn’t dream about the powerful computers of today which can be used to optimize agricultural processes to help feed people, recognize certain types of cancer better than human doctors to help heal people, and generate a plethora of text, pictures and even videos using deep neural networks.

When John Bardeen, Walter Brattain, and William Shockley constructed the first bipolar junction transistor, it was hard to imagine that today billions of nanometer-sized transistors could be combined into a single chip to make powerful tools such as personal computers, laptops and smartphones available to almost everybody, connecting people around the world and accelerating the creation of knowledge to unknown heights.

When Pohl et al. [PAN⁺10] started their yearslong journey to measure the proton radius with higher precision than ever before using laser spectroscopy on muonic hydrogen, they didn’t expect to find that the proton RMS charge radius $\sqrt{\langle r^2 \rangle}$ had been significantly overestimated. This result motivated many other experimentalists to remeasure $\sqrt{\langle r^2 \rangle}$ and confirm smaller values for the radius and the Rydberg constant R_∞ as well as theorists to refine nuclear and atomic models. Other nuclei, such as the deuteron, the helion and α , have also been measured and each of their radii’s precision has been improved. A lot of technical and theoretical insights had to be gathered to create and interpret the necessary data. How this knowledge will one day be used to improve life, only time can tell. Nevertheless, the importance of fundamental research cannot be overstated.

The stable isotopes of hydrogen (deuteron [PNF⁺16]) and helium (helion [TSF⁺23], α [KSA⁺21]) were measured in this and associated work groups using high precision laser spectroscopy. The next lightest nuclei are those of tritium (^3H) and lithium. Both are planned to be examined in this group. During this thesis, both lithium isotopes ^6Li and ^7Li were used, with a focus on ^6Li . The lithium isotopes are simple enough to allow for high accuracy *ab initio* calculation but complex enough to necessitate that several subtle effects are taken account in their theoretical description, such as electron shielding by the inner shell, the nuclei’s polarizabilities, three-nucleon forces, or quantum interference. Lithium is therefore the perfect testbed for verifying modern theoretical predictions.

At room temperature, lithium is naturally occurring in a solid state, albeit as a soft, light metal. In this form, performing laser spectroscopy on it is not possible. To allow for any experimentation, a gaseous target has to be created. The goal of this

work was the creation of such a target in the form of a magneto-optical trap (MOT). The several steps which had to be taken towards a functioning setup are presented in the thesis at hand.

As its name suggests, a magneto-optical trap comprises a magnetic field and an optical component: laser light. The multiple setups that produce the required laser beams are explained in section 2. As these setups contain diode lasers, i.e. laser systems that are built around a semiconductor chip emitting coherent and directed light, this section starts with an in-depth look on laser diodes and how to build a complete system around them. The home-built laser in section 2.1 serves as an example of an external cavity diode laser (ECDL) which can produce a beam of tunable frequency and low power. This laser is then used to explain the principle of Doppler-free saturated absorption spectroscopy (DFSAS, section 2.1.7). Many frequency measurements in this thesis were gauged using this technique. Finally, the setup is completed by a tapered amplifier (section 2.1.8), a special type of laser diode designed to further increase the beam's output power to make it usable as a Zeeman slower laser.

The second laser that was used followed the same design, although it is commercial rather than home-built. It is used to drive the MOT and is explained in section 2.2. The bought laser exhibits a higher stability than the first system and hence it is used to examine the first energy levels of ${}^6\text{Li}$ and ${}^7\text{Li}$: the $2S_{1/2}$, $2P_{1/2}$, and $2P_{3/2}$ states. The dipole-allowed transitions between these states, the so-called D lines, are analyzed in section 2.2.1 using DFSAS. Especially the ${}^6\text{Li } 2S_{1/2} \rightarrow 2P_{3/2}$ transitions are important to understand because the MOT runs on these transitions.

The solid sample of ${}^6\text{Li}$ has to be brought into the gas phase to allow for spectroscopy. This is done by heating it up to create a hot atomic beam, i.e. the ${}^6\text{Li}$ atoms have a longitudinal velocity distribution corresponding to a high temperature: broad and with a high mean velocity. Many of these atoms are too fast to be captured by the MOT. To increase its efficiency, the atoms have to be cooled down. This was done using a Zeeman slower which is described in section 3. A Zeeman slower uses a laser beam and a time-independent but position-dependent magnetic field to cool down an atomic beam. The laser beam is kept at a constant frequency but atoms see it Doppler-shifted depending on its own velocity. The magnetic field changes the atoms' resonance frequencies via the Zeeman effect to compensate for the Doppler shift.

It is common knowledge, that the anomalous Zeeman effect shifts an atom's energy levels depending on their magnetic quantum numbers and the strength of the magnetic field. For small fields, one speaks of the Zeeman effect while for strong fields the name Paschen-Back effect is used to signify the decoupling of the atom's different spins. But what happens at the transition between these domains? How do different field strengths influence the possible transitions? What is a *good* quantum number?

The effect has been analyzed to answer these questions and the results are presented in section 3.2. Using this knowledge, a Monte Carlo simulation (section 3.4) was built to predict the behavior of atoms inside a Zeeman slower and to better understand said behavior. In section 3.6, these predictions are then finally compared to fluorescence measurements (section 3.5) of the real Zeeman slower setup (section 3.3) to evaluate the validity of the simulation.

Lastly, the MOT is introduced in section 4. The setup, as it is described in section 4.1, comprises a magnetic quadrupole field and three retroreflected laser beams, one for each spatial direction. The beams are generated by the previously reviewed laser system and additional optical elements (section 4.2). The MOT's fluorescence is then analyzed to determine the number of trapped atoms (section 4.3) as well as its loading and unloading times (section 4.4).

With the current setup, the MOT could not be fully characterized. Unfortunately, the final temperature of the trapped atoms could not be determined because the magnetic field could not be quenched fast enough. Nevertheless, the general procedure to calculate the temperature by analyzing the absorption and expansion of a hot atomic cloud is explained in section 4.5. In the hope of the possibility of further research on the lithium MOT in the future, exemplary data of a rubidium MOT serves as an example to demonstrate the procedure.

In the end, the results of this work are concluded and a short outlook on other, related experiments in the group and potential improvements to this work are given in section 5.

2. The Laser Setups

A multitude of different laser beams is necessary to run a magneto-optical trap, operate a Zeeman slower, and do spectroscopy at the same time. Lasers are fitting light sources for these purposes as they produce highly coherent, stable and intense light beams. Different lasers were used over the course of this project, all of them external cavity diode lasers (ECDLs). In this chapter, the technical functionality of these devices is explained and their specific properties are analyzed.

A home-built ECDL which is described in section 2.1 will serve as an example for the general physics behind laser diodes and their use in experimental atomic physics are dissected. Another ECDL, a commercially available system, is explained in section 2.2. This system was used primarily to create the laser beams which were used to capture the lithium atoms in the magneto-optical trap. Additionally, several scans of the lithium resonance spectrum were produced with the help of this laser, as its stability and large scan range are ideal for this task. The procedure of gauging the frequency of a scan is explained in this section as well.

2.1. Home-built External Cavity Diode Laser

A laser is a useful tool to produce intense, stable and coherent beams of light which can be used for multiple purposes. Many different types of lasers exist:

- Solid-state lasers [Koe96], dye lasers [DH90] and gas lasers [EW07] which are based on solid, liquid and gaseous gain media. This gain medium is contained in a cavity to select the amplified wavelength.
- Free-electron lasers [FA18] aren't lasers in the original sense. No gain medium is used for amplification. These light sources produce beams by utilizing the fact that accelerated charges generate synchrotron radiation. High energy electrons are guided through spatially alternating magnetic fields of a so-called undulator, thus creating a beam of guided light.
- Diode lasers [San05] are based on semiconductor technology. If an electrical current flows through a diode it can emit light. Depending on the used material a wide variety of wavelengths can be produced.

While the latter might not produce the most intense light, compared to the alternatives, diode lasers are affordable, easy to build and run, and can be installed in very compact setups. The lasers that are currently being used to produce the light for the Zeeman slower as well as the lithium MOT beams are therefore based on laser diodes. In this section the functionality of laser diodes is explained by examining the home-built external cavity diode laser (ECDL).

2.1.1. Laser Diode Theory

A special type of diodes¹ are light emitting diodes (LEDs), specifically laser diodes. In contrast to light bulbs or other thermal radiation producing elements which emit a wide spectrum of light, the luminescence of an LED is based on excitation of electrons into the conduction band and their subsequent deexcitation and recombination with a hole. Therefore, they produce far narrower spectra. The transitions can be classified into three types [SNL21], which are visualized in fig. 2.1:

1. Interband transition:
 - a) intrinsic emission very close to the band gap,
 - b) high energy emission with energetic or hot charge carriers.
2. Transition with imperfections or physical defects:
 - a) from the conduction band E_C to an acceptor with energy E_A ,
 - b) from a donor with energy E_D to the valence band E_V ,
 - c) from a donor to an acceptor (pair emission),
 - d) interband transition via a low defect E_1 .
3. Intraband transitions with hot charge carriers:
 - a) completely within the conduction band E_C (*bremstrahlung*),
 - b) completely within the valence band E_V (Auger process).

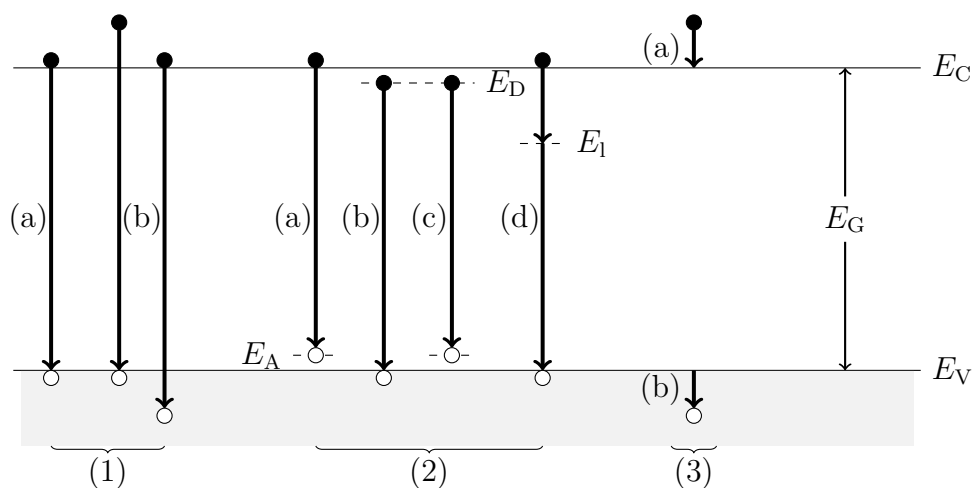


Figure 2.1: Possible recombination processes in LEDs as described in [SNL21]: (1) interband transitions, (2) transitions with physical defects, (3) intraband transitions. E_D and E_A are donor and acceptor levels, E_1 is a low defect, while E_G denotes the band gap.

¹For more information on diodes in general, see appendix A.

Transitions based on near band gap interband recombinations are the most probable and therefore changing the band gap by altering the composition of the semiconductor material or its temperature are an easy way to change the wavelength of the emitted photons [Str97].

To build a laser, three things are necessary [Dem11]: a gain material, an energy pump and a cavity. A laser diode can offer all these elements at once. Usually the valence band is far more populated than the conduction band² but by applying a high enough forward bias voltage, a region of population inversion around the p-n junction can be created as shown in fig. 2.2. Electrons in this region can recombine with holes by emitting photons of energy E_ν . This emission can be stimulated by other photons with the correct energy, thus amplifying light that passes the inversion region by a gain factor of $g > 1$. The acronym *laser* describes this process fittingly: *light amplification by stimulated emission of radiation*.

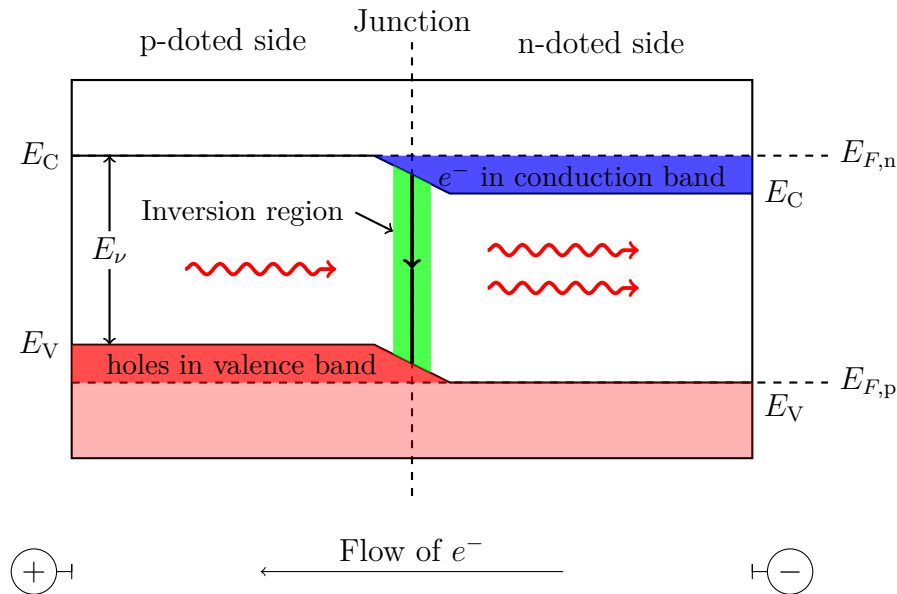


Figure 2.2: If a voltage is applied to a laser diode, it starts producing light. Once the resulting current is high enough, a region around the p-n junction forms where population inversion is present and electrons in the conduction band E_C can recombine with holes in the valence band E_V . Light with the correct frequency E_ν/h that passes this region can stimulate the recombination and emission of additional photons. This amplification doesn't necessarily have to happen from the p-doped to the n-doped side. Any light that passes this region is amplified.

The amplification itself is not enough to build a laser. The two opposite facets on both sides of the diode's p-n-junction form a Fabry-Pérot cavity [Her86] of optical length $L' = n \cdot L$, where n is the materials reflective index and L is it's length³. In

²Normally the conduction band of semiconductors isn't populated at all because the Fermi level E_F is below the conduction band. If it was above the band the material wouldn't be a semiconductor anymore but a normal conductor.

³More information on the Fabry-Pérot cavity can be found in appendix B.

this cavity, light of the correct wavelength ($\lambda = 2L'/m$, $m \in \mathbb{N}$) can bounce back and forth between the reflecting sides and pass the gain region again and again. With every passing, the light accumulates more power and subsequently leaves the diode as a high intensity, highly directed beam. The result is a simple homojunction laser diode [Sun15] as depicted in fig. 2.3.

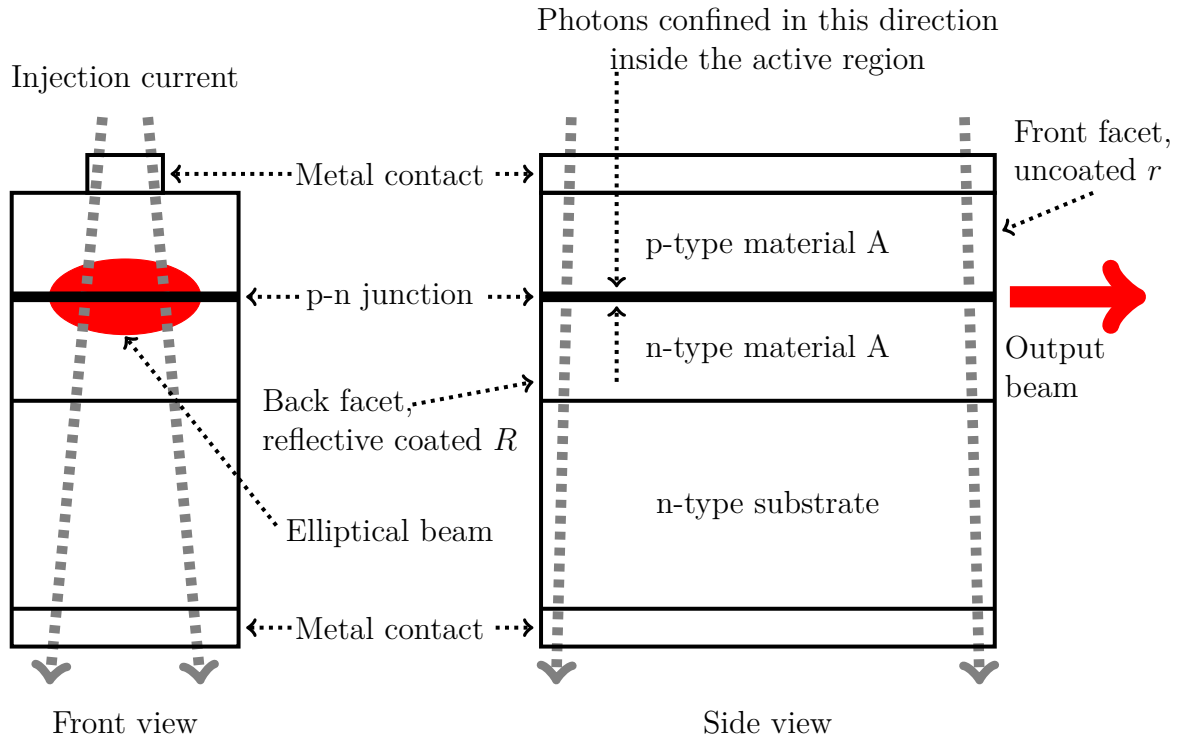


Figure 2.3: A simple laser diode based on a p-n junction. The diode itself is the gain medium. Both its facets form a Fabry-Pérot cavity and one of them is coated with a reflective layer which makes its reflective index R much greater than the respective index r of the uncoated facet ($R \gg r$). Therefore, the diode has a predominant direction in which it emits light. Picture based on [Sun15].

This simple design still has some flaws. The light mode that builds up is defined by the spatial boundaries set by the diode. In the direction of the beam, the boundary is given by the length of the cavity, i.e. the distance between the facets and the refractive index of the material. In the vertical direction, the mode is limited by the size of the depletion layer of the p-n junction where stimulated emission is happening. The gain profile in horizontal direction depends directly on the electrical current. Lasing can only happen where current flows through the material because only there population inversion is present. To conclude, this setup is defined by its gain and is therefore called a gain-guided laser diode. The electric field as well as the electron and hole density is not well confined to the active layer, i.e. the p-n junction, which results in a low recombination rate, low lasing efficiency and a high lasing threshold [Sun15].

To overcome these flaws, double heterojunction laser diodes were developed in which

semiconductors of different dotings are sandwiched between one another. Such a diode is depicted in fig. 2.4. The active gain region is encapsulated by a different material with a different refractive index. The innermost pair of layers confines the minority charge carriers to the active region, while the outer layers confine the optical beam [Koe96]. This type of laser diode is index-guided.

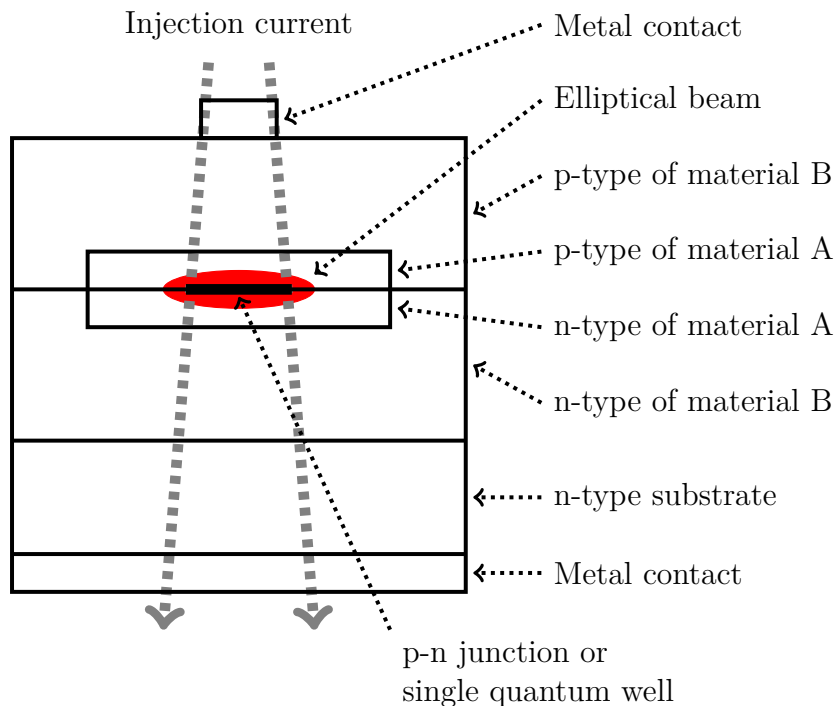


Figure 2.4: Front view of an embedded double heterojunction laser diode. Each material has a different composition and refractive index. The p-n-junction is so thin, it forms a quasi-two-dimensional quantum well. Picture based on [Sun15].

By further decreasing the height of the active region to 10 nm and below a quasi-two-dimensional quantum well is formed. Its behavior is described as in [Zap04]. The optical and electrical properties of the material, such as transition rates, polarization, and optical gain, change significantly. The reduction of the dimension leads to a quantization of the charge carrier's allowed energies. Instead of a continuous band of possible states which is present in a bulk three-dimensional material, the energy level become discrete again. Assuming a thickness t and an energy depth E_w which is the difference in energy gap between the well and the surrounding layers, a total of

$$n_{\max} = 1 + \text{int} \left(\sqrt{\frac{2m^* E_w t^2}{q\pi^2 \hbar^2}} \right) \quad (2.1)$$

levels are allowed where the function $\text{int}(x)$ rounds down to the next integer. The coefficient m^* describes the effective mass of the charge carriers. In solid materials, electrons and holes move as if they are particles in a vacuum with mass m^* , often

given in units of electron masses m_e . For $(\text{Al}_x\text{Ga}_{1-x})_{0.5}\text{In}_{0.5}\text{P}$ which is the III-V-semiconductor comprised by the used laser diode, the respective values are $m_e^* = 0.113m_e$ and $m_h^* = 0.635m_e$ [CLS⁺08]. Assuming an infinitely deep energy well, the possible energy level are given by

$$E_n = \frac{\hbar^2\pi^2}{2m^*t^2}n^2. \quad (2.2)$$

As usual, n is the main quantum number with $n \in \mathbb{N}$. Both valence band and conduction band possess these discrete levels so an expression for the total energy difference between the lowest energy levels ($n = 1$) can be given as

$$E_\gamma = E_g + \frac{\hbar^2\pi^2}{2t^2} \left(\frac{1}{m_e^*} + \frac{1}{m_h^*} \right). \quad (2.3)$$

Photons of the energy E_γ can be emitted from or absorbed into the quantum well. It should be noted that E_γ is greater than the band gap E_g of the bulk material. The quantum well increases and narrows the frequencies which the laser diode can produce. Multiple quantum wells can be stacked on top of each other to build a laser diode with higher output power, narrower line width and more controllable light frequencies.

2.1.2. The Real Laser Diode: Collimation

The laser diode that was used for this home-built ECDL setup is a multi quantum well AlGaInP diode, specifically a HL6756MG [Tho08]. Some of its characteristics are listed in table 2.1.

The transitions that are probed are resonant to 671 nm light. As can be seen in the last row of the table, the emitted wavelengths vary quite broadly. This is normal behavior for semiconductor components, variance during the manufacturing process leads to different properties of the diodes. Therefore, multiple diodes were tested to find the most suitable one. The chosen diode with adequate power, stability and scanning range around 671 nm is presented in this section.

Table 2.1: Optical and electrical characteristics of an HL6756MG laser diode at temperature $T = 25^\circ\text{C}$ and output power $P_O = 15\text{ mW}$. Data taken from datasheet [Tho08].

	Symbol	Min	Typ	Max	Unit
Operating current	I	-	35	45	mA
Beam divergence parallel to the junction	θ_{\parallel}	5	8	11	$^\circ$
Beam divergence parallel to the junction	θ_{\perp}	20	24	28	$^\circ$
Lasing wavelength	λ	660	670	680	nm

Firstly, the light beam has to be collimated. The aforementioned table states beam divergences between $5^\circ \leq \theta_{\parallel} \leq 11^\circ$ and $20^\circ \leq \theta_{\perp} \leq 28^\circ$. Note that the perpendicular divergence is much larger than its parallel counterpart. This is a direct consequence of the way multi quantum well diodes produce light. The active region is highly constrained in the vertical direction but not so much horizontally. A contour plot of the emitted beam's profile taken at 20 cm distance from the diode is depicted in fig. 2.5b. The diode was operated at a current of 30 mA and a temperature of 20°C .

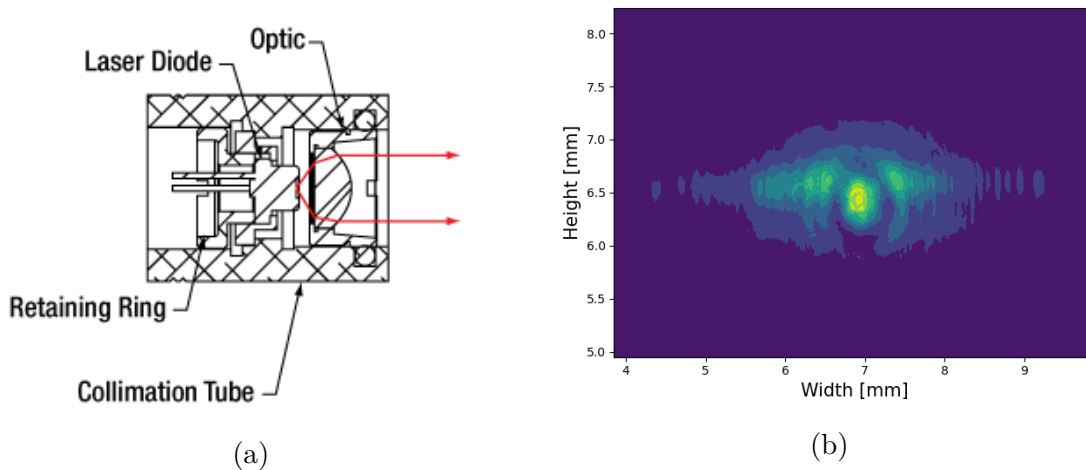


Figure 2.5: Schematic of a laser diode and a collimation lens (a, taken from [Thoa]) and a measured profile of the emitted light at 20 cm distance (b). As expected for a multi quantum well diode, the produced beam is far from Gaussian.

Ideally, a laser beam's profile has a Gaussian intensity distribution⁴ following

$$I(\vec{r}) = I_0 e^{-\vec{r}^T M \vec{r}}. \quad (2.4)$$

The vector \vec{r} and its transposed \vec{r}^T are given by the transverse distance to the center of the beam $\vec{r} = x \cdot \hat{e}_x + y \cdot \hat{e}_y$. In this notation, the beam propagates into the z -direction. For a Gaussian beam M is a simple diagonal matrix

$$M_o = \begin{pmatrix} \frac{1}{2\sigma^2} & 0 \\ 0 & \frac{1}{2\sigma^2} \end{pmatrix} \quad (2.5)$$

which results in the intensity distribution becoming

$$I(x, y) = I_0 e^{-\frac{x^2+y^2}{2\sigma^2}} = I_0 e^{-\frac{r^2}{2\sigma^2}} = I(r) \quad (2.6)$$

where the radius r replaces the transverse coordinates x and y . The measured profile is elliptic rather than circular symmetric, so the matrix should be written as

⁴A Gaussian beam is easier to handle because it is angularly symmetric, has its highest intensity in the center, and it can be coupled with high efficiency into light guiding fibers.

$$M_{\text{ellipse}} = \begin{pmatrix} \frac{1}{2\sigma_x^2} & 0 \\ 0 & \frac{1}{2\sigma_y^2} \end{pmatrix}, \quad (2.7)$$

with two separate standard deviations σ_x and σ_y , one for the major and one for the minor axis. Additionally, the ellipse could be tilted by an angle θ . A function describing such an intensity profile (including a constant background I_0) is given by

$$I(x, y) = I_0 + I_1 e^{-\frac{((x-\mu_x)\cos(\theta)-(y-\mu_y)\sin(\theta))^2}{2\sigma_x^2} - \frac{((x-\mu_x)\sin(\theta)+(y-\mu_y)\cos(\theta))^2}{2\sigma_y^2}}. \quad (2.8)$$

The measured beam profile is not Gaussian, it isn't even symmetric. The bright spot in the middle is below the less bright area and several vertical lines can be made out where the intensity drops. Nevertheless, using eq. (2.8) to approximate the beam profile is helpful to classify the collimation of the beam. A non-linear least square procedure [VGO⁺20] was used to fit the given distribution to several intensity profiles taken at different distances to the laser diode. The data is given as a two-dimensional histogram, x and y specify the bin's position and z its height. The positional coordinates are assumed to be errorless while z which represents a counted number of photons⁵ has the error $\Delta z = \sqrt{z}$. One such fit is shown in fig. 2.6. The errors are also obtained from the fit algorithm. A seven-dimensional (one for each fit parameter) covariance matrix is calculated, its diagonal entries are the squares of the respective errors, assuming uncorrelated fit parameters.

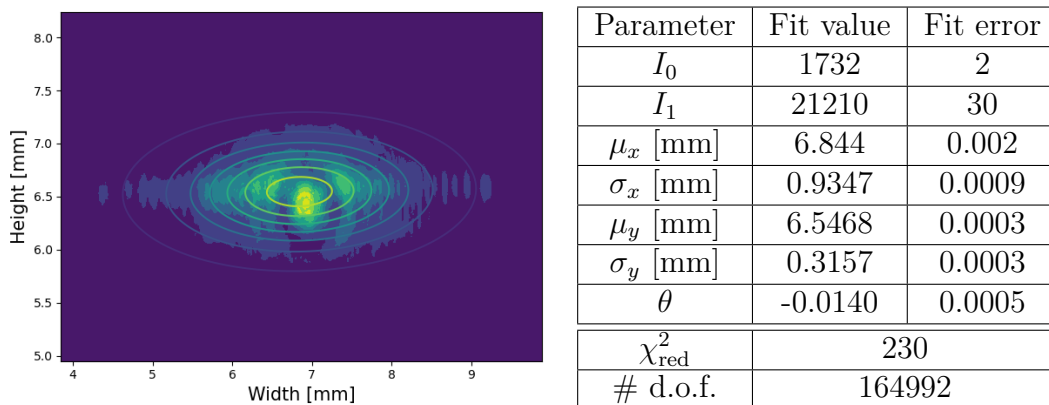


Figure 2.6: Fit of a measured beam profile of the light emitted by a laser diode. Measured at a distance of 20 cm. The reduced chi-square χ_{red}^2 is expectedly high, as the used fit function doesn't incorporate most features of the measured data. The number of degrees of freedom (d.o.f.) is also given.

⁵The beam profiler is based on a CCD sensor. Every photon that hits a sensor cell has certain probability of exciting an electron of the material to the conduction band, the so-called quantum efficiency. The current that is measured when the cells are flushed is proportional to the amount of excited electrons. Therefore, stochastic counting error is justified as a conservative error estimation.

The widths of the intensity ellipses' semi-major and semi-minor axes are proportional to the standard deviations σ_x and σ_y of the gaussian fit function given above. Therefore, plotting these values against the distance of the beam profiler to the diode, as depicted in fig. 2.7, gives an insight on the collimation of the laser beam. It is easy to see, that the beam is diverging because the lens in front of the diode is not positioned ideally. Nevertheless, for the purpose of building an ECDL this setting is sufficient. The broadening is negligible considering the lasers compact setup.

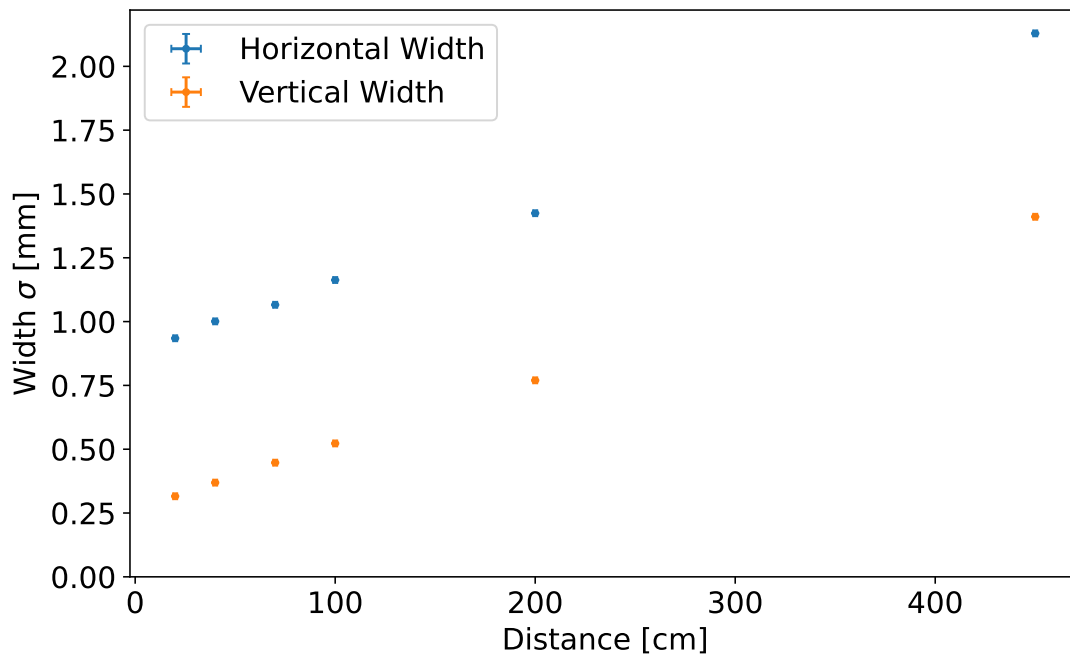


Figure 2.7: Standard deviations extracted from beam profile fits depending on the distance from the light emitting laser diode.

2.1.3. The Real Laser Diode: P-I-Curve

For the laser diode to produce light, an electrical current I must flow through it. The measured output power P depends on I and so a P - I -curve was taken, as shown in fig. 2.8. Up to a certain threshold current $I_{\text{th}} \approx 15 \mu\text{A}$, the measured power doesn't increase significantly. The diode behaves like a normal LED and emits incoherent red light without amplification. But once I_{th} is reached, the power of the emitted light grows linearly with I because it depends on the amount of electrons that can be excited to the conduction band. The more electrons are in the conduction band, the more can be deexcited by a passing photon, the higher the gain of the material. These electrons are delivered by the applied current. Thus, increasing I increases P in a linear fashion until saturation effects come into play which are not shown here.

These effects occur at higher values of I which were not probed to avoid damaging the diode.

The diode's output power at $I = 35$ mA and temperature $T = 20^\circ\text{C}$, which is the typical operating current (see table 2.1), is measured to be $P = 18.7(1)$ mW. This is above the typical power output stated by the manufacturer, making this diode a promising candidate for building an ECDL.

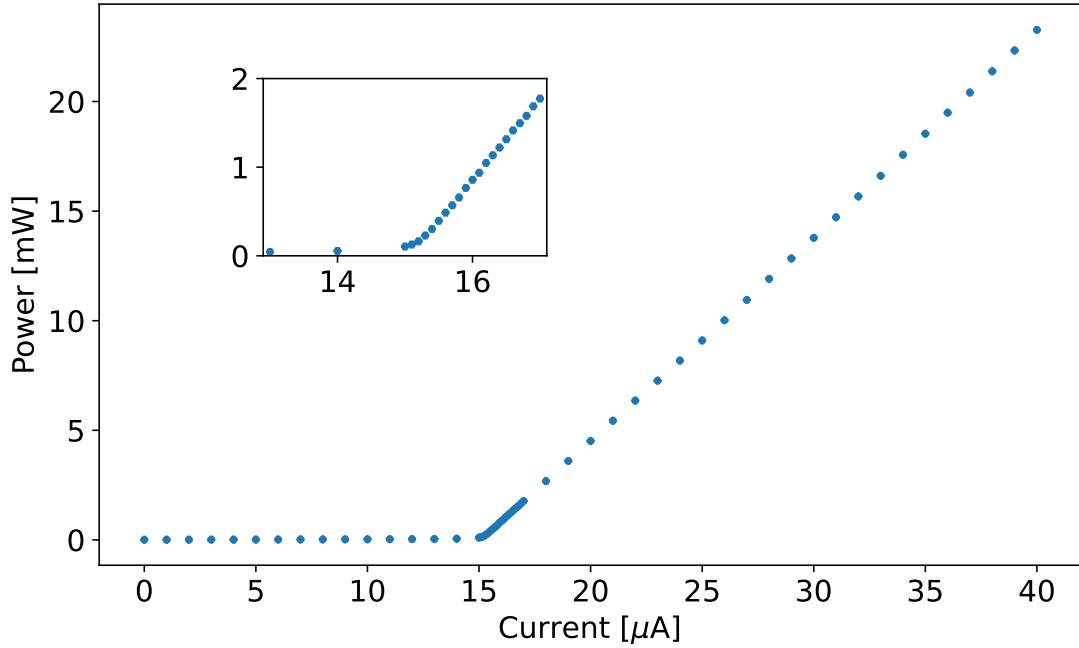


Figure 2.8: P - I -curve of the used laser diode and a zoom-in of the low current regime. Below a certain threshold I_{th} the diode behaves like a regular LED, it produces incoherent light without amplification. For $I > I_{\text{th}}$ population inversion exists in the active layer and coherent laser light is emitted.

2.1.4. The Real Laser Diode: Frequency Tuning via Temperature

A diode that constitutes a good candidate for the ECDL should be tunable to a wavelength of $\lambda = 671$ nm or a frequency $\nu = 446.8$ THz, respectively. Two factors affect the output of the diode: its temperature and the electrical current that flows through it. The reason for this can be found in eq. (2.3). The photon energy and therefore its frequency is linearly dependent on $\frac{1}{t^2}$ where t is the thickness of the active region in the diode. Increasing t leads to decreasing frequencies.

The length of the diode is also important. As mentioned above, the high-reflective back facet of the diode and its front facet form a Fabry-Pérot cavity in which such wavelengths λ_n that fulfill

$$\lambda_n = \frac{2L'}{m} = \frac{2nL}{m} \quad (2.9)$$

experience a maximum of amplification. Here, L' is the optical length of the cavity, i.e. the distance from the front to the back facet of the diode L multiplied by the material's refractive index n , and $m \in \mathbb{N}$. Depending on the reflectivities of the facets, here denoted as R and r for the back and front respectively, the intensity I of the emitted radiation is⁶

$$I \propto \frac{1}{1 + Rr - 2\sqrt{Rr} \cos\left(\frac{4\pi L'}{\lambda}\right)} \quad (2.10)$$

which is maximal for $\cos\left(\frac{4\pi L'}{\lambda}\right) = 1$. This yields the requirement for λ stated above. But wavelengths that don't satisfy this condition can still lead to a non-zero intensity.

While eq. (2.3) defines the possible frequencies, eq. (2.10) sets limits to the wavelengths. Together they confine the produced laser light. At first, the temperature⁷ T was scanned over a small range from 19 to 21 °C. The light was guided into a wavelength meter with a 30 MHz absolute accuracy⁸ [Hig23] and T was adjusted. After 2 min, T and therefore λ settled, i.e. its drift over time became significantly lower than the wavemeter's accuracy, the frequency ν was read out and T was adjusted anew. The results and the targeted frequency which is necessary for spectroscopy on ⁶Li and ⁷Li are depicted in fig. 2.9.

Typically, materials that are heated expand and so does the diode. This increases the thickness t and L and therefore the emitted frequency declines. This decline was fitted using a linear model

$$\nu(T) = \nu_0 - c \cdot (T - T_0), \quad (2.11)$$

because the expansion was considered to be sufficiently small for a first-order approximation to be adequate.

Two such linear features are present. As the temperature increases above a certain limit, the equations that govern the possible amplified frequencies allow multiple modes at once. The laser becomes unstable and jumps back and forth between these modes until the temperature is high enough to only allow a single mode again. This mode competition and the resulting mode hopping is explained below in section 2.1.5. Both features were fitted using a weighted orthogonal distance regression procedure [BD89]. Their respective parameters are listed in table 2.2. The constant T_0 was not fitted but chosen as 20 °C.

⁶A derivation can be found in the appendix appendix B.

⁷This temperature is not the temperature of the diode itself. The diode is installed on an aluminum block that is cooled by a Peltier element to hold it at a constant temperature.

⁸The absolute accuracy describes the error of the absolute value of a frequency measurement. Relative to a different frequency, the device can determine a frequency with an accuracy of 1 MHz.

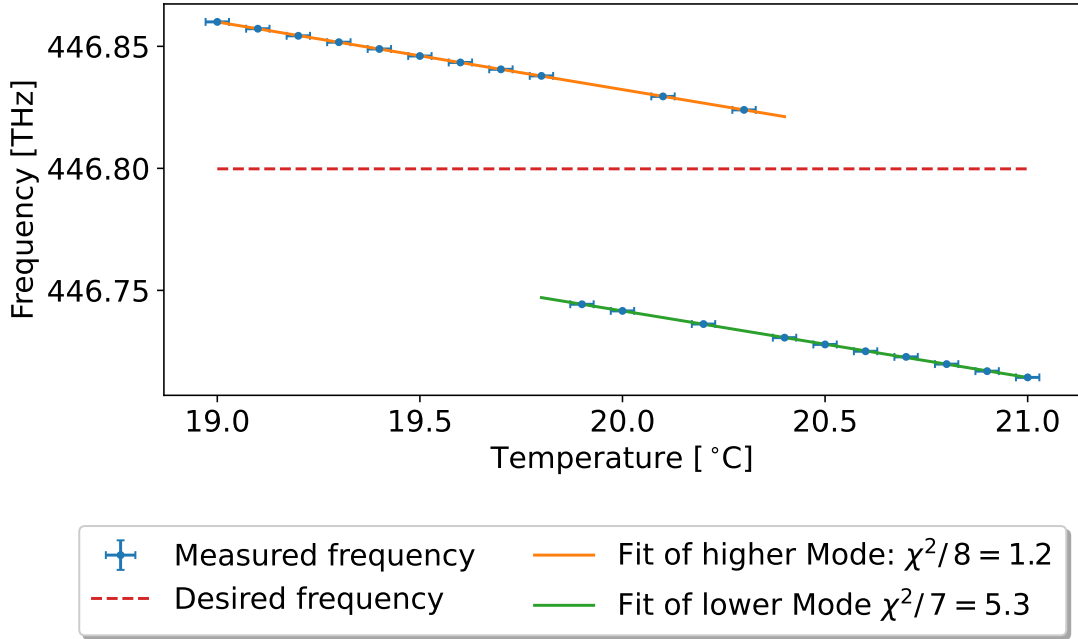


Figure 2.9: Measured laser frequency versus temperature at current $I = 35$ mA. The diode can produce multiple frequencies in two oscillation modes, roughly 90 GHz apart. These modes are shown as linear fits. Note that although the reduced χ^2 are given, the fits were produced using orthogonal distance regression to take horizontal and vertical errorbars into account. The χ^2_{red} are therefore not necessarily close to 1. The light jumps from high to low frequencies once a certain threshold is passed. Nevertheless, the desired frequency cannot be reached by temperature adjustment alone.

Table 2.2: Parameters of linear fits to temperature dependance of frequency of light produced by a laser diode.

Mode	ν_0 [THz]	c [GHz/K]
High	446.83223(3)	27.70(5)
Low	446.74159(7)	27.3(1)

The parameters ν_0 and c describe two fundamental properties of the diode, its length and its thermal expansion. In a first-order approximation the length L of the diode depends on the temperature T following

$$L(T) = L_0 + \alpha_L(T - T_0), \quad (2.12)$$

where L_0 is the length at a certain temperature T_0 and α_L is the thermal expansion coefficient. According to eq. (2.9) this change in length directly changes the wavelength of the light

$$\begin{aligned}\lambda_n(T) &= \frac{2L_0}{n} + \frac{2\alpha_L}{n}(T - T_0) \\ &= \lambda_{n,0} + \alpha_{\lambda_n}(T - T_0),\end{aligned}\tag{2.13}$$

where $\lambda_{n,0}$ is the wavelength of the n -th longitudinal mode of the cavity formed by the diode at T_0 and α_{λ_n} is the rate of change in this wavelength. It is important to note that λ_n is the wavelength in the medium of the cavity, i.e. of the diode. Because α_{λ_n} is a function of n , different modes change differently with temperature and therefore the frequency ν changes differently as seen in the above table. With a medium- and frequency-dependent speed of light c_ν , the frequency is given by

$$\begin{aligned}\nu_n(T) &= \frac{c_\nu}{\lambda_{n,0} + \alpha_{\lambda_n}(T - T_0)} \\ &\approx \frac{c_\nu}{\lambda_{n,0}} - \frac{c_\nu \alpha_{\lambda_n}}{\lambda_{n,0}^2}(T - T_0),\end{aligned}\tag{2.14}$$

A comparison with the fit function eq. (2.11) reveals that $b = \frac{c_\nu}{\lambda_{n,0}} = \frac{c_\nu n}{2L_0}$ and $m = \frac{c_\nu \alpha_{\lambda_n}}{\lambda_{n,0}^2} = \frac{\alpha_L c_\nu n}{2L_0^2}$. Under the assumption that the difference of phase velocity between the modes is negligible and that the two frequencies depicted belong to the n -th and the $n + 1$ -th mode, their mode numbers can be determined by

$$\frac{b_{n+1}}{b_n} = \frac{n+1}{n} \Rightarrow n = \frac{b_n}{b_{n+1} - b_n}.\tag{2.15}$$

Consequentially, the depicted lines correspond to the 4929 ± 4 -th and the 4930 ± 4 -th mode, respectively, with a free spectral range (FSR) of $\Delta\nu_{\text{FSR}} = b_{n+1} - b_n = 90.60(8)$ GHz.

Unfortunately, the length of the diode and the refractive index of its material could not be reliably determined. The datasheet [Tho08] mentions a diode length of 1.27 mm, while a cavity of length $L = \frac{c}{2\Delta\nu_{\text{FSR}}} = 1.654(1)$ mm would produce the measured free spectral range for a refractive index of 1. To correct for the difference, the diode material would need to have a refractive index of $n_r = \frac{L}{1.27 \text{ mm}} = 1.303 \pm 0.001$ but AlGaInP has a value of $n_r \approx 3.4$ [PX14]. It is well possible that the refractive index is similar to the calculated value because it depends on the chemical composition of the material which is unknown. The formation of the light mode inside the cavity that is created by the diode also changes the index by locally heating up the material.

If it is assumed that the calculated value and the length given by the datasheet are correct the thermal expansion coefficient α_L is found to be

$$\alpha_{L,\text{Low}} = \frac{2 L_0^2 m_{\text{Low}} n_r}{c n_{\text{Low}}} = 0.777(3) \frac{\text{nm}}{\text{K}} \quad (2.16)$$

for the lower mode and

$$\alpha_{L,\text{High}} = \frac{2 L_0^2 m_{\text{High}} n_r}{c n_{\text{High}}} = 0.788(2) \frac{\text{nm}}{\text{K}} \quad (2.17)$$

for the higher mode. It's obvious that both these values must be the same but they are only similar in magnitude. A cause for the mismatch could be an insufficient fit model. It was assumed that the only effect that changes the wavelength is the linear thermal expansion of the diode. But as eq. (2.3) shows, the energy of the produced photons depends on the thickness of the amplification layer. This value also changes as the diode expands. This effect is not incorporated yet. Further investigation is needed to develop an adequate theory to better characterize the diodes temperature dependence.

Finally, a red dashed line can be seen in fig. 2.9 which shows the desired frequency needed for performing spectroscopy on ${}^6\text{Li}$ and ${}^7\text{Li}$. While both fits theoretically cross this line at a certain temperature the frequency itself is unreachable as the diode's mode "jumps" right over it. Change of temperature alone is not sufficient to control the frequency so another parameter has to be considered: the diode current.

2.1.5. The Real Laser Diode: Frequency Tuning via Current

The laser light's frequency in relation to the current applied to the diode was measured and is depicted in fig. 2.10. The temperature of the aluminum block which serves as the diode's heat sink was kept at $T = 20^\circ\text{C}$. As the driving current increases, the frequency decreases. Higher currents lead to higher temperatures within the diode itself which in turn decrease the frequency as explained in the last section. Additionally, the change in current changes the amount of charge carriers at the p-n junction which in turn changes the refractive index and the maximum photon energy [SNL21].

Just like in fig. 2.9 mode hops are visible. At certain currents the laser becomes unstable and hops to a lower mode. A linear function in the form of

$$\nu(I) = \nu_0 - c \cdot (T - T_0) \quad (2.18)$$

was used to fit the lower three of the visible modes with $x_0 = 35 \text{ mA}$. The results of the fit can be found in table 2.3 and are represented in fig. 2.10.

Table 2.3: Parameters of linear functions fitted to different laser oscillation modes in dependence of diode current.

	ν_0 [THz]	c [GHz/mA]
Higher Mode	446.92354(8)	7.46(2)
Central Mode	446.83236(5)	7.74(5)
Lower Mode	446.7423(1)	8.12(3)

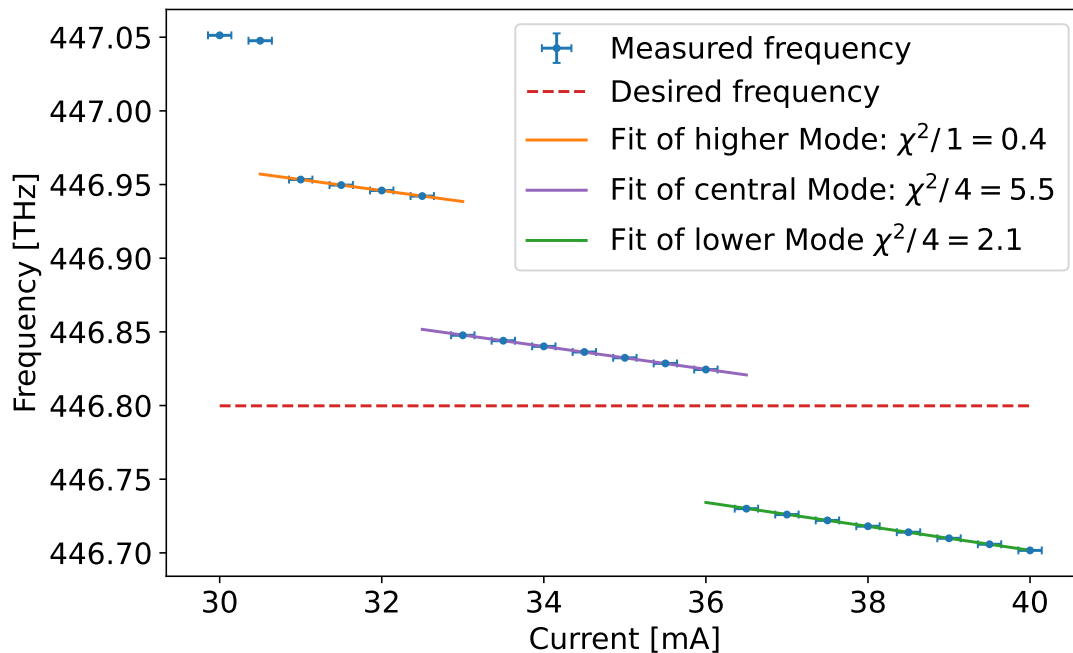


Figure 2.10: Laser frequency versus diode current. Multiple modes of oscillation are visible with sudden jumps between them at certain currents. The lower three modes were fitted using a linear function. Note that although the reduced χ^2 are given, the fits were produced using orthogonal distance regression to take horizontal and vertical errorbars into account. The χ_{red}^2 are therefore not necessarily close to 1. Additionally, a dashed line indicates the frequency which is needed to do spectroscopy of the lithium D lines. The fit parameters are listed in table 2.3.

The free spectral range can be given by $\nu_{0,H} - \nu_{0,C} = 91.18(9)$ GHz or $\nu_{0,C} - \nu_{0,L} = 90.1(1)$ GHz or $(\nu_{0,H} - \nu_{0,L})/2 = 90.62(6)$ GHz where $\nu_{0,H}$, $\nu_{0,C}$, and $\nu_{0,L}$ are the offset parameters of the higher, the central, and the lower oscillation mode, respectively. In magnitude they are all similar to each other and the value that was found during the investigation of temperature dependence $\Delta\nu_{\text{FSR}} = 90.60(8)$ GHz. However, they are not the same. This is because a change in current not only alters the amount of charge carriers in the amplification layer and the gain profile of the material but also changes the temperature of the diode and therefore the length of the cavity which it forms⁹.

⁹The diode cannot be cooled directly, it is connected to a temperature stabilized heat sink. Even if the outside of the diode could be cooled directly, the current within would heat up the active

Consider eq. (2.10), which gives a relation between the frequency ν of light in a cavity of length L and the power P of said light. Only certain frequencies, certain modes of oscillation, experience amplification in this cavity. This relation is plotted in fig. 2.11 for a theoretical diode with reflectivities of $R = 100\%$ and $r = 30\%$ and a length of $L = 1.654\text{ mm}$ so it produces similar laser modes as the real diode that is characterized in this chapter. Additionally, consider this diode amplifies light depending on its frequency. The gain experienced by the light depends on a multitude of the material's attributes, one of them being the current that flows through it. Unfortunately, it was not possible to measure the amplification profile of the real diode, so it is simply assumed that the profile of our model diode follows a normal distribution

$$A(\nu) \propto e^{-\left(\frac{\nu - \nu_0(I)}{\sqrt{2}\sigma}\right)^2}. \quad (2.19)$$

In this model, the center frequency ν_0 is a function of the current I , specifically a linearly declining function¹⁰. Increasing the current lowers the frequency which is amplified the most. This is also depicted in fig. 2.11. The last feature in the aforementioned plot is the product of both amplification mechanisms. As there is only a limited amount of electrons in the conduction band to recombine with holes, the different oscillation modes compete for these electrons. Therefore, the resulting laser light will have the frequency for which the total amplification is the highest. Different situations are shown in the plot:

- a) A clear maximum of the gain product is visible. The diode emits light of this frequency.
- b) The current has been increased slightly. The diode's gain profile moves to lower frequencies and so do the cavity modes because the higher current slightly increases the diode's internal temperature. The diode expands and the cavity which is formed by its back and front facet therefore amplifies smaller frequencies than before. The highest gain product still belongs to the same mode as before (albeit at a lower frequency) but the next lower mode's total gain is now similar in height. The modes start competing for minority charge carriers.
- c) The current has been increased even further. The diode gain moved so far to lower frequencies that the total gain of the previous mode is not the maximum anymore. A sudden mode jump to a lower mode occurs.

The model diode shows the same behavior as the real one. Small changes in current lead to small linear changes in laser frequency. The frequency decreases as the

region and thereby increase the active region's temperature and the temperature gradient from the diode's center to its edge.

¹⁰It has to be declining because the mode jumps to lower frequencies.

temperature increases because longer cavities correspond to lower resonance frequencies. At certain currents, a mode hop appears. The light's frequency abruptly drops because the diode gain profile moves faster to lower frequencies than the cavity gain profile. If it moved slower or even in the other direction, the modes would jump to higher frequencies or not at all. The temperature dependence shows a similar behavior which can be explained the same way.

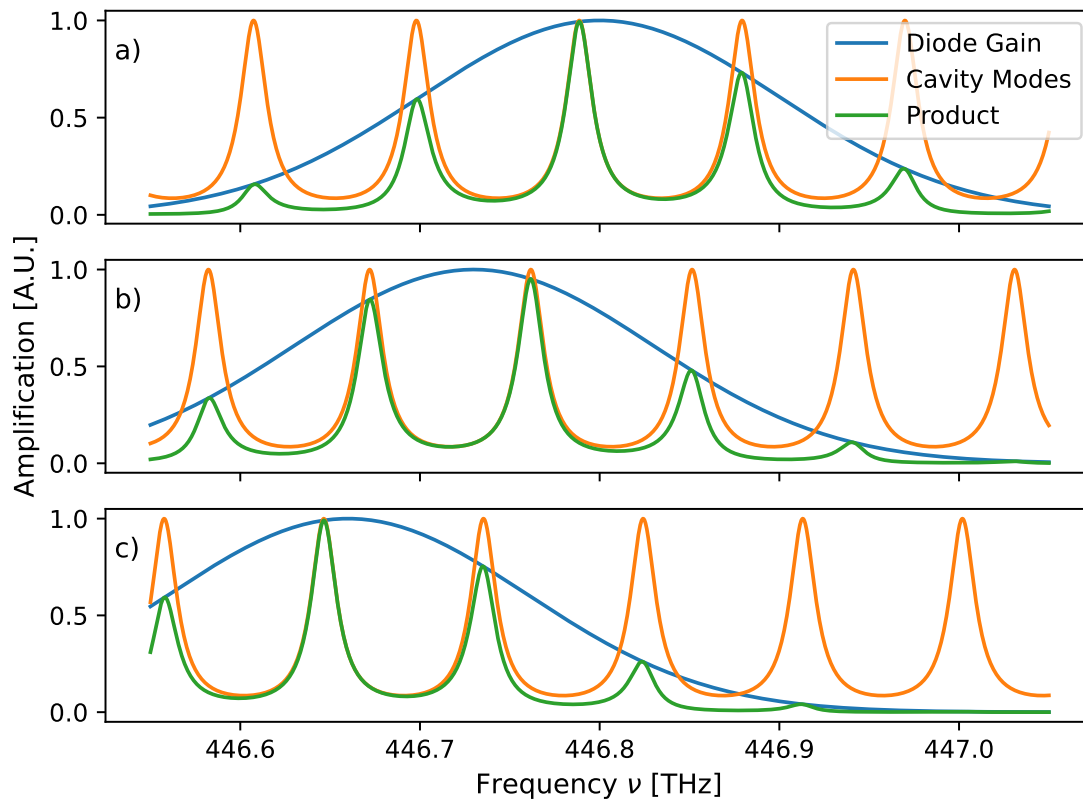


Figure 2.11: Schematics of different amplification factors of a theoretical model diode for increasing currents: **a)** Starting current. A clear amplification maximum is visible. **b)** Current is slightly increased. The cavity modes and the diode gain move to lower frequencies. The highest gain can be found for the same mode as before. **c)** Current is increased even further. A lower mode now experiences the highest gain. This results in a mode hop.

Finally, the desired frequency to perform spectroscopy on lithium is also plotted in fig. 2.10 and just like in section 2.1.4 this specific frequency cannot be reached. With achievable parameters for T and I , the diode alone is therefore not sufficient for the purpose of this experiment. An additional element is needed, i.e. a reflection grating to form an external cavity. The resulting setup is discussed in the next section.

2.1.6. External Cavity Diode Laser Setup

To achieve laser light at the desired frequency another wavelength sensitive element has to be added. Two possible solutions were tested during this thesis: a setup using an interference filter [BGB⁺06, JZT⁺16] or a reflection grating [AWB98, CMM⁺14]. As the latter produced more reliable results, a design based on [RWE⁺95] was chosen which is shown in fig. 2.12. A grating which reflects some part of the beam back into the diode creates an external cavity further restricting the allowed wavelengths. This setup is therefore called an external cavity diode laser or ECDL.

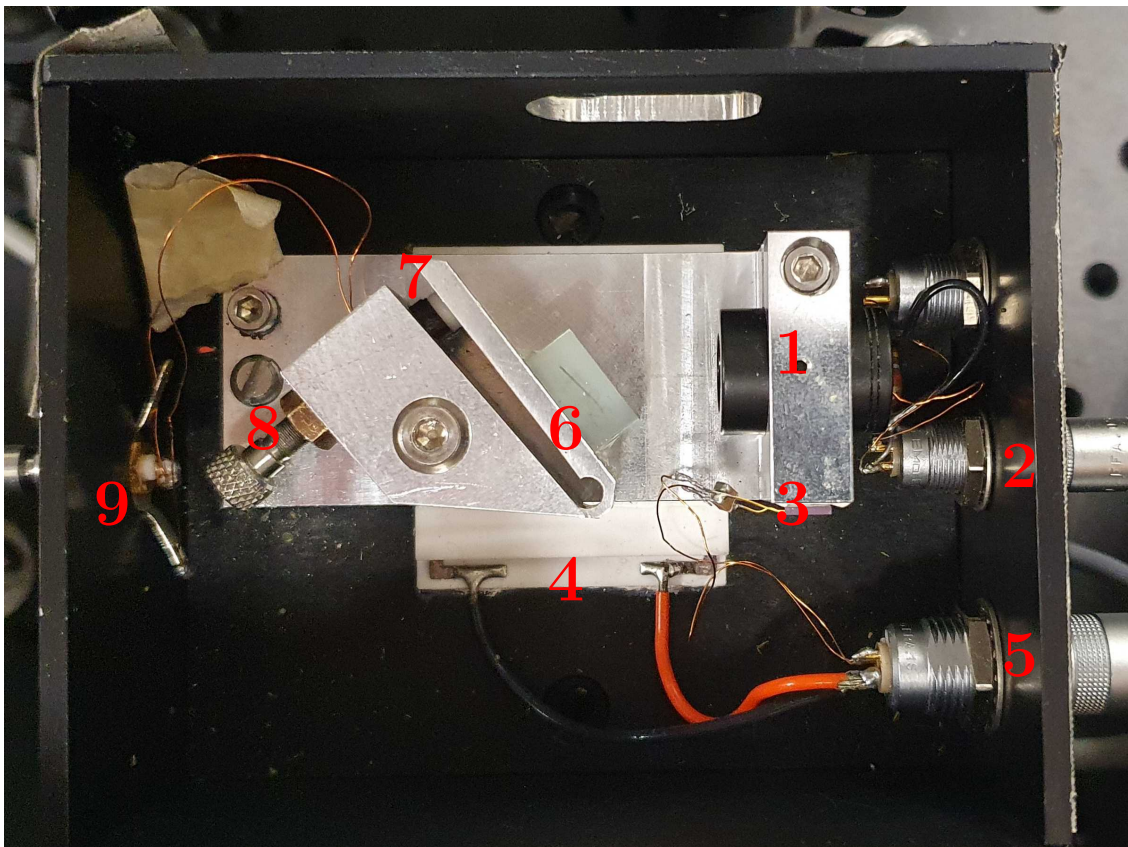


Figure 2.12: Photograph of the ECDL setup.

A multitude of elements, most of them on an aluminum block, is visible in fig. 2.12:

1. The laser diode that was examined in the previous sections. It is contained in a black collimation tube (Thorlabs LT230P-B) with an aspheric lens ($f = 4.51$ mm).
2. A DC connection to supply the diode with a controllable current.
3. A sensor (Analog Devices AD590JF) to measure the temperature T at a point close to the diode is glued to the aluminum block. Therefore, the measured T is not the diode's temperature but rather of its heat sink.

4. A Peltier element (Laird Technologies CP1.0-127-05L) is used to heat or cool the aluminum block.
5. The temperature sensor and the Peltier element are connected to a PID controller, adjusting the current through the Peltier element to stabilize T of the aluminum heat sink.
6. The reflection grating is glued to a bendable arm. It reflects light back into the diode creating an external cavity of length L .
7. To bend the arm on which the grating is placed a Piezo element (Piezomechanik PSt150/4/7) is installed. A voltage of up to 150 V can be applied to extend the length of the element by up to 7 μm . This allows fine tuning the length of the external cavity.
8. For coarser length tuning, a micrometer screw is used. Two additional screws control the horizontal tilt of the grating.
9. A PID controller (not shown, home-built) is connected to the Piezo element to apply a controlled voltage to the latter.

The used reflective grating has 1800 grooves per mm, evenly spaced at a distance $a = \frac{1}{1800}$ mm, and it is wavelength selective in two ways:

1. The external cavity supports only such wavelengths that fulfill $\lambda = 2L/n$ ($n \in \mathbb{N}$). This external cavity is longer than the one formed by the diode itself, i.e. its FSR is smaller. For comparison, the FSR of the diode is roughly 90 GHz while the external cavity has an FSR of approximately 7 GHz.
2. The grating is only truly back-reflective, if the wavelength fulfills the condition

$$\lambda = 2a \sin(\theta) \tag{2.20}$$

where θ is the angle at which the laser light hits the grating's surface. This means that the frequency of the laser is scannable by changing θ with the help of the micrometer screw or the Piezo element.

To make sure the back reflection is adjusted correctly another P - I -curve was recorded. The results are plotted in fig. 2.13 together with the P - I -curve of the laser diode alone (see fig. 2.8). Once the external cavity is formed the lasing threshold I_{th} drops because the cavity amplifies the power of the light within it. Lower currents will already provide enough light power to drive a transition that fits the diode cavity, its gain profile and the external cavity. But it's also clearly visible that the maximum power declines because the mode that fits all these conditions is not the

mode that experiences the highest amplification by the diode alone. Additionally, some power gets lost due to higher-order reflections.

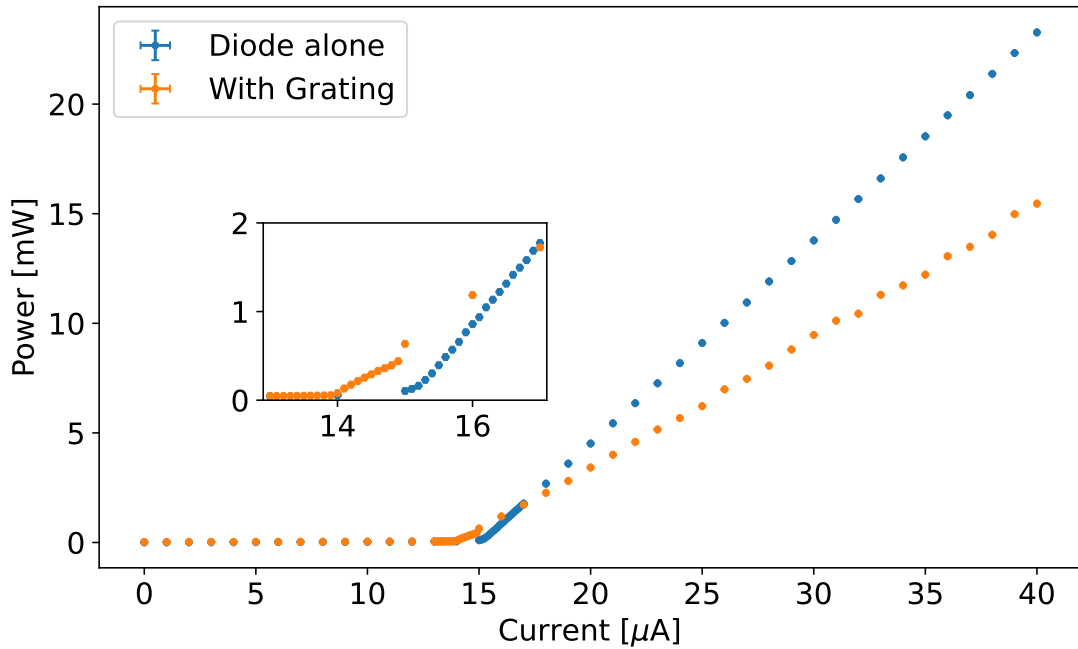


Figure 2.13: P - I -curve of the laser with and without reflective grating and a zoom-in of the low current regime. The integration of the grating decreases the lasing threshold I_{th} but also the maximum output.

Lastly, to show that the ECDL is working as intended, fig. 2.14 portrays the measurement of a mode hop-free scan of the laser frequency over a 2 GHz range. The frequencies which are necessary to perform spectroscopy of the ${}^6\text{Li}$ D_2 and the ${}^7\text{Li}$ D_1 lines are well within the scan range.

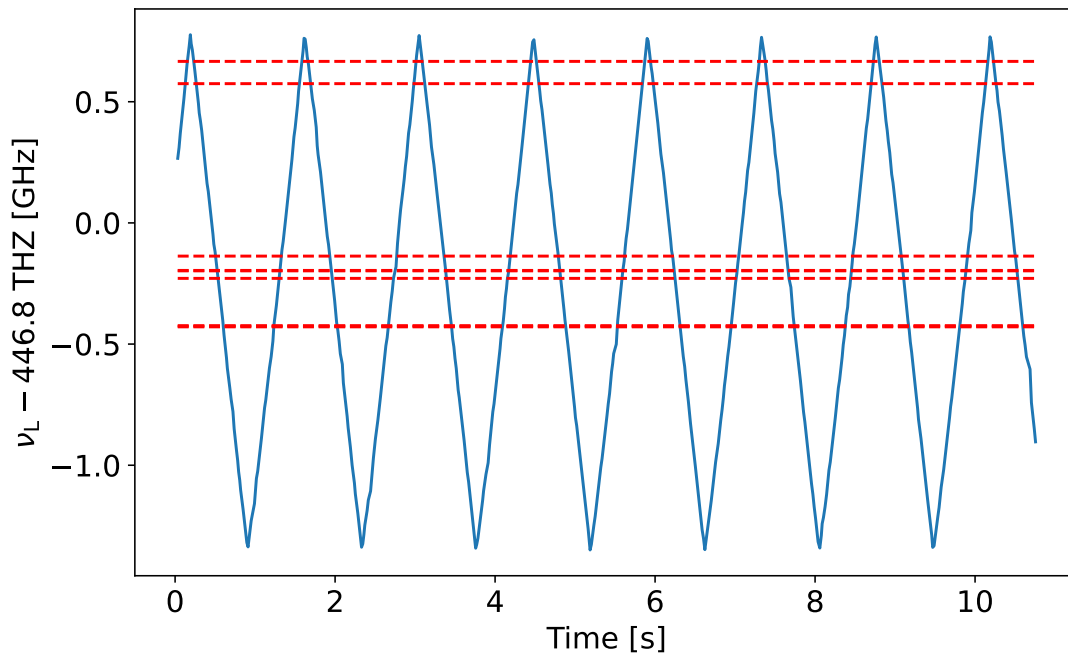


Figure 2.14: Measured mode hop-free scan of the ECDL. The dashed horizontal lines indicate the frequencies of the ${}^6\text{Li D}_2$ and the ${}^7\text{Li D}_1$ lines. All transitions are well within the scannable range.

2.1.7. Doppler-Free Saturated Absorption Spectroscopy

At room temperature lithium is a solid metal. The material has to be brought into the gas phase to create a usable target. The only way to achieve this is by heating the Li. In a fine vacuum, Li needs to be heated up to roughly 300°C to generate such a gaseous target.

A high temperature leads to a broad velocity distribution which in turn broadens the range of frequencies that can be absorbed by the gaseous Li. Whether an atom absorbs a photon, depends on the photon's frequency measured in the atom's rest frame ν' . The probability of absorption ρ follows a Lorentzian distribution

$$\rho(\nu') \propto \frac{1}{(\nu_0 - \nu')^2 + \Gamma^2/4}, \quad (2.21)$$

where ν_0 is the resonance frequency, and Γ is the natural linewidth or full width at half maximum (FWHM). Due to relativistic effects, ν' is not necessarily the photon's frequency in the lab frame ν but it depends on the atom's velocity \vec{v} . The Doppler shift is given by

$$\nu' = \nu (\gamma - \gamma\beta \cos(\phi)) \approx \nu - \frac{\vec{v} \cdot \vec{k}}{2\pi}. \quad (2.22)$$

Here, $\beta = c/v$ and $\gamma = 1/\sqrt{1-\beta^2}$ are the well-known relativistic parameters and \vec{k} is the photon wave vector. The approximated right-hand side of eq. (2.22) is the

first-order Doppler shift and valid for small values of $|\vec{v}|$. If multiple atoms are probed and they form a hot ensemble, i.e. their velocities v in the direction of the incoming light follow a Gaussian distribution with temperature T :

$$f(v) = \sqrt{\frac{m}{2\pi k_B T}} e^{-\frac{mv^2}{2k_B T}}, \quad (2.23)$$

with m being the atomic mass and k_B the Boltzmann constant, the same frequency ν can be seen as many different ν' and different velocity classes will thus absorb different frequencies of light. This results in a line broadening of

$$\Delta\nu_{\text{Doppler}} = \frac{\nu_0}{c} \sqrt{\frac{8k_B T \ln(2)}{m}}. \quad (2.24)$$

This broadening effect can be overcome in two ways. Either the gas is cooled down, e.g. in a MOT, or a Doppler-free measurement technique is used, such as Doppler-free saturated absorption spectroscopy (DFSAS). The latter is explored in this section using the ${}^7\text{Li}$ D₂ line as an example. The exact level structure of ${}^7\text{Li}$ will be examined in section 2.2.1, for now it is only important to note that there are two ground states $|g_1\rangle$ and $|g_2\rangle$ which can both be excited to one excited state $|e\rangle$.

But first, we simplify even more and assume only one ground state $|g\rangle$. The frequency needed to excite an atom is $\nu_0 = 446.81$ THz and the natural linewidth of this transition is $\Gamma = 5.9$ MHz. At a temperature of 300 °C and with ${}^7\text{Li}$ atoms having a mass $m = 1.165 \times 10^{-26}$ kg, the respective transition will be Doppler-broadened by $\Delta\nu_{\text{Doppler}} = 2.9$ GHz.

DFSAS is a form of absorption spectroscopy in which a laser beam of frequency ν_L passes an absorbing medium and the remaining power of the beam is measured, usually by a photodiode. The beam will be most likely to be absorbed by atoms that see ν_L as ν_0 after it has been Doppler-shifted into the rest frame of the atom. Therefore, a decreasing transmitted power is measured once ν_L gets closer to ν_0 . A schematic absorption spectroscopy setup is depicted in fig. 2.15a. The resulting spectrum is the convolution of the natural Lorentzian line shape of the resonance and the Gaussian Doppler-broadened spectrum. This is resulting in a Voigt profile but because $\Delta\nu_{\text{Doppler}} \gg \Gamma$ it is adequate to describe it as a Gaussian. Thus, the photodiode produces a signal which is shown in fig. 2.15b. An off-resonant beam will pass the medium mostly undisturbed.

A real measurement is not as clear as the shown spectrum and noise limits the attainable precision in the determination of ν_0 . It is therefore necessary to find a way to suppress the Doppler broadening and one approach is to add a second counter-propagating laser to the setup like in fig. 2.16a. Both beams have the same frequency and one of them, the so-called probe beam, has a much lower power than the other which is named pump beam. The ratio is roughly 10:90. Due to the fact

that their wavevectors have opposite signs $\vec{k}_{\text{probe}} = -\vec{k}_{\text{pump}}$, they interact with opposite velocity classes, i.e. one beam is absorbed by atoms with longitudinal velocity $v = c\left(\frac{\nu_0}{\nu_L} - 1\right)$ and the other is absorbed by atoms with $v = c\left(1 - \frac{\nu_0}{\nu_L}\right)$. Here, c is the speed of light and longitudinal means in the direction of the laser beams.

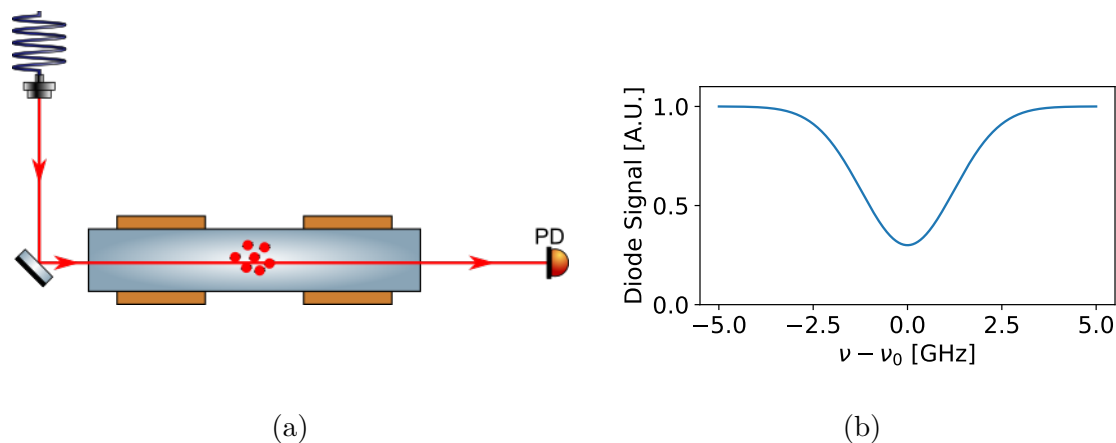


Figure 2.15: Stylized absorption spectroscopy setup and signal. **(a)** A laser exits a fiber, passes a hot gaseous target and its remaining power is then measured by a photodiode (PD). **(b)** Signal measured by the photodiode as a function of the laser's frequency detuning $\nu - \nu_0$.

The probability distribution $\rho_g(v)$ for finding an atom in the ground state as a function of the atom's transverse velocity is plotted in fig. 2.17 for two different cases: off- and on-resonant laser frequency. The distribution follows a Gaussian because of the Doppler effect (see eq. (2.23)). But at certain velocities ρ_g (the solid line) drops and deviates from the original normal distribution indicated by a dashed line. The atoms that absorb photons aren't in the ground state anymore and are therefore missing in ρ_g . These spectral holes have a width of

$$\Delta\nu_{\text{hole}} = \Gamma \sqrt{1 + \frac{I}{I_{\text{sat}}}} \quad (2.25)$$

where I is the intensity of the laser beam and I_{sat} is the saturation intensity of the transition [Foo05], which is 2.54 mW/cm^2 for the discussed ${}^7\text{Li}$ transition [Fis23]. Notice how the position of the holes in fig. 2.17a are on opposite sites of the peak but the more intense pump beam creates a deeper and broader hole than the probe beam. As long as these holes are apart, the signal as measured by the photodiode doesn't change. But as ν_L approaches ν_0 at $v \cong 0$, the holes start overlapping and in this so-called Lamb-dip the target becomes more transparent. The measured probe intensity increases because the pump beam saturates a large portion of the atoms and the spectrum shows Doppler-free features depicted in fig. 2.16b, hence the name: Doppler-free saturated absorption spectroscopy.

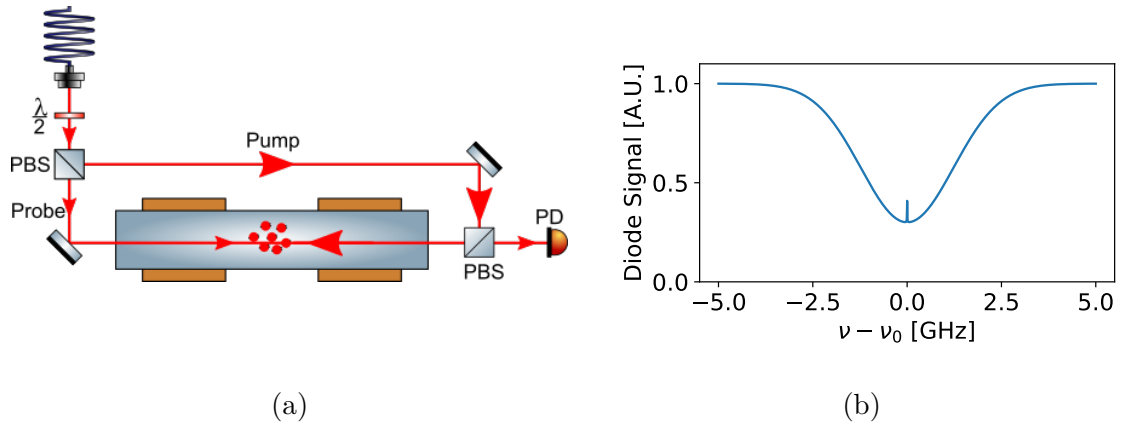


Figure 2.16: Doppler-free saturated absorption spectroscopy setup **(a)** and signal **(b)**. A laser exits a fiber, its polarization is adjusted by a half-wave plate ($\frac{\lambda}{2}$), is then split into two counter-propagating beams (a high intensity pump beam and a low intensity probe beam) by a polarizing beam splitter (PBS) and passes a hot gaseous target. The probe beam's remaining power is then measured by a photodiode (PD).

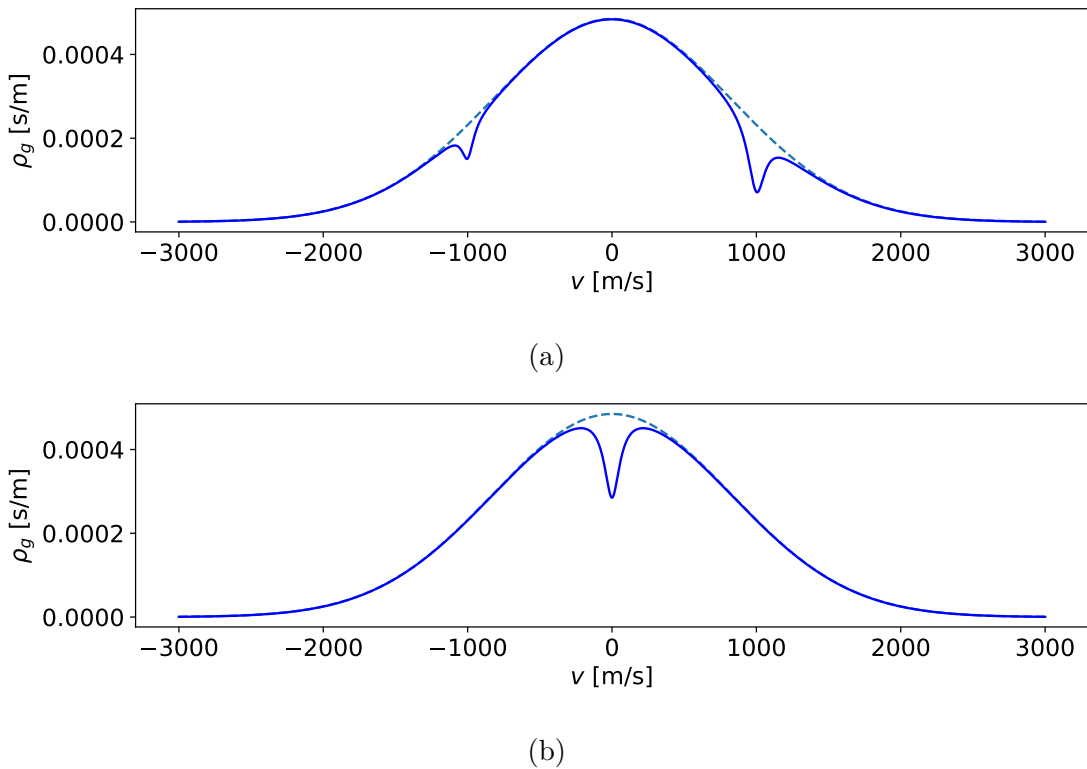


Figure 2.17: Probability density function for finding an atom with velocity $v + \delta v$ in a hot (300°C) sample in the ground state. Two counter-propagating laser beams with the same frequency (**(a)** off-resonant and **(b)** on-resonant) pass the sample and excite atoms. The resulting spectral holes or Bennett-holes decrease the capacity to absorb further photons and once the holes overlap to form the Lamb-dip, the transmitted beam power increases. The dashed line indicates the expected distribution without the presence of any laser beams.

Now that the basic procedure of DFSAS is clear, the D_2 line of ${}^7\text{Li}$ is examined as a real-life example. As mentioned above, two resonances¹¹ are present at $\nu_{\text{high}} = 446.809\,883(8)$ THz and $\nu_{\text{low}} = 446.810\,693(4)$ THz [BWP⁺13]. The frequencies ν_{low} and ν_{high} are named after the ground state their respective transition belongs to, i.e. the lower and the higher ground state. According to the previous theoretical explanation, two narrow peaks inside a broad Gaussian valley are expected to be seen in the spectrum. In fig. 2.18 these two peaks are in fact visible and for higher frequencies the measured signal rises indicating said valley. The whole valley cannot be seen because the laser can only be scanned over a range of 1.2 GHz and more than twice as much would be necessary.

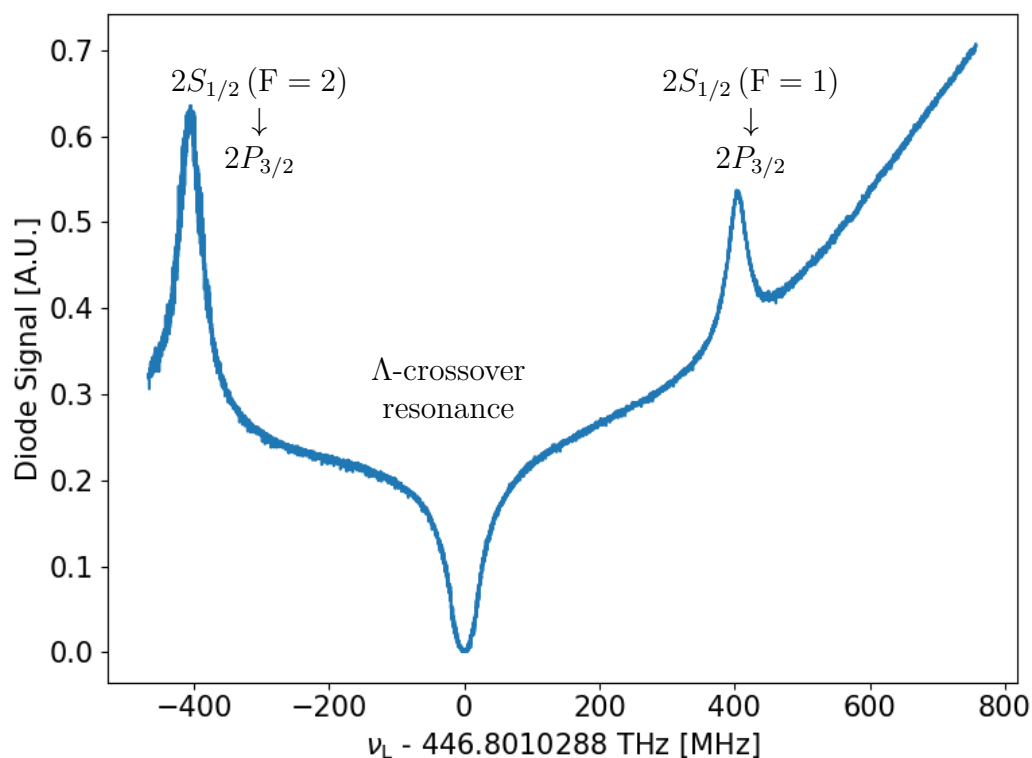


Figure 2.18: Measured Doppler-free saturated absorption spectrum of the ${}^7\text{Li}$ D_2 line. The spectrum was produced with a home-built ECDL. The following transitions are visible (from left to right): from the upper ground state $2S_{1/2}$, $F = 2$ to the excited states $2P_{3/2}$, $F' = 1, 2, 3$; Λ -crossover resonance between the two ground states and the excited states; from the lower ground state $2S_{1/2}$, $F = 1$ to the excited states $2P_{3/2}$, $F' = 0, 1, 2$. On the right side of the spectrum the rising flank of the Doppler-valley is visible.

¹¹In principle there are six transitions: three from the lower ground states to three of the four excited states and three from the higher ground states. But the HFS of the excited states is comparable to the natural linewidth which makes them hard to differentiate in the spectrum.

Between ν_{high} and ν_{low} a dip is visible which is as narrow as the peaks of the resonances. This so-called "crossover" resonance is an artifact of the DFSAS technique. It is a consequence of the fact that for moving atoms the same light can be used to drive different transitions depending on the direction of the light relative to the movement of the atom.

Crossover resonances can be observed whenever more than one lower or higher state exist. The first one which is discussed here is the Λ -configuration shown in fig. 2.19 because it matches the simplified ${}^7\text{Li}$ level structure.

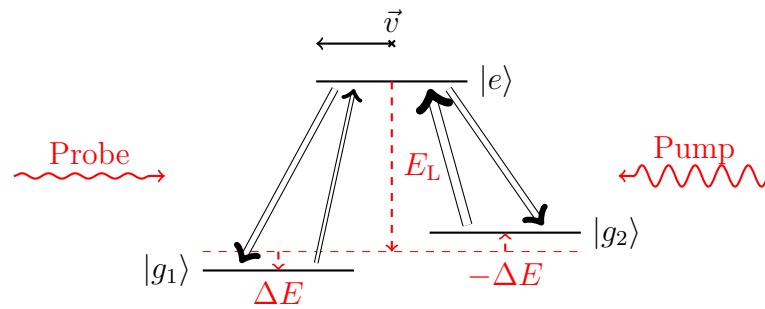


Figure 2.19: Λ -configuration. A low intensity probe and a more intense pump beam excite atoms moving towards the probe beam with velocity $|\vec{v}|$. Arrows from state to state represent transitions, with wider arrows indicating more frequent transitions. Effectively, atoms are pumped from the $|g_2\rangle$ state into $|g_1\rangle$. For opposite velocity this is switched.

Imagine atoms with two ground states $|g_1\rangle$ and $|g_2\rangle$ from which a transition to the same excited state $|e\rangle$ is allowed. From the left, the probe beam shines through the sample while the pump beam is coming from the right. The laser frequency is exactly between the frequencies that drive the two possible transitions

$$\nu_L = \frac{\nu_{|g_1\rangle \rightarrow |e\rangle} + \nu_{|g_2\rangle \rightarrow |e\rangle}}{2}. \quad (2.26)$$

The photons therefore have the energy $E_L = h\nu_L$ and cannot be absorbed by atoms that are at rest because a certain amount of energy ΔE is either missing or too much. But some atoms are moving and certain velocity classes experience Doppler shifted light with photon energies

$$E_\gamma = E_L \pm \hbar k v = E_L \pm \Delta E \quad (2.27)$$

which are exactly the energies that are needed to drive the two transitions¹². The \pm in eq. (2.27) indicates that the atoms of these velocity classes are moving towards one laser beam while moving away from the other. Henceforth, it is assumed that

¹²For the probed ${}^7\text{Li}$ D₂ lines, atoms with $v = \pm 272(3)$ m/s experience the center frequency between ν_{high} and ν_{low} Doppler-shifted to the real resonance frequencies.

the atoms move toward the probe beam with this necessary velocity v . They could just as well move towards the pump beam, the end result would be the same but the reactions of the ground states would be switched.

Some atoms which are in $|g_1\rangle$ absorb the probe beam while many more that are in $|g_2\rangle$ absorb the pump beam. But both reach the same excited state $|e\rangle$. From there the atoms can spontaneously deexcite into both ground states depending almost completely on the multiplicities of the states which are comparable in size. Effectively, the atoms are pumped into the $|g_1\rangle$ state increasing the amount of probe beam photons that can be absorbed and thus the transmitted power drops. A dip appears in the spectrum, as can be seen in fig. 2.16.

The second type of crossover resonance can be found in level structures with a V-configuration, i.e. one common ground state $|g\rangle$ that can be excited to two excited states $|e_1\rangle$ and $|e_2\rangle$. Such a configuration is shown in fig. 2.20. The frequency of the laser is

$$\nu_L = \frac{\nu_{|g\rangle \rightarrow |e_1\rangle} + \nu_{|g\rangle \rightarrow |e_2\rangle}}{2}, \quad (2.28)$$

exactly between the frequencies that would drive the transitions from $|g\rangle$ to $|e_1\rangle$ and $|e_2\rangle$ for stationary atoms, respectively. It is not necessary to limit this explanation to a single velocity group. As long as the atoms have the correct velocity to see ν_L as a resonant frequency, they will be resonant to both beams at the same time. The result is very similar to the regular DFSAS process explained above: the ground state $|g\rangle$ is depopulated by the high intensity pump laser and because less atoms can therefore absorb the probe beam, the intensity of the transmitted beam increases. A peak can be seen in the spectrum in the middle of the peaks created by real resonances. This feature can be found in the ${}^7\text{Li}$ D₁ line which is examined in section 2.2.1.

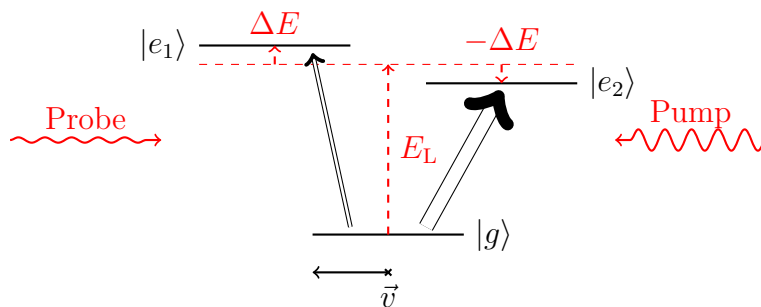


Figure 2.20: V-configuration. A low intensity probe and a more intense pump beam excite atoms moving towards the probe beam with velocity $|\vec{v}|$. Arrows from state to state represent transitions, with wider arrows indicating more frequent transitions. Effectively, the amount of atoms in the $|g\rangle$ states is lowered, making it more probable for a probe beam photon to pass the atoms. This would also be the case if the atoms moved into the other direction but the arrows would be switched.

2.1.8. Tapered Amplifier

The home-built ECDL produces light at the correct wavelength and can be scanned over a wide enough range to probe all transitions of interest. But it only produces relatively low power beams of roughly 10 to 15 mW. While this is enough for spectroscopy, we need more power for slowing and trapping. Therefore, the beam's power has to be amplified.

This is again done with a light producing diode. In contrast to the laser diode examined in section 2.1.1, this diode is not designed to create a singular frequency laser beam on its own. Its surfaces are not treated to make them more reflective but rather anti-reflective. The geometry of this diode is shown in fig. 2.21a. A narrow entrance area, in which a laser beam can be injected, transitions into a tapered gain region. Because a large current (up to 1 A) is applied to the diode, its material is already excited and each injected photon stimulates the emission of several photons of the same frequency and phase, thus amplifying the power of the seed beam. The intensity of the laser gets so high that it would destroy the material if the amplification region didn't spread out, thus the taper. This leads to a deformation of the (ideally) Gaussian injection beam into a high intensity multi-modal laser beam shown in fig. 2.21b. Unfortunately, the multi-modal beam results in low efficiencies if the laser is to be coupled into a single-mode fiber (here approx. 30%). Because of its form and function such a component is called a tapered amplifier (TA) [VSSH01, KHG⁺14].

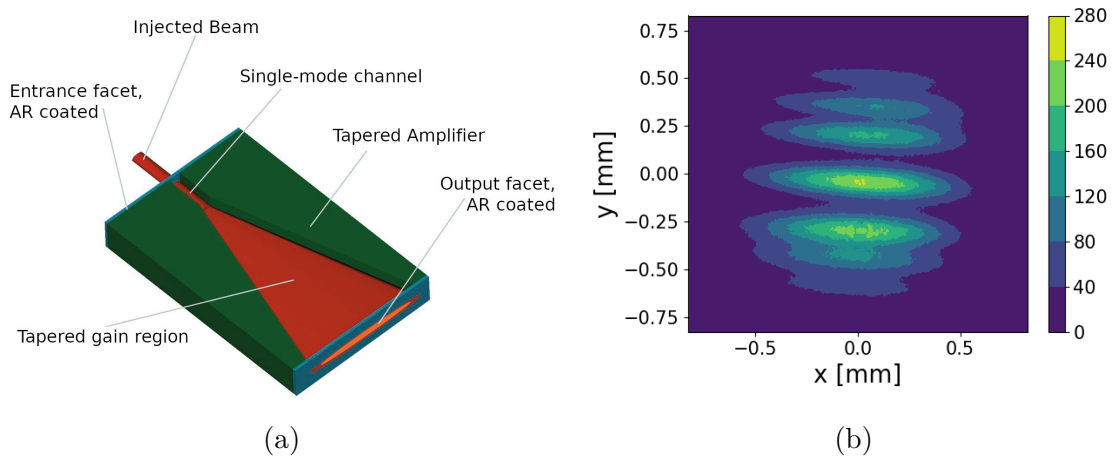


Figure 2.21: A schematic of a tapered amplifier (taken from [Thob]) (a) and a measured profile of the amplified output beam (b). The depicted beam has already been collimated by a set of lenses. The multi-modal profile results in relatively low efficiencies when coupling this beam into a single-mode fiber.

Additional optical elements are needed to focus the seed laser into the TA and make the wide spread amplified beam usable. These optical elements are depicted in fig. 2.22.

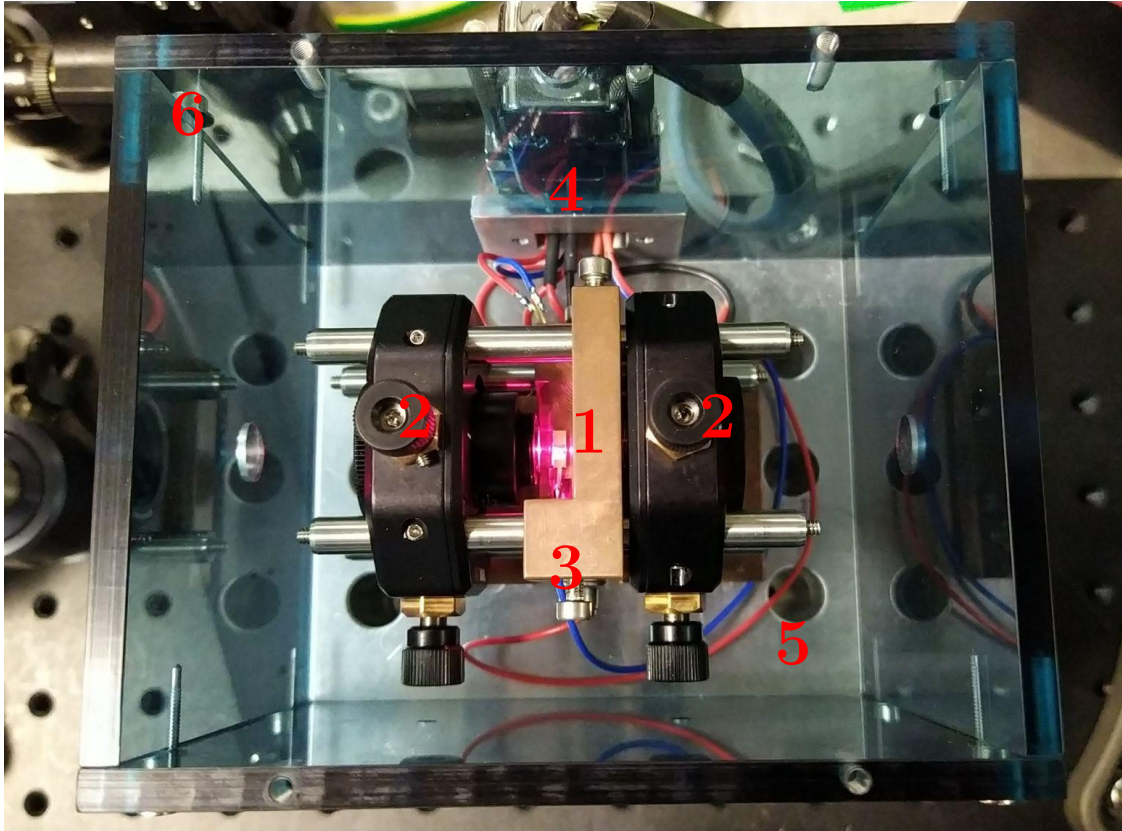


Figure 2.22: Photograph of the tapered amplifier setup. The numbered elements are explained in the text. The seed laser enters from the right.

The numbered elements are listed below:

1. In the middle of the picture, the TA diode (Toptica EYP-TPA-0670-00500-2003-CMT02-0000) can be seen. A current of 100 mA is applied to it so that it produces light on its own to make it more visible. The current is far enough below the design value of 1000 mA to not damage the TA.
2. The seed laser needs to be precisely coupled into the TA and the amplified output beam must be collimated. Therefore, a XYZ-translator (Thorlabs CXYZ05A/M) which holds an aspheric lens (Thorlabs A375TM-B) with a focal length $f = 7.5$ mm is placed on each side of the diode. Stainless steel rods hold both translators at a certain distances and the micrometer screws can be used to move the focusing/collimating lens to the desired position.
3. The TA is fixed to a copper block which fulfils two functions. First, it serves as an anode. The driving current flows into the copper block via the red cable, through the TA and back through the blue cable. Additionally, the TA needs to be held at a fixed temperature and the block serves as a heat sink. The block itself is cooled by a Peltier element which is placed under the block.

4. Supply cables for the copper block's temperature sensor, the Peltier element and the TA lead to a D-Sub connector, which connects these elements to their respective controllers.
5. An aluminum block serves as a base for the whole setup. It can be screwed to the table to provide further stability. Additionally, it serves as a heat sink for the Peltier element cooling the copper block on which the diode is installed.
6. To avoid dust settling on the optics and the diode, as well as stopping airflow through the setup, an acrylic glass case is put around it.

Not shown in fig. 2.22 is a cylindrical lens to the left of the setup. The amplified beam emitted by the TA can be collimated vertically by the aspheric lens alone but the horizontal direction is highly divergent and an additional lens is needed. The entire setup is schematically depicted in fig. 2.23. On the left, the ECDL (see section 2.1.6) emits the broad seed beam, which is reshaped by a pair of anamorphic prisms to make it rounder. The beam passes on optical isolator and a $\frac{\lambda}{2}$ -plate before it is split into two separate beams. One of which is guided into the wavemeter to measure its frequency while the other is steered into the TA. The amplified beam passes another optical isolator¹³ and is subsequently guided into a fiber to the experiment.¹⁴ The wavemeter is connected to the ECDL's Piezo actuator and produces a voltage which stabilizes the laser to $\nu_L = 446.799\,40(3)$ THz.

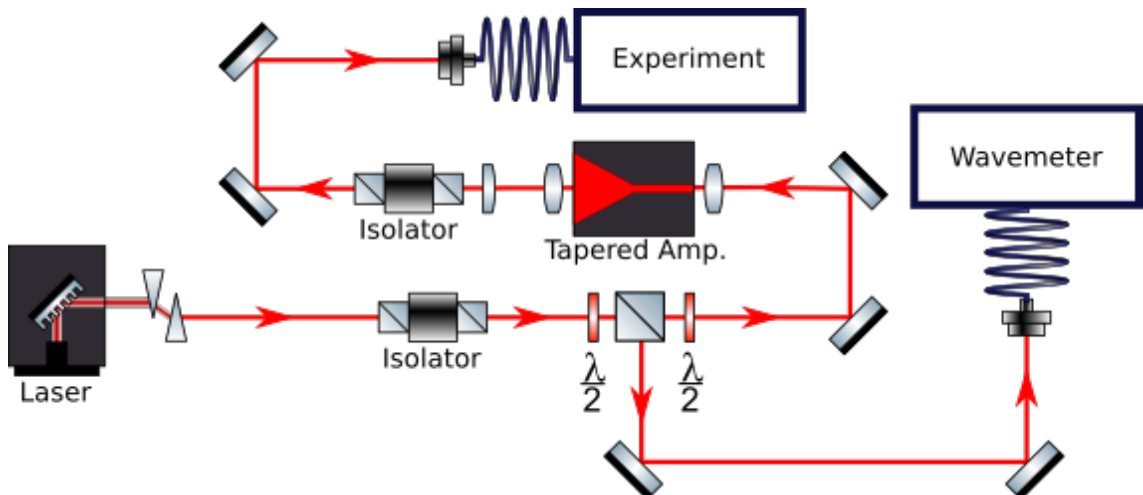


Figure 2.23: Schematic of the complete laser setup including the tapered amplifier in the center of the picture.

¹³This isolator is needed because any back reflections that entered the TA through its output side would be amplified and "focused" in the tapered region. The resulting beam intensity would be high enough to destroy the TA diode.

¹⁴Further explanation on some of the used optical elements can be found in appendix C.

The TA and the power P_{out} of the beam it produces, depends on several factors: the power of the seed beam P_{in} , its polarization angle θ^{15} , the current I through the TA, and its temperature T . The TA's current dependent output is shown in fig. 2.24. For this measurement, the parameters that maximize P_{out} were chosen. They are listed in table 2.4 and their determination is explained further below.

Table 2.4: The parameters which were chosen for the measurement depicted in fig. 2.24.

T	15.0(1) °C
I	1000(10) mA
P_{in}	9.3(1) mW
θ	39(1) °

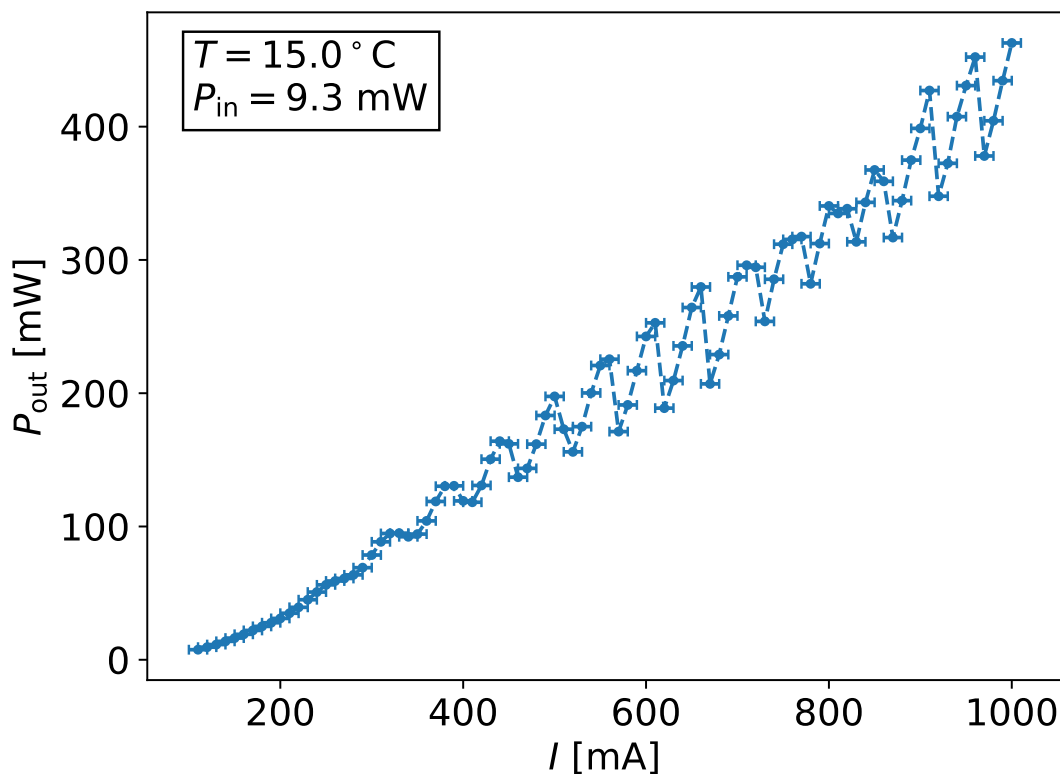


Figure 2.24: Tapered Amplifier output power as a function of applied current. Higher currents generally lead to higher output. Additionally, a periodic behavior can be seen.

Generally, a higher current leads to higher P_{out} because more charge carriers are delivered to the diode's p-n-junction which can then recombine to emit more photons. An additional periodic behavior is also visible. One possible explanation is that as I increases, the TA emits more light by itself out of both its output and

¹⁵In this case, θ is the rotation angle of the rotation mount that holds the $\frac{\lambda}{2}$ -plate right before the TA. An angle of 39° corresponds to horizontally polarized light.

input facet. The many optical elements on the input side (including the end facets of the TA itself) reflect this light back into the TA, effectively forming an etalon. The resulting increase in input power might be minimal but small changes in P_{in} can drastically increase P_{out} . Additionally, at specific currents a cavity for the seed light might form. The refractive index of the TA could change or the diode could thermally expand accordingly. In this case, output powers up to $P_{\text{out}} = 463(1)$ mW at $I = 1000(10)$ mA can be achieved.¹⁶

The light which the TA emits is polarized parallel to the plane of the diode's p-n junction. It is therefore only transparent for seed light of the same polarization. To get the highest amplification, the polarization of the seed laser has to match the TA's. As can be seen in fig. 2.23, before the beam reaches the TA, it is reflected by two mirrors and passes a polarization turning $\frac{\lambda}{2}$ -plate. The retarder's angle can be changed with the help of a rotation mount. The output power of the TA was measured against the angle θ of this mount which is depicted in fig. 2.25.

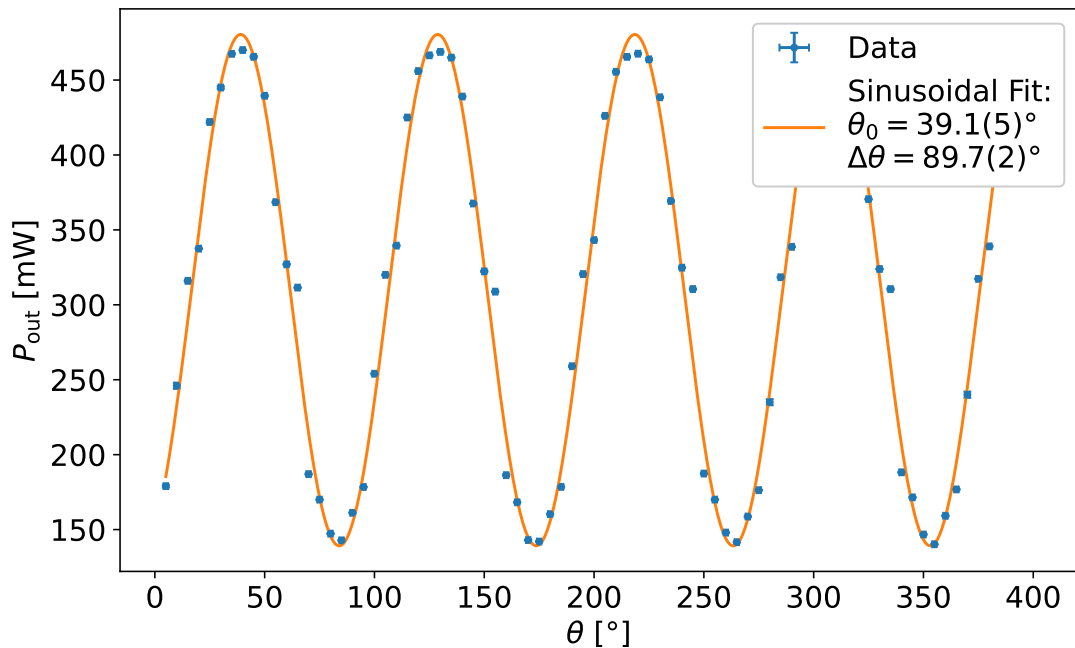


Figure 2.25: TA output power versus polarization of seed beam. A sinusoidal function was fitted to the data. The maximum/minimum angles correspond to horizontal/vertical polarization of the seed laser beam. For high powers the data flattens out because the TA saturates.

¹⁶In principle, even higher P_{out} are achievable, but the datasheet recommends a maximum power of 500 mW at an absolute maximum current $I = 1.2$ A. Increasing the current would assumably decrease the lifetime of the TA which is not desired.

A function of the form

$$P(\theta) = P_0 + P_1 \cdot \cos\left(2\pi \frac{\theta - \theta_0}{\Delta\theta}\right) \quad (2.29)$$

is fitted to the data. At roughly $\theta_{\max} = 39.1(5)^\circ + n \cdot 89.7(2)^\circ$ the output power is maximal, while it's minimal for $\theta_{\min} = 84.7(4)^\circ + n \cdot 89.7(2)^\circ$, where $n \in \mathbb{Z}$. These angles correspond to horizontal and vertical polarization, respectively. Interestingly, the periodic behavior is not purely sinusoidal. For the best angles the power flattens out into a plateau because the TA is saturated, for the worst angles the power drops to the levels of an unseeded TA¹⁷ ($P_{\text{out}} \approx 150$ mW), and inbetween a medium output power state seems to exist.

The TA is a light producing diode and just like the laser diode its performance is dependent on its temperature which is depicted in fig. 2.26. The current dependence of P_{out} is plotted for multiple temperatures. The general behavior is always the same, higher currents lead to higher output powers. Furthermore, as the temperature decreases, the TA's gain profile changes and the seed laser experiences more and more amplification. The output power is not totally separated by different temperatures. For some currents, higher T result in higher outputs than lower T . This has the same reason as the periodic $P - I$ behavior seen in fig. 2.24. A cavity forms at certain currents which increases the output power.

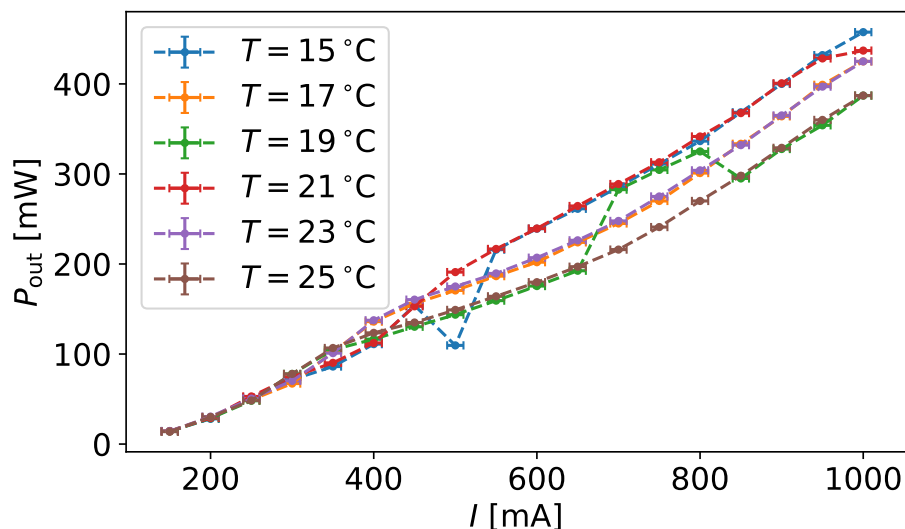


Figure 2.26: TA output power versus current. The measurement was done for different temperatures at fixed input power $P_{\text{in}} = 9.3(1)$ mW. While the general relation between current and output power is the same (the higher I , the higher P_{out}), a drop in T leads to increased amplification resulting in higher P_{out} .

¹⁷A TA should never be operated without a seed laser, as this might destroy the amplifier.

Lastly, the relation between P_{out} and the power of the seed beam P_{in} is to be examined. This is plotted in fig. 2.27 and as expected, the higher the input power, the higher the output power. Nevertheless, the unstable growth is still present. Some currents result in higher P_{out} than higher currents. Additionally, P_{out} saturates for larger P_{in} . This is better shown in fig. 2.28. Therein, the highest achieved P_{out} of each input power measurement is plotted against P_{in} and the first three points were used to fit a linear function to highlight the diminishing returns because the TA shows saturation effects.

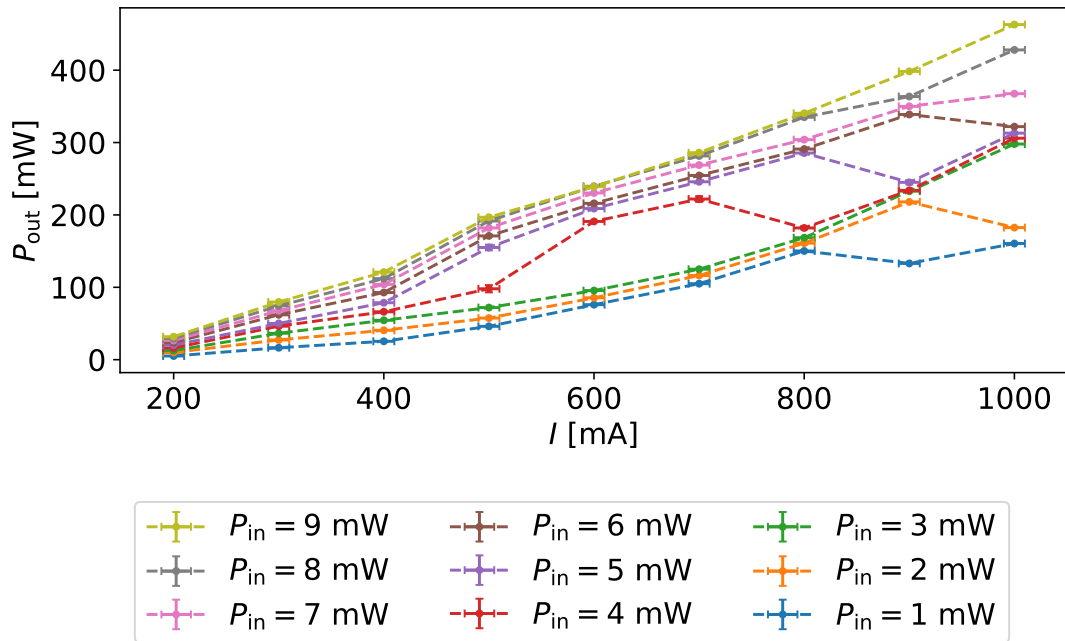


Figure 2.27: TA output power versus current. The measurement was done for different input powers at fixed temperature $T = 15.0(1)^\circ\text{C}$. While the general relation between current and output power is the same (the higher I , the higher P_{out}), an increase in P_{in} leads to increased amplification resulting in higher P_{out} .

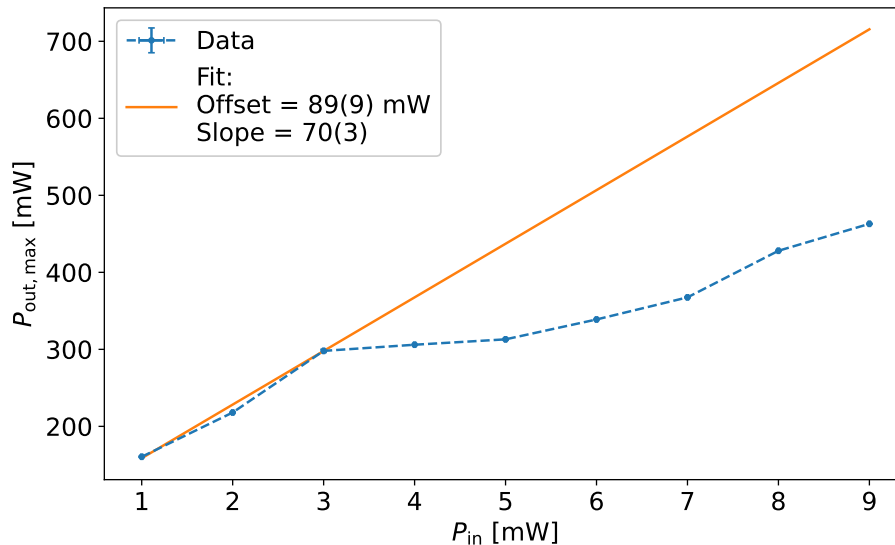


Figure 2.28: Saturation of the maximum TA output power for different seed powers P_{in} . The fit shows the slope efficiency for small input powers.

2.2. Commercial ECDL

The second laser in use is a commercial TApr by TOPTICA Photonics. In principle, this laser is a smaller, more compact version of the previously explained setup. An ECDL with a proprietary design emits light at $\lambda = 671$ nm which is guided through an optical isolator and into a tapered amplifier which increases the laser beam's power to up to 460 mW. The beam is then coupled into a fiber after passing a $\frac{\lambda}{2}$ - and a $\frac{\lambda}{4}$ -plate to set it to the correct polarization. Roughly 200 mW can be coupled into the fiber. A picture of the setup is shown in fig. 2.29.

A small part of the unamplified beam is coupled out via a partly transparent mirror. This monitoring beam is used to characterize the laser in the following. Firstly, the frequency of the produced laser light is monitored. A mode-hop free scan over 31 GHz is shown in fig. 2.30. As before, the data was taken using a High Finesse WS7-30 wavemeter. The lithium resonances at $\nu_{6LiD_1} \approx 446.79$ THz, $\nu_{6LiD_2} \approx \nu_{7LiD_1} \approx 446.8$ THz, and $\nu_{7LiD_2} \approx 446.81$ THz are well within the scan range.

The monitoring beam of the laser was guided through a vacuum cell containing hot lithium. The photodiode signal which corresponds to the transmitted power is depicted in fig. 2.31. The x -axis has already been translated from Piezo voltage to an offset $\delta\nu$ to the nominal frequency $\nu_n = 446.8$ THz. From left to right the ${}^6\text{Li}$ D₁ line, the ${}^6\text{Li}$ D₂ and ${}^7\text{Li}$ D₁ lines, and the ${}^7\text{Li}$ D₂ line are visible. The different signal amplitudes are a result of the lithium sample which is inside the vacuum cell comprising mostly ${}^7\text{Li}$ and only small amounts of ${}^6\text{Li}$ in a natural ratio of roughly 92.6 % and 7.4 %, respectively.

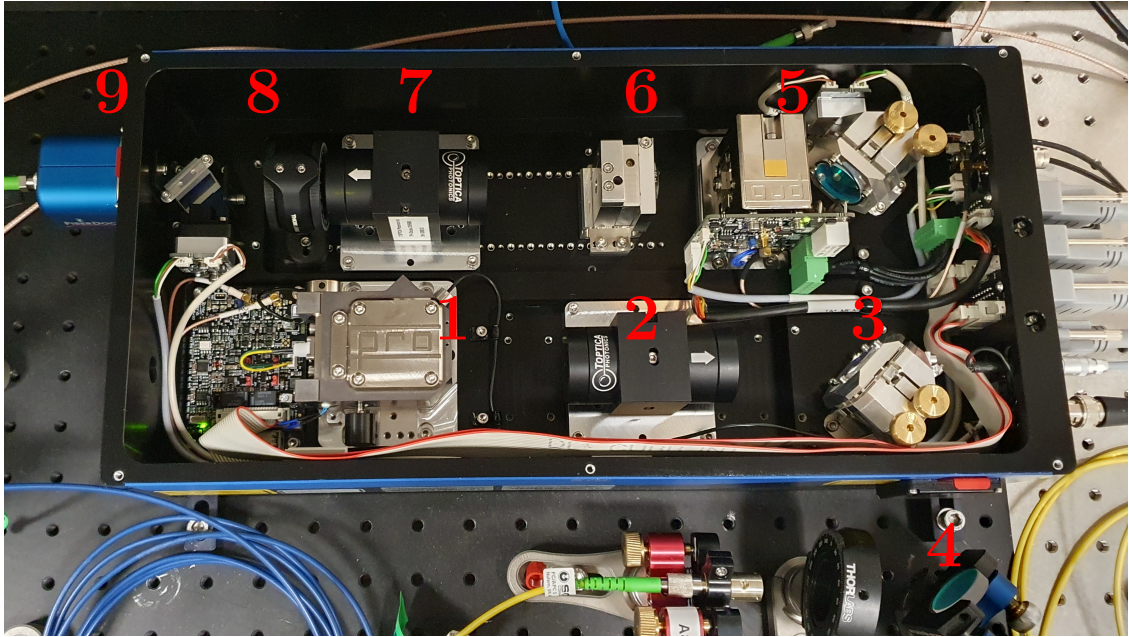


Figure 2.29: Photograph of the insides of the Toptica TApr. The red numbers mark important elements. These are: **1** external cavity diode laser; **2** Faraday isolator to protect the ECDL from back reflections; **3** partly transparent mirror to couple out a small fraction of the laser; **4** fiber coupling for the monitoring beam; **5** tapered amplifier including focusing lenses to increase beam intensity; **6** cylindrical lens to recollimate beam; **7** another Faraday isolator to protect the TA from back reflections; **8** quarter- and half-wave plates to correct the beam's polarization; **9** main output fiber coupling.

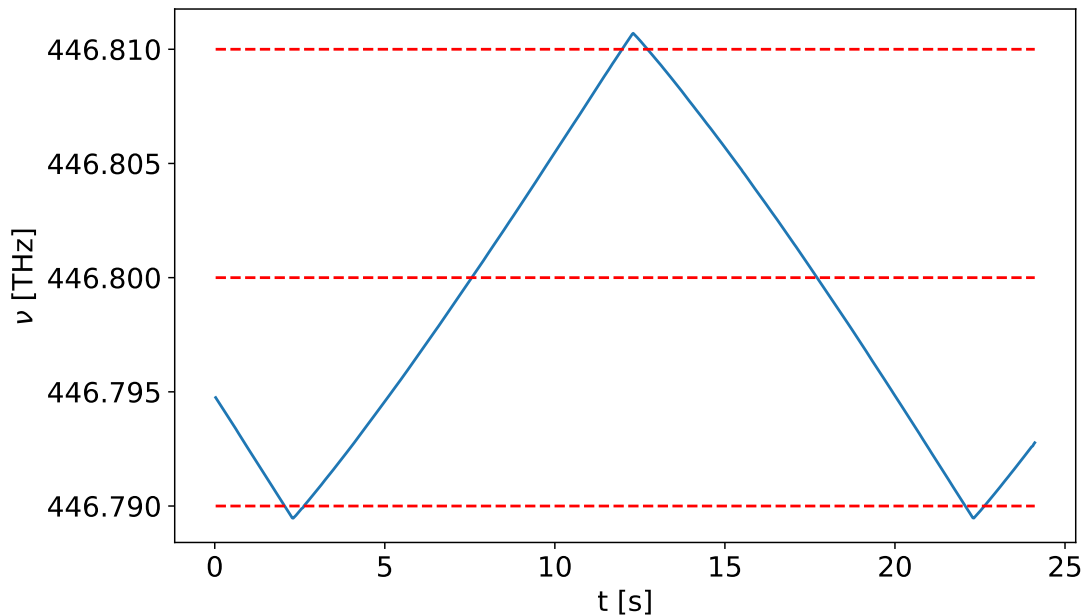


Figure 2.30: The TApr can scan over more than 20 GHz. The horizontal dashed lines show the rough position of the ${}^6\text{Li}$ D₁ line, the ${}^6\text{Li}$ D₂ and the ${}^7\text{Li}$ D₁ line, and the ${}^7\text{Li}$ D₂ line (from lowest to highest).

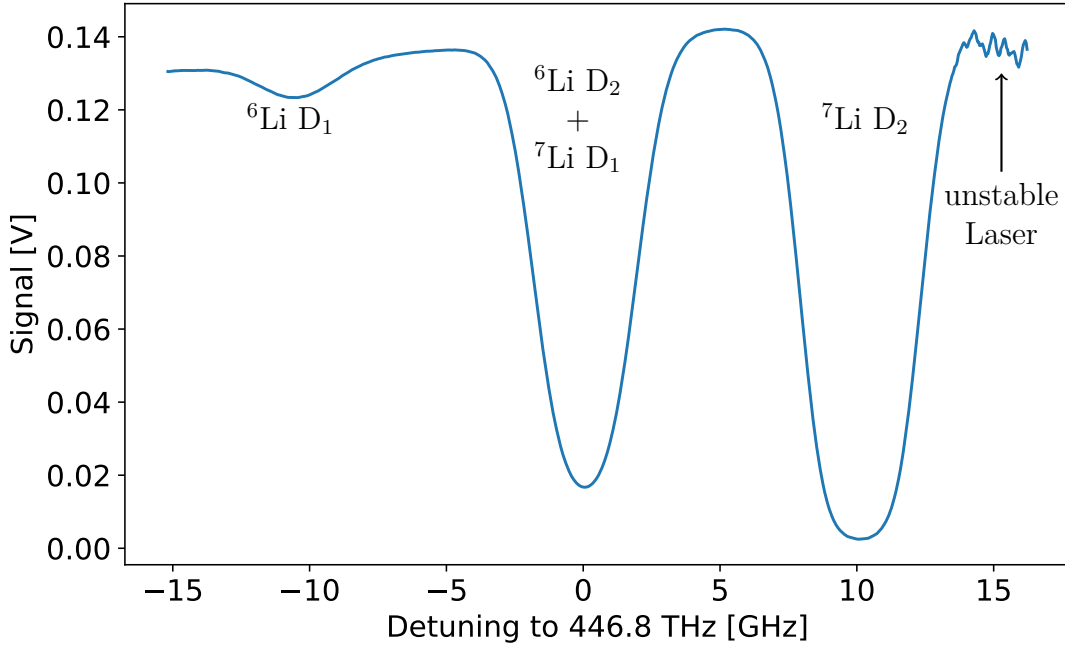


Figure 2.31: Transmitted signal after passing a gaseous sample of ${}^6\text{Li}$ and ${}^7\text{Li}$ versus the frequency of the TAprö. From left to right, the dips correspond to the ${}^6\text{Li}$ D₁ line, the ${}^6\text{Li}$ D₂ and the ${}^7\text{Li}$ D₁ lines, and the ${}^7\text{Li}$ D₂ line. The unstable behavior in the high frequency region stems from the spectroscopy laser starting to run multi-mode.

It has to be noted, that the laser starts to run multi-mode at higher frequencies. At the upper limit of fig. 2.31, a more unstable behavior is visible. Here, the seed laser starts to run multi-mode, i.e. multiple oscillation modes have similar gain factors and all of them compete for a limited number of recombinable holes and electrons in the gain medium. The range in which this multi-modal behavior occurs, depends on the laser's temperature, its current, and the setup of its external cavity. All these properties were adjusted in such a way that the laser runs with a single oscillation mode within the regions of interest: the lithium D lines.

Finally, to investigate the frequency stability of the free-running laser, the TAprö monitor output was connected to the wavemeter and then a long-term frequency measurement was started. The results are shown in fig. 2.32. While a constant drift of the frequency is clearly visible, a drift over just 650 MHz in 225 000 s \approx 2.6 days is proof of the long-term stability of the laser. To get a better understanding of the short-term stability, the Allan deviation [Bar90]

$$\sigma_y(\tau) = \sqrt{\frac{1}{2} \langle (y_{n+1} - y_n)^2 \rangle} \quad (2.30)$$

was measured, with $y_n = \langle \delta\nu/\nu_n \rangle$ being the normalized frequency offset of the n -th sample. Here, the offset $\delta\nu$ is the difference between the measured frequency

and the nominal frequency ν_n as given above. The result is depicted in fig. 2.33. The complete frequency measurement was divided into sections of length τ between 200 ms and 9000 s. Unfortunately, shorter section lengths couldn't be measured as the wavemeter needs roughly 37 ms to take one data point which limits τ to values higher than that. A better frequency measurement scheme, e.g. comparing ν to a locked frequency comb and measuring the beat frequency, could help to generate values for even lower τ .

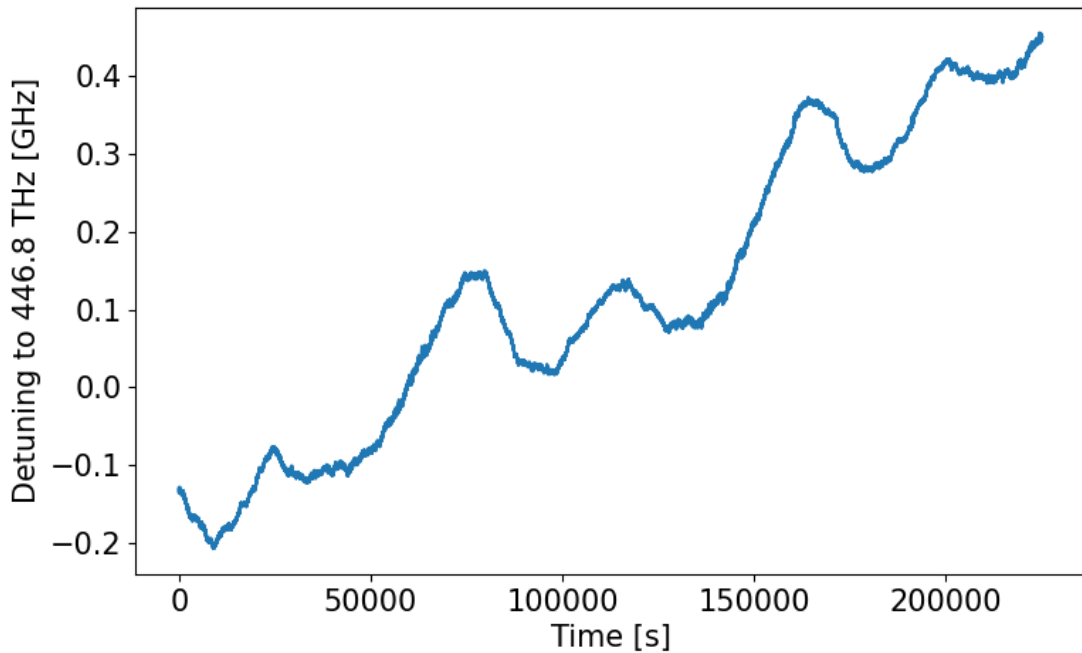


Figure 2.32: Detuning to 446.8 THz of the free-running TAprø versus time. In roughly 2.6 days the laser drifted approximately 650 MHz.

The Allan variance and its square root, the Allan deviation, are measures of an oscillator's stability. The smaller the deviation, the more stable the oscillator. The meaning of *stability* strongly depends on the interpreted time frame. A laser's frequency can be easily modulated at multiple MHz. If one were to look at ν every ns, it would have changed quite significantly in this time frame. If one were to look at it every s, the fast modulation would average out and one might identify ν as stable. That's why σ_y is measured for different values of τ .

Three general regions can be differentiated. For $0.2 \text{ s} < \tau < 1 \text{ s}$, σ_y is at its minimum. This is the stable region in which the main noise source is frequency flicker noise (noise which scales with $1/\nu$) [RH08]. For a nominal frequency of $\nu_n = 446.8 \text{ THz}$, deviation values between $4 \cdot 10^{-10} < \sigma_y < 5 \cdot 10^{-10}$ can be interpreted as frequency uncertainties of approximately 200 kHz. The probed transitions have a natural linewidth of $\Gamma = 5.9 \text{ MHz}$, the uncertainties are well below this value. This commercial laser therefore is suitable to measure the lithium spectra, provided that a single measure-

ment, i.e. a complete scan over a region of interest, is performed in a comparable time frame.

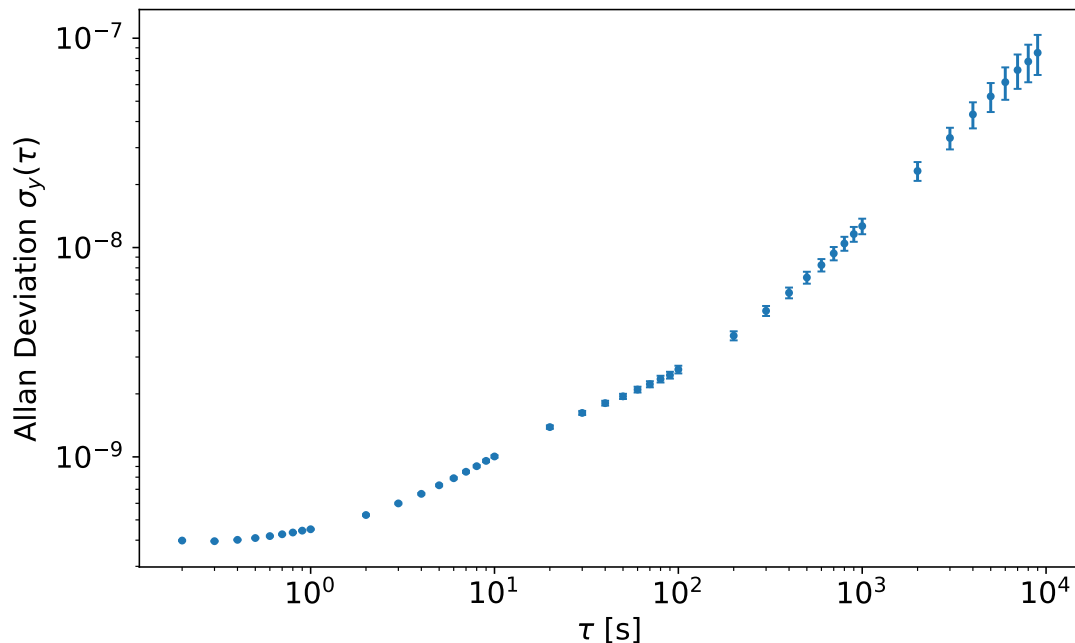


Figure 2.33: Allan Deviation of the TAprö which produces laser light around a nominal value $\nu_n = 446.8$ THz.

For $2\text{ s} < \tau < 100\text{ s}$ the frequency follows a random walk (random movements up and down) and for $200\text{ s} < \tau$ the frequency drifts (movement in one direction). For longer time frames, the laser's behavior, i.e. its frequency, becomes harder to predict. It is not as stable as it is for low τ . However, the laser doesn't need to be stable in these time frames for the purpose of the following analysis. To increase stability, various stabilization techniques are available.

2.2.1. Li D Lines

Lithium appears in the form of two stable isotopes: ${}^6\text{Li}$ and ${}^7\text{Li}$. The former has a nuclear spin $I = 1$ while the latter has $I = 3/2$. Two of the three electrons of the atom reside in the $1s$ shell and therefore, it is filled up completely and the third remaining valence electron resides in the $2s$ shell, making $2S$ the ground state of lithium. Nevertheless, because the nuclear spins couple to the angular momentum and the spin of the valence electron, the atoms have total angular momenta that are half-integer (${}^6\text{Li}$) and integer (${}^7\text{Li}$). ${}^6\text{Li}$ is therefore called fermionic lithium while ${}^7\text{Li}$ is bosonic.

The transitions from the $2S_{1/2}$ ground state to the $2P$ excited states are the so-called D lines¹⁸. Because of the fine structure splitting, the D lines roughly split into the D_1

¹⁸The name "D-line" stems from historic convention. When Joseph von Fraunhofer studied the solar spectrum he found dark features at specific wavelengths. The most prominent features

and the D₂ line. This splitting is already shown in fig. 2.31. To resolve the hyperfine splitting and see more features, Doppler-free spectroscopy methods, such as saturated absorption spectroscopy, have to be used. This can be inferred from fig. 2.34 which shows the level scheme of both lithium isotopes. At the temperatures needed to bring lithium into the gas phase, the Doppler broadening is $\Delta\nu_{\text{Doppler}} \approx 3 \text{ GHz}$ which is much higher than the ground state hyperfine splittings of ⁶Li and ⁷Li : 228 MHz and 803 MHz, respectively. The D lines were therefore investigated using DFSAS which was explained in section 2.1.7.

were labeled using upper-case letters. Number 4 at roughly 589 nm was therefore called the D-line. Some time thereafter, it was found out that this absorption corresponds to the transition of the ground state to the first excited state in sodium (and also to the 587.6 nm transition of helium). Analogously, all transitions of alkali metals from the ground state to the first excited states were called D lines.

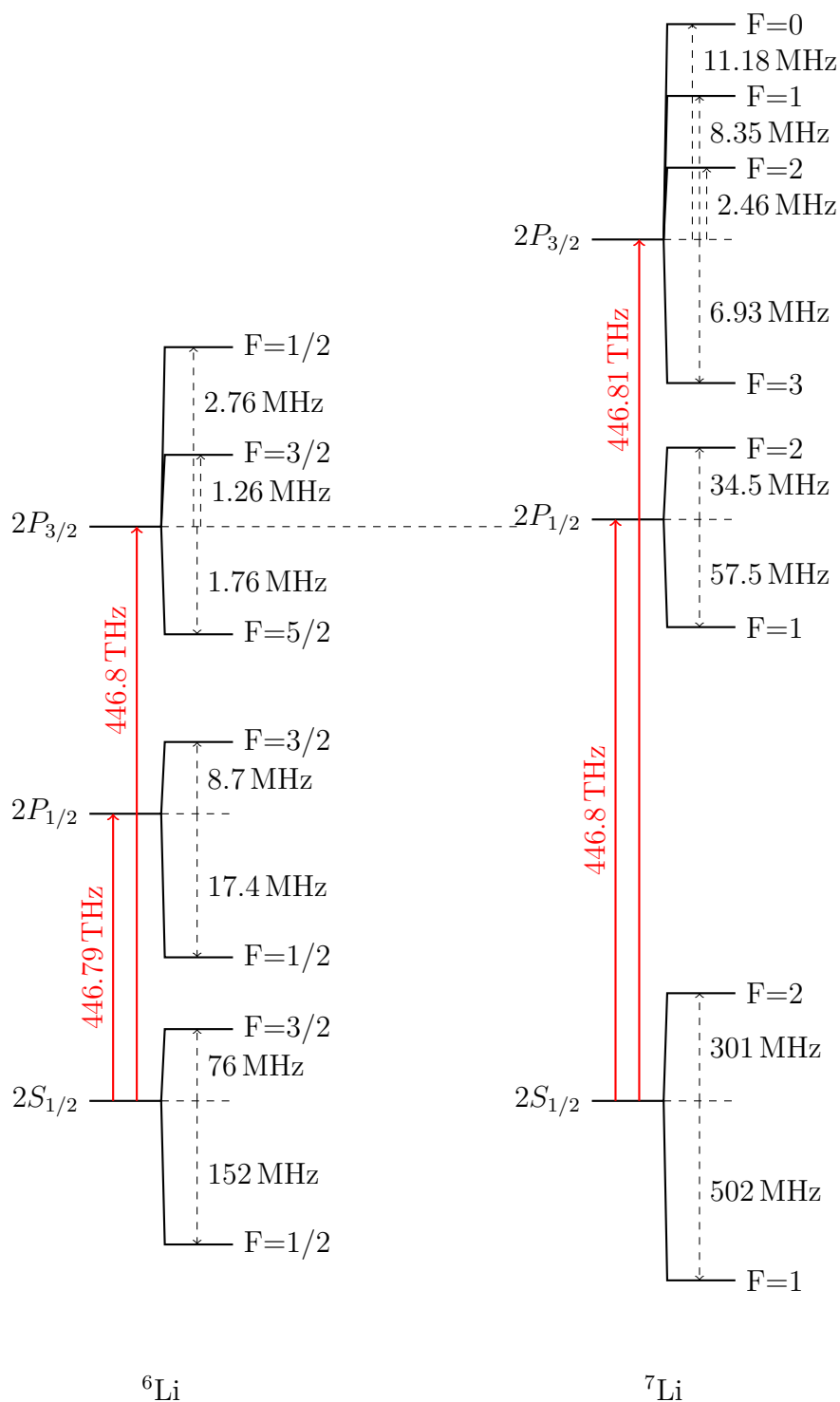


Figure 2.34: ${}^6\text{Li}$ (left) and ${}^7\text{Li}$ (right) level scheme. Not to scale. Note that although the ground states are depicted right next to each other, the total binding energies of the valence electrons are not the same. This was done to point out that the ${}^6\text{Li}$ D_2 line and the ${}^7\text{Li}$ D_1 line have similar transition frequencies. Values [DN07] rounded for better readability.

The ${}^6\text{Li}$ D_1 line incorporates the transitions from the $2S_{1/2}$ ground state to the first excited state $2P_{1/2}$. The possible transitions as well as their respective frequencies are listed in table 2.5. The possible crossover resonances are also listed. The spectrum is plotted in fig. 2.35.

Table 2.5: Ground state and excited state quantum numbers and frequencies of ${}^6\text{Li}$ D_1 line transitions as well as the possible Λ - and V -crossover resonances. Values taken from [LWR⁺20].

F_{gs}	F_{es}	ν [MHz]
3/2	1/2	446 789 502.6393(9)
3/2	3/2	446 789 528.7442(9)
1/2	1/2	446 789 730.8424(23)
1/2	3/2	446 789 756.9439(8)
3/2	V	446 789 515.6918(6)
Λ	1/2	446 789 616.741(1)
Λ	3/2	446 789 642.8441(6)
1/2	V	446 789 743.893(1)

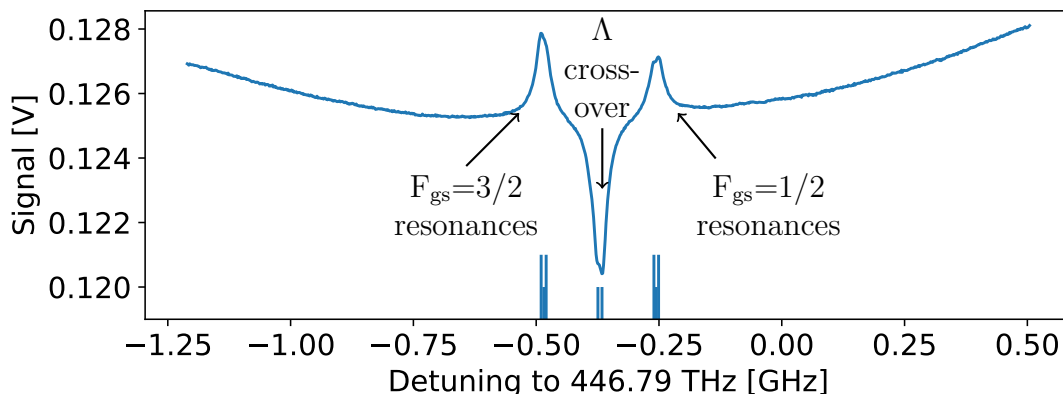


Figure 2.35: ${}^6\text{Li}$ D_1 line measured using Doppler-free saturated absorption spectroscopy. The blue, vertical lines indicate the positions of the resonances. The shorter lines correspond to crossover resonances.

Within the Doppler valley, two peaks and a dip can be found. The peaks actually consist of three peaks each: two real resonances and one crossover resonance. Because both real peaks come from transitions which share the same ground state a third peak appears exactly at the center frequency. The width of each transition is $\Gamma = 5.9$ MHz and in combination with other broadening effects (higher-order and residual first-order Doppler broadening, power broadening, pressure broadening), these peaks start overlapping and differentiating them becomes quite difficult. The dip in the middle comprises the crossover resonances of those transitions that have $F_{\text{es}} = 1/2$ as excited state and those that have $F_{\text{es}} = 3/2$. The hyperfine splitting between these states is roughly 26.1 MHz and the crossover dips are therefore 26.1 MHz apart.

The spectral feature around $\nu = 446.80$ THz is more complex as it contains the resonances of the ${}^6\text{Li}$ D₂ line and the ${}^7\text{Li}$ D₁ line. The frequencies, quantum numbers of involved states and crossover resonances are listed in table 2.6 and table 2.7 for ${}^6\text{Li}$ and ${}^7\text{Li}$, respectively. The measured spectrum is plotted in fig. 2.36.

Table 2.6: Ground state and excited state quantum numbers and frequencies of ${}^6\text{Li}$ D₂ line transitions as well as the prominent Λ -crossover resonances. For the crossover resonance only a mean value is given. The ID and color-coding identifies the resonance in fig. 2.36. Values taken from [LWR⁺20]

F_{gs}	F_{es}	ν [MHz]	ID
3/2	5/2	446 799 571.0796(19)	A
3/2	3/2	446 799 573.9743(19)	A
3/2	1/2	446 799 575.6861(19)	A
1/2	3/2	446 799 802.1758(16)	D
1/2	1/2	446 799 803.8876(16)	D
Λ		446 799 688.9(9)	B

Table 2.7: Ground state and excited state quantum numbers and frequencies of ${}^7\text{Li}$ D₁ line transitions as well as the Λ - and V-crossover resonances. The ID and color-coding identifies the resonance in fig. 2.36. Values taken from [SSG⁺11].

F_{gs}	F_{es}	ν [MHz]	ID
2	1	446 799 771.121(13)	C
2	2	446 799 862.994(12)	F
1	1	446 800 574.608(19)	J
1	2	446 800 666.494(9)	L
2	V	446 799 817.058(9)	E
Λ	1	446 800 172.86(1)	G
1,2	1,2	446 800 218.804(7)	H
Λ	2	446 800 264.744(8)	I
1	V	446 800 620.55(1)	K

The first thing to note is that for the ${}^6\text{Li}$ $2P_{3/2}$ state the order of F flips. While for the lower states higher F correspond to higher energy levels, here the highest energy belongs to the lowest F. This can also be seen in the case of ${}^7\text{Li}$. Not all of the listed lines are visible. As mentioned above, the width of all transitions is $\Gamma = 5.9$ MHz but the ${}^6\text{Li}$ hyperfine splitting is only 4.5 MHz in total and inbetween each pair of transitions there is an additional V-crossover. All ${}^6\text{Li}$ $F_{\text{gs}} = 3/2 \rightarrow F_{\text{es}}$ transitions therefore merge into one feature in the DFSAS spectrum. The same is true for the ${}^6\text{Li}$ Λ -crossover resonance and therefore only the mean frequency of it is listed. The ${}^6\text{Li}$ $F_{\text{gs}} = 1/2$ resonances on the other hand are not really visible because they are too close to the much more prominent ${}^7\text{Li}$ $F_{\text{gs}} = 2$ resonances.

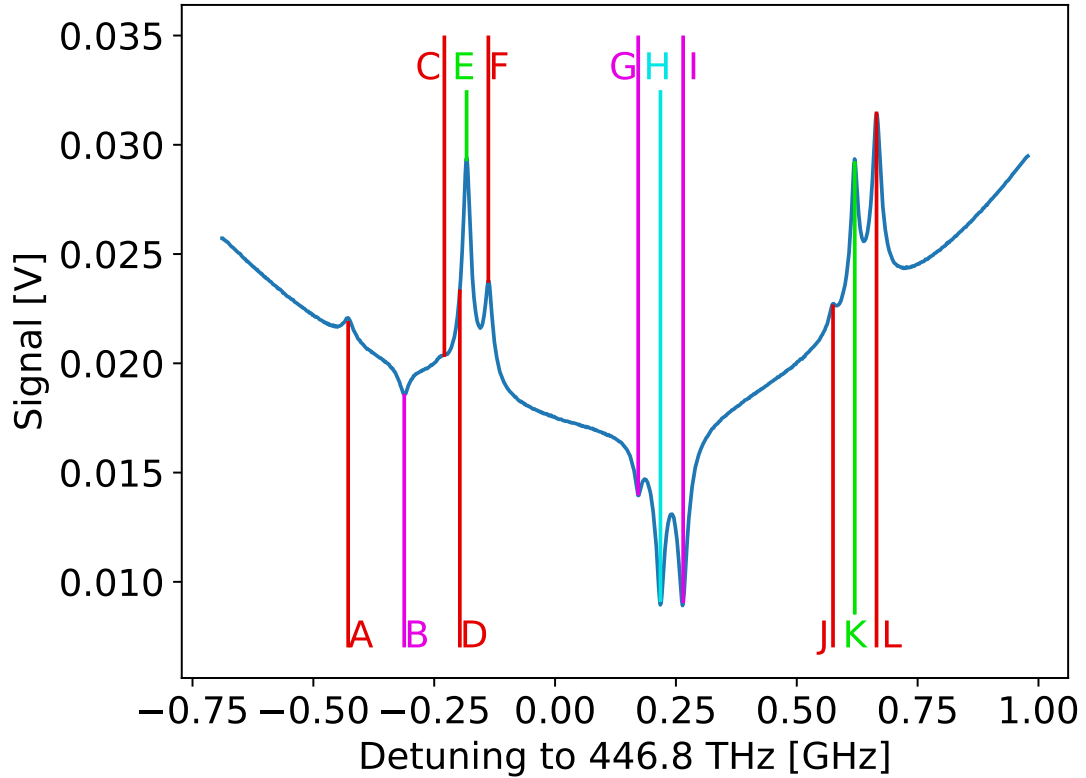


Figure 2.36: ${}^6\text{Li}$ D_2 and ${}^7\text{Li}$ D_1 lines measured using Doppler-free saturated absorption spectroscopy. The resonances are marked with color-coded lines to better identify the type of resonance: **red** for real resonances, **pink** for Λ -crossover resonances, **green** for V-crossover resonances, and **light blue** for second-order crossover resonances. The specific transitions are listed in table 2.6 and table 2.7.

There, the excited state hyperfine splitting is large enough so that every resonance can be easily recognized in the spectrum, although in the case of $F_{\text{gs}} = 2 \rightarrow F_{\text{es}} = 1$ the resonance appears only as a shoulder of the $F_{\text{gs}} = 2$ V-crossover resonance. On the higher end of the spectrum, the $F_{\text{gs}} = 1 \rightarrow F_{\text{es}}$ resonances as well as their Λ -crossover resonance can be found. However, the most interesting features are found in the center of the spectrum. The left and right dips are easily identified as the Λ -crossover resonances with the excited state $F_{\text{es}} = 1$ and $F_{\text{es}} = 2$, respectively. They lie 92 MHz apart and exactly in between the real resonances of the left and right triplet peaks. The center dip (marked by line **H**) is different as it is not in the middle of two real resonances but two crossover resonances.

This second-order crossover resonance appears between two "imaginary" states: one in the middle of the ground states and one in the middle of the excited states as depicted in fig. 2.37.

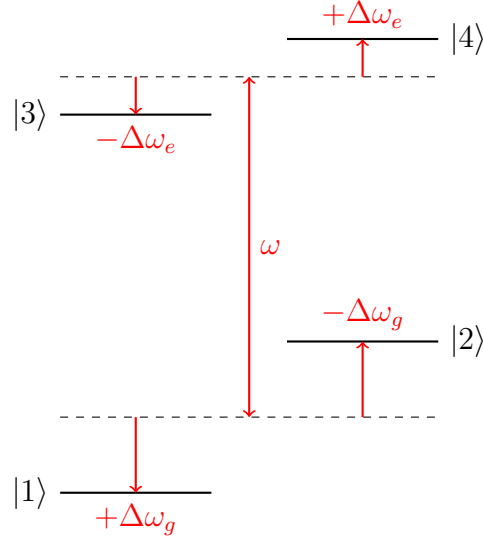


Figure 2.37: Level scheme of the central ${}^7\text{Li}$ D₁ crossover resonance dip.

The laser's frequency of ω is not resonant to any of the four possible transitions. Their respective frequencies are:

$$\omega_{|1\rangle\rightarrow|3\rangle} = \omega + \Delta\omega_g - \Delta\omega_e, \quad (2.31)$$

$$\omega_{|1\rangle\rightarrow|4\rangle} = \omega + \Delta\omega_g + \Delta\omega_e, \quad (2.32)$$

$$\omega_{|2\rangle\rightarrow|3\rangle} = \omega - \Delta\omega_g - \Delta\omega_e, \quad (2.33)$$

$$\omega_{|2\rangle\rightarrow|4\rangle} = \omega - \Delta\omega_g + \Delta\omega_e. \quad (2.34)$$

If atoms of a certain velocity group see one of the laser beams Doppler-shifted to $\omega_{|1\rangle\rightarrow|3\rangle}$, they will also see the other beam shifted to $\omega_{|2\rangle\rightarrow|4\rangle}$ because they have opposite wavevectors \vec{k} . Thus, one velocity group will absorb either of the two beams depending on the ground state which the individual atom occupies.

The process is similar to the one of the regular Λ -crossover resonance. The high intensity pump beam excites atoms of one ground state $|G\rangle$ into one of the excited states $|E\rangle$. From there, they spontaneously decay into either $|G\rangle$ or the other ground state $|g\rangle$, effectively pumping atoms from $|G\rangle$ to $|g\rangle$. In this state, they can now absorb the probe beam and are excited to the second excited state $|e\rangle$. Therefore, less photons of the pump beam pass the atom cloud and the signal measured by the photodiode sinks. And because four velocity classes are affected by this, the resulting feature is very prominent in the spectrum.

Finally, the highest frequency resonance, the ${}^7\text{Li}$ D₂ line is discussed. The possible transition frequencies are listed in table 2.8 and the spectrum is depicted in fig. 2.38. Although many transitions are listed only three features can be made out in the spectrum. As was the case before in the ${}^6\text{Li}$ spectra, the hyperfine splitting of the excited state too small. The splitting is larger than Γ but due to the DFSAS measurement

scheme crossover resonances fill the gaps in the spectrum and the many peaks merge into one broad peak. This is true for the real resonances on the low and the high frequency end of the spectrum which also give rise to V-crossover resonances, as well as the dip in the middle which comprises many different Λ -crossover resonances.

Table 2.8: Ground state and excited state quantum numbers and frequencies of ${}^7\text{Li}$ D_2 line transitions as well as the prominent Λ -crossover resonance. For the crossover resonance only a mean value is given. Values taken from [BWP⁺13].

F_{gs}	F_{es}	ν [MHz]
2	3	446 809 874.895(20)
2	2	446 809 884.357(20)
2	1	446 809 890.170(20)
1	2	446 810 687.873(25)
1	1	446 810 693.687(25)
1	0	446 810 696.445(25)
Λ		446 810 289(3)

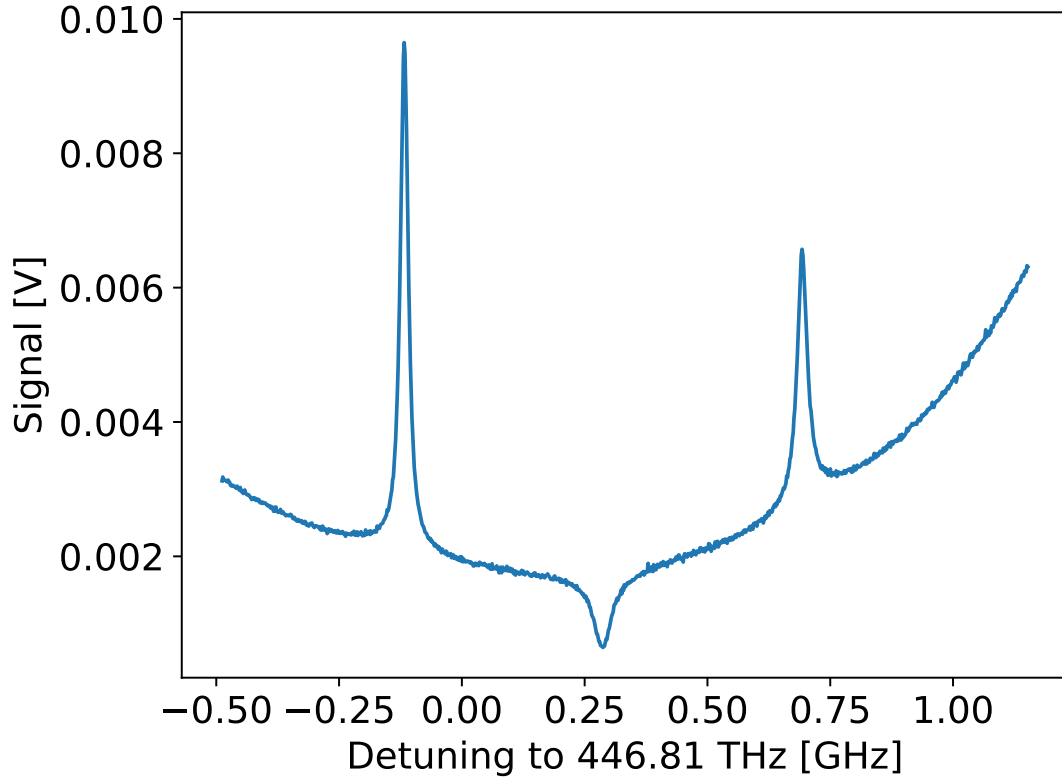


Figure 2.38: ${}^7\text{Li}$ D_2 line measured using Doppler-free saturated absorption spectroscopy.

2.2.2. Eliminating the Doppler Background

The previously shown spectra contain several features such as narrow peaks and dips that stem from the atom's hyperfine structure and the broad Doppler-valleys in which they lie. The Doppler-valleys form an unwanted background to the signal of interest which slightly changes the position of the peaks and therefore, it is desirable to get rid of it. To achieve this, the DFSAS setup was slightly modified. A mechanical beam chopper and a lock-in amplifier were added as shown in fig. 2.39.

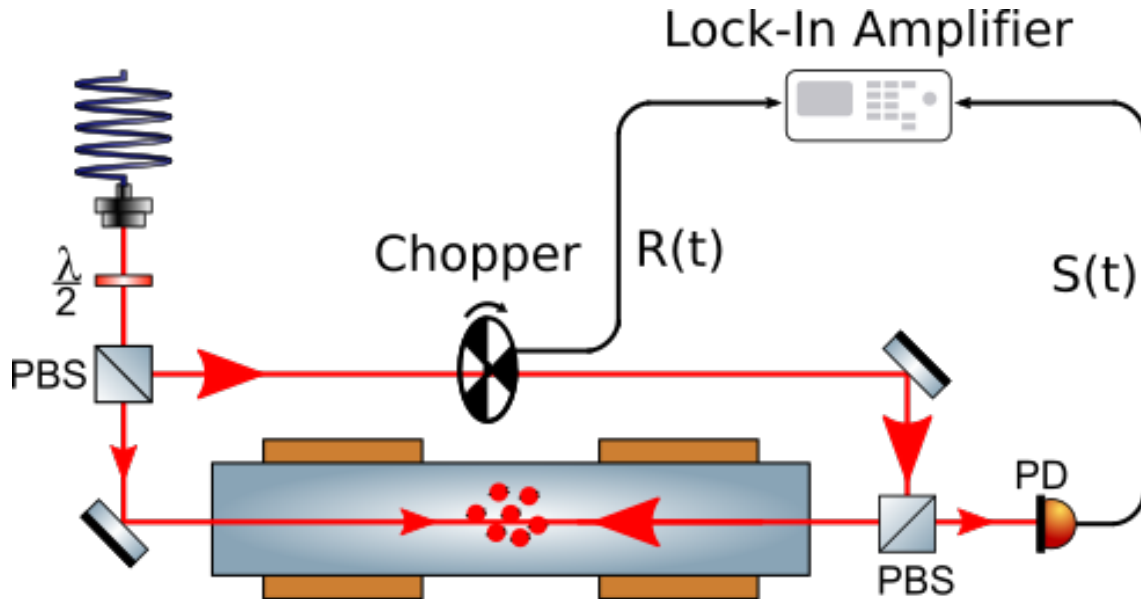


Figure 2.39: DFSAS setup with chopper and lock-in amplifier (LIA). The chopper (or rather its controller) sends a reference signal $R(t)$ to the LIA. Then, the LIA mixes it with the signal $S(t)$ delivered by the photodiode.

An electric signal can contain many different frequencies ω . This is depicted in fig. 2.40. The signal may contain continuous parts and discrete frequencies but one is only really interested in one certain frequency and the rest is considered noise¹⁹. To pick out only the amplitude of the frequency of interest, a lock-in amplifier can be used.

Suppose a signal S that comprises many different frequencies ω_i with their respective amplitudes A_i

$$S(t) = \sum_i A_i \sin(\omega_i t), \quad (2.35)$$

and a reference signal

$$R(t) = a_R \sin(\omega_R t + \Delta\phi), \quad (2.36)$$

with its own amplitude a_R and a phase shift $\Delta\phi$ relative to the signal component of the same frequency. Both signals are fed into the lock-in amplifier which mixes

¹⁹This is comparable to when someone wants to listen to a certain radio station. The antenna picks up every signal and every frequency but one is only interested in a specific one of them.

them, i.e. multiplies them. Subsequently, an internal low-pass filter integrates the signal over an integration time T :

$$f(t, T) = \frac{1}{T} \int_{t-T}^t S(\tau)R(\tau)d\tau \approx A_R a_R \frac{\cos(\Delta\phi)}{2}. \quad (2.37)$$

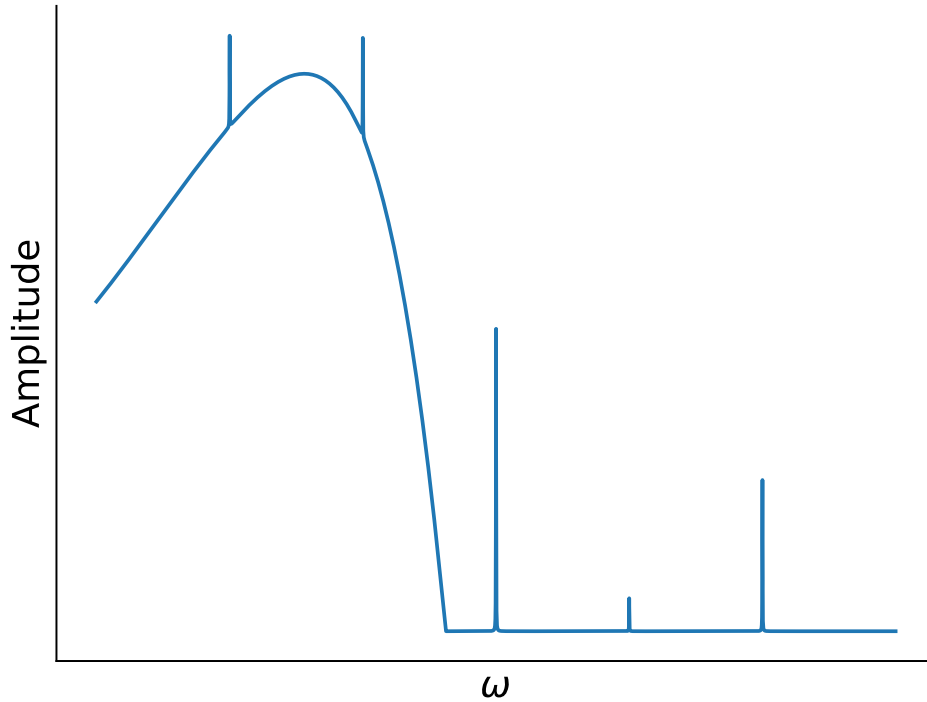


Figure 2.40: Schematic depiction of an arbitrary signal which contains many different frequencies ω with individual amplitudes. Some frequencies appear as discrete features, some frequencies are part of a continuous spectrum.

Of course, it is assumed that S contains ω_R with the amplitude A_R . The result is only given approximately because S might contain frequencies within the range $[\omega_R - \frac{2\pi}{T}, \omega_R + \frac{2\pi}{T}]$ which would lead to an oscillating component in the lock-in amplifiers output. Schematically, this sequence is depicted in fig. 2.41. The used lock-in amplifier is an SR510 by Stanford Research Systems and the parameter ω_R , $\Delta\phi$, and T are adjustable to generate a clean and high-amplitude output.

As the chopper blocks and unblocks the pump beam with frequency ω_R , the measured signal periodically changes from the regular Doppler-broadened transmission signal to the already explained DFSAS signal and back again. As an example, both types of signal are shown in fig. 2.42 for the ${}^6\text{Li D}_2$ and ${}^7\text{Li D}_1$ lines. Basically, their only difference is the occurrence of the hyperfine structure peaks and crossover resonances. The Doppler-background is mostly the same.

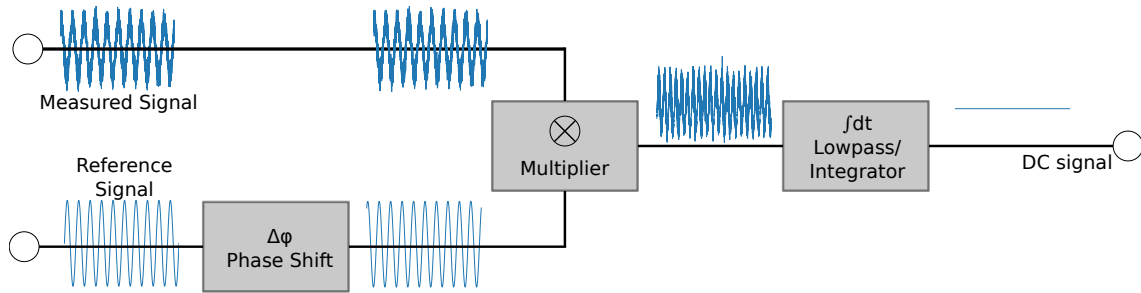


Figure 2.41: Schematic of the principle working of a lock-in amplifier.

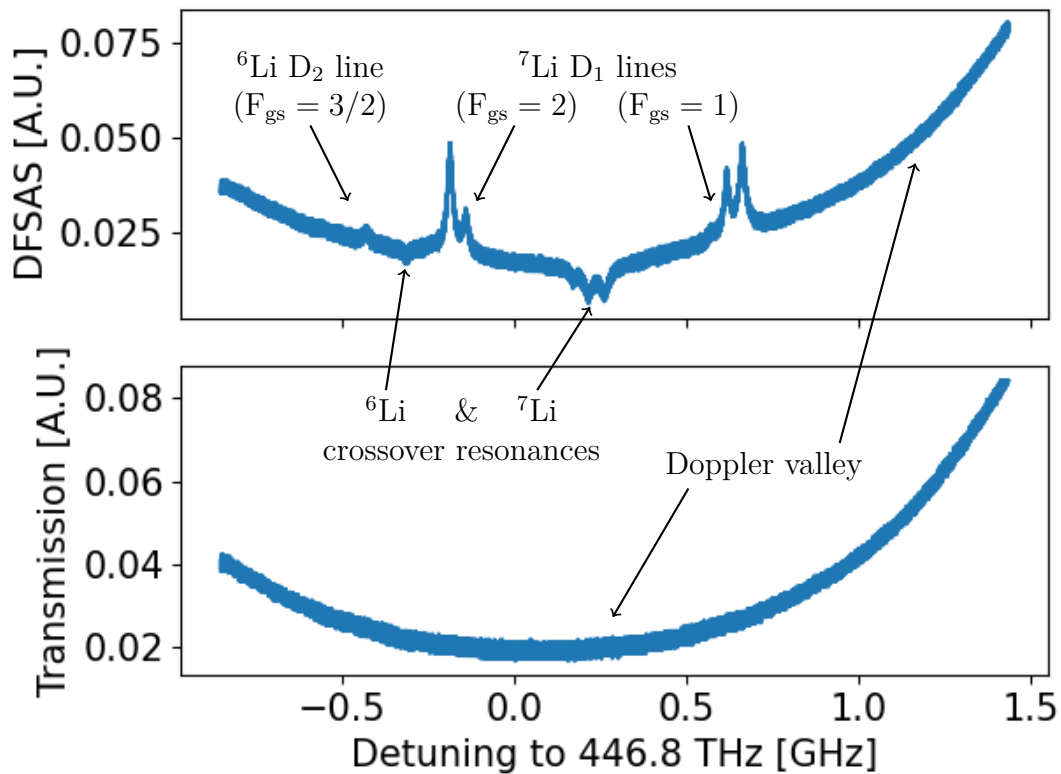


Figure 2.42: Comparing the ${}^6\text{Li D}_2$ and ${}^7\text{Li D}_1$ spectra measured with DFSAS (top) and measured using regular transmission spectroscopy (bottom).

Assuming that the chopper frequency ω_R is much faster than the scan frequency of the laser, i.e. the laser frequency ω_L is considered constant over the integration time, the output signal of the lock-in amplifier only depends on the difference between the regular transmission signal and the DFSAS signal. The resulting signal is shown in fig. 2.43. The background disappears and features that were covered by noise are suddenly visible such as the ${}^7\text{Li } F_{gs} = 2 \rightarrow F_{es} = 1$ transition. A reader with a keen eye might also detect the ${}^6\text{Li } F_{gs} = 1/2$ transitions on the left shoulder of the ${}^7\text{Li } F_{gs} = 2$ crossover resonance.

Without the presence of the Doppler background, their relative distances correspond to the real differences in their transition frequencies. Additionally, the more peaks

can be identified, the more accurate will be the frequency gauging, the procedure of which is explained in the next section.

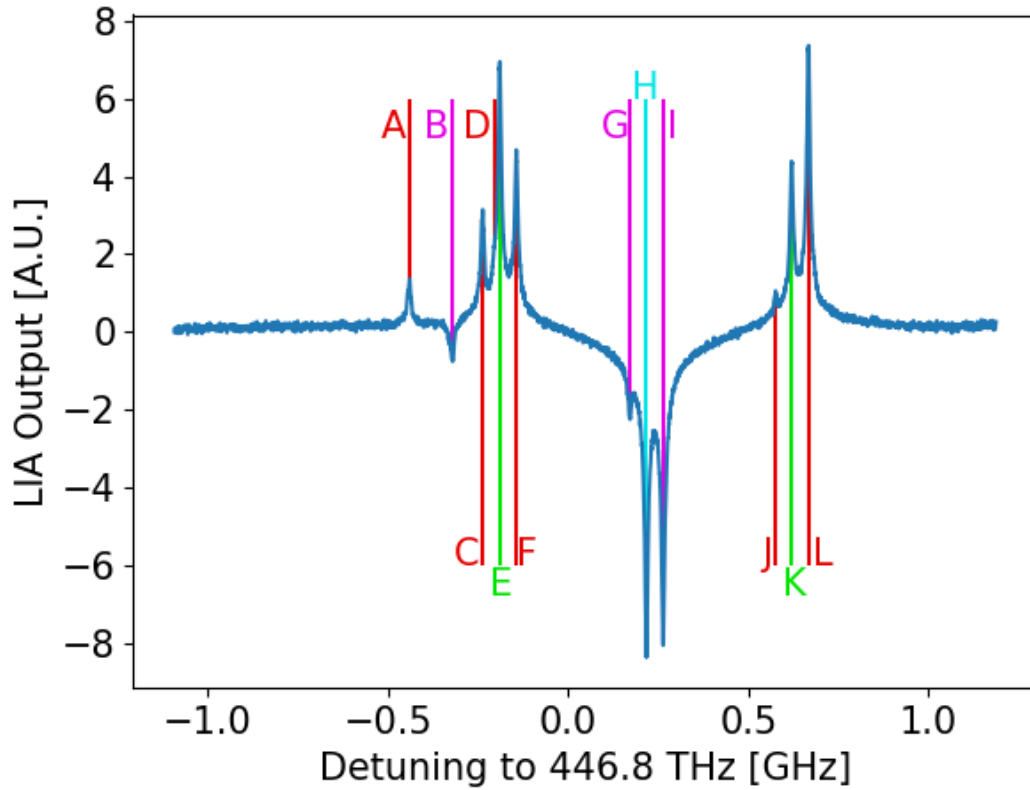


Figure 2.43: Lock-in amplified ${}^6\text{Li}$ D_2 and ${}^7\text{Li}$ D_1 DFSAS spectrum with removed background. The color-coding and naming is explained in table 2.6 and table 2.7.

2.2.3. Frequency Calibration Procedure

When a DFSAS spectrum is taken and the spectroscopy laser's frequency is scanned continuously over time following $\nu(t)$, the signal measured by the photodiode is $V(t)$ rather than $V(\nu)$ and a way to translate t to ν has to be found. One might use a second laser of well-known frequency, e.g. a laser locked to a frequency comb, to constantly measure the beat frequency $\Delta\nu(t)$ between the two lasers so that the detuning is always known. One might also measure a reference spectrum and use the position of its features to infer a mapping function from t to ν [Fra21]. The latter approach is the one which was followed in the rest of this thesis.

To build and characterize a magneto-optical trap for ${}^6\text{Li}$, the ${}^6\text{Li}$ D_2 and ${}^7\text{Li}$ D_1 spectra are the ideal reference. The frequencies are quite close to each other and have many easily identifiable features as shown in the last section. Using fit functions with well-defined local maxima/minima allows for a stable approach. The function

of choice is a combination of multiple Lorentz distributions L and a constant background f_0

$$f(t) = f_0 + \sum_{i=1}^{15} N_i \cdot L(t_{0,i}, \Gamma_i), \quad (2.38)$$

where $t_{0,i}$ and Γ_i are the centers and widths of the individual distributions, respectively. Although there are only 12 features in fig. 2.43, 15 distributions are used to approximate the spectrum. At the position of the peaks, especially the crossover resonances around $t \approx 0$, features that stem from systematic effects of unknown origin are visible in the residuals plot, indicating the need for corrections to the fit function. Nevertheless, the center positions were precise enough to determine an adequate frequency scale.

The feature positions $t_{0,i} \pm \Delta t_{0,i}$ are then compared to their respective frequencies $\nu_i \pm \Delta \nu_i$ taken from literature [LWR⁺20] and a second-order polynomial

$$\nu(t, a, b) = \nu_0 + a \cdot t + b \cdot t^2 \quad (2.39)$$

serves as a mapping function, with ν_0 , a , and b being fit parameters. The resonance frequencies have been measured quite precisely, in fact more precisely than the frequency calibration that can be achieved here, and the errors $\Delta t_{0,i}$ have to be taken into account. Therefore, this optimization step was not done minimizing a regular χ^2 but rather a modified

$$\begin{aligned} \chi_{\text{mod}}^2 &= \sum_i \frac{(\nu_i - \nu(t_{0,i}, a, b))^2}{\Delta \nu_i^2 + \Delta t_{0,i}^2 \cdot \left(\frac{\partial \nu(t, a, b)}{\partial t} \Big|_{t=t_{0,i}} \right)^2} \\ &= \sum_i \frac{(\nu_i - \nu_0 - a \cdot t_{0,i} - b \cdot t_{0,i}^2)^2}{\Delta \nu_i^2 + \Delta t_{0,i}^2 \cdot (a^2 + 4abt_{0,i} + 4b^2t_{0,i}^2)}. \end{aligned} \quad (2.40)$$

The quadratic term in the mapping function eq. (2.39) is assumed to be small and small changes in t are thus expected to affect $\nu(t)$ linearly. The total squared error of any data point is the sum of all its individual squared errors: errors due to uncertainties of the frequency literature values $\Delta \nu_i$ and the linear effects of variations in $t_{0,i}$.

The spectrum with a translated x -axis is again plotted in fig. 2.45. In addition, the uncertainty of the frequency calibration $\Delta \nu$ in dependence of ν is shown. To calculate this uncertainty, the covariance matrix M_{cov} of the fit parameters is needed.

$$M_{\text{cov}} = \begin{pmatrix} \text{cov}(\nu_0, \nu_0) & \text{cov}(\nu_0, a) & \text{cov}(\nu_0, b) \\ \text{cov}(a, \nu_0) & \text{cov}(a, a) & \text{cov}(a, b) \\ \text{cov}(b, \nu_0) & \text{cov}(b, a) & \text{cov}(b, b) \end{pmatrix} = \begin{pmatrix} \Delta \nu_0^2 & \text{cov}(\nu_0, a) & \text{cov}(\nu_0, b) \\ \text{cov}(\nu_0, a) & \Delta a^2 & \text{cov}(a, b) \\ \text{cov}(\nu_0, b) & \text{cov}(a, b) & \Delta b^2 \end{pmatrix}. \quad (2.41)$$

This matrix is symmetric and contains the covariances of all fit parameter pairings. Its diagonal entries are therefore identified as the squared errors of the fit parameters $\Delta\nu_0$, Δa , and Δb . With this, $\Delta\nu$ becomes

$$\Delta\nu(t) = \sqrt{\Delta\nu_0^2 + 2M_{\text{cov},1,2}t + (\Delta a^2 + 2M_{\text{cov},1,3})t^2 + 2M_{\text{cov},2,1}t^3 + \Delta b^2t^4}. \quad (2.42)$$

In the region of interest, i.e. the ${}^6\text{Li}$ D₂ spectrum, this leads to small errors relative to the width of the resonances which is also depicted in fig. 2.45. The uncertainty is well below 1 MHz while $\Gamma = 5.9$ MHz. This is by far not enough to allow for high-precision spectroscopy but it is sufficient to characterize the Zeeman slower and the magneto-optical trap that were built during this thesis.

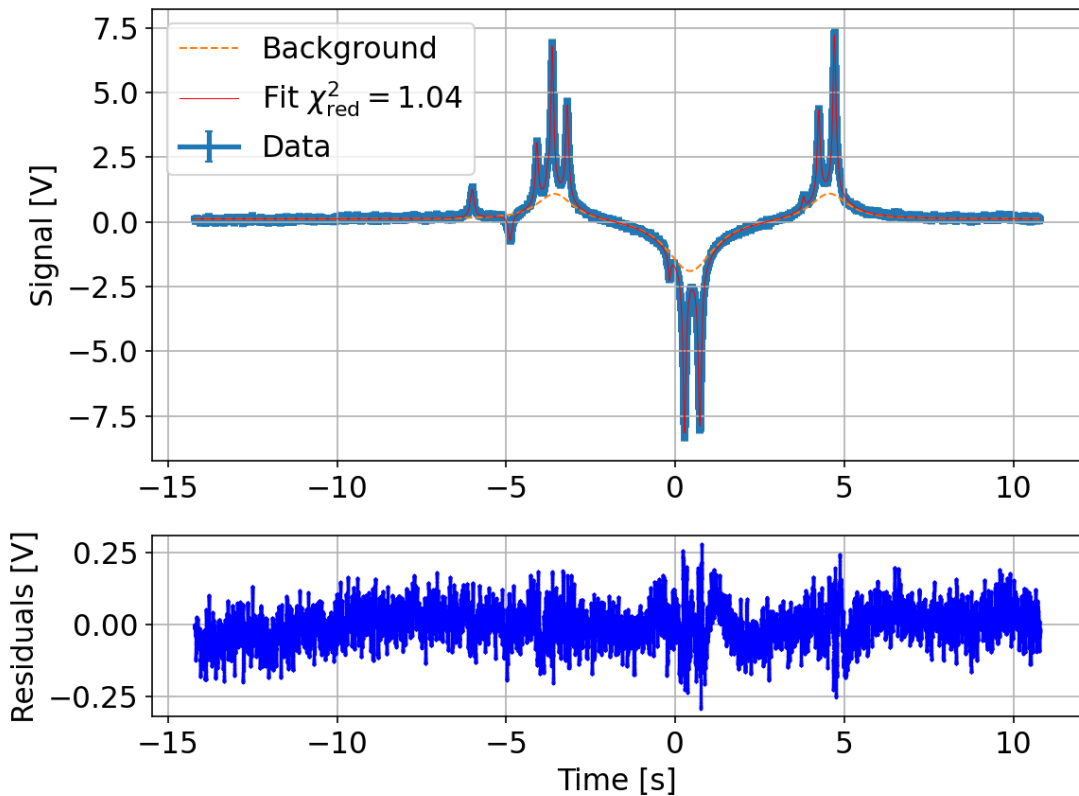


Figure 2.44: Lock-in amplifier cleaned ${}^6\text{Li}$ D₂ and ${}^7\text{Li}$ D₁ spectrum with a fitted function. Additionally, the differences between data and fit function are given as residuals.

To achieve a better frequency calibration, the other procedures that were mentioned in the beginning of this section are necessary. Unfortunately, neither a frequency comb nor an adequate reference cavity were available in time to be used, but in the future, a setup with a precise beat-offset lock and an acousto-optical modulator to tune the laser is planned.

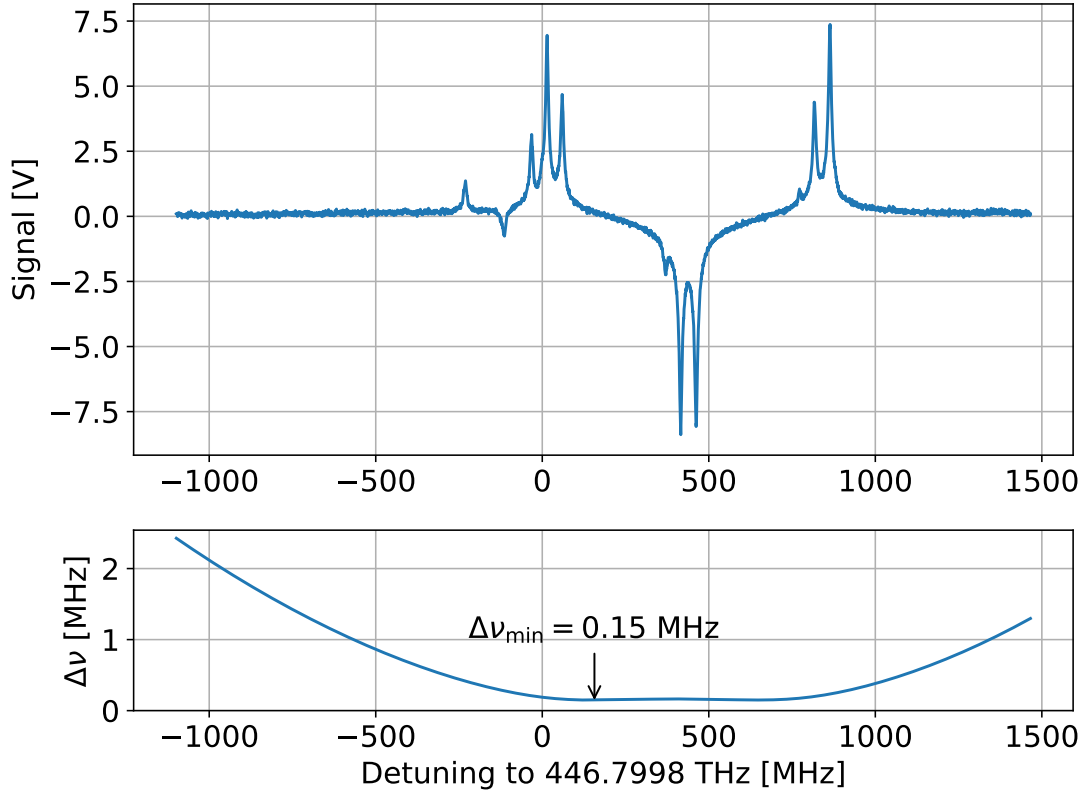


Figure 2.45: Lock-in amplifier cleaned ${}^6\text{Li D}_2$ and ${}^7\text{Li D}_1$ spectrum where the x -axis has been translated to frequency. Additionally, the frequency uncertainty is given with a minimum uncertainty $\Delta\nu_{0,\min} = 0.15 \text{ MHz}$ at a detuning of 156.7 MHz.

2.2.4. Laser Locking

For high precision spectroscopy, the laser's linewidth should be as small as possible. As shown in fig. 2.33, the laser's frequency, if left by itself, drifts over time. This section explains how (and how well) this drift can be compensated.

In this work, it was decided to lock the laser to a resonance of ${}^7\text{Li}$, using a Pound-Drever-Hall technique [DHK⁺83, Bla98, Bla01]. In previous sections, ${}^7\text{Li}$ measurements have already been presented and many prominent resonances lie close to the desired ${}^6\text{Li D}_2$ frequencies. The ${}^7\text{Li D}_1$ lines offer a good reference to which the laser can be stabilized. By making some adjustments to the DFSAS setup as it is shown in fig. 2.16a, the laser can be easily stabilized to the lowest frequency crossover resonance of the ${}^7\text{Li D}_1$ line. This new setup is depicted in fig. 2.46.

The first elements which the beam passes are two $\frac{\lambda}{2}$ -retarders and an electro-optic modulator. By applying a voltage V to a birefringent crystal (in this case, lithium niobate LiNbO_3) its refractive indices can be changed, depending on the crystal's symmetry and point group. For different V , light that passes the EOM acquires a

different phase ϕ and hence by modulating V , ϕ is directly modulated as well.²⁰ If V is modulated sinusoidally with amplitude ΔV and frequency ω_m , the phase follows

$$\phi(t) = \phi_0 + \Delta\phi(\Delta V) \cdot \sin(\omega t) \quad (2.43)$$

and after it passes the EOM the laser beam's electric field E becomes

$$\begin{aligned} E(t) &= E_0 e^{i\omega t} e^{i\Delta\phi \cdot \sin(\omega t)} \\ &= E_0 e^{i\omega t} e^{\frac{\Delta\phi}{2}(e^{i\omega_m t} - e^{-i\omega_m t})} \\ &= E_0 e^{i\omega t} \sum_{n=-\infty}^{\infty} J_n(\Delta\phi) e^{in \cdot \omega_m t} \\ &= E_0 \sum_{n=-\infty}^{\infty} J_n(\Delta\phi) e^{i(\omega + n \cdot \omega_m)t}. \end{aligned} \quad (2.44)$$

The phase modulation of the EOM splits an incoming monochromatic beam into one carrier of the original frequency ω and an infinite number of sidebands separated by a multiple of ω_m . Each frequency component is scaled by a Bessel function J_n of the respective order n . The step from the second to the third line uses the fact that a Laurent series can be used to generate the Bessel functions:

$$e^{\frac{x}{2}(t - \frac{1}{t})} = \sum_{n=-\infty}^{\infty} J_n(x) t^n.$$

Here, the phase modulation happens at $\omega_m = 2\pi \cdot 5$ MHz.

After passing the EOM, the beam is guided through an acousto-optic modulator in cat-eye configuration. The working principle of an AOM is described in section 4.2. It's only necessary to know that this double-pass AOM shifts the beam's frequency by $2\nu_{\text{AOM}}$. The $\frac{\lambda}{4}$ -plate, shifts the laser's polarization by 90° so that the light, which previously passed the PBS, is now reflected by it. The laser will be locked to one specific ${}^7\text{Li}$ resonance whose frequency will naturally not overlap with the ${}^6\text{Li}$ resonances of interest. The AOM allows the frequency of the laser ν_{Laser} to be set independently of the lock frequency. In the end, $\nu_{\text{AOM}} = +80$ MHz, the laser therefore produces light 160 MHz below the locked-on resonance. However, for the purpose of this analysis, this shift is neglected to better depict the lock to said specific resonance²¹. Finally, the beam enters a regular DFSAS setup and a photo diode measures a spectrum $S(\nu)$, as explained in section 2.1.7. Due to the EOM however, $S(\nu)$ contains the

²⁰This assumes that the polarization of the laser and the major or minor axis of the phase ellipse overlap. If not, the polarization of the light is modulated and an amplitude modulation can be realized by adding a polarization filter. Additionally, the main axes might also change direction with V . Fortunately, there exists a stable axis for LiNbO_3 .

²¹A shift of 160 MHz would also shift the DFSAS spectrum shown below by this value. The ${}^7\text{Li}$ features, as they are explained in section 2.2.1, wouldn't be, where the reader might expect them to be.

modulation frequency ω_m and can thus be demodulated to generate an error signal $E(\nu)$ using a lock-in amplifier. In this case, the resulting $E(\nu)$ becomes a function of $S(\nu)$'s slope, i.e. its derivative $S'(\nu)$. A control signal $C(\nu)$ is produced by applying several filters and amplifiers to $E(\nu)$ to suppress unwanted noise and improve the stability of the lock. Then, $C(\nu)$ is directly fed back into the laser system to keep $E(\nu) = \text{const.}$ and thereby lock the laser to a specific frequency.

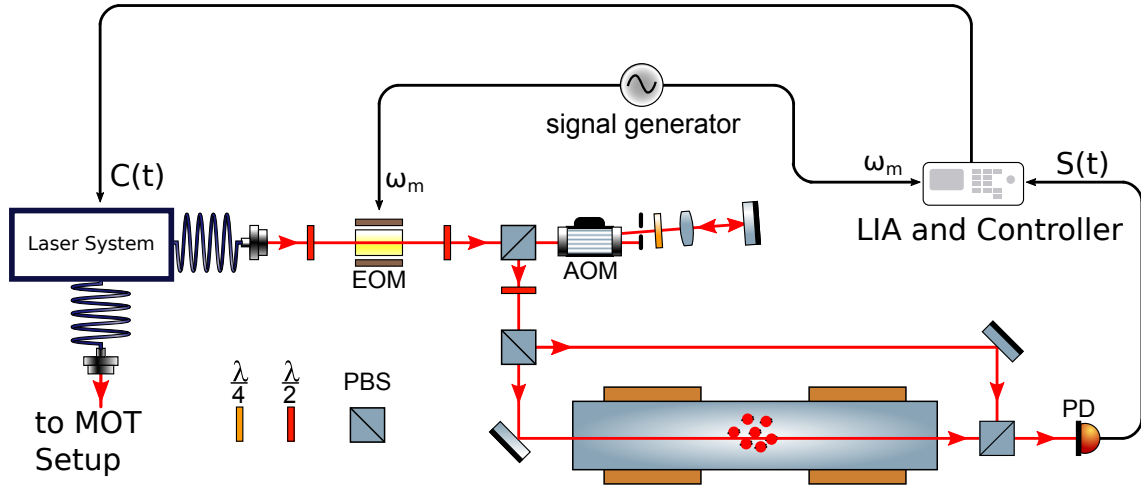


Figure 2.46: Schematic locking setup. A small part of the laser is coupled out and guided into the setup. The laser passes an electro-optic modulator (EOM), which applies a phase modulation to the beam, generating sidebands around the original carrier frequency. The laser's frequency is then shifted by an acousto-optic modulator (AOM) in a cat-eye configuration to allow for a frequency adjustment independent of the resonance, which the laser is locked to. The modulated beam then passes a regular DFSAS setup and a photo diode (PD) is used to measure the resonance spectrum $S(t)$. The signal is then demodulated to create an error signal which in turn is used to create a feedback $C(t)$ into the laser system to finally stabilize the frequency. Although these signals are depicted as functions of time t , they can just as well be understood as functions of the laser frequency ν , as explained in section 2.2.3.

The signals $S(\nu)$ and $C(\nu)$ (without feedback) are depicted in fig. 2.47. Both signals were measured ten times within a second, their mean values in frequency ν and voltage V as well as their corresponding errors ($\frac{\sigma}{\sqrt{N}}$) were calculated to account for signal fluctuations. The transmission peaks (shown in red) correspond to the lowest ν ${}^7\text{Li D}_2$ lines: $F_{\text{gs}} = 2 \rightarrow F_{\text{es}} = 1$, $F_{\text{gs}} = 2 \rightarrow F_{\text{es}} = 2$, and their respective crossover resonance. As expected, the control signal (shown in blue) has zero-crossings at $S(\nu)$'s local maxima and minima.

A good error signal should have a high peak-to-peak amplitude to allow for a good read-out and a steep slope around the lockpoint with high sensitivity to small deviations $\Delta\nu$. Of the three shown transmission features, the central crossover peak is

the most prominent and exhibits the best error signal with a slope around the zero-crossing of $\frac{\Delta V}{\Delta \nu} = -1.006(1)$ V/MHz. This value was gained by performing a linear fit around the central zero-crossing, as can be seen in fig. 2.47. Of course, the sign of $E(\Delta \nu)$ has to be correct and match the laser system's response. For this specific laser, the frequency increases when a higher voltage is applied to the Piezo element and decreases for lower voltages. If the frequency is below the lockpoint ($\Delta \nu < 0$), the error signal will be positive and hence push ν to higher values and vice versa.

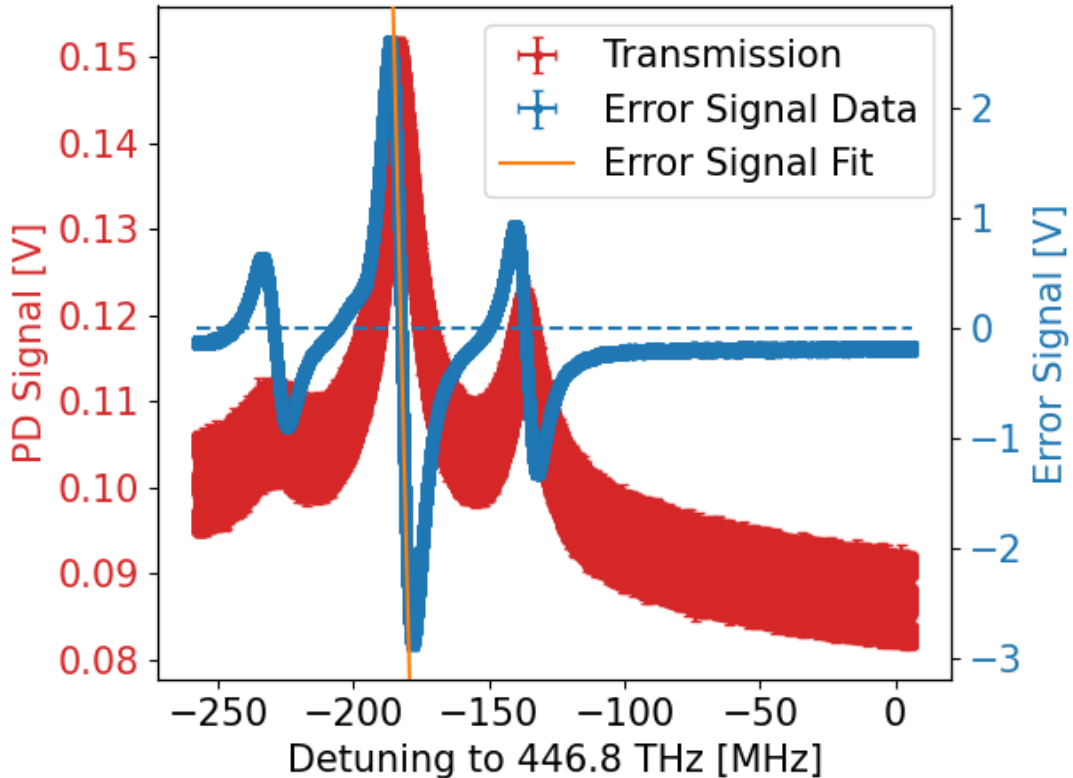


Figure 2.47: Measurement of modulated DFSAS signal (red) and demodulated, amplified error signal (blue) with scan signal on and lock off. Depicted are the lower frequency ${}^7\text{Li D}_1$ lines: $F_{\text{gs}} = 2 \rightarrow F_{\text{es}} = 1$, $F_{\text{gs}} = 2 \rightarrow F_{\text{es}} = 2$, and their respective crossover resonance. Additionally, the error signal's zero-crossing (dashed blue line) corresponding to the crossover resonance was fitted using a linear function. Its slope serves as an estimation of the lock quality.

Once the feedback is turned on, the laser's frequency stabilizes. This manifests in the fact, that the error as well as the photodiode signal start scattering around certain values, as is depicted in fig. 2.48. The y -ranges of both signals were kept the same compared to the unlocked plot to make comparison easier but the x -axis changed from frequency to time. Of course, ν cannot be extracted from the transmission signal if the laser isn't scanned. However, ν corresponds to the crossover resonance. This was confirmed using the wavemeter which was mentioned in previous sections.

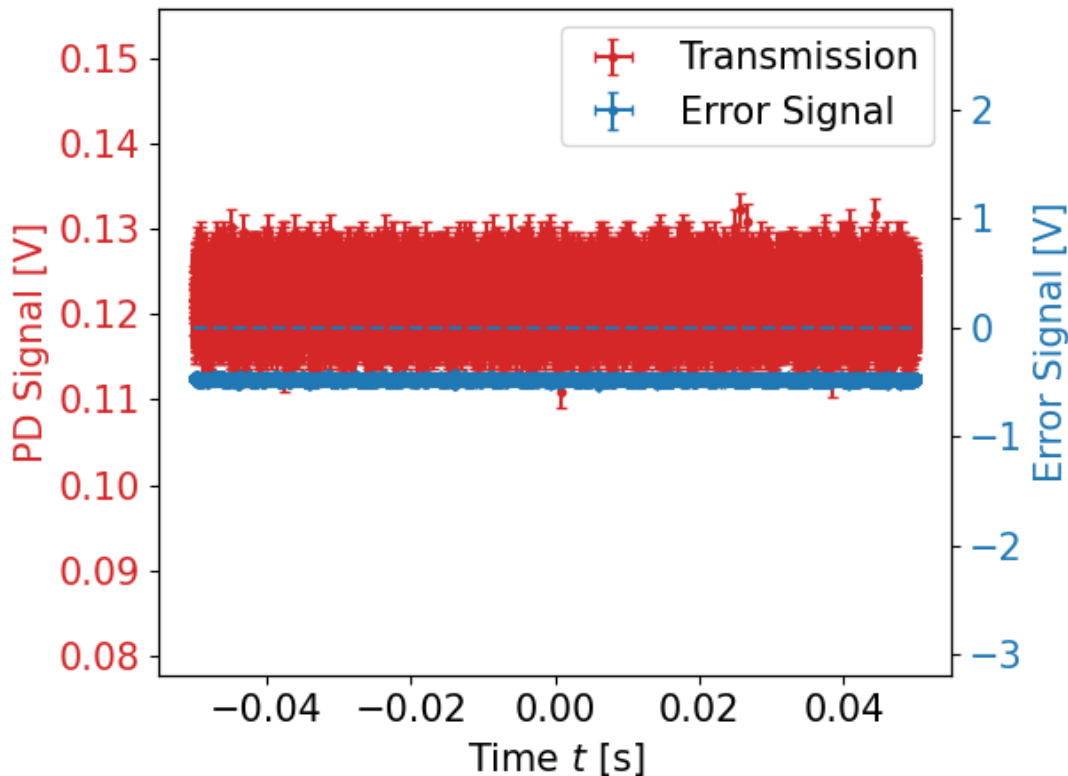


Figure 2.48: Measurement of modulated DFSAS signal (red) and demodulated, amplified error signal (blue) with scan signal off and lock on. The same y -range as in fig. 2.47 was chosen to make comparison easier. Although the DFSAS signal stays at the height of the $F = 2 \rightarrow F' = 2$ resonance, the real frequency corresponded to the locked on crossover resonance. The amplitude of the error signal corresponds to a laser line width of $0.12(1)$ MHz

The control signal does not lock onto 0, but a constant value²². By comparing the locked signal to the unlocked one and translating back to frequency (including errors), the laser's frequency can be determined to be $\nu_{\text{Locked}} = 446\,799\,818.0(6)$ MHz. By comparing the locked control signal's peak-to-peak amplitude ΔC to the slope derived before, the linewidth can be calculated using

$$\Gamma_{\text{Locked}} = \Delta C / \frac{\Delta V}{\Delta \nu}. \quad (2.45)$$

Obviously, the locked linewidth $\Gamma_{\text{Locked}} = 0.12(1)$ MHz is smaller than the error of ν_{Locked} . While the frequency itself cannot be determined definitely, due to an unknown offset from $E(\Delta \nu)$'s exact zero-crossing, both values are perfectly adequate

²²The exact lockpoint can be adjusted by modifying the lock-in amplifier settings. Most often, one wants to lock the laser to a zero-crossing of the error signal, as there, the frequency should be well-known. By slightly changing the lockpoint, the frequency can be set to different values. Additionally, the control function $C(\nu)$ can differ from the error signal $E(\nu)$ by a constant value. A non-zero $C(\nu)$ therefore doesn't mean a non-zero $E(\nu)$

to allow for the usage of the locked laser system to drive the magneto-optical trap as it is presented in section 4.

A better lock with smaller Γ_{Locked} can be realized with an ultra-high finesse cavity and to better determine ν_{Locked} , a frequency comb can be used. Unfortunately, both devices weren't available during data taking. It is advised to explore these possible improvements in the future. For now, as high-precision spectroscopy is not performed, the presented laser system is sufficient.

3. The Zeeman Slower

In our ultra-high vacuum setup, we use a temperature of over 450 °C to vaporize the lithium sample and create a sufficiently intense hot atom beam. This temperature results in atoms with a mean velocity of $\bar{v} \approx 1600$ m/s, which is well above the capture velocity of our MOT $v_c = 60$ m/s. Only a fraction of all atoms is caught, many just fly through the trap. To increase the yield, the Li atoms have to be slowed down first.

One way to slow down a neutral atom is by shining a nearly resonant laser at it which exerts a force of

$$\vec{F} = \hbar \vec{k} \frac{\Gamma}{2} \frac{s}{1 + s + (2\delta/\Gamma)^2} \quad (3.1)$$

on the atom, because the atoms absorb the photons produced by the laser and therefore also absorb their momentum. Here, $\vec{k} = \hat{e}_k \frac{2\pi\nu}{c}$ is the wave vector of the photons which the laser produces, Γ is the linewidth of the used cooling transition, s is the saturation parameter, and δ is the difference between the laser frequency ν and the transition frequency ν_0 . The atom moves with a velocity \vec{v} and sees the laser light Doppler shifted to a frequency ν' of

$$\nu' = \nu (\gamma - \gamma\beta \cos(\phi)) \approx \nu - \frac{\vec{v} \cdot \vec{k}}{2\pi}, \quad (3.2)$$

where $\beta = |\vec{v}|/c$ and $\gamma = 1/\sqrt{1 - \beta^2}$ are the well-known relativistic coefficients and ϕ is the angle between \vec{k} and \vec{v} . For velocities much smaller than the speed of light c , this shift shows an approximately linear behaviour, the so-called first-order Doppler shift.

To effectively slow down the atom, the light has to be kept resonant to the atom ($\nu' = \nu_0$) but as the atom decelerates, ν' changes and the laser falls out of resonance. One way to solve this problem and to slow and cool down hot atom beams is by using a Zeeman slower. This is the technique that was chosen in this thesis.

Many of the results in this section were created together with Julia Daum [Dau20] and Konrad Franz [Fra21] during their Master's theses. For further information the reader is highly advised to look into their theses.

3.1. Hot Atomic Beams

The most left part of fig. 3.1 depicts the oven in which metallic chunks of lithium are contained. The oven is heated up by two independent heating elements running at temperatures of $T \approx 450$ °C and $T \approx 500$ °C, respectively, and the hot gas shoots to the right through a cross with a vacuum pump and through the tube of the Zeeman slower into the MOT chamber where it is not yet captured but probed by a scannable laser. In this section, the expected fluorescence signal is first derived and

subsequently measured.

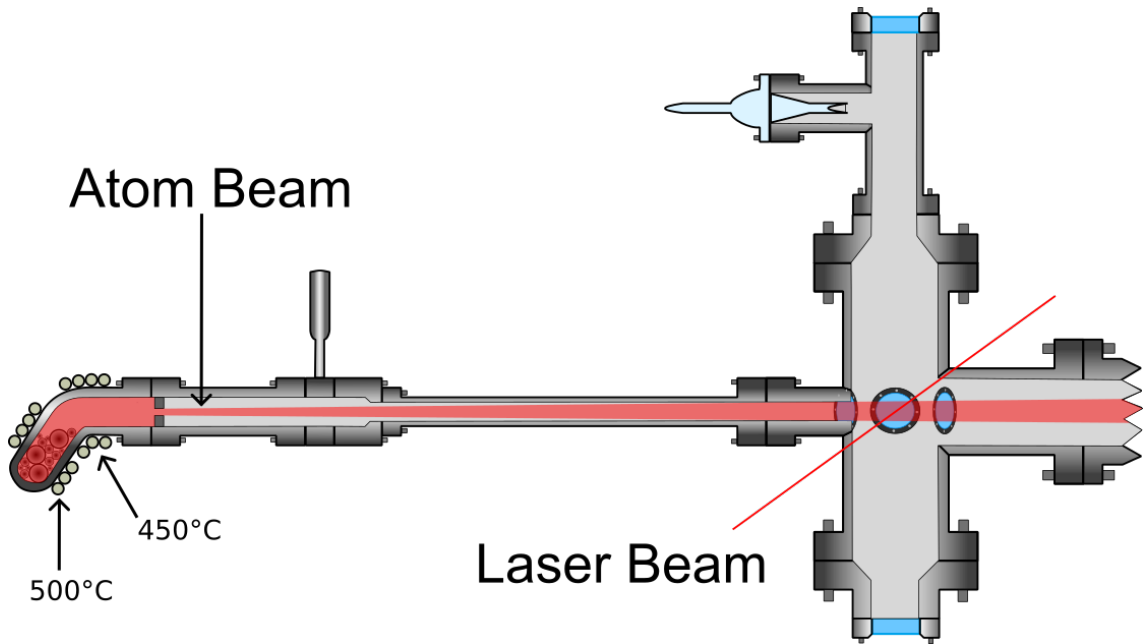


Figure 3.1: Schematic side view of the experimental setup. In the oven section to the left side, solid chunks of ${}^6\text{Li}$ are heated up by two separate heating elements. The gaseous ${}^6\text{Li}$ atoms pass an aperture and travel to the central chamber where they are probed by a tunable laser beam. Elements like vacuum pumps and magnets are omitted for simplicity. They are depicted in fig. 3.9.

The atoms need to pass a small aperture to leave the oven and be able to fly to the MOT chamber. The probability for an atom to pass this slit within any given time span is proportional to its speed v [Ram86]. In contrast to a regular Maxwell-Boltzmann distribution which contains a factor of v^2 , this additional velocity dependency leads to a modified probability density function which also depends on v^3 and is given by

$$\rho(v) = \frac{m^2}{2k_{\text{B}}^2 T^2} v^3 e^{-\frac{mv^2}{2k_{\text{B}}T}}. \quad (3.3)$$

In the following, it is assumed that $v_x = v_y = 0$, i.e. the atoms move only in the z -direction into the MOT chamber with a velocity v between 0 and the speed of light c , and a spectroscopy laser is illuminating them at a certain angle ϕ as depicted in fig. 3.2. The frequency of the laser light is scanned while the fluorescence of the atoms is projected onto a photodiode.

Because fluorescence only occurs if the laser photons are absorbed by the atoms and the probability of absorption is proportional to

$$p(\nu') \propto \frac{s}{1 + s + (2(\nu_0 - \nu')/\Gamma)^2}, \quad (3.4)$$

where ν' is the Doppler shifted laser frequency as defined in eq. (3.2), the observed photodiode signal is a function of ν as well as the atoms' velocity distribution.

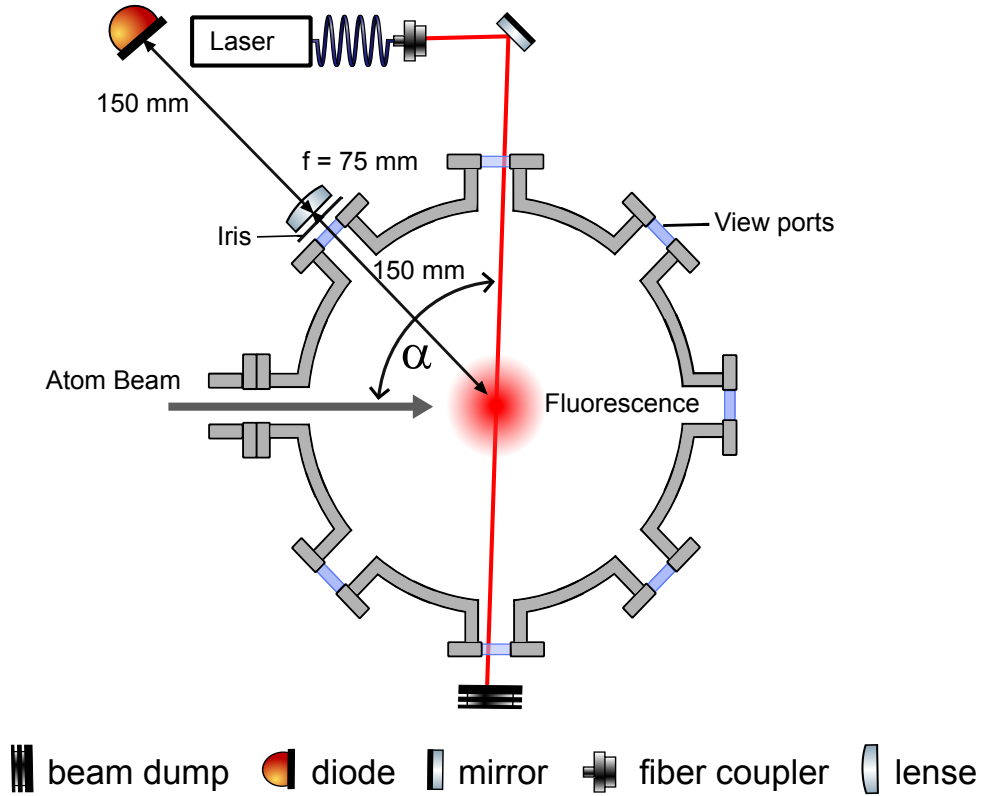


Figure 3.2: Schematic top view of the spectroscopy setup. A beam of hot ${}^6\text{Li}$ atoms enter the experimental chamber from the left side. In the central region, the atoms are illuminated by a laserbeam with tunable wavelength. The atoms' fluorescence is then projected onto a photodiode. The angle between the atom and the laser beam is given by α .

Therefore, the resulting signal is described by a convolution of eq. (3.3) and eq. (3.4)

$$f(\nu) = N \int_0^c dv \frac{s}{1 + s + \left(2 \frac{\nu_0 - \nu \left(1 - \frac{v}{c} \cos(\phi)\right)}{\Gamma}\right)^2} v^3 e^{-\frac{mv^2}{2k_B T}}, \quad (3.5)$$

with the normalization parameter N . This integral is not analytically solvable. But because the velocity distribution's width leads to a broadening which is multiple orders of magnitude higher than Γ , another approximation can be made. Only such

atoms absorb light of frequency ν that see it at $\nu' \approx \nu_0$. Therefore, eq. (3.4) turns into a Dirac delta distribution and eq. (3.5) becomes

$$\begin{aligned}
f(\nu) &= N \int_0^c dv \delta\left(\nu \left(1 - \frac{v}{c} \cos(\phi)\right) - \nu_0\right) v^3 e^{-\frac{mv^2}{2k_B T}} \\
&= N \int_0^c dv \frac{\delta\left(v - \frac{c}{\cos(\phi)} \left(1 - \frac{\nu_0}{\nu}\right)\right)}{\frac{\nu}{c} \cos(\phi)} v^3 e^{-\frac{mv^2}{2k_B T}} \\
&= N \left(H(\cos(\phi)) H(\nu - \nu_0) - H(-\cos(\phi)) H(\nu_0 - \nu) \right) \\
&\quad \cdot \frac{c^4}{\nu^4 \cos^4(\phi)} (\nu - \nu_0)^3 e^{-\frac{c^2 m (\nu - \nu_0)^2}{2k_B T \nu^2 \cos^2(\phi)}},
\end{aligned} \tag{3.6}$$

with $H(x)$ being the Heaviside function. For $\phi < 90^\circ$ the laser light is red-shifted, i.e. frequencies $\nu > \nu_0$ are absorbed, and vice-versa for $\phi > 90^\circ$. Note, that for $\phi = 90^\circ$, this functions fails to produce any reasonable results, because in this case the Dirac delta doesn't contain a function of v anymore.

The photodiode signal as well as the function fitted to it (fixed to $\phi = 93.3^\circ$) are shown in fig. 3.3 together with the extracted velocity distributions of the $F_{\text{gs}} = 3/2$ and $F_{\text{gs}} = 1/2$ atoms. The explicit fit function has the form of

$$\begin{aligned}
f(\delta) &= V_0 \\
&\quad + H(\nu_{F=3/2} - \nu_{F=1/2} - \delta) N_{F=3/2} \frac{c^4}{(\delta + \nu_{F=1/2}) \cos^4(\phi)} \\
&\quad \cdot \left(\frac{\nu_{F=3/2}}{\delta + \nu_{F=1/2}} - 1 \right)^3 e^{-\frac{c^2 m \left(1 - \frac{\nu_{F=3/2}}{\delta + \nu_{F=1/2}}\right)^2}{2k_B T \cos^2(\phi)}} \\
&\quad + H(-\delta) N_{F=1/2} \frac{c^4}{(\delta + \nu_{F=1/2}) \cos^4(\phi)} \\
&\quad \cdot \left(\frac{\nu_{F=1/2}}{\delta + \nu_{F=1/2}} - 1 \right)^3 e^{-\frac{c^2 m \left(1 - \frac{\nu_{F=1/2}}{\delta + \nu_{F=1/2}}\right)^2}{2k_B T \cos^2(\phi)}},
\end{aligned} \tag{3.7}$$

where $\nu_{F=3/2} = 446.799\,573(2)$ THz and $\nu_{F=1/2} = 446.799\,803(1)$ THz are the weighted means of the ${}^6\text{Li}$ D₂ line transition frequencies [LWR⁺20] as listed in table 3.1.

Table 3.1: Resonance frequencies of the ${}^6\text{Li}$ D₂-lines ($2S_{1/2} \rightarrow 2P_{3/2}$) according to [LWR⁺20].

Ground State F_{gs}	Excited State F_{es}	ν_0 [MHz]
3/2	5/2	446 799 571.0796(19)
3/2	3/2	446 799 573.9743(19)
3/2	1/2	446 799 575.6861(19)
1/2	3/2	446 799 802.1758(16)
1/2	1/2	446 799 803.8876(16)

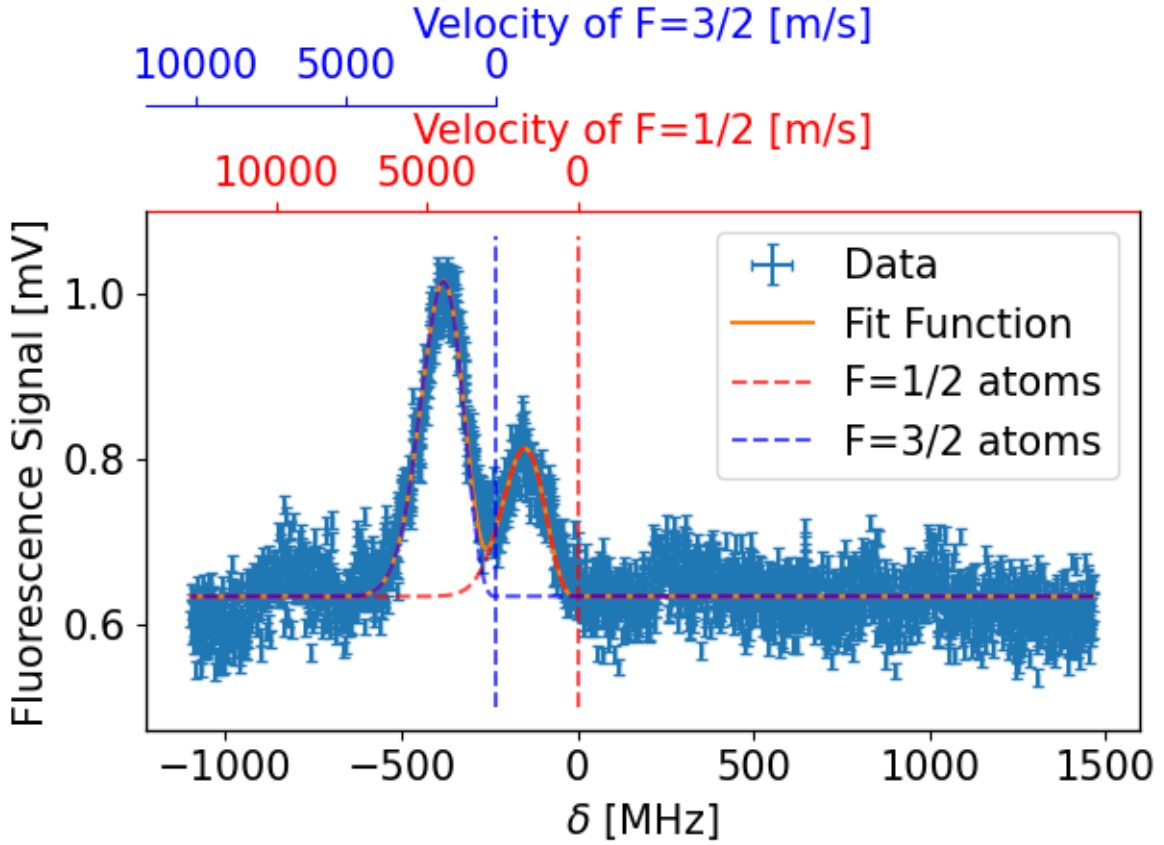


Figure 3.3: Measured Fluorescence of a hot ${}^6\text{Li}$ atom beam. Additionally, a fit using eq. (3.7) is shown. For this, the angle between atom beam and laser beam was assumed to be $\phi = 93.3^\circ$.

Here, the detuning δ is defined as $\delta = \nu - \nu_{F=1/2}$. It is apparent from eq. (3.7) that the normalization factors N and the temperature T are correlated by the angle ϕ . It is not possible to fit the function to the data and produce reasonable values for N , T , and ϕ at the same time. It was therefore tried to determine T by measuring the oven's temperature. The heating elements are coiled around different parts of the oven section and each one holds a type K thermocouple sensor between itself and the oven's bare metal. Even when assuming that the vacuum setup, the sensors, and the heating elements have good thermal contact and the oven section's outside temperatures can be determined precisely, a temperature gradient within the oven is still expected²³. The sample's temperature is therefore estimated conservatively to $T = 475(25)^\circ\text{C}$ and ϕ cannot be determined with a single fit.

But ϕ is needed to calculate the corresponding velocity of the atoms. Therefore,

²³The lower part of the oven is held at approximately 500°C while the upper part is brought to 450°C . During fluorescence measurements of the atom beam, which are discussed in later sections, it was shown that higher temperatures lead to higher fluorescence signals. The heating elements were therefore operated at their maximum allowed temperatures (according to their data sheets).

ϕ was fixed to different values before fitting. For $\phi = 93.3^\circ$ this yielded the values shown in table 3.2 while different temperatures depending on ϕ are plotted in fig. 3.4. To show the range of ϕ that are compatible with the data, gray areas indicate temperatures that are outside the assumed temperature range of $450^\circ\text{C} < T < 500^\circ\text{C}$ and only such ϕ that generate a T within this range are considered. A quadratic function was fitted to the allowed angles and the ϕ which generate $T(\phi) = 450^\circ\text{C}$ and $T(\phi) = 500^\circ\text{C}$ were determined. This results in an estimated value $\bar{\phi} = 93.29(6)^\circ$. Knowing $\bar{\phi}$ is essential to calibrate the upper x-axes in fig. 3.3 which is necessary to identify the efficiency of the Zeeman slower by the end of this chapter.

Table 3.2: Optimized parameter for fit depicted in fig. 3.3.

V_0	0.633 85(10)	mV
$N_{F=3/2}$	57.05(7)	mV/m ⁴ Hz ³
$N_{F=1/2}$	26.84(7)	mV/m ⁴ Hz ³
T	471.7(9)	°C
ϕ	93.3	°

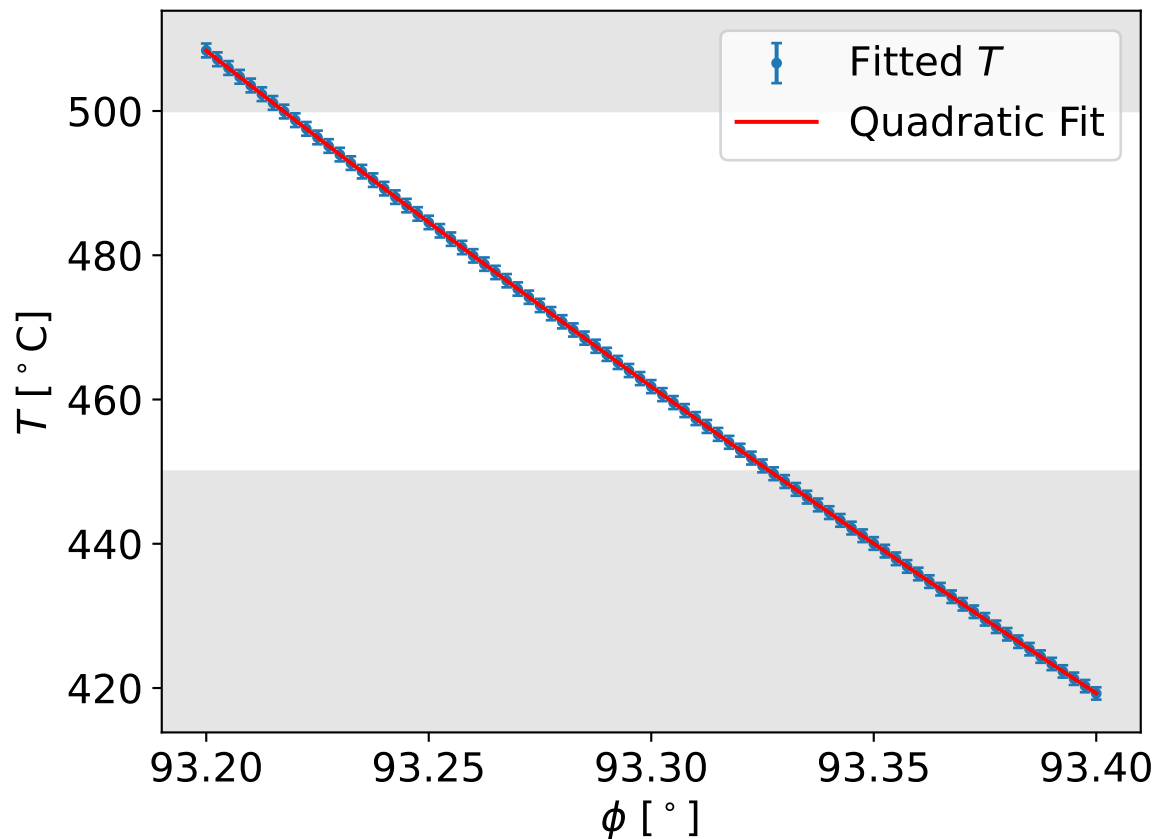


Figure 3.4: Fitted temperature T depending on fixed angle ϕ . The gray area indicates $T < 450^\circ\text{C}$ or $T > 500^\circ\text{C}$. These values don't make much sense, because the oven produces temperatures within this range.

3.2. The Zeeman Effect on the Lithium D Lines

The Hamiltonian of an atom placed in a magnetic field can be written as

$$\left(\hat{H}_0 + \hat{H}_{\text{FS}} + \hat{H}_{\text{HFS}} + \hat{H}_Z\right) \Psi = E\Psi. \quad (3.8)$$

The separate elements are as follows:

- \hat{H}_0 : This Hamiltonian describes the lithium atom. Its solution is defined by the main quantum number n . The energy E is mostly governed by \hat{H}_0 . For many practical purposes, one can approximate \hat{H}_0 with the simple Hamiltonian of a hydrogen atom, which is solvable analytically.
- \hat{H}_{FS} : Fine Structure. The fine structure splitting in lithium between states such as the ground state $2S_{1/2}$ and the first two excited states $2P_{1/2}$ and $2P_{3/2}$ is defined by the total angular momentum \vec{J} . The spin \vec{S} of the valence electron and the orbital angular momentum \vec{L} both create their own magnetic moment. These magnetic moments interact with each other and change the energy of the state. The order of magnitude of the resulting splitting is $\mathcal{O}(10 \text{ GHz})$.
- \hat{H}_{HFS} : Hyperfine Structure. The total angular momentum \vec{J} of the valence electron and the atom's nuclear spin \vec{I} add up to the total spin \vec{F} . In a similar fashion to how \vec{J} creates the fine structure, \vec{F} creates a splitting of the energy levels, although much smaller, hence the name hyperfine structure. The expected splitting is in the order of $\mathcal{O}(1 - 100 \text{ MHz})$.
- \hat{H}_Z : Zeeman Interaction. The state's energy is usually degenerate, i.e. states with the same L , J , or F but different magnetic quantum numbers m_L , m_J , or m_F share the same energy. In a magnetic field B this degeneracy is lifted. The field strengths in this experiment lead to an energy shift which is comparable to the hyperfine structure splitting.

Often times the Zeeman Hamiltonian can be treated as a small perturbation. For small $B = |\vec{B}|$, the Zeeman splitting is assumed to be smaller than the hyperfine splitting and F is assumed to be a "good" quantum number, i.e. it still identifies the atom's quantum state. For increased values of B , the Zeeman effect surpasses the hyperfine splitting and the situation changes. \hat{H}_{HFS} is treated as a small perturbation, F and m_F aren't considered good quantum numbers anymore, and J and m_J are used to describe the quantum state. In this regime, the anomalous Zeeman effect is hence called the Paschen-Back effect.

In case of the lithium D lines, what happens between these regimes at medium B fields, how this influences which transitions from state to state are allowed, and how their respective strengths change was examined in Julia Daum's M.Sc. thesis

[Dau20], whose main conclusions will be presented in the following.

The wavefunction of the atom is assumed to be known down to the fine structure. The hyperfine structure and the interaction with the external magnetic field perturb this state and together they form the interaction Hamiltonian [Arm71]

$$\hat{H}_{\text{int}} = A_F \vec{J} \cdot \vec{I} + B_F \frac{3(\vec{J} \cdot \vec{I})^2 + \frac{3}{2} \vec{J} \cdot \vec{I} - \vec{J}^2 \vec{I}^2}{2J(2J-1)I(2I-1)} + g_J \mu_B \vec{J} \cdot \vec{B}. \quad (3.9)$$

The magnetic hyperfine structure coefficient A_F and the electric quadrupole fine structure coefficient B_F depend on the specific state. Their values are given in table 3.3. The last term contains the interaction of the electron's total angular momentum and the external magnetic field. Its strength depends on the Bohr magneton μ_B and the Landé factor g_J . Any interaction between the nuclear spin and the external field is omitted because the corresponding Landé factor g_I is orders of magnitude smaller than g_J [AIV77].

Table 3.3: Values of the hyperfine structure constants A_F and B_F of different states in ${}^6\text{Li}$ [SKJW96].

Constant	Value [MHz]
$A_{2S_{1/2}}$	152.136 840 7(20)
$A_{2P_{1/2}}$	17.375(18)
$A_{2P_{3/2}}$	-1.155(8)
$B_{2P_{3/2}}$	-0.10(14)

The eigenfunctions of the nucleus $|I, m_I\rangle$ and the electron shell $|J, m_J\rangle$ form a complete basis for each fine structure state, i.e. every solution $|\Psi\rangle$ can be expressed as

$$|\Phi^\gamma\rangle = \sum_{m_I, m_J} \phi_{m_I, m_J}^\gamma |I, m_I\rangle |J, m_J\rangle. \quad (3.10)$$

In total, there are $(2I+1)(2J+1)$ states, e.g. 6 states for the $2^2S_{1/2}$ ground state of ${}^6\text{Li}$ and 12 for its excited state $2^2P_{3/2}$. Because F and m_F become useless to describe the state above a certain value of $|\vec{B}|$, the index γ is introduced to identify the state. The Hamiltonian can be written in matrix form [Ude94] as

$$\begin{aligned}
\hat{H}_{\text{int}}[p][q] = & \delta_{m_J, m'_J} \delta_{m_I, m'_I} B \mu_B g_J m_J \\
& + A_F^\gamma \cdot 2\pi\hbar \cdot (-1)^{m'_J + m_I + J + I} \cdot \sqrt{J(J+1)(2J+1)I(I+1)(2I+1)} \\
& \cdot \begin{pmatrix} J & 1 & J \\ m'_J & m_J - m'_J & -m_J \end{pmatrix} \cdot \begin{pmatrix} I & 1 & I \\ m'_I & m'_J - m_J & -m_I \end{pmatrix} \\
& + B_F^\gamma \cdot 2\pi\hbar \cdot (-1)^{m'_J + m_I - J - I} \\
& \cdot \frac{15(2J+1)(J+1)(2I+1)(I+1)}{2(2J-1)(2I-1)} \\
& \cdot \begin{pmatrix} J & 2 & J \\ m'_J & m_J - m'_J & -m_J \end{pmatrix} \cdot \begin{pmatrix} I & 2 & I \\ m'_I & m'_J - m_J & -m_I \end{pmatrix} \\
& \cdot \begin{Bmatrix} 1 & J & J \\ J & 1 & 2 \end{Bmatrix} \cdot \begin{Bmatrix} 1 & I & I \\ I & 1 & 2 \end{Bmatrix}.
\end{aligned} \tag{3.11}$$

where the indices p and q label the p -th and q -th $|m_J, m_I\rangle$ spin state. These explicit states are listed in table 3.5a for the $2S_{1/2}$ ground state and in table 3.5b for the $2P_{3/2}$ excited state. The $\{:::\}$ operators are the Wigner 3-j symbols. When two states couple to each other, their angular momenta add up. This addition can be expressed by using Clebsch-Gordan coefficients or alternatively the Wigner 3-j symbols. Similarly, the Wigner 6-j symbols $\{:::\}$ are used to calculate the addition of three angular momenta.

Table 3.4: Chosen spin state numbering γ for the $2S_{1/2}$ ground state (a) and the $2P_{3/2}$ excited state (b) of ${}^6\text{Li}$.

State Number γ	m_J	m_I
0	$-\frac{1}{2}$	-1
1	$-\frac{1}{2}$	0
2	$-\frac{1}{2}$	1
3	$\frac{1}{2}$	-1
4	$\frac{1}{2}$	0
5	$\frac{1}{2}$	1

(a)

State Number γ	m_J	m_I
0	$-\frac{3}{2}$	-1
1	$-\frac{3}{2}$	0
2	$-\frac{3}{2}$	1
3	$-\frac{1}{2}$	-1
4	$-\frac{1}{2}$	0
5	$-\frac{1}{2}$	1
6	$\frac{1}{2}$	-1
7	$\frac{1}{2}$	0
8	$\frac{1}{2}$	1
9	$\frac{3}{2}$	-1
10	$\frac{3}{2}$	0
11	$\frac{3}{2}$	1

(b)

The first term of eq. (3.11) contains the external magnetic field's effect on the atom. This effect is only present if $m_J = m'_J$ and $m_I = m'_I$ because it was assumed that the fine structure state isn't changed by \vec{B} .

The second term contains Wigner 3-j symbols that describe the interaction with the magnetic dipole fields which are created by the valence electron and the nucleus. This interaction is of course due to photons which carry a spin of 1. The interaction does not change the original spins I and J but can change the respective z component.

Lastly, the third term also contains Wigner 6-j symbols to incorporate electric quadrupole fields which is the superposition of two electric dipole's fields, both producing photons with spin 1 which add up to a spin of 2. Only very specific combinations of quantum numbers produce non-zero entries. For the ${}^6\text{Li}$ ground state ($I=1$, $J=1/2$, $A_F^{\text{gs}} \approx 152 \text{ MHz}$, $B_F^{\text{gs}} = 0$, $g_J = 2.002$) the resulting Hamiltonian looks as follows:

$$\hat{H}_{\text{int}} = \begin{pmatrix} A_1 + A_2 \cdot B & 0 & 0 & 0 & 0 & 0 \\ 0 & A_2 \cdot B & 0 & A_3 & 0 & 0 \\ 0 & 0 & -A_1 + A_2 \cdot B & 0 & A_3 & 0 \\ 0 & A_3 & 0 & -A_1 - A_2 \cdot B & 0 & 0 \\ 0 & 0 & A_3 & 0 & -A_2 \cdot B & 0 \\ 0 & 0 & 0 & 0 & 0 & A_1 - A_2 \cdot B \end{pmatrix}. \quad (3.12)$$

With

$$A_1 = 76.07 \text{ MHz} \cdot h, \quad (3.13)$$

$$A_2 = -14.01 \frac{\text{MHz}}{\text{mT}} \cdot h, \quad (3.14)$$

$$A_3 = 107.58 \text{ MHz} \cdot h \quad (3.15)$$

and for $B = 0$ it's easy to show that this leads to two different eigenvalues, the first occupied by two, the second occupied by four separate states: $\Delta E = -152 \text{ MHz} \cdot h$ and $76 \text{ MHz} \cdot h$. The ground state splits into $F_{\text{gs}} = 1/2$ and $F_{\text{gs}} = 3/2$ hyperfine states, with two and four magnetic substates, respectively. Of these six substates, the $|m_F| = 1/2$ states consist of combinations of different $|J, m_J, I, m_I\rangle$. This expresses in off-diagonal entries in the \hat{H}_{int} matrix. On the contrary, the $|m_F| = 3/2$ states translate to one specific $|J, m_J, I, m_I\rangle$, namely $|1/2, 1/2, 1, 1\rangle$ and $|1/2, -1/2, 1, -1\rangle$. They correspond to the upper-left and the lower-right entry of the matrix.

To find the eigenstates of \hat{H}_{int} and their specific response to different magnetic fields, eq. (3.12) has to be diagonalized. Their eigenvalues are listed in table 3.6. As mentioned before, the states aren't ordered by their total spin F anymore but are

simply numbered²⁴ from 0 to 5. Nevertheless, to identify the states for small values of B , $|F, m_F\rangle$ is also listed. The corresponding eigenvectors depending on the spin eigenstates $|m_j, m_I\rangle$ are also given in eq. (3.16) to eq. (3.21).

Table 3.6: Zeeman shift eigenvalues of the ${}^6\text{Li}$ -ground states and the corresponding $|F, m_F\rangle$ states for small magnetic fields B .

State Number	Zeeman Shift	Corresponding $ F, m_F\rangle$
0	$\frac{1}{2} \left(-A_1 - \sqrt{A_1^2 + 4A_1A_2B + 4A_2^2B^2 + 4A_3^2} \right)$	$ \frac{1}{2}, \frac{1}{2}\rangle$
1	$\frac{1}{2} \left(-A_1 + \sqrt{A_1^2 - 4A_1A_2B + 4A_2^2B^2 + 4A_3^2} \right)$	$ \frac{3}{2}, \frac{1}{2}\rangle$
2	$\frac{1}{2} \left(-A_1 - \sqrt{A_1^2 - 4A_1A_2B + 4A_2^2B^2 + 4A_3^2} \right)$	$ \frac{1}{2}, -\frac{1}{2}\rangle$
3	$\frac{1}{2} \left(-A_1 + \sqrt{A_1^2 + 4A_1A_2B + 4A_2^2B^2 + 4A_3^2} \right)$	$ \frac{3}{2}, -\frac{1}{2}\rangle$
4	$A_1 + A_2 \cdot B$	$ \frac{3}{2}, -\frac{3}{2}\rangle$
5	$A_1 - A_2 \cdot B$	$ \frac{3}{2}, \frac{3}{2}\rangle$

$$\begin{aligned}
|0\rangle = & \frac{1}{\sqrt{1 + \left(\frac{A_1 - 2A_2B + \sqrt{A_1^2 - 4A_1A_2B + 4A_2^2B^2 + 4A_3^2}}{2A_3} \right)^2}} \\
& \cdot \left(-\frac{A_1 - 2A_2B + \sqrt{A_1^2 - 4A_1A_2B + 4A_2^2B^2 + 4A_3^2}}{2A_3} \left| -\frac{1}{2}, 1 \right\rangle + \left| \frac{1}{2}, 0 \right\rangle \right)
\end{aligned} \tag{3.16}$$

$$\begin{aligned}
|1\rangle = & \frac{1}{\sqrt{1 + \left(\frac{A_1 - 2A_2B - \sqrt{A_1^2 - 4A_1A_2B + 4A_2^2B^2 + 4A_3^2}}{2A_3} \right)^2}} \\
& \cdot \left(-\frac{A_1 - 2A_2B - \sqrt{A_1^2 - 4A_1A_2B + 4A_2^2B^2 + 4A_3^2}}{2A_3} \left| -\frac{1}{2}, 1 \right\rangle + \left| \frac{1}{2}, 0 \right\rangle \right)
\end{aligned} \tag{3.17}$$

$$\begin{aligned}
|2\rangle = & \frac{1}{\sqrt{1 + \left(\frac{A_1 + 2A_2B - \sqrt{A_1^2 + 4A_1A_2B + 4A_2^2B^2 + 4A_3^2}}{2A_3} \right)^2}} \\
& \cdot \left(\frac{A_1 + 2A_2B - \sqrt{A_1^2 + 4A_1A_2B + 4A_2^2B^2 + 4A_3^2}}{2A_3} \left| -\frac{1}{2}, 0 \right\rangle + \left| \frac{1}{2}, -1 \right\rangle \right)
\end{aligned} \tag{3.18}$$

²⁴This numbering is not the same numbering as above. While the 4th and 5th \hat{H}_{int} eigenstates might be the same as the 0th and 5th fine structure eigenstates, the others are combinations of them with weights that shift depending on the applied magnetic field. The numbering follows no specific order and is kept the same as in [Dau20].

$$|3\rangle = \frac{1}{\sqrt{1 + \left(\frac{A_1 + 2A_2B + \sqrt{A_1^2 + 4A_1A_2B + 4A_2^2B^2 + 4A_3^2}}{2A_3}\right)^2}} \cdot \left(\frac{A_1 + 2A_2B + \sqrt{A_1^2 + 4A_1A_2B + 4A_2^2B^2 + 4A_3^2}}{2A_3} \left|-\frac{1}{2}, 0\right\rangle + \left|\frac{1}{2}, -1\right\rangle\right) \quad (3.19)$$

$$|4\rangle = \left|-\frac{1}{2}, -1\right\rangle \quad (3.20)$$

$$|5\rangle = \left|\frac{1}{2}, 1\right\rangle \quad (3.21)$$

The frequency shifts for the six ${}^6\text{Li}$ ground states are depicted in fig. 3.5. The behaviour of ground states 4 and 5 is purely linear because they translate to one specific combination of electron shell and nuclear spin. The other states comprise a mixture of different states and change their behaviour depending on B . For high positive values of B , the states 1 and 3 behave like $|J = 1/2, m_J = 1/2\rangle$, while state 0 and 2 can be approximated by $|J = 1/2, m_J = -1/2\rangle$. This flips for high negative values of B .

The same procedure can be done for the $2P_{3/2}$ excited states. This can be looked up in [Dau20] or appendix E. The results are plotted in fig. 3.6 and the relation between a states number and its F and m_F for small magnetic fields is shown in table 3.7. Note that the plot range is much smaller than the range of fig. 3.5 because the transition from the Zeeman to the Paschen-Back regime happens at much lower values of B . This means that for small but non-zero values of B ($0.1 \text{ mT} < |B| < 10 \text{ mT}$), transitions from an $|F, m_F\rangle$ ground state to a $|J, m_J, I, m_I\rangle$ excited state have to be considered. This makes the selection rules not as straight forward as $\Delta F = \pm 1, 0$ and $\Delta m_F = \pm 1, 0$.

Table 3.7: $2P_{3/2}$ eigenstates of ${}^6\text{Li}$ and the corresponding $|F, m_F\rangle$ states for small magnetic fields B .

State Number	Corresponding $ F, m_F\rangle$
0	$\left \frac{5}{2}, \frac{3}{2}\right\rangle$
1	$\left \frac{3}{2}, \frac{3}{2}\right\rangle$
2	$\left \frac{5}{2}, -\frac{1}{2}\right\rangle$
3	$\left \frac{1}{2}, -\frac{1}{2}\right\rangle$
4	$\left \frac{3}{2}, -\frac{1}{2}\right\rangle$
5	$\left \frac{5}{2}, -\frac{3}{2}\right\rangle$
6	$\left \frac{3}{2}, -\frac{3}{2}\right\rangle$
7	$\left \frac{1}{2}, \frac{1}{2}\right\rangle$
8	$\left \frac{5}{2}, \frac{1}{2}\right\rangle$
9	$\left \frac{3}{2}, \frac{1}{2}\right\rangle$
10	$\left \frac{5}{2}, -\frac{5}{2}\right\rangle$
11	$\left \frac{5}{2}, \frac{5}{2}\right\rangle$

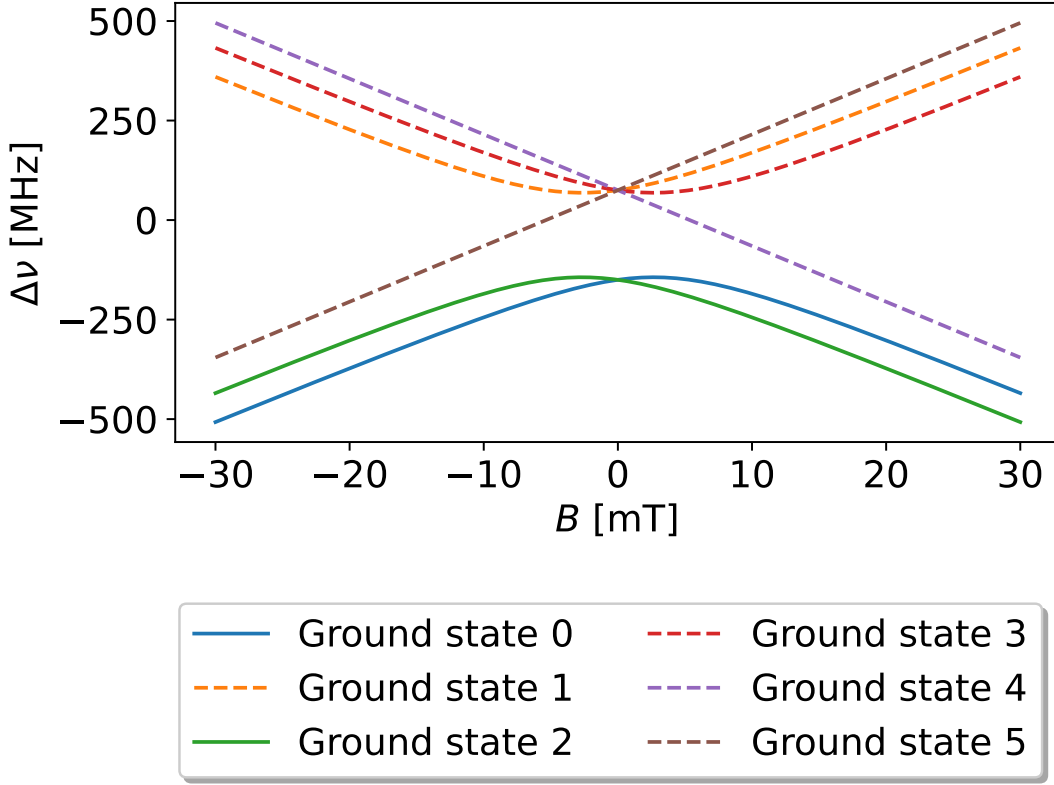


Figure 3.5: Zeeman frequency shift of the ${}^6\text{Li}$ ground states. States that correspond to $F_{\text{gs}} = 3/2$ are drawn as dashed lines, the $F_{\text{gs}} = 1/2$ states as solid lines.

A multiplicity of selection rules for electric dipole transitions have to be considered:

$$\begin{aligned}
 \Delta m_J &= -1, 0, +1, \\
 \Delta m_I &= -1, 0, +1, \\
 \Delta J &= -1, 0, +1, \\
 \Delta I &= 0, \\
 \Delta m_F &= -1, 0, +1, \\
 \Delta F &= -1, 0, +1.
 \end{aligned} \tag{3.22}$$

Following these rules, depending on the polarization of the driving light (σ^- , π , or σ^+), different transitions are possible. They are listed in table 3.8. The transition strength S of an allowed transition can be calculated using

$$S = \sum_{\text{GS,ES}} |(-1)^{J_{\text{ES}} - m_J} \cdot \begin{pmatrix} J_{\text{ES}} & 1 & J_{\text{GS}} \\ -m_J & \sigma & m_j - \sigma \end{pmatrix} \cdot (EV_{\text{ES}} \cdot EV_{\text{GS}})^2|, \tag{3.23}$$

which is the sum over all $|m_J, m_I\rangle$ ground and excited states weighted by the corresponding entry in their respective \hat{H}_{int} eigenvector EV . The light's polarization is

given by $\sigma = -1, 0$ or 1 , for σ^- , π , and σ^+ , respectively. For σ^+ polarization, the behaviour of S for different values of B is plotted in fig. 3.7. Whether a transition can be driven depends on the value of S and the frequency of the driving light. If multiple transitions are possible, the probability of exciting to a certain state can be found by evaluating the ratio of this specific transition's strength to the total transition strength. More transition plots can be found in appendix E and [Dau20].

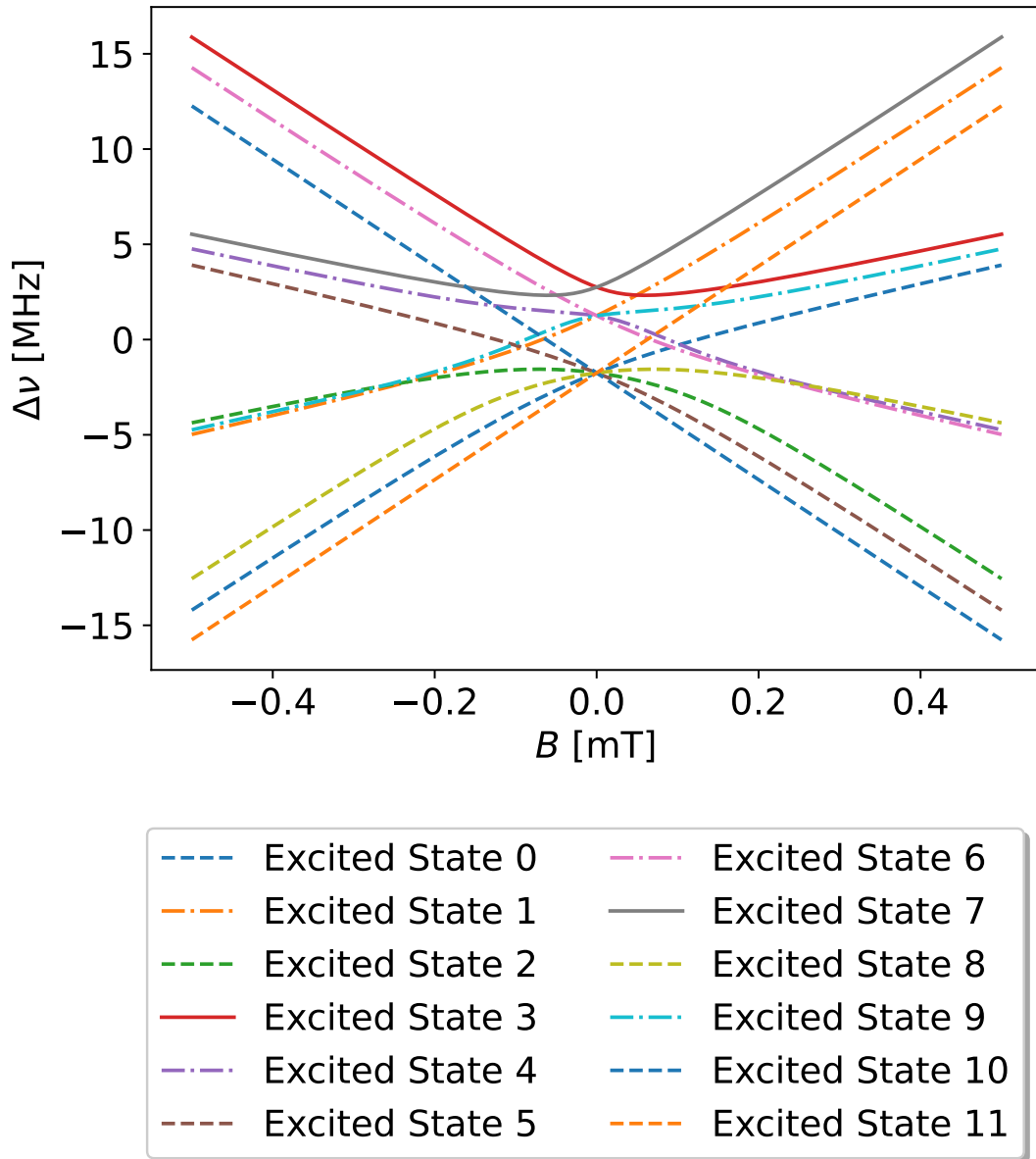


Figure 3.6: Zeeman frequency shift of the ${}^6\text{Li } 2P_{3/2}$ excited states. The line styles of the different states are coded to their corresponding hyperfine F quantum number at low values of B . Straight lines correspond to $F_{\text{es}} = 1/2$, dashed-dotted lines to $F_{\text{es}} = 3/2$, and dashed lines to $F_{\text{es}} = 5/2$.

Table 3.8: Allowed transitions from all ${}^6\text{Li } 2S_{1/2}$ ground states to all $2P_{3/2}$ depending on photon polarization.

σ^-	π	σ^+
$0 \rightarrow 2$	$5 \rightarrow 0$	$0 \rightarrow 0$
$1 \rightarrow 2$	$5 \rightarrow 1$	$1 \rightarrow 0$
$0 \rightarrow 3$	$2 \rightarrow 2$	$0 \rightarrow 1$
$1 \rightarrow 3$	$3 \rightarrow 2$	$1 \rightarrow 1$
$0 \rightarrow 4$	$2 \rightarrow 3$	$4 \rightarrow 2$
$1 \rightarrow 4$	$3 \rightarrow 3$	$4 \rightarrow 3$
$2 \rightarrow 5$	$2 \rightarrow 4$	$4 \rightarrow 4$
$3 \rightarrow 5$	$3 \rightarrow 4$	$2 \rightarrow 7$
$2 \rightarrow 6$	$4 \rightarrow 5$	$3 \rightarrow 7$
$3 \rightarrow 6$	$4 \rightarrow 6$	$3 \rightarrow 8$
$5 \rightarrow 7$	$0 \rightarrow 7$	$2 \rightarrow 8$
$5 \rightarrow 8$	$1 \rightarrow 7$	$2 \rightarrow 9$
$5 \rightarrow 9$	$0 \rightarrow 8$	$3 \rightarrow 9$
$4 \rightarrow 10$	$1 \rightarrow 8$	$5 \rightarrow 11$
	$0 \rightarrow 9$	
	$1 \rightarrow 9$	

In conclusion, it should be noted that only two excited states are reachable with one specific transition: 10 and 11. This means that these states can only deexcite to ground states 4 and 5, respectively. Exciting the ground state to the excited state therefore leads to a closed cycle transition. Their transition strengths are constant with B and the resonance frequency changes linearly with B . This is why $5 \rightarrow 11$ was chosen as the ideal transition for the Zeeman slower.

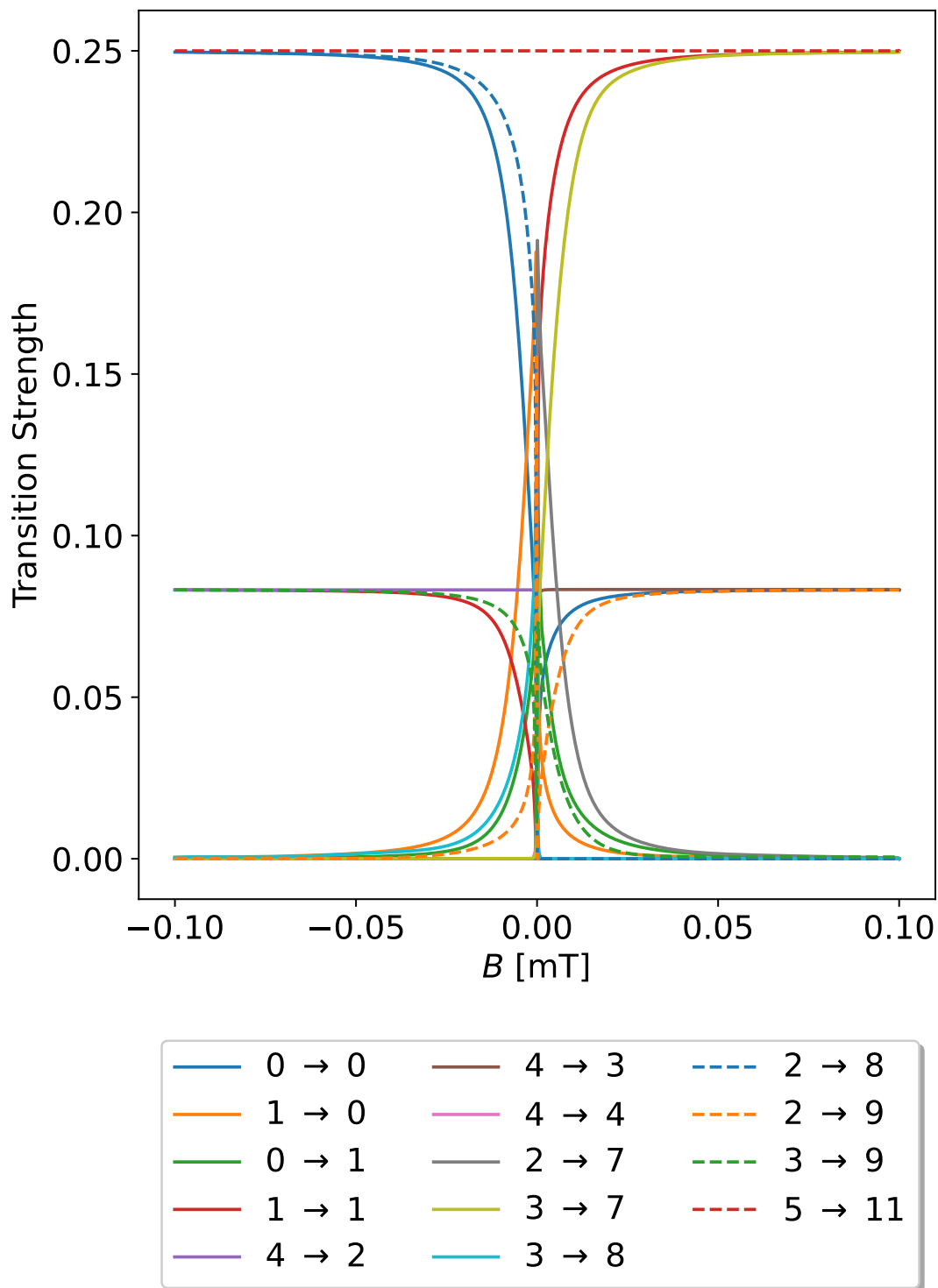


Figure 3.7: Strength of allowed transitions driven by σ^+ light for different magnetic field strengths.

3.3. The Setup

A Zeeman slower uses the momentum transfer from photon scattering to slow and cool down atoms with a laser beam. The Zeeman effect ensures that this slowing can be accomplished with constant laser frequency. The spatial variation of a magnetic field B compensates the Doppler shift $\Delta\nu_{\text{Doppler}}$.

As explained in the beginning of this chapter (see section 3), a laser exerts a force on an atom if it has the right frequency to be absorbed. In a magnetic field an atom of mass m moving at a velocity v against a laser beam with wavenumber k and frequency $\nu = \nu_0 - \delta$ experiences a maximum deceleration of

$$a_{\text{max}} = \frac{\hbar k \Gamma}{2m} \frac{s_0}{1 + s_0 + 4 \left(\frac{\delta + \mu B - \frac{kv}{2\pi}}{\Gamma} \right)^2} \Bigg|_{v = \frac{2\pi\mu B}{k}}, \quad (3.24)$$

with $\mu = 14.0174 \text{ MHz/mT}$ for the chosen transition from ground state 5 to excited state 11 (see table 3.8).

This deceleration is held constant by making the Zeeman shift μB and the (first-order) Doppler shift $kv/2\pi$ cancel each other out. Because this is the maximally possible deceleration, B cannot change too fast or else the resonance condition is lost. For a constant deceleration, $a = -\frac{\partial v}{\partial z}v$ and B has to follow

$$-\left(\frac{2\pi\mu}{k}\right)^2 \frac{\partial B}{\partial z} B = a = \eta a_{\text{max}} \leq a_{\text{max}} \quad (3.25)$$

Because the experimental setup cannot produce a perfect B -field, a parameter $\eta < 1$ has been introduced to take flaws in the setup into account²⁵. Therefore,

$$B(z) = \frac{k}{2\pi\mu} \sqrt{v_i^2 - 2\eta a_{\text{max}} \cdot z}, \quad (3.26)$$

with the maximum slowing velocity $v_i = 2\pi(\mu B - \delta)/k|_{z=0}$.

Such an apparatus will decelerate all atoms between v_i and a final velocity v_f ($v_i > v_f$), provided it is long enough and the atoms don't fall out of resonance. If the slowing laser beam is red-detuned ($\delta < 0$), this final velocity isn't necessarily 0 but approximately $v_f \approx c \cdot \frac{|\delta|}{\nu}$, where c is the speed of light. The exact value depends on the chosen transition's FWHM and the laser's power. A constant bias field B_0 can be added to allow for deceleration to $v_f = 0$ with a detuned laser beam:

$$B(z) = \frac{k}{2\pi\mu} \sqrt{v_i^2 - 2\eta a_{\text{max}} \cdot z + B_0}. \quad (3.27)$$

²⁵Also, scattering is a stochastic process and some atoms take longer than the average time between to scatter events.

In the experiment, the slowing laser is $\delta \approx -170$ MHz detuned ($\nu = 446.7994$ THz). The maximum deceleration which a ${}^6\text{Li}$ atom absorbing this laser can experience is $a_{\text{max}} \approx 1\,833\,000$ m/s². An ideal field without bias and a conservative $\eta = 0.3$ that could be used to slow down such atoms is depicted in fig. 3.8. Over a length of 0.4 m this field could slow atoms with $v_i \approx 760$ m/s down to $v_f \approx 110$ m/s.

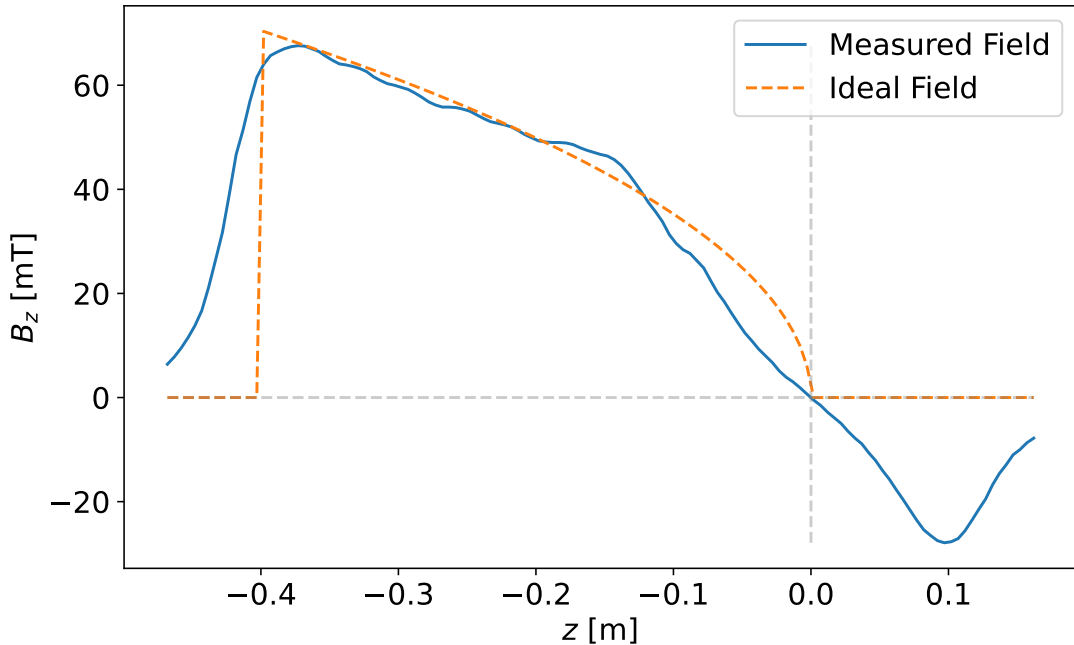


Figure 3.8: Magnetic field of an ideal Zeeman slower ($\eta = 0.3$) following eq. (3.26) which could decelerate atoms with an initial velocity $v_i \leq 760$ m/s down to $v_f \approx 110$ m/s over a distance of 0.4 m. Additionally, the measured magnetic field of the real Zeeman slower and the MOT coils is also depicted.

In our setup, the magnetic field is created by eight solenoid coils together with the quadrupole field of the MOG magnets [Koh16], based on a design by [Phi10]. The slower is depicted in fig. 3.9. From left to right, the elements shown in fig. 3.9 are:

1. Oven section, filled with ${}^6\text{Li}$. It is wrapped with heating elements to bring it to a temperature between 450 and 500 °C and make it gaseous.
2. Cross with ion getter pump in the background.
3. Valve to turn the atom beam on and off.
4. Eight Zeeman slower coils, each producing a smaller B -field than its left neighbours.
5. Pressure gauge.

6. MOT coils. They produce the MOT B -field, as well as the last part of the Zeeman slower field.
7. Another vacuum chamber with additional pumps and windows for the Zeeman slower laser beam are not drawn.

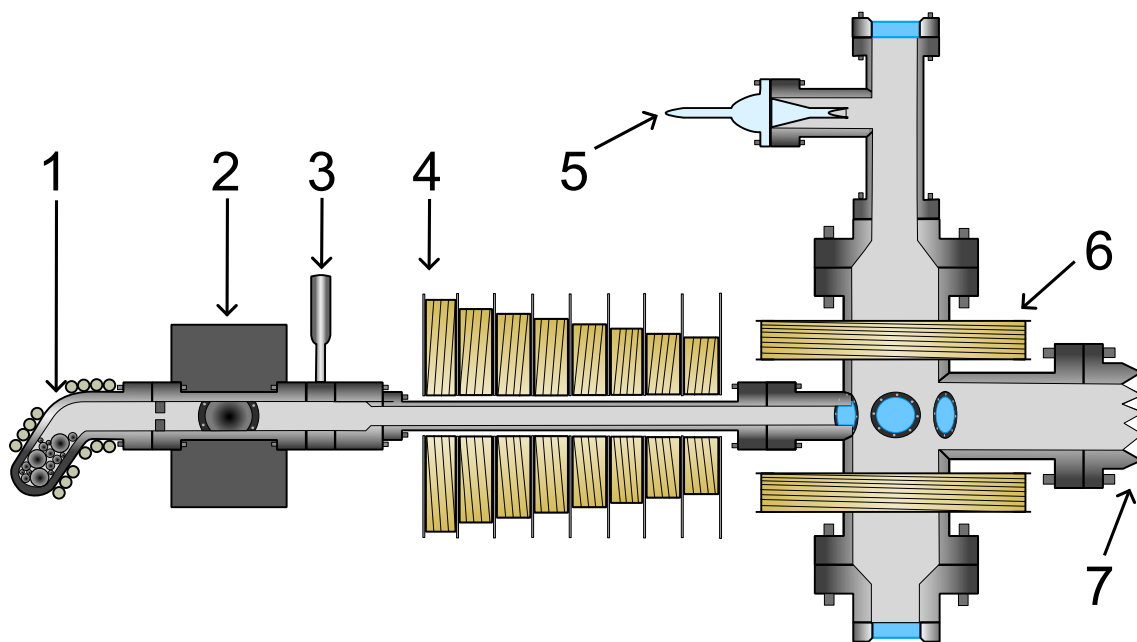


Figure 3.9: Experimental setup of the Zeeman slower + MOT.

The magnet coils produce a field B_z in the direction of the atom beam. The coils were built in such a way that the measured field, which is also plotted in fig. 3.8, approximates the ideal field. The grey lines indicate the center of the MOT at $z = 0$ and zero magnetic field. In contrast to the ideal field, the real field becomes negative after the center of the MOT. This allows for lower final velocities with a red-detuned laser. Also note, that at $z \approx -14$ cm, the measured field starts to drop more sharply and its slope becomes steeper than the ideal field's slope. For design parameters η close to 1, this could lead to atoms falling out of resonance. But as mentioned above, the ideal field's parameter is $\eta = 0.3$. It was chosen relatively small to allow for such slopes in the real field.

3.4. Slowing – Simulation Algorithm

In [Dau20], a Monte Carlo simulation was built to examine the efficacy of a Zeeman slower for ${}^6\text{Li}$ with our measured magnetic field operating on the transition described in the previous section. The idea of this algorithm is discussed in the following.

A ${}^6\text{Li}$ atom in one of its six ground states (as discussed in section 3.2) is created with a starting velocity v_z which follows the modified v^3 Maxwell-Boltzmann distribution derived in section 3.1. It flies down the beam line through a magnetic field and sees

a laser of known intensity and frequency. This laser beam can contain σ^- , π , and σ^+ polarized parts²⁶ and has a finite diameter so the atom can potentially move to a region where it's no longer slowed down by the laser. The polarization composition is determined by parameters σ , one for each polarization component, with $0 \leq \sigma \leq 1$. For example, the laser could comprise 70% σ^+ , 25% π , and 5% σ^- , which would make $\sigma_{\sigma^+} = 0.75$, $\sigma_{\pi} = 0.25$, and $\sigma_{\sigma^-} = 0.05$.

First, the magnetic field gradient is calculated to determine the maximum step length L_{\max} . Because $\left| \frac{\partial B}{\partial z} B \right| \leq (k/2\pi\mu)^2 \cdot a_{\max}$, the step size of the simulation must depend on the magnetic field and its gradient. In a slowly changing field, the atoms will most likely still be in resonance with the laser beam after a certain distance. In a rapidly changing field, the atoms that don't absorb a photon and are therefore not slowed down, might travel the same distance and fall out of resonance with the laser. But they could have interacted with the laser in the meantime. To not lose these atoms in the simulation, the step size is adjusted.

When an atom is nearly resonant to the laser beam, the scatter rates from the current ground state to all excited states are calculated using the scattering rates on each transition

$$\Gamma_i = \Gamma_{\text{nat}} \sigma \frac{s_i}{2(1 + s_i)}, \quad (3.28)$$

with the natural linewidth Γ_{nat} and

$$s_i = \frac{1}{2} \frac{\Omega_i^2}{\delta^2 + \frac{\Gamma_0^2}{4}} \quad (3.29)$$

is the saturation parameter for each transition, which takes into account power broadening. With the electric-dipole operator \hat{d} , the transition matrix element d_i which connects two states $|a\rangle$ and $|b\rangle$, and the laser light's electric field \vec{E} , the Rabi frequency Ω_i is given by

$$\begin{aligned} \Omega_i &= \frac{\langle b | \hat{d} \cdot \vec{E} | a \rangle}{h} \\ &= \frac{d_i E_0}{h}, \end{aligned} \quad (3.30)$$

where h is Planck's constant and E_0 is the amplitude of \vec{E} . The latter can be expressed in terms of the laser's intensity I and by using the transition strength S_i (which depends on the magnetic field B as seen in fig. 3.7), the Rabi frequency can be approximated [Dau20] as

$$\Omega_i \approx S_i(B) \cdot \sqrt{I} \frac{\text{cm}}{\sqrt{\text{mW}}} \cdot 16.48 \text{ MHz}. \quad (3.31)$$

²⁶At least if the beam is consisting of multiple independent lasers. While circular and linear polarization can occur together in the form of elliptical polarization, two circular polarizations in a single laser cannot.

The total scattering rate is then given by

$$\Gamma_{\text{tot}} = \sum_i \Gamma_i \quad (3.32)$$

and it's a direct measure of the excitation probability for the local B -field. A ground state atom might absorb a photon, thereby changing its momentum and then decay into any allowed ground state. This process happens after a time

$$\tau_{\text{exc}} = -\frac{1}{\Gamma_{\text{tot}}} \ln(R), \quad (3.33)$$

with R being a random number between 0 and 1. This creates an exponential lifetime of the excited state in the simulation. In this time, the atom moves a distance of

$$L_{\text{exc}} = \tau_{\text{exc}} \cdot \sqrt{v_x^2 + v_y^2 + v_z^2}, \quad (3.34)$$

but only if $L_{\text{exc}} < L_{\text{max}}$. Else, there is no excitation and the atom moves L_{max} . The atom's position \vec{x} then becomes

$$\vec{x}_{\text{new}} = \vec{x}_{\text{old}} + \frac{\min(L_{\text{exc}}, L_{\text{max}})}{\sqrt{(v_x^2 + v_y^2 + v_z^2)}} \cdot \begin{pmatrix} v_x \\ v_y \\ v_z \end{pmatrix}. \quad (3.35)$$

If an excitation occurred, the excited state is chosen by generating a second random number R' . The probabilities to excite to specific states

$$P_i = \frac{\Gamma_i}{\Gamma_{\text{tot}}} \quad (3.36)$$

are then stacked as visualized in fig. 3.10. This stacking determines ranges and if R' falls into one of these ranges, the corresponding excited state is chosen.

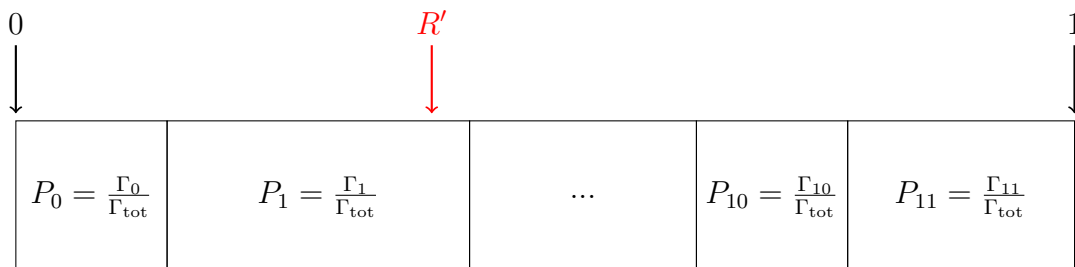


Figure 3.10: Determining the excited state by generating a random number R' .

By absorbing the photon and its momentum, the atom's velocity \vec{v} changes to

$$\vec{v}_{\text{new}} = \vec{v} + \frac{\hbar \vec{k}}{m} = \begin{pmatrix} v_x \\ v_y \\ v_z \end{pmatrix} - \frac{2\pi\hbar}{\lambda} \begin{pmatrix} 0 \\ 0 \\ 1 \end{pmatrix}. \quad (3.37)$$

Here, m is the atom's mass and λ is the wavelength of the Zeeman laser's light. The laser is assumed to be directed purely in the negative z -direction which means that every excitation leads to a decline of the atom's velocity.

The deexcitation however is neither depending on the polarization of the Zeeman laser nor its \vec{k} , assuming that stimulated emission is negligible. A new total deexcitation rate has to be calculated following

$$\Gamma_{\text{deexc, tot}} = \sum_i \Gamma_{\text{nat}} S_i(B). \quad (3.38)$$

and third random number R'' is generated to decide the final ground state in a similar fashion to the selection of the excited state.

Finally, the atom emits a photon with wavelength λ in a random direction. Therefore, two uniformly distributed numbers are generated ($\phi_{\text{rnd}} \in (0, 2\pi)$ and $\cos(\theta)_{\text{rnd}} \in (-1, 1)$) and the atom's velocity changes again:

$$\vec{v}_{\text{new}} = \vec{v} - \frac{2\pi\hbar}{\lambda m} \begin{pmatrix} \sqrt{1 - (\cos(\theta)_{\text{rnd}})^2} \cos(\phi_{\text{rnd}}) \\ \sqrt{1 - (\cos(\theta)_{\text{rnd}})^2} \sin(\phi_{\text{rnd}}) \\ \cos(\theta)_{\text{rnd}} \end{pmatrix}. \quad (3.39)$$

This cycle of absorption, movement, excitation, and deexcitation is repeated until the atom reaches a certain z -coordinate, where its state and speed is read out, or it moves outside the area which is illuminated by the slowing laser and is therefore lost.

3.5. Slowing – Velocity Measurement

In the real setup, which has the magnetic field as depicted in fig. 3.8, a laser beam (home-built ECDL, see section 2.1) of frequency $\nu_Z = 446.799\,40(3)$ THz²⁷ and a power $P = 127(1)$ mW serves as a Zeeman slower beam. A scannable laser (commercial ECDL, see section 2.2) with less power ($P = 6.0(1)$ mW) is aimed at the MOT center at $z = 0$. This scan laser hits the atom beam at an angle $\phi = 93.29(6)^\circ$ to use the Doppler shift to determine the velocity of the atom. How this angle was obtained as well as the general scanning procedure is explained in section 3.1.

The fluorescence of the atom beam was measured for two different settings, once

²⁷This frequency roughly corresponds to an offset $\delta \approx -400$ MHz to the $F_{\text{gs}} = 1/2 \rightarrow F_{\text{es}}$ transition.

without and once with the slowing laser present. The former setting is the same as in the aforementioned section. The results are shown in fig. 3.11. In between the measurements, the photodiode setup was realigned, the signal strengths were therefore different. To make both signals comparable by eye, the slowed beam's signal has been rescaled and an offset has been added. The most striking difference is the presence of a sharp peak around $\delta = 0$ MHz, i.e. $v = 0$ m/s for atoms in the lower ground state $F_{\text{gs}} = 1/2$. The feature of the upper ground state is also distorted. Slower velocity groups of atoms are pumped into the $F_{\text{gs}} = 3/2$ state, where they are cooled down even further and finally fall down to the $F_{\text{gs}} = 1/2$ state once the magnetic field reaches $|\vec{B}| = 0$, as shown in section 3.4.

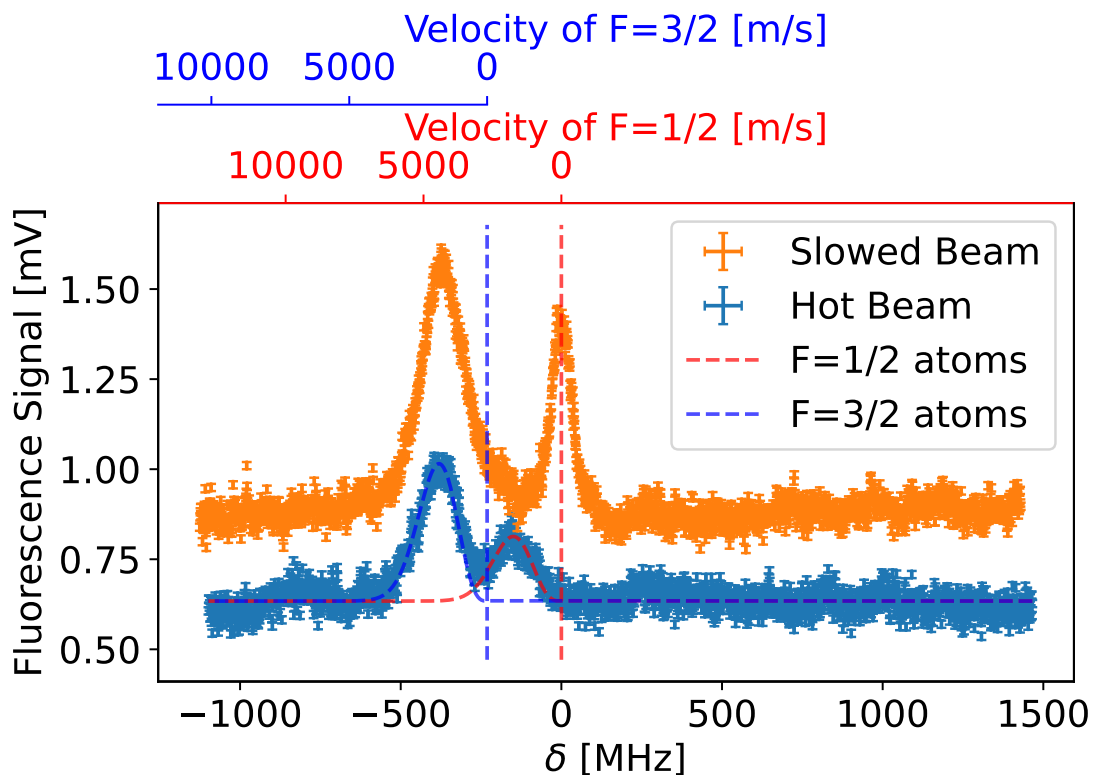


Figure 3.11: Measured fluorescence signal of an unslowed hot (blue) and a slowed (orange) atom beam. The slowed signal was rescaled and an offset was added to make comparison by eye easier.

In the following, it is assumed that the peak around $\delta = 0$ stems exclusively from $F_{\text{gs}} = 1/2$ ground state atoms because $F_{\text{gs}} = 3/2$ atoms would have to have transverse velocities $|v_t| > 150$ m/s or fly backwards to contribute to this fluorescence feature and that the Zeeman slower works as intended, i.e. the longitudinal velocity

v_l of a slowed atom is strictly dependent on its z -position and the transverse velocity v_t is normally distributed following

$$\rho_{v_t}(v) = \sqrt{\frac{m}{2\pi k_B T_t}} e^{-\frac{mv^2}{2k_B T_t}}, \quad (3.40)$$

where k_B is the Boltzmann constant, m is the mass of ${}^6\text{Li}$ and T_t is the so-called "transverse temperature".

Because the spectroscopy laser illuminates the atoms under a certain, fixed angle ϕ and they differ in v_t , they show fluorescence for different frequencies ν . Considering only the first-order Doppler shift, the spectrum is expected to follow

$$\rho(\nu) = \sqrt{\frac{m}{2\pi k_B T_t}} e^{-\frac{m\left(\frac{v_l}{\tan(\phi)} + \frac{c(\nu_0 - \nu)}{\nu \sin(\phi)}\right)^2}{2k_B T_t}} \frac{c\nu_0}{\nu^2 \sin(\phi)}, \quad (3.41)$$

with the speed of light c and the resonance frequency ν_0 . As ϕ contains errors, an offset is present, and the frequency is not given by ν but by the detuning to the resonance frequency $\delta = \nu_0 - \nu$, the function chosen to fit the data becomes

$$f(\nu) = y_0 + y_1\nu + y_2\nu^2 + N e^{-\frac{m\left(A + c\frac{\delta}{\nu_0 - \delta}\right)^2}{2k_B B}} \left(\frac{\nu_0}{\nu_0 - \delta}\right)^2. \quad (3.42)$$

Here, y_0 , y_1 , and y_2 describe the background signal (constant offset + residual $F_{\text{gs}} = 3/2$ fluorescence), while $A = v_l \cos(\phi)$ and $B = T_t \sin(\phi)^2$ contain the longitudinal velocity and the transverse temperature, respectively. The normalization is given by N . To incorporate the uncertainty in frequency offset δ , the parameters were fitted using a orthogonal density regression procedure [BD89]. The results are listed in table 3.9, while the zoomed-in data and the fit function are shown in fig. 3.12. These values translate to $v_l = 8.9(6)$ m/s and $T_t = 254(2)$ mK. The parameter errors were produced by the fit algorithm. They correspond to the square roots of the diagonal elements of the resulting covariance matrix scaled with $1/\sqrt{\chi_{\text{red}}^2}$.

Table 3.9: Fit parameters and errors of fluorescence fit as shown in fig. 3.12.

χ_{red}^2	7.4	
d.o.f.	13493	
A	-0.50(3)	m/s
B	0.254(2)	K
N	0.454(1)	mV
y_0	0.962(1)	mV
y_1	-0.145(3)	$\mu\text{V}/\text{MHz}$
y_2	-0.004 27(8)	$\mu\text{V}/\text{MHz}^2$

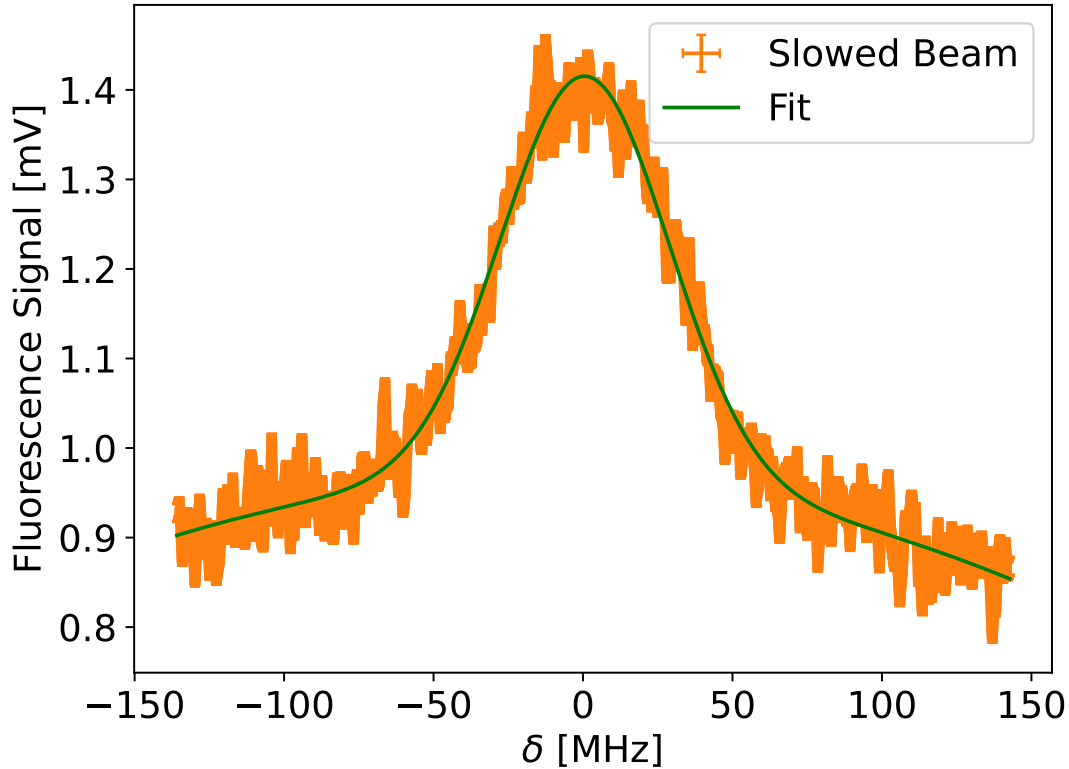


Figure 3.12: Measured fluorescence peak of atoms cooled by the Zeeman slower. The fluorescence is seen around the resonance frequency of the ${}^6\text{Li}$ D_2 $F_{\text{gs}} = 1/2 \rightarrow F_{\text{es}}$ transitions (see fig. 3.11). The signal shape is assumed to stem from a thermalized cloud of atoms. A corresponding normal distribution fit (including background) is also shown. Its parameters are shown in table 3.9.

Finally, by integrating the non-background part of the fit function eq. (3.42) and comparing the result to the total integral I of the data for the slowed beam (without background), the ratio of fluorescence that stems from cooled down atoms can be estimated. For this, the part of the slowed beam spectrum that's not part of the signal ($\delta < -600$ MHz and $\delta > 300$ MHz) is approximated using a 4th-order polynomial²⁸ which is then subtracted from the measured data. Subsequently, the integral is calculated numerically using

$$I = \sum_{i=0}^{n-1} \frac{V_i + V_{i+1}}{2} |\delta_{i+1} - \delta_i|, \quad (3.43)$$

where i is the index of the data point (δ_i, V_i) of which there are a total of n . The ratio is thus calculated by simple division to be 18(1) %.

²⁸This analysis was done multiple times for increasing order of the background polynomial, until the change of I from step i to $i + 1$ was smaller than the integral's uncertainty.

3.6. Slowing – Comparing Simulation Results and Measurement

This section compares the results of both the Zeeman slower simulation and the measurements of the previous sections to test the presented simulation.

In the simulation, atoms ($N = 10^7$) are generated at the exit of the oven section and while their initial z -position is always the same, their x - and y -positions are randomly and uniformly chosen within the limits of the oven's outlet. The respective starting velocities v_x and v_y , on the other hand, are always $v_x = v_y = 0$ while v_z follows the modified Boltzmann distribution eq. (3.3). The initially populated ground state is also randomly chosen from the six possible ground states. For more information on how these values were generated, see appendix F. The simulation was repeated several times for starting temperatures T ranging from $T = 450^\circ\text{C}$ to $T = 500^\circ\text{C}$ in steps of 5 K.

The atoms propagate through the Zeeman slower and once they reach the MOT center, their fluorescence is calculated which is depending on the atom's velocity \vec{v} and the spectroscopy laser's detuning from the ${}^6\text{Li D}_2 F_{\text{gs}} = 1/2 \rightarrow F_{\text{es}}$ transition $\Delta\nu$ as well as the angle ϕ under which this laser is directed into the setup. The atom's fluorescence is then calculated assuming a magnetic field of $B = 0$, thus ignoring the Zeeman shift which should be negligible in the trap center. This is done for all atoms, once with a turned-on ($\nu_{\text{Slower}} = 446.7994\text{ THz}$, σ^+ -polarized) and once with a turned-off slower beam, and their total expected fluorescence signals are calculated. The resulting signals, together with the real measured data, are depicted in fig. 3.13 and fig. 3.14, respectively.

As explained in section 3.1, the fluorescence signal's form strongly depends on both T and ϕ . And while in section 3.1 ϕ was evaluated by probing several different angles and checking which produce reasonable T , here it is the other way around. Earlier, ϕ was determined to be $\phi = 93.29(6)^\circ$. A similar value (specifically $\phi = 93.3^\circ$) was chosen to calculate the fluorescence signals for different temperatures. The signals s were linearly scaled to minimize the squared deviations $\sum_i (s(\Delta\nu_i) - d(\Delta\nu_i))^2$ to their respective real data d , where the index i indicates the i -th frequency bin. The simulation result with the lowest squared deviation in its unslowed signal ($T = 485^\circ\text{C}$) should describe the data best and was therefore chosen for presentation and further analysis²⁹. As before, the background of the data was cut by approximating the background region with a polynomial and subtracting it from the data.

The plots that correspond to simulated fluorescence in fig. 3.13 and fig. 3.14 are depicted as lines of different color. Therein, the orange dashed line describes the signal originating from the upper ground state ($F_{\text{gs}} = 3/2$) while the green signal belongs to the lower ground state ($F_{\text{gs}} = 1/2$) and the red line represents the total signal.

²⁹Of course, this procedure hinges on the facts that the temperature steps of 5 K are quite large for a total range of 50 K and that the calculation of the sum of squared deviations required the elimination of the background of the real data set.

The unslowed signals overlap without much deviation except for the background region $\Delta\nu > 0$ MHz because the simulation cannot produce any background signal. The atoms are v^3 -Maxwell distributed and there is no magnetic field present which could distort the atoms' fluorescence spectrum.

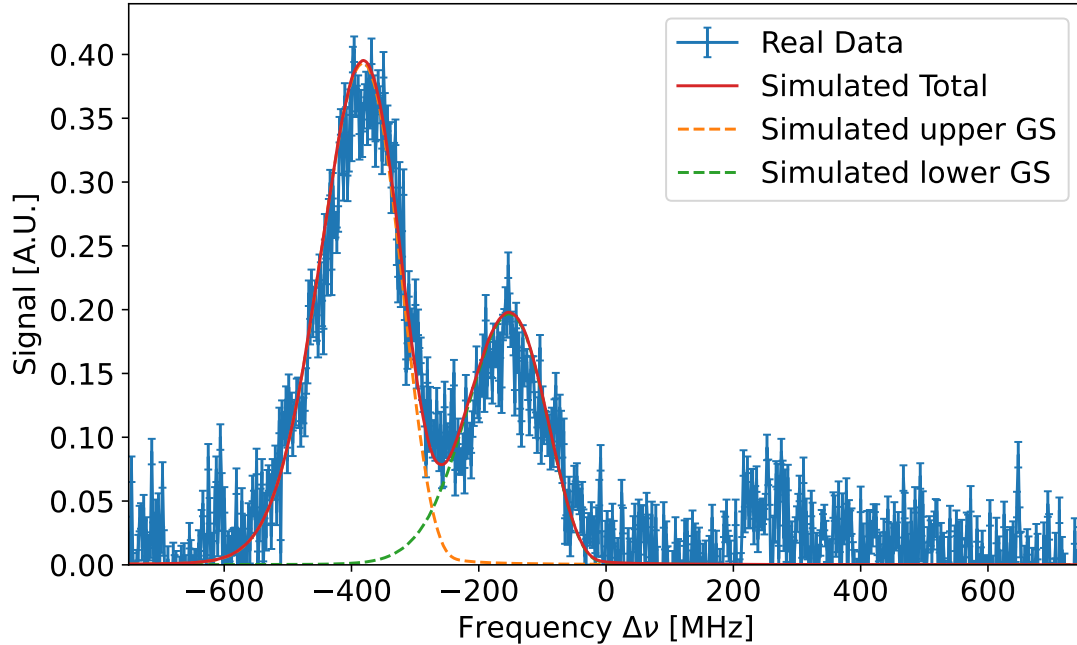


Figure 3.13: Measured data of an unslowed beam with subtracted background and expected fluorescence of unslowed simulated atoms. The atoms were simulated at $T = 485^\circ\text{C}$ and their fluorescence when interacting with a spectroscopy beam entering the setup at an angle $\phi = 93.3^\circ$ was calculated. In the simulation, it is known whether an atom is in the upper ($F_{\text{gs}} = 3/2$) or lower ($F_{\text{gs}} = 1/2$) ground state. The expected signals are therefore color coded to make their origins identifiable. The calculated and the measured signals show very similar fluorescence features. However, the simulation does not produce any background signal ($\Delta\nu > 0$ MHz and $\Delta\nu < -700$ MHz). There, data and simulation differ considerably.

The slowed spectra show significant differences, of which the most striking one is the absence of the peak around $\Delta\nu = 0$ MHz in the simulated spectrum. This peak was assigned to the cooled down ^6Li atoms in the $F_{\text{gs}} = 1/2$ ground state. Additionally, an excess of fast atoms in the upper ground state leads to more fluorescence than expected for $\Delta\nu < -300$ MHz. Many fast atoms from the lower ground state were pumped into the upper state during the slowing process were they fell out of resonance and couldn't be slowed down any further, leaving a dip in the spectrum around $\Delta\nu = -200$ MHz. The final ratio of upper to lower state atoms is 84% to 16%.

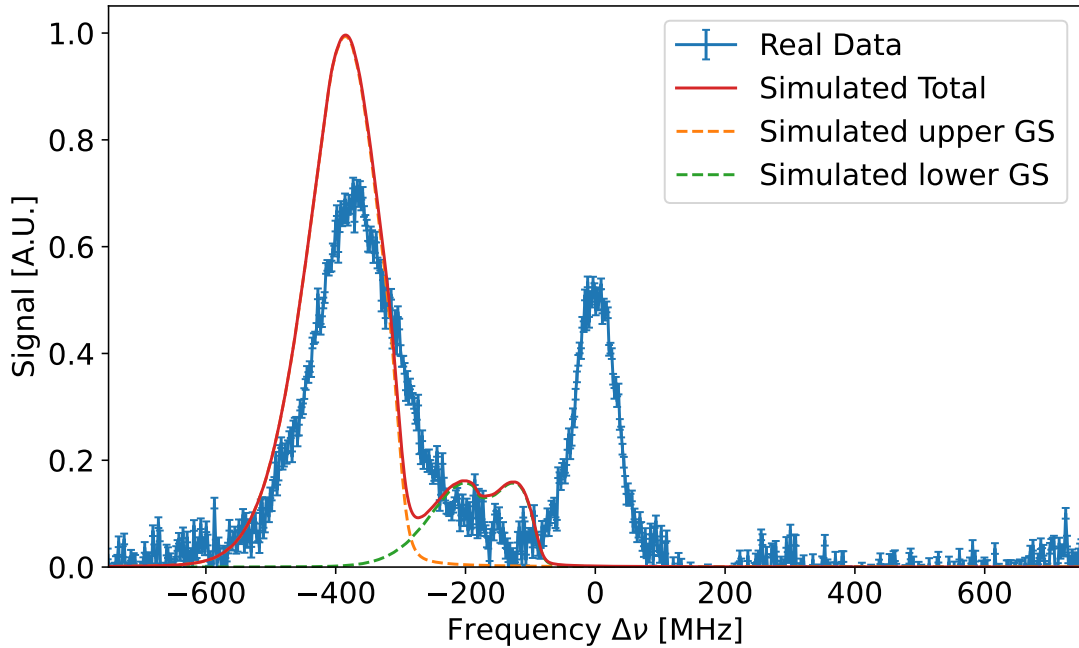


Figure 3.14: Measured data of a slowed beam with subtracted background and expected fluorescence of slowed simulated atoms. The atoms were simulated at $T = 485^\circ\text{C}$ and their fluorescence when interacting with a spectroscopy beam entering the setup at an angle $\phi = 93.3^\circ$ was calculated. In the simulation, it is known whether an atom is in the upper ($F_{\text{gs}} = 3/2$) or lower ($F_{\text{gs}} = 1/2$) ground state. The expected signals are therefore color coded to make their origins identifiable. The real and the simulated signal differ significantly. Fluorescence for $\Delta\nu > -100$ MHz disappears and the feature around $\Delta\nu = 0$ is not present. Instead, an excess in fluorescence stemming from fast atoms in the $F_{\text{gs}} = 3/2$ state atoms appears. Fast atoms from the lower ground state were pumped into the upper ground state, where they fell out of resonance and couldn't be slowed down any further.

There are no atoms with $v_z \approx 0$ m/s around the MOT center in the simulation. Nevertheless, the simulation allowed for a more precise analysis of the atoms' velocities v_z as a function of their positions z in the Zeeman slower. For this, 100 atoms with starting velocities in the range $v_z \in [15, 1500]$ m/s were observed during the simulation. The path of each atom was simulated from $z = 0$ until they either reached the MOT center at $z = 0.468$ m, reached a velocity $v_z < 0$ (i.e. they turned around), or left the slowing laser beam and thus couldn't be slowed down any further. The development of their $v_z(z)$ is depicted in fig. 3.15.

Faster atoms (starting velocity $v_z > 850$ m/s) might experience some slowing but fall out of resonance and do not reach $v_z = 0$. Atoms with 400 m/s $< v_z(0) < 850$ m/s reach $v_z = 0$ at a position 0.42 m $< z < 0.44$ m which is before the MOT center. As only the fluorescence of atoms that reached the MOT region is shown in fig. 3.14, these atoms could not produce a sharp peak of slowed atoms. Atoms with lower

starting velocities mostly experience too much transverse heating, leave the laser beam, and are thus not slowed to $v_z = 0$.

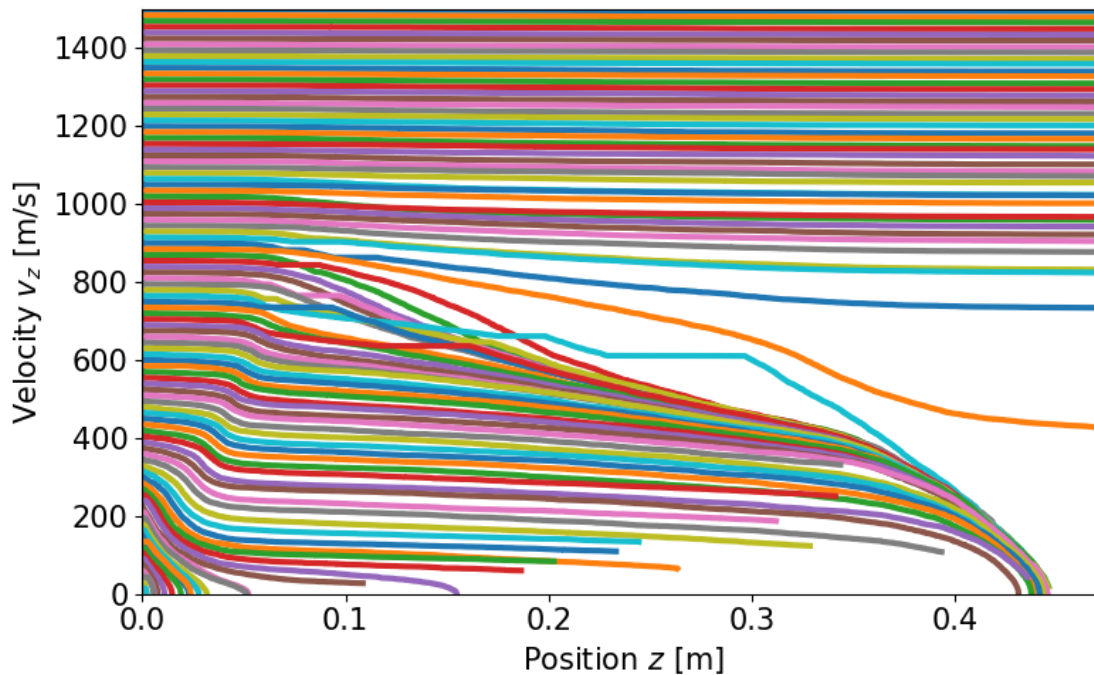


Figure 3.15: Velocity v_z as a function of position z in the Zeeman slower setup for simulated atoms with different starting velocities. The MOT center ($B = 0$) is at $z = 0.468$ m. The atoms that are slowed down to $v_z = 0$ do not reach the center. Lines that stop prematurely belong to atoms that leave the slowing laser beam due to transverse heating and are thus not simulated any further.

In the simulation, the last point of interaction with the slowing laser was saved. If all atoms which had their last interaction after $z > 0.42$ m were also taken into account, a spectrum as depicted in fig. 3.16 would be expected (for $B = 0$). When these atoms are included, a peak is clearly visible in the fluorescence spectrum. However, this peak is not at $\Delta\nu \approx 0$ MHz but $\Delta\nu \approx -228$ MHz which corresponds to the $F_{\text{gs}} = 3/2$ transitions of ${}^6\text{Li}$. The simulation's result is directly contradicted by the measurement. The atoms should be in the lower ground state.

An earlier version of the simulation [Wie19] predicts a fitting behavior. During the slowing within the Zeeman slower's magnetic field B , the atoms cycle in a closed transition from the upper ground state to the excited state. As long as $B > 0$, the atoms always deexcite to the upper ground state. Only when the atoms reach the MOT center, where $B = 0$, and the magnetic substates are degenerate again, the atoms are pumped from $F_{\text{gs}} = 3/2$ to $F_{\text{gs}} = 1/2$. In the simulation's current version, the slowed down atoms don't reach the MOT center and therefore stay in the upper ground state. Additionally, by integrating over the area of the peak, it can be determined to comprise 4.6(1)% of the total fluorescence, which is less than

the 18(1) % for the measured spectrum estimated in section 3.5. For the atoms that are slowed down, the simulation overestimates the slowing efficiency and stops them too early. At the same time, it doesn't slow enough atoms³⁰.

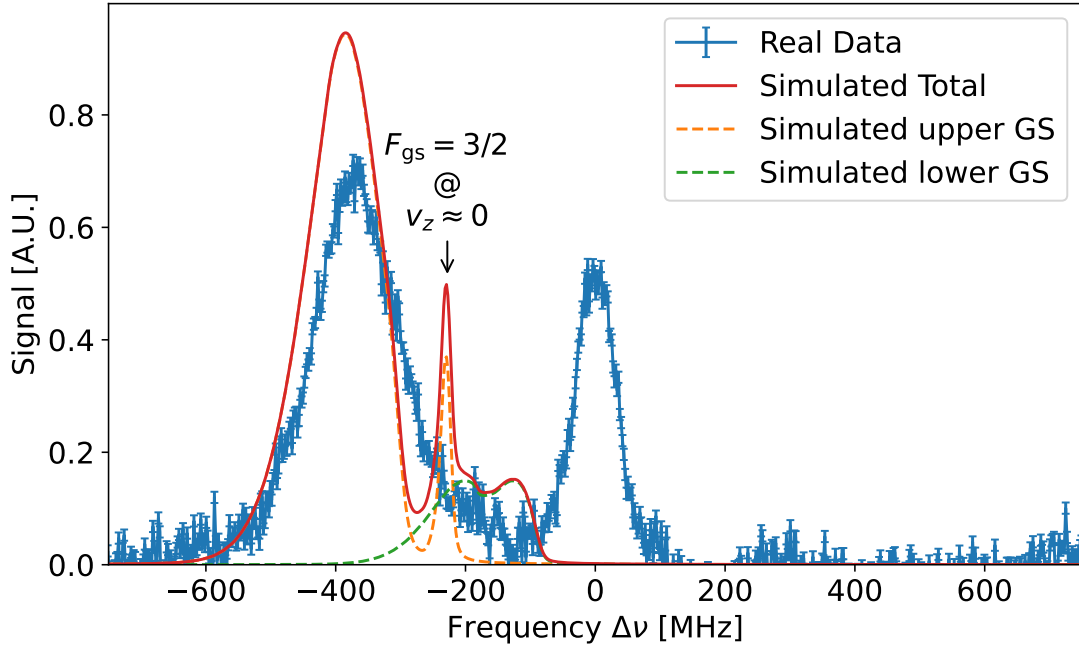


Figure 3.16: Measured data of a slowed beam with subtracted background and expected fluorescence of slowed simulated atoms. The plot depicts the same situation as fig. 3.14 but in addition to only those atoms that reach the MOT center (as seen in fig. 3.14), atoms that had their last interaction after $z = 0.42$ m were also taken into account. They produce a sharp peak but not at $\Delta\nu = 0$ MHz because these atoms are in the upper ground state with velocity $v_z \approx 0$.

The final velocity distribution of the atoms (including those with their last interaction at $z > 0.42$ m) is shown in fig. 3.17. 99.5(1) % of the 10^7 simulated atoms are contained. Only a small remainder is lost before due to transverse heating. This fraction is small because the total number of atoms with low starting velocities is itself low.

There are virtually no lower ground state atoms with a final velocity $v_z < 1000$ m/s, all atoms that are slowed down are pumped into the $F_{\text{gs}} = 3/2$ state and of these atoms, many fall out of resonance during the slowing process. Only the 4.6(1) % men-

³⁰It's also possible that the slow atoms would react multiple times with the spectroscopy laser while faster atoms don't. Thus, slower atoms would produce more fluorescence than hotter ones. However, in this calculation it is assumed that each atom only interacts once with the spectroscopy beam.

tioned above reach $v_z < 180$ m/s. Following the definition of transverse temperature T_t used in eq. (3.40) and identifying

$$\sigma = \sqrt{\frac{k_B T_t}{m}} \quad (3.44)$$

as the standard deviation of the velocity distribution, T_t for these slowed atoms can be evaluated to $T_t = 15.0(1)$ mK. This is significantly lower than the $254(2)$ mK of the measured slowed atoms. The simulation incorrectly predicts less transverse heating than experimentally observed.

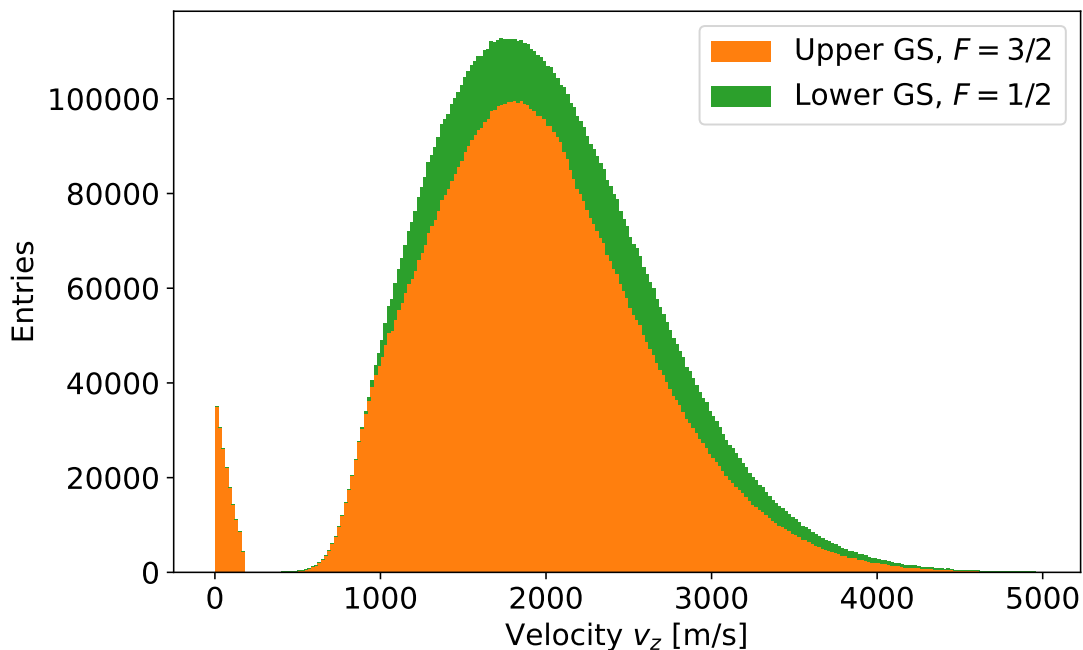


Figure 3.17: Stacked velocity distribution of simulated ${}^6\text{Li}$ atoms after they have been slowed down by the Zeeman slower. Taken into account are atoms that reach the MOT center or have their last interaction at $z > 0.42$ m. The left bins contain slow ($v_z < 180$ m/s) atoms and represent $4.6(1)\%$ of the total area.

To visualize the change per velocity class, the hot and the slowed beams' v_z distributions are compared in fig. 3.18 by calculating

$$\Delta N(v_z) = N_{\text{unslowed}}(v_z, \Delta v_z) - N_{\text{slowed}}(v_z, \Delta v_z), \quad (3.45)$$

where $N_i(v_z, \Delta v_z)$ is the number of atoms with a downstream velocity v_z in the velocity class $v_z \in [v_z - \frac{\Delta v_z}{2}, v_z + \frac{\Delta v_z}{2}]$. In this depiction, a net removal of atoms from their velocity class in the process of slowing is shown in red, while a net surplus is visualized by green bins. Ideally, all bins for $v_z > 0$ should be red and describe a perfect modified v^3 -Boltzmann distribution while the leftmost bin that contains $v_z = 0$ should be green and should contain as many entries as the red bins in total.

The red area contains 5.5 % of all simulated atoms and it obviously doesn't follow a v^3 -Boltzmann distribution. The Zeeman slower has a finite length and a finite magnetic field strength which limit the maximum velocity of slowable atoms (estimated to $v_z \approx 760$ m/s in section 3.3). The slowing laser has a high intensity and the resulting power broadening leads to atoms with higher velocities also being partially slowed. But those are just a fraction of all hot atoms.

The green area contains only 1.7 % of all simulated atoms. The discrepancy stems from slowed atoms being lost due to transverse heating. This contains atoms that had their last interaction with the laser before and after $z = 0.42$ m.

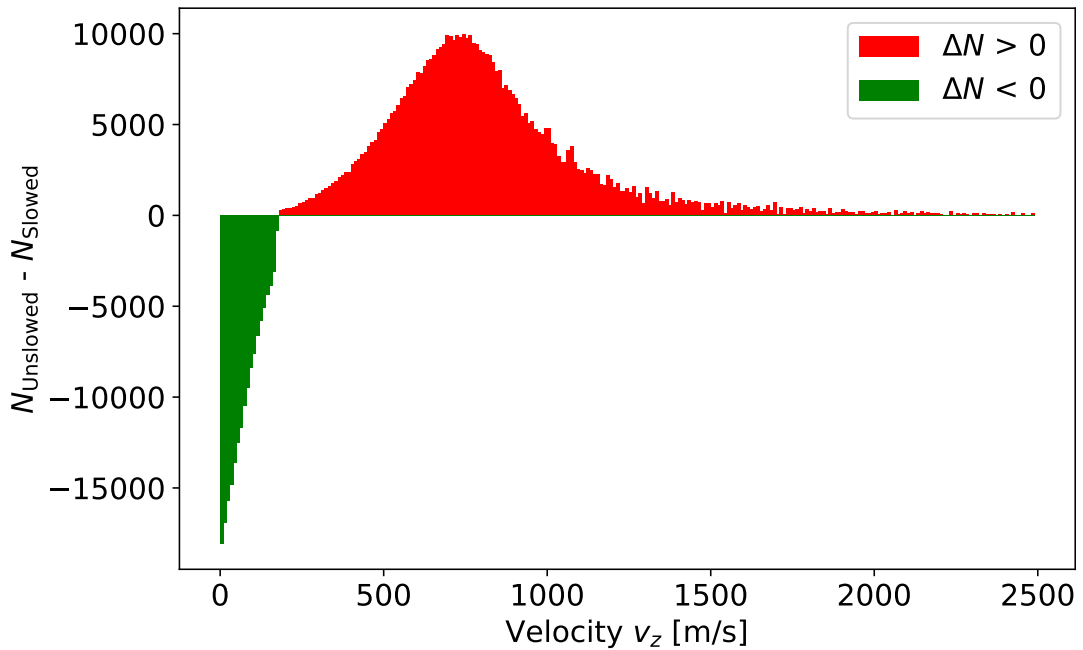


Figure 3.18: Difference in atoms within in a certain velocity class for the unslowed and the slowed beam. The red area corresponds to a surplus in the unslowed data (5.5 % of all simulated atoms). After slowing, these atoms are missing from their specific velocity class. The green area describes the appearance of more atoms in this velocity class after the slowing process (1.7 % of all simulated atoms). Differences are due to loss of atoms because of transverse heating.

The simulation is very promising and with its integration of transition strengths for varying magnetic fields it could be a helpful and powerful tool for future experiment planning.

Interestingly, the simulation overestimates the effectiveness of the Zeeman slower as those atoms, that are slowed down, reach $v_z = 0$ before the actual center of the MOT and are subsequently lost due to transverse heating. At the same time, the efficiency is also underestimated because not as many atoms participate in the slowing process as have been expected from the analysis of experimental data (5.5 % instead of 18(1) %). The simulated atoms' transverse temperature is also lower than

expected.

The simulation needs further fine-tuning to reproduce the results of the real Zeeman slower. In addition, the simulation could also be upgraded to not only describe the behavior of atoms within a Zeeman slower but also within a magneto-optical trap with multiple lasers.

4. The Magneto-Optical Trap

As the name suggests, a magneto-optical trap (MOT) is an apparatus which confines atoms to a certain volume with the help of a magnetic field and light. We explain the basic principle in 1D, but generalization to 2D or 3D is trivial. A simple atom species with a ground state with angular momentum $l_g = 0$ and an excited state with $l_e = 1$ sits close to the field-free region of a linear magnetic field $B(x)$. This results in a level scheme depicted in fig. 4.1. The ground state energy doesn't change with increasing B because $m_l = 0$, while the excited state shows the typical splitting of the anomalous Zeeman effect.

From one side σ^+ - and from the other side σ^- -laser light shines at the atom. Both beams are slightly red detuned, i.e. their frequency is below the atom's resonance frequency to such a degree that the excitation probability for a non-moving atom in a zero-field can be assumed to be negligible. Should the atom move towards one of these laser beams, the light would be Doppler-shifted and the probability of absorbing photons and thereby changing the atoms momentum would increase, effectively slowing down the atom. Should the atom reach an x -position where the Zeeman shift compensates the laser detuning for one magnetic substate (while keeping the detuning for the second and increasing it for the third), a transition from the ground state to this substate can be driven, which again changes the atom's momentum and pushes it back into the center of the trap.

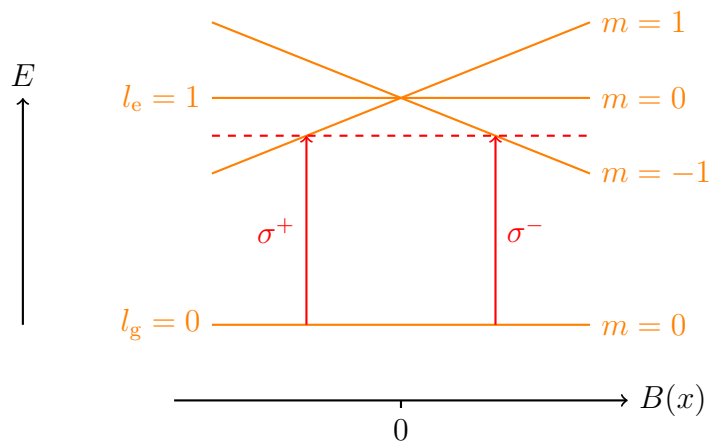


Figure 4.1: Level scheme of a simple atom in a 1D-MOT. The atom has a single ground state and its excited state splits into three magnetic substates in the B -field of the MOT. From the left, a σ^+ red detuned laser beam slows down atoms that move to the left or pushes atoms that are too far left of center back. A σ^- beam of the same frequency does the same but for the right side.

The resulting force F , in first-order and around the trap center, takes the form

$$F(x, v) = -c_x x - c_v v, \quad (4.1)$$

where c_x and c_v are positive constants describing the linear relation between the restoring force, the distance to the center x and the velocity of the atom v . This equation describes the motion of a damped harmonic oscillator. The atoms are not only confined inside the MOT region but they are also slowed down. Thus, the MOT can be used to generate a sample of cold atoms.

By changing the magnetic field configuration and adding a second pair of laser beams, a 2D-MOT can be built. This is possible using permanent magnets [TGLW09] and was also done as another project in the workgroup [Wes21, Sch22]. The setup of the 3D-MOT is examined in section 4.1, how the necessary laser beams are generated is explained in section 4.2, and the real trap is presented in section 4.3. Measurements of the loading and unloading processes specifically are evaluated in section 4.4 and although the final temperature could not be determined, the general procedure to extract this value from absorption measurements performed on an atom cloud is outlined in section 4.5.

4.1. General Setup

A three-dimensional MOT requires a magnetic field with a zero-crossing and a monotonous behaviour around said zero-crossing. A quadrupole field which satisfies these requirements can easily be realized using an Anti-Helmholtz coil pair as depicted in fig. 4.2. Two solenoids with opposite directions of electric current create a magnetic field \vec{B} which can be approximated near the MOT center to

$$\vec{B}(x, y, z) \approx B_0 \begin{pmatrix} x \\ y \\ -2z. \end{pmatrix} \quad (4.2)$$

In contrast to the coordinate system used in section 3, the z -axis is not the axis of the atomic or Zeeman slower beam but the vertical axis while the axes of x and y describe the horizontal plane. The vertical magnetic field component is negative and its absolute value grows twice as fast as the horizontal components. This is a direct consequence of the Maxwell equation $\vec{\nabla} \cdot \vec{B} = 0$. Lastly, the field strength is governed by B_0 . For two infinitely thin solenoids of radius R and distance $2a$ it is given by

$$B_0 = -\frac{3\mu_0 n I a R^2}{4(R^2 + a^2)^{5/2}}, \quad (4.3)$$

where μ_0 is the vacuum permeability and I is the current which flows through the coil's n windings. Of course, the coils are not infinitely thin but expanded. They have inner layers and their windings have differing vertical distances to the MOT center. Therefore, B_0 can be approximated by the field strengths of multiple solenoid pairs with radii $R = R_0 + \Delta R(i_{\text{layer}} - 1)$ and distances $2a = 2(a_0 + \Delta a(i_{\text{winding}} - 1))$. Here, $i_{\text{layer/winding}}$ labels the i -th layer/winding of the total n_{layer} layers or n_{winding} windings, respectively, ΔR is the thickness and Δa is the height of the wire which was used to wind the coils.

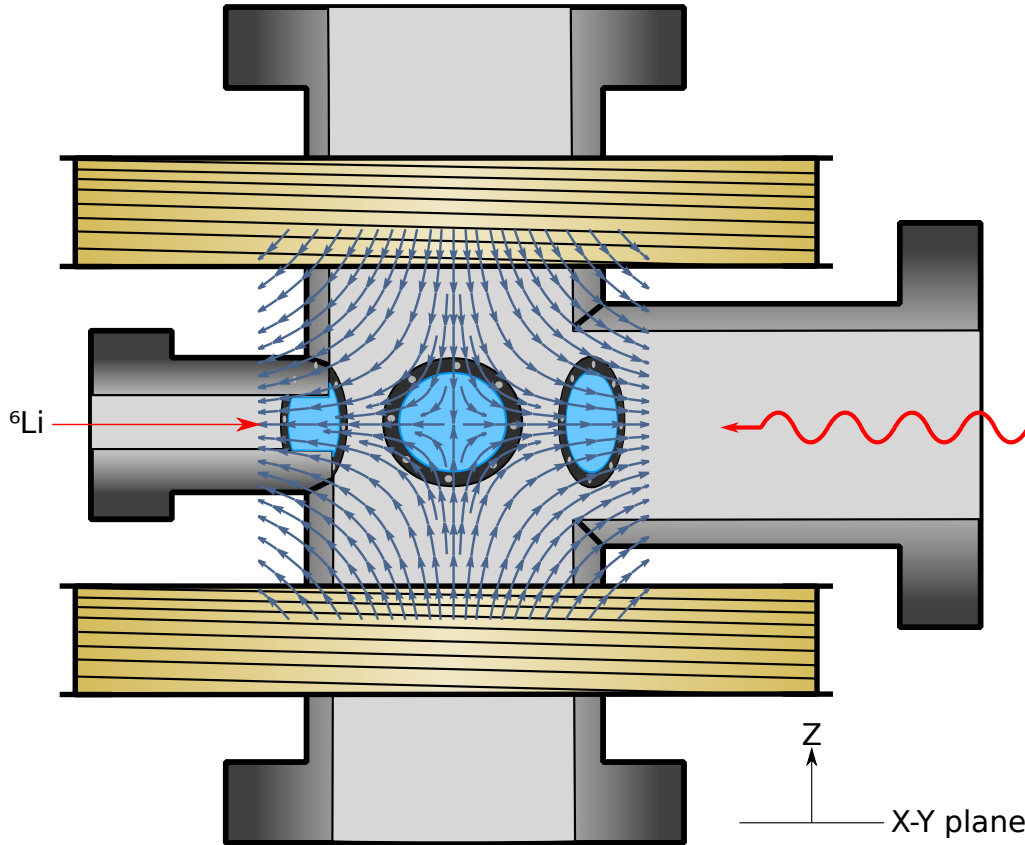


Figure 4.2: Magnetic quadrupole field within the MOT chamber. From the left, the hot atom beam enters the chamber. It is slowed by the Zeeman slower laser beam coming from the right.

The Zeeman slower is constantly operating, i.e. the last coils of the slower, which also consist of multiple windings and layers, slightly influence the magnetic field within the trapping region (some millimeters around the MOT center). The final field is therefore the same as shown in fig. 3.8. A zoomed in version with an additional linear fit ($\chi^2 = 20.9$, n.d.o.f. = 17) around the MOT center is also shown in fig. 4.3. Note that the position describes the distance to the center and the B field component are both measured in the direction of the atom beam which lies in the middle of the x - and y -axes. The field strength parameter B_0 can thus be determined by the slope of the fit to be $B_0 = -2466(25)$ mT/m. As explained before, the field would grow twice as fast in the z -direction.

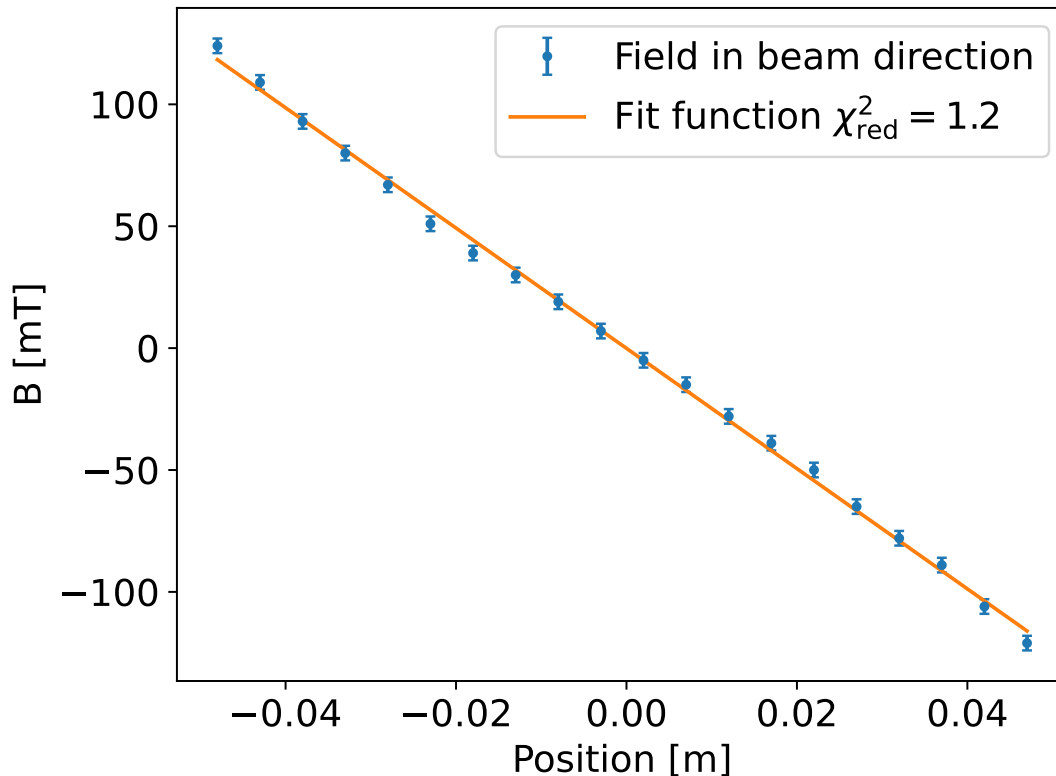


Figure 4.3: Zoom in of the \vec{B} field component pointing in the atom beam direction. The data describes the field strength around the MOT center. A linear function was fitted to the data to extract B_0 . Due to the rotation-symmetric geometry, the field components in the x - and y -direction show the same behaviour, while the z -component has twice the slope.

Six laser beams are necessary to trap an atom in a 3D-MOT: two for each spatial direction. These beams can be provided by a single laser, whose output is split into three separate beams using semi-transparent mirrors or beamsplitters. One beam per axis is enough because this beam can be reflected back using a mirror and a quarter-wave plate. The laser setup around the MOT chamber is shown in fig. 4.4. The magnetic coils as well as the Zeeman laser and the atomic beam are not shown to keep the picture simple. Each laser beam is linearly polarized when reaching the setup. They have to pass a first quarter-wave plate to make them circular polarized. In convenient nomenclature, polarization may be called either right-handed or left-handed, depending on the quantization axis chosen to align with the axes of the cartesian coordinate frame. A left-hand polarized beam might be either perceived as σ^+ - or σ^- -light depending on the direction in which it passes the chamber. The same goes for right-handed light.

As shown in the introduction to section 4, the MOT laser beams need to be σ^+ from one side and σ^- from the other. By simply adding a mirror without a second quarter-wave plate to reflect the beam, the mirror would change the lights wave

vector \vec{k} to $-\vec{k}$ as well as its helicity and therefore, what was σ^+ would stay σ^+ and there would effectively be no restoring force. A MOT could not be created. The second quarter-wave plate ensures the correct helicity by making the beam linearly polarized prior to its reflection.³¹

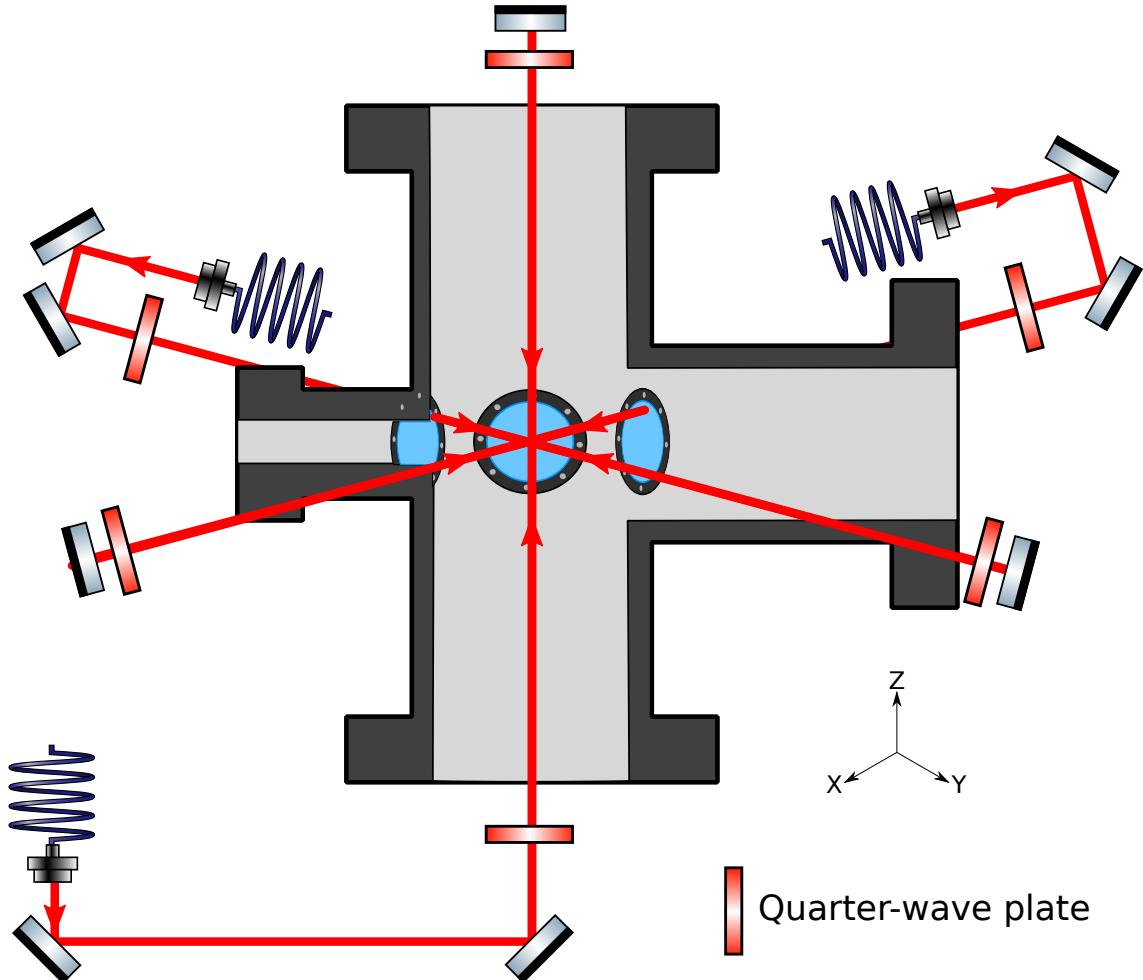


Figure 4.4: MOT laser setup. Three laser beams are emitted from separate fibers. Each beam is steered through the center of the MOT chamber using mirrors. Before entering and after leaving the chamber, each beam passes a $\frac{\lambda}{4}$ -plate to control their circular polarization within the chamber.

4.2. Trapping Beams

A stabilized laser (see section 2.2.4) serves as a starting point for generating the laser beams which are necessary to create a ${}^6\text{Li}$ MOT, as shown in section 4.1.

Because of its hyperfine structure, ${}^6\text{Li}$ has two ground states: the lower $F_{\text{gs}} = 1/2$ and the upper $F_{\text{gs}} = 3/2$ state. The hyperfine splitting between these states is 228.202(2) MHz [LWR⁺20] and although closed transition cycles are possible, atoms might fall into a non-resonant dark state should only one laser frequency be applied.

³¹A more rigorous examination using the formalism of Jones calculus [Jon41] can be found in appendix D.

An example: an atom in the upper ground state sits in the center of the MOT. It moves slightly to the side of negative magnetic field values and interactions with the red-shifted σ^+ -laser beam become more probable. Assuming that the magnetic field is so small that the ground state as well as the excited states are still in the Zeeman regime, i.e. F and m_F are still good quantum numbers, the transitions shown in table 4.1 are allowed. Of these nine transitions, only one ($|F_{\text{gs}} = 3/2, m_F = 3/2\rangle \rightarrow |F_{\text{es}} = 5/2, m_F = 5/2\rangle$) leads to a closed cycle. The atom either reaches the closed cycle transition or eventually decays to the $F_{\text{gs}} = 1/2$ ground state³² which is too far detuned to the laser's frequency to drive any transition.

If an atom in the $|F_{\text{gs}} = 3/2, m_F = 3/2\rangle$ ground state reaches the $B > 0$ region, it becomes more resonant to the σ^- beam and can experience a transition as listed in table 4.2. None of these transitions form a closed cycle. Again, the atom either reaches the $|F_{\text{gs}} = 3/2, m_F = -3/2\rangle \rightarrow |F_{\text{es}} = 5/2, m_F = -5/2\rangle$ transition or it falls into the dark state. Thus, every atom will ultimately reach the dark state when it moves from one side of the MOT to the other. The usual way to solve this problem is by applying an additional laser frequency, i.e. using a repumper. A second, collinear laser beam with a detuning of 228.202(2) MHz is needed.

Table 4.1: Dipole-allowed σ^+ -transitions from the ${}^6\text{Li}$ $F_{\text{gs}} = 3/2$ ground state to any of the $2P_{3/2}$ excited states.

$F_{\text{ground state}}$	$m_{F,\text{ground state}}$		$F_{\text{excited state}}$	$m_{F,\text{excited state}}$
3/2	3/2	\rightarrow	5/2	5/2
3/2	1/2	\rightarrow	5/2	3/2
3/2	1/2	\rightarrow	3/2	3/2
3/2	-1/2	\rightarrow	5/2	1/2
3/2	-1/2	\rightarrow	3/2	1/2
3/2	-1/2	\rightarrow	1/2	1/2
3/2	-3/2	\rightarrow	5/2	-1/2
3/2	-3/2	\rightarrow	5/2	-1/2
3/2	-3/2	\rightarrow	5/2	-1/2

Table 4.2: Dipole-allowed σ^- -transitions from the ${}^6\text{Li}$ $|F_{\text{gs}} = 3/2, m_F = 3/2\rangle$ ground state to any of the $2P_{3/2}$ excited states.

$F_{\text{ground state}}$	$m_{F,\text{ground state}}$		$F_{\text{excited state}}$	$m_{F,\text{excited state}}$
3/2	3/2	\rightarrow	5/2	1/2
3/2	3/2	\rightarrow	3/2	1/2
3/2	3/2	\rightarrow	1/2	1/2

³²For example, an atom might start in the ground state $|F_{\text{gs}} = 3/2, m_F = 1/2\rangle$ and reach the closed cycle via $|F_{\text{gs}} = 3/2, m_F = 1/2\rangle \rightarrow |F_{\text{es}} = 5/2, m_F = 3/2\rangle \rightarrow |F_{\text{gs}} = 3/2, m_F = 3/2\rangle$ or decay into the lower ground state via $|F_{\text{gs}} = 3/2, m_F = 1/2\rangle \rightarrow |F_{\text{es}} = 3/2, m_F = 3/2\rangle \rightarrow |F_{\text{gs}} = 1/2, m_F = 1/2\rangle$.

To turn one single-frequency laser beam into three two-frequency laser beams, we use 2 AOMs at ± 114 MHz as shown in fig. 4.5. A frequency-stabilized laser beam is first guided through a telescope, i.e. a combination of lenses to decrease the waist of the beam, and is then split into two separate beams using a polarizing beam splitter (PBS). To control the power which goes into each arm, a quarter-wave plate is placed before the PBS. Both beams are then guided through an acousto-optic modulator (AOM³³) [Hun09], which shift the laser frequency by means of an applied RF frequency of $f_{\text{RF}} = \pm 114$ MHz. Their working principle is explained below. Subsequently, the beams are overlapped again, spatially and polarization-wise. A 50/50 beam splitter has to be used for the overlapping, to create beams of the correct polarization. A PBS cannot be used without an additional half-wave plate after the upper AOM. Finally, the beams are guided into optical fibers which transport them to the MOT setup via regular fiber coupling setups.

An AOM can be understood as a crystal (in this case, tellurium dioxide TeO_2) through which a sound wave of controllable frequency in the RF region and amplitude travels. A piezoelectric transducer creates these waves on one side and an absorber material absorbs them on the other side of the crystal to avoid the formation of standing waves. This is schematically depicted in fig. 4.6. In the language of second quantization, the density waves that move through the crystal are phonons which can perform Brillouin scattering [GM22] with the photons of the passing laser beam. Thereby, photons either absorb $n \in \mathbb{N}$ phonons or emit them by inducing lattice oscillations in the crystal. Of course, the photon could also pass the AOM without interacting at all. The absorption or emittance changes the photon's momentum, i.e. its wave vector \vec{k} and therefore also its frequency ν and angle ϕ . An interaction with a number $z \in \mathbb{Z}$ of phonons of momentum $\hbar\vec{q}$ and frequency f changes the photons properties according to

$$\vec{k}' = \vec{k} + z \cdot \vec{q}, \quad (4.4)$$

$$\nu' = \sqrt{\nu^2 + \left(\frac{cz \cdot |q|}{2\pi}\right)^2} + 2\nu \frac{cz \cdot |q|}{2\pi} \cos(\alpha) \approx \nu + z \cdot f, \quad (4.5)$$

$$\phi = \arccos\left(\frac{|\vec{k}| + z \cdot |\vec{q}| \cos(\alpha)}{|\vec{k}'|}\right) \approx \arccos\left(\frac{\nu + z \cdot |\vec{q}| \cos(\alpha) \frac{c}{2\pi}}{\nu + z \cdot f}\right), \quad (4.6)$$

where α is the angle between the incoming laser beam and the phonons. The efficiency, in which an unmodulated beam (0-th order) is diffracted and its frequency is changed by $\pm f$ (1st or -1st order), $\pm 2f$ (2nd or -2nd order) or more, is highly dependent on the angle in which the AOM is placed. To maximize the photon-

³³The AOMs in use are AOMO 3110-120 produced by G&H.

phonon scattering probability for the correct order, the position and rotation of the AOM has to be adjusted precisely.

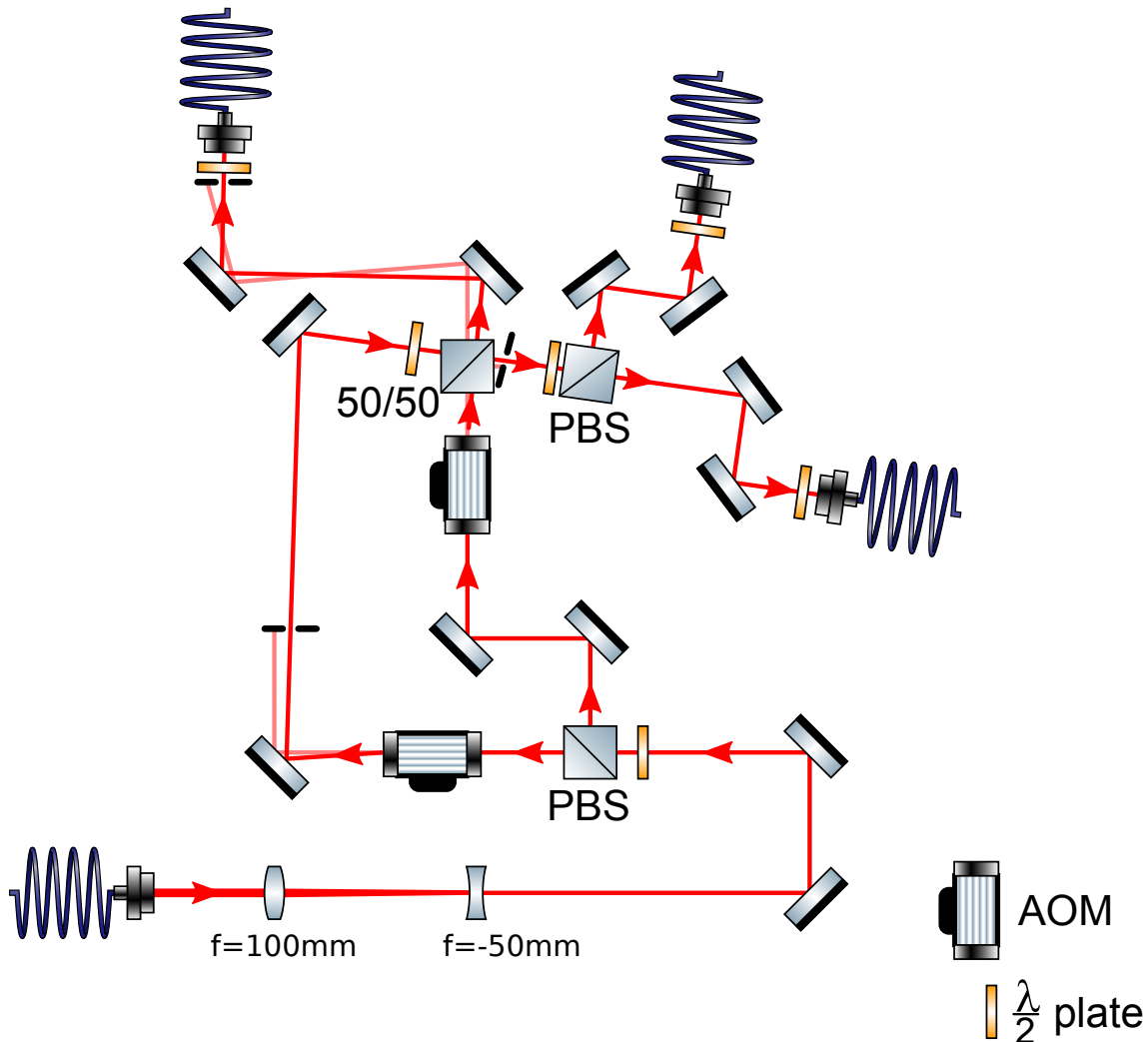


Figure 4.5: Setup to turn one single-frequency laser beam into three separate beams which each consist of two frequencies detuned by $\pm 114\text{ MHz}$ in regard to the original frequency. The shifts are generated using acousto-optic modulators (AOMs). The setup after the AOMs is drawn exaggeratedly tilted to indicate that the AOMs emit these frequency-shifted beams at an angle which has to be compensated down the line to correctly overlap the beams.

The difference of an AOM without (off) and with an applied RF signal (on) is shown in fig. 4.7. Without a driving signal the beam simply passes the AOM with an efficiency of 98(1) %, meaning only a tiny fraction of the laser power is absorbed by the AOM, either by the crystal itself or the AOM's aperture. Once the signal³⁴ is turned on, multiple orders of diffraction are visible. The higher orders with higher frequency are deflected to the right while the lower orders are found to the left of the carrier. This change in direction requires an adjustment of all following optical

³⁴In this case a 114 MHz RF signal with roughly 1 W of power is used to drive the AOM.

elements to correct for the new angle of the beams. This is exaggeratedly depicted in fig. 4.5.

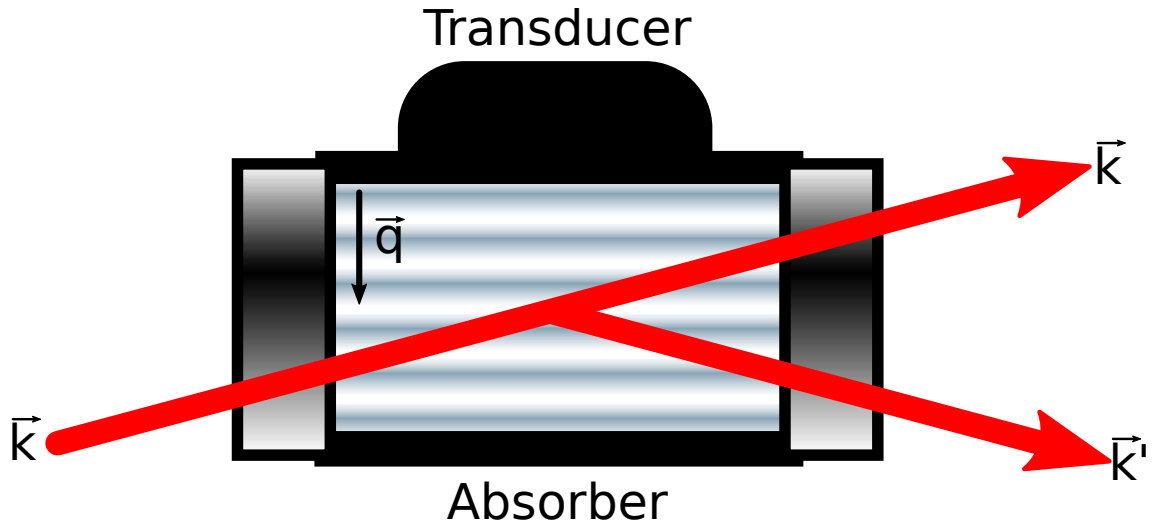


Figure 4.6: Schematic depiction of an acousto-optic modulator. A piezoelectric transducer sends waves of wavenumber $|\vec{q}|$ through a crystal. An absorber on the other side prevents reflection and the formation of standing waves. The phonons \vec{q} can scatter with the incoming laser beam \vec{k} to produce a new beam \vec{k}' with a different direction and frequency. Although only one scattered beam is shown, multiple orders of diffraction are possible.

In this setup, the 1st order contains 73(1) % of the input beam's power operating at 114 MHz and 1 W input RF power. The other AOM is used to produce the -1st order frequency shift and it works with an efficiency of 82(1) %.

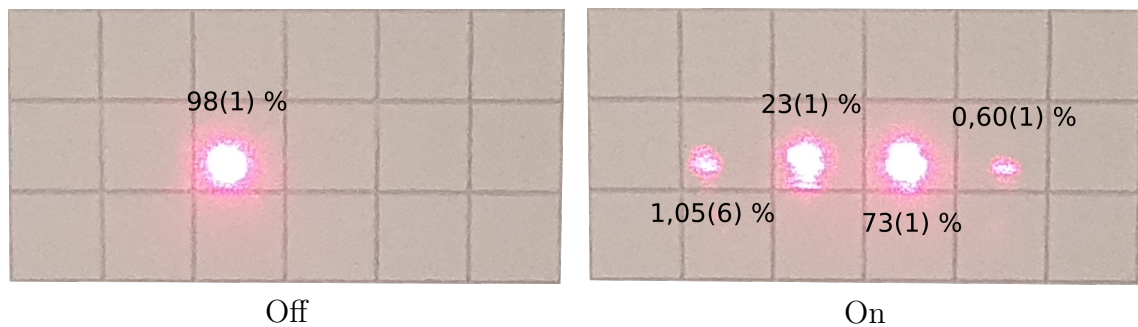


Figure 4.7: A laser beam passes a turned off AOM (left). When an RF signal is applied, the input beam is split into multiple outputs, each frequency-shifted by multiples of the RF frequency f (right). From left to right, these outputs are called the -1st, the zeroth, the 1st, and the 2nd order. The AOM position and rotation is adjusted specifically to maximize the power of the 1st order beam.

Although the absorber should prevent standing waves, areas of higher optical density form anyway. This is shown in fig. 4.8: once the RF signal is turned on, visible, horizontal lines form within the AOM's crystal. The specific form and size of the more opaque area depends on the frequency and amplitude of the driving

RF signal and the AOM itself, i.e. its crystal, its absorber and its piezoelectric transducer. While the incoming laser beam's intensity profile is mostly Gaussian, which is ideal for coupling the beam into single-mode fibers with high efficiency, the dark feature in the AOM crystal blocks a part of the beam and therefore changes the transverse mode of the beam.

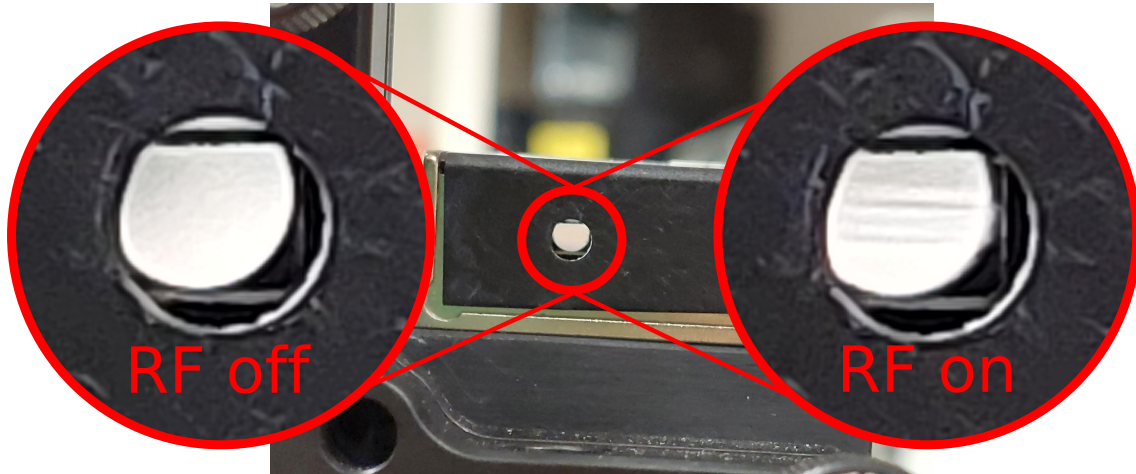


Figure 4.8: Picture of the crystal of an AOM without (left) and with (right) a driving RF signal. Turning on the RF signal creates optically denser areas within the crystal. The passing laser beam is scattered on the created lattice and the subsequent beam profile is not Gaussian anymore.

4.3. A Filled Trap

The results of the following chapter were produced during a supervised master thesis. For an alternative view on the presented data, the reader is advised to take a look at [Fra21].

After it was proven that the atoms could be slowed down to catchable speeds (see section 3.5) using the home-built diode laser amplified by a TA (section 2.1) and the TApr has been stabilized to an appropriate wavelength (section 2.2.4) to generate the trapping laser beams (section 4.2), the lithium oven was heated up and the magnets were turned on. With a loading time of 2.12(2)s (see section 4.4), a bright cloud of fluorescing atoms formed in the main experimental chamber. The MOT is depicted in fig. 4.9: a view through one of the chamber windows reveals a pinkish collection of atoms floating in the center of the setup. The pink light on the edges of the viewport stems from reflections of the multiple laser beams and is not produced by atoms.

The total power of the MOT beam laser (before being split and frequency shifted into a +114 MHz and a -114 MHz part) was measured to be 202(1) mW and it was frequency stabilized to 446.799 657(1) THz. Therefore it is slightly red-shifted (30(1) MHz) to the ${}^6\text{Li}$ D₂ lines. While the lower $F_{\text{gs}} = 1/2$ ground state comprises

two m_F substates, the upper $F_{\text{gs}} = 3/2$ ground state has four. Assuming a totally random distribution and equal transition strengths³⁵, the ratio of atoms resonant to the -114 MHz component to those resonant to $+114$ MHz is 2 to 1. The best result, i.e. the brightest MOT, was achieved for a ratio of 130 mW (lower frequency) to 70 mW (higher frequency) after the first PBS in fig. 4.5 which roughly matches the expectations. Deviations from the 2-to-1 ratio likely stem from different modulation efficiencies of the AOMs and different incoupling efficiencies in the fiber couplers because the beams have different path lengths and different beam profiles when they are guided into the optical fibers, and the shift in transition strength experienced within the inhomogeneous magnetic field.

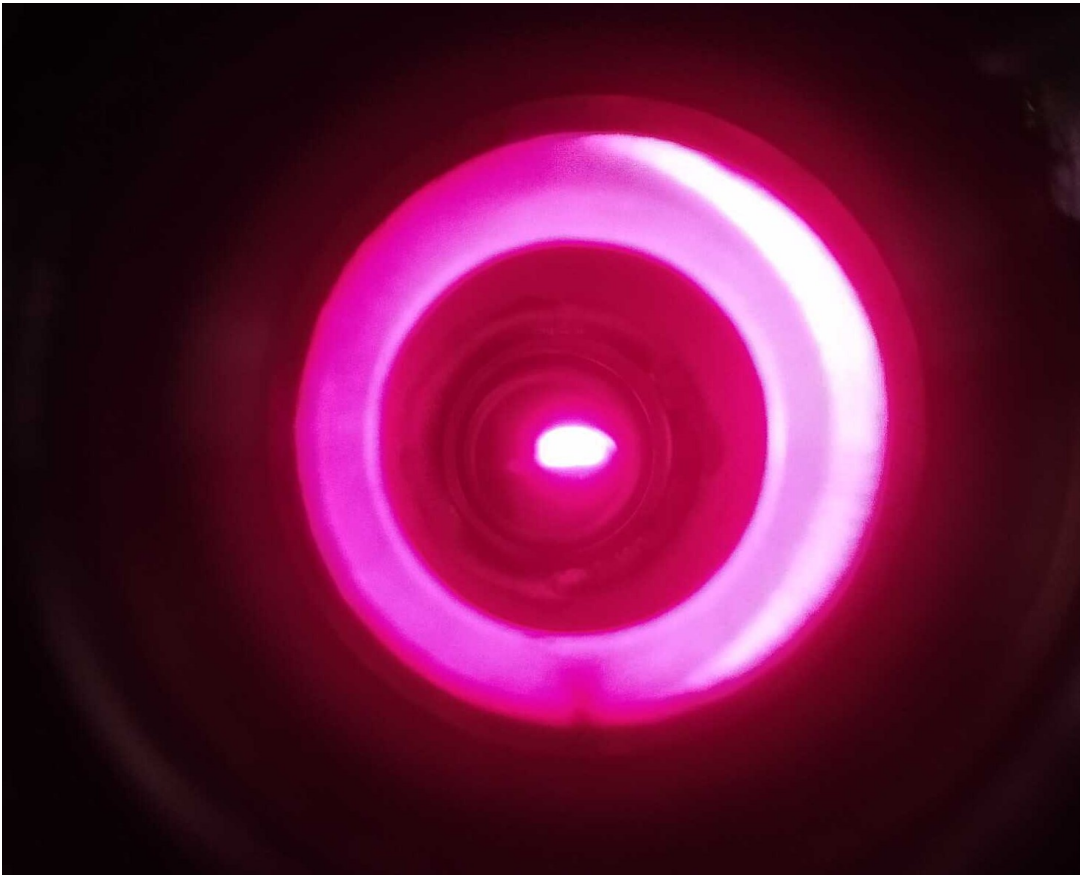


Figure 4.9: Photograph of the view through a window of the experimental chamber. The bright, pink spot in the center is the fluorescence of a cloud of ${}^6\text{Li}$ atoms which is held in this position by the applied trapping beams. The atoms absorb the lasers' photons, are pushed back into the MOT center and deexcite by emitting red-pinkish light. The bright ring is not generated by fluorescence. It is merely the reflection of all the laser beams in the MOT chamber.

Note, that only one frequency combination for the trapping lasers was tested and that the brightest fluorescence doesn't necessarily equates to the "best" possible

³⁵Approximately, this holds true around the MOT center ($B = 0$) as shown in section 3.2.

MOT. A bright MOT corresponds to either many atoms being fast enough to see the trapping beams Doppler shifted to resonance (high temperature) or many atoms being far from the center so that the Zeeman-shift makes them resonant to the lasers (high pressure/ density in the center). Further tests are required to fully analyze the MOT. This was not entirely possible during this thesis as is explained in section 4.5. The Zeeman slower laser has to fulfill two conflicting requirements:

1. the laser has to cool the hot atom beam and therefore its light must be in resonance to a certain transition,
2. the laser mustn't interfere with the already trapped atoms.

In the case of the existing Zeeman slower, which comprises a magnetic field which starts at $B > 0$ and ends in the MOT center at $B = 0$, a compromise between the two requirements is needed. While the previous analysis of the Zeeman slower was conducted at a frequency $\nu_{\text{Zeeman}} = 446.799\,40(3)$ THz, this light unfortunately deformed the MOT and pushed it out of the center of the setup. Therefore, the laser was adjusted to $\nu_{\text{Zeeman}} = 446.799\,33(3)$ THz which is even further detuned than before. The exact slowing efficiency of this setting was not examined. A different Zeeman slower design which also uses negative magnetic field strengths, a so-called spin-flip Zeeman slower, might resolve the issues mentioned above because it can be operated with a more red-shifted laser. The efficacy of such a slower was simulated in [Dau20] but the slower itself has not yet been realized.

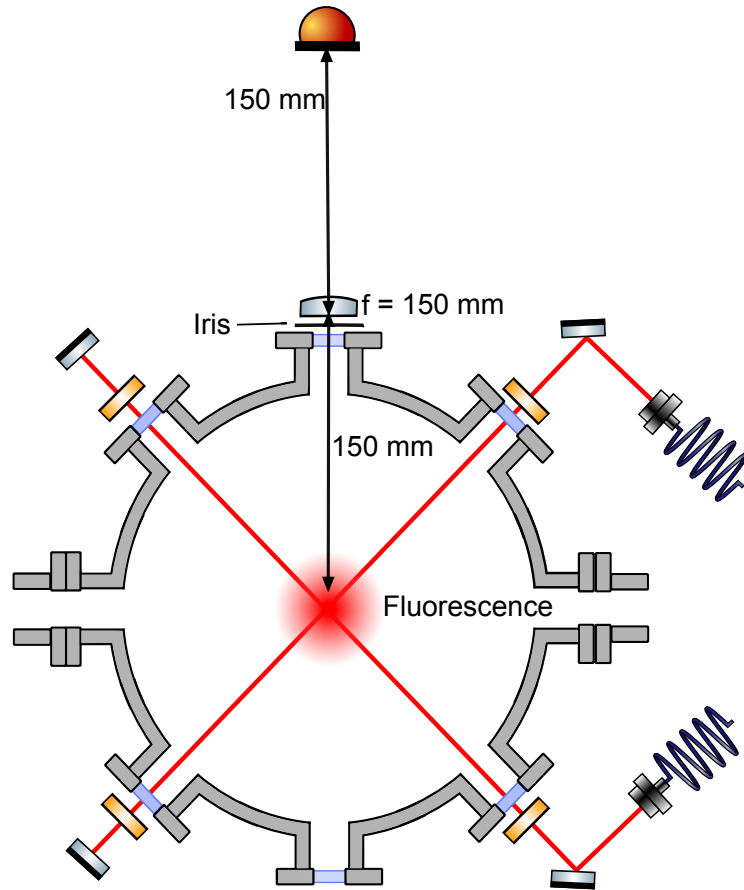
Lastly, the number of atoms within the MOT can be roughly estimated by analyzing its fluorescence. The atoms absorb the light of the applied lasers and deexcite by emitting photons isotropically. By surveying a solid angle and measuring the fluorescence, the total emitted power can be calculated. A simplified setup for this measurement is shown in fig. 4.10.

The MOT as well as the Zeeman slower are operating normally, i.e. all magnets are turned on and all laser beams are applied. It is therefore assumed that the MOT is at maximum capacity and fluorescence at all times. This fluorescence leaves the chamber through a window and is focused by a lens of diameter $d = 3.0(1)$ cm onto a photodiode³⁶. The lens is $D = 15.0(5)$ cm away from the center of the MOT. This setup spans a solid angle of

$$\Omega = 2\pi \left(1 - \sqrt{\frac{D^2}{D^2 + \frac{d^2}{4}}} \right) = 0.031(3), \quad (4.7)$$

which corresponds to 0.25(2) % of the total solid angle of 4π . The light has to pass a vacuum viewport with a transmission coefficient of 92.86(5) %. Therefore, the photodiode sees 0.23(2) % of the total fluorescence.

³⁶Thorlabs DET36A2 [Thod]



quarter wave plate
 diode
 mirror
 fiber coupler
 lens

Figure 4.10: Schematic top view of a setup used to measure the fluorescence of the ${}^6\text{Li}$ MOT. Note that some mirrors and the vertical MOT beams are neglected for reasons of simplification. The atoms captured within the MOT produce isotropic fluorescence. The light of a certain solid angle is projected onto a photodetector to extrapolate the total fluorescence.

The photodiode produces a current I which corresponds to the amount of photons of a certain wavelength that hit its sensor. At the fluorescence wavelength $\lambda = 671 \text{ nm}$, $\epsilon = 0.358 \text{ A/W}$ is expected. The current is supplied by a 12 V battery. Applying a resistor and measuring the voltage U at said resistor allows for a determination of I using Ohm's law. However, the photodiode displays saturation effects for $U \approx 12 \text{ V}$, hence the resistance had to be adjusted to decrease the measured voltage below said value. Applying a total resistance of $R = 2.47 \text{ M}\Omega$ led to $U = 9.82(1) \text{ V}$. Therefore, the photodiode provides $I = 3.976(4) \mu\text{A}$ and sees a power $P = 11.11(1) \text{ nW}$. Thus, the total emitted power is $P_{\text{total}} = 4.8(4) \text{ mW}$. Note that the background light, such as reflections from the lasers or the general lab lighting, has already been taken into account in the determination of U by measuring a base signal without the presence of the MOT and subtracting this base voltage from the

signal measured with the MOT.

The total power of the combined MOT beams (x -, y -, and z -beams; two frequencies each) is $P_0 = 120(1)$ mW. As the Gaussian beams are brought to the setup via polarization maintaining fibers with mode field diameters $D = 4.5(5)$ μm (Thorlabs PM630-HP, [Thoc]) and are collimated using lenses with focal length $f = 50$ mm, the resulting beams have a $1/e^2$ -diameter $2\omega_0$ of

$$2\omega_0 = \frac{4\lambda f}{\pi D} = 9(1) \text{ mm}, \quad (4.8)$$

where ω_0 is the waist of the beam and λ is the wavelength of the laser light. Unfortunately, the beam was too big to be reliably measured with a CCD based beam profiler. The maximum intensity I_0 of the beams is given by

$$I_0 = \frac{2P_0}{\pi\omega_0^2} = 339(75) \frac{\text{mW}}{\text{cm}^2}. \quad (4.9)$$

The scattering rate R_{scatter} is given by

$$R_{\text{scatter}} = \frac{S}{1+S} \frac{\Gamma/2}{1 + \frac{4\delta^2}{\Gamma^2(1+S)}}, \quad (4.10)$$

where $\Gamma = 5.87$ MHz [LWR⁺20] is the natural linewidth and $S = I/I_{\text{sat}}$ is the saturation parameter. For the ${}^6\text{Li}$ D_2 lines, the saturation intensity is $I_{\text{sat}} = 2.54$ mW/cm² [Geh03].

In the following, it is assumed that the MOT is spatially small, i.e. all atoms are in the center of the MOT and therefore experience no magnetic field (and therefore no Zeeman shift) while interacting with the maximum intensity of light I_0 . This assumption is not true. Unfortunately, the exact size of the MOT could not be determined, but from the picture fig. 4.9 it can be expected to be roughly 1 mm in height³⁷. At the edges of the MOT, the magnetic field reaches absolute values of 2.5 mT, which corresponds to a Zeeman shift of ≈ 35 MHz for the transitions of interest. This fully compensates the red-detuning of the MOT laser beams and increases R_{scatter} . Additionally, for the previously determined beam size, the laser beam intensities reduce to 90 % of I_0 , decreasing R_{scatter} for atoms farther away from the center. The total scattering rate would therefore be

$$R_{\text{scatter,total}} = \int_V d\vec{r} \rho(\vec{r}) \frac{S(\vec{r})}{1+S(\vec{r})} \frac{\Gamma/2}{1 + \frac{4\delta^2(\vec{r})}{\Gamma^2(1+S(\vec{r}))}}, \quad (4.11)$$

³⁷By comparing the size of the window in the front and the one in the back (both being DN40 windows with a 38 mm aperture), assuming the MOT to be approximately in the middle between the windows, and using the intercept theorem this value can be estimated with the help of a simple ruler.

i.e. the integral of all scattering rates over the density distribution $\rho(\vec{r})$ of the MOT. As mentioned before, $\rho(\vec{r})$ could not be determined. Therefore, the following results should only be regarded as a rough order of magnitude estimation of the number of ${}^6\text{Li}$ atoms inside the MOT.

With a detuning of $\delta = 30(1)$ MHz the approximate scattering rate (eq. (4.10)) becomes $R_{\text{scatter}} = 1.6(2)$ MHz. By multiplying the amount of scatter events with the energy of a photon of frequency $\nu \approx 446.8$ THz the emitted energy per atom can be calculated and compared to the total measured energy P_{total} . Thus, the amount of atoms in the MOT can be estimated to

$$N = \frac{P_{\text{total}}}{R_{\text{scatter}} h \nu} = (10 \pm 1) \cdot 10^9, \quad (4.12)$$

with h being the Planck constant. This value is 1 to 2 orders of magnitude above those of other ${}^6\text{Li}$ MOTs (10^8 in [LWR⁺20], $6 \cdot 10^8$ in [LZG⁺15]).

4.4. Loading and Unloading the MOT

The results of the following chapter were produced during a supervised master thesis. For an alternative view on the presented data, the reader is advised to take a look at [Fra21].

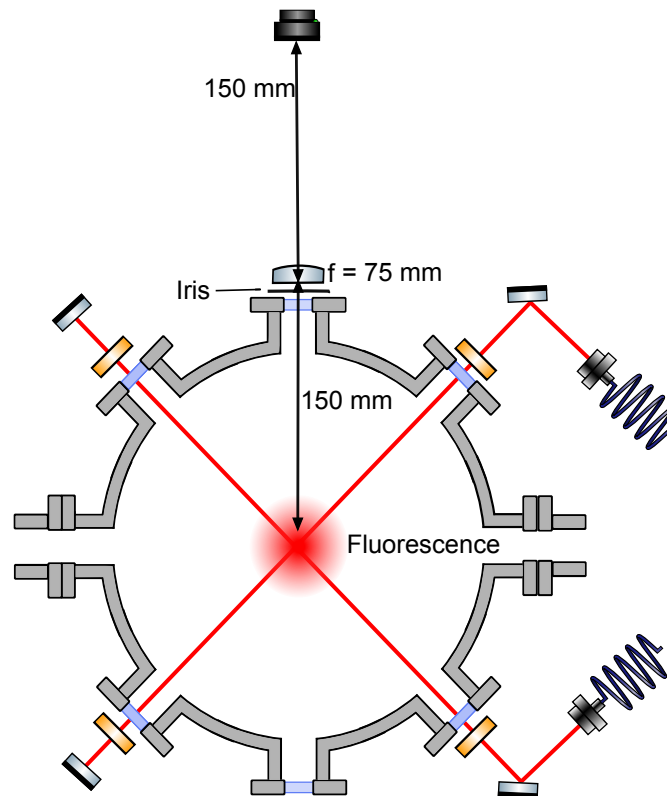
Ultimately, the MOT will serve as a cold and dense sample for high-precision laser spectroscopy of ${}^6\text{Li}$. Ideally, the measurement is completely automated:

1. the MOT's and the Zeeman slower's magnetic field and their lasers are turned on and the valve which blocks the atom beam (see element 3 in fig. 3.9) is opened,
2. while the MOT is loading up, the spectroscopy laser is tuned to the frequency which is to be probed next,
3. at maximum MOT intensity, the valve is closed again, the magnetic field and the trapping beams are turned off, and the spectroscopy laser is unblocked,
4. the fluorescence is measured and the process starts again.

The first step is easily implemented using numerous digital controllers for power supplies, beam blockers and the valve. The second step comprises waiting for the MOT to be filled, while the third step has to happen within a certain time window. The loading and unloading times, t_{loading} and $t_{\text{unloading}}$, are examined in this section. This is done by using a CCD camera³⁸ and placing it in the setup, as depicted in fig. 4.11. This setup differs from the one shown in fig. 4.10 by a lens of shorter focal length, i.e. $f = 75$ mm instead of $f = 150$ mm, and the camera [Vis22] in place of

³⁸The camera used is a Guppy F-038B by Allied Vision.

a simple photodetector. The new lens allows for a 1-to-1 image of the MOT on the camera.



 quarter wave plate
  camera
  mirror
  fiber coupler
  lens

Figure 4.11: Schematic top view of a setup used to measure the loading and unloading process of a MOT. Note that some mirrors and the vertical MOT beams are neglected for reasons of simplification. The atoms captured within the MOT produce isotropic fluorescence. A lens then produces a 1-to-1 image of this fluorescence on a CCD camera.

The camera has a rasterized sensor with 768 pixels in width (x) and 492 pixels in height (y). Each pixel covers an area ($x \times y$) of $8.4 \mu\text{m} \times 9.8 \mu\text{m}$. An exemplary picture is shown in fig. 4.12. It represents the exposure of the camera's CCD chip. This integer value is roughly proportional to the number of photons that hit the specific pixel. The camera produces a digital output, i.e. each pixel can return a value between 0 ($2^0 - 1$, no absorption) and 255 ($2^8 - 1$, pixel saturated). The exposure is not only depending on the intensity of the captured light but also the exposure time t_{exp} . The pixels collect the energy of the incoming photons for the duration t_{exp} and afterwards they return a corresponding value. It is therefore important to set t_{exp} in such a way that no pixel returns 255, to exclude oversaturation. Another striking feature is the seeming presence of two illuminated areas. This is due to the camera's readout being interlaced. Only the upper halves of this and other pictures are used for analysis.

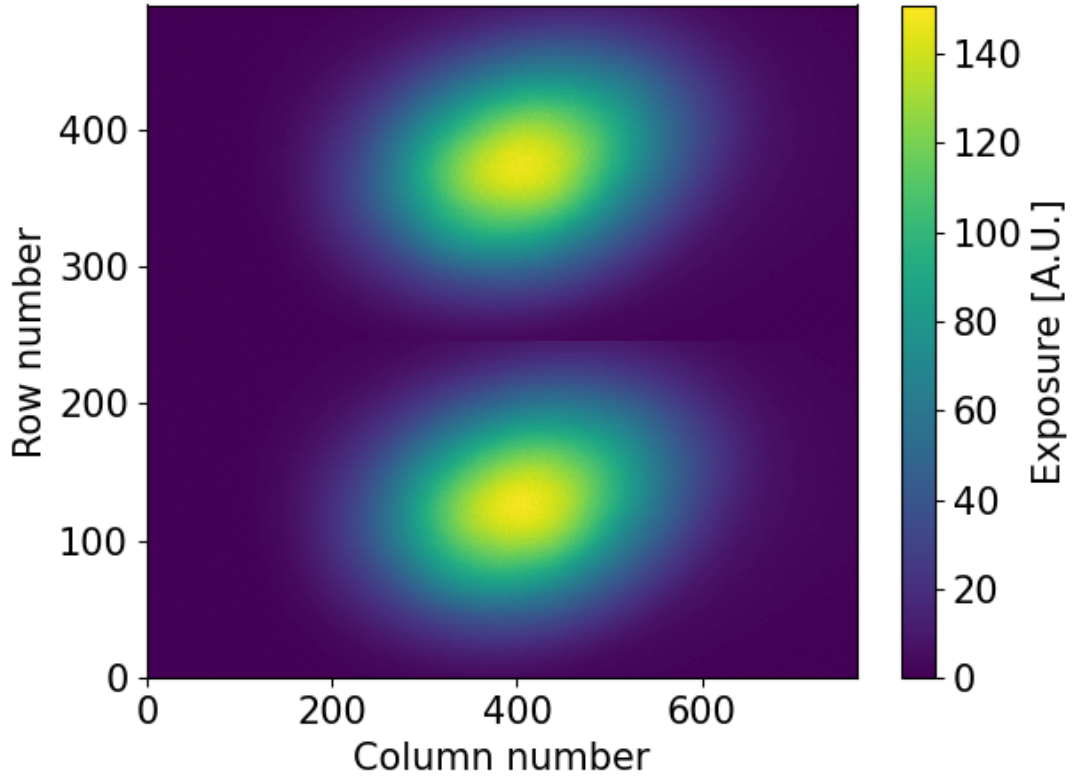


Figure 4.12: An exemplary 1-to-1 image of the MOT fluorescence recorded by a CCD camera.

A 2D Gaussian function f which includes a constant offset f_0 was fitted to the data. By then calculating the integral of the Gaussian part, the level of luminescence was determined. The used fit function is given by

$$f(x, y) = f_0 + A \cdot e^{-a(x-x_0)^2 - 2b(x-x_0)(y-y_0) - c(y-y_0)^2}$$

with

$$a = \frac{\cos^2(\theta)}{2\sigma_x^2} + \frac{\sin^2(\theta)}{2\sigma_y^2}, \quad (4.13)$$

$$b = -\frac{\sin(2\theta)}{4\sigma_x^2} + \frac{\sin(2\theta)}{4\sigma_y^2},$$

$$c = \frac{\sin^2(\theta)}{2\sigma_x^2} + \frac{\cos^2(\theta)}{2\sigma_y^2},$$

where the amplitude A , the position of the maximum (x_0, y_0) , the standard deviations $\sigma_{x/y}$, and the rotation angle θ are additional fit parameters. The integral can thus be calculated using

$$I(A, \sigma_x, \sigma_y, \theta) = 8 A \pi \sqrt{\frac{2 \sigma_x^4 \sigma_y^4}{\sigma_x^4 + 30 \sigma_x^2 \sigma_y^2 + \sigma_y^4 - (\sigma_x^2 - \sigma_y^2)^2 \cos(8\theta)}}. \quad (4.14)$$

The pixels return integer values E (for exposure) that correspond to the number of photons that each pixel is hit by. It is therefore logical (and a conservative estimation) to assume the error ΔE to be the same as the error in a stochastic counting experiment: $\Delta E = \sqrt{E}$. Many pixels will have to return a value of $E = 0$. To avoid division by zero, the error of these pixels is set to $\Delta E = 1$. An exemplary fit using the same measurement shown above is depicted in fig. 4.13.

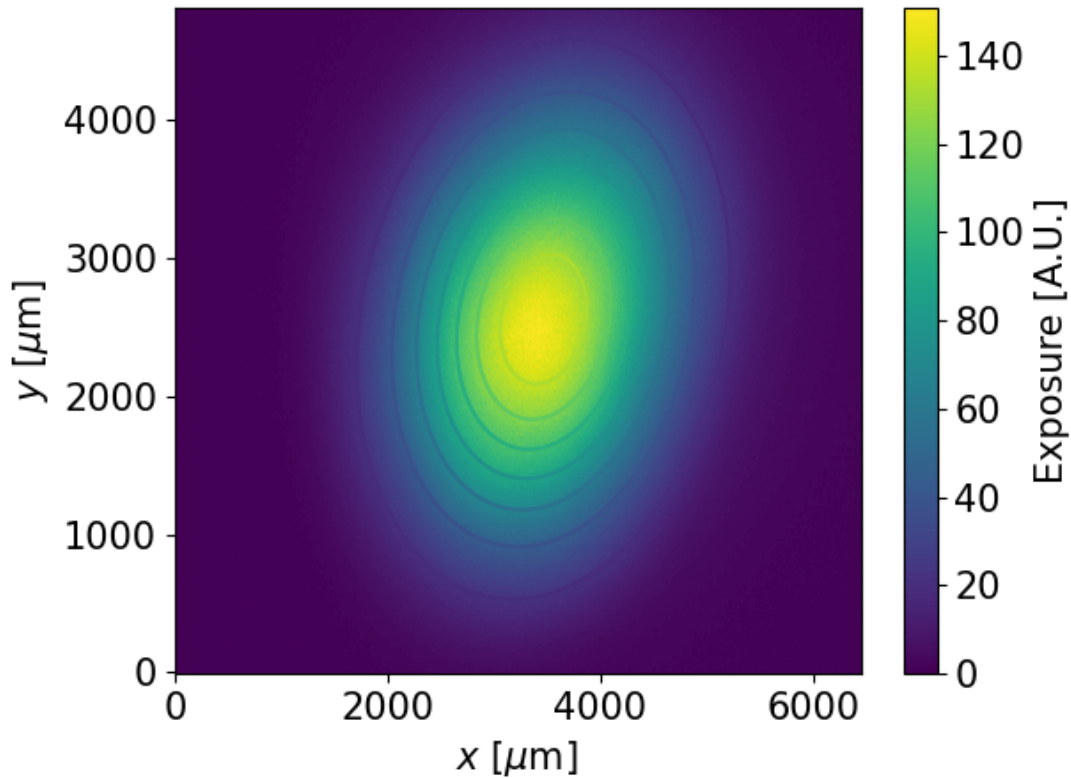


Figure 4.13: Two-dimensional Gaussian fit of the measurement shown in fig. 4.12. Note that x - and y -axis are scaled differently.

With 188920 degrees of freedom, the function above results in a $\chi^2 \approx 58297.4$. This value is unusually small which most often stems from overestimating the errors. To compensate for this, all errors were multiplied with the square root of the reduced chi-square $\sqrt{\chi_{\text{red}}^2}$ and the fit was redone. Consequentially, this resulted in $\chi_{\text{red}}^2 = 1$. The corresponding parameters as well as their errors are listed in table 4.3. The according integral is $I = 818(40) \cdot 10^6$.

By analyzing many more of these pictures in the presented way, the loading and the loss curves, i.e. the increasing exposure when the MOT is being filled and the decreasing exposure when the MOT's supply with new atoms is stopped, can be measured.

Table 4.3: Fit parameters of the exemplary exposure measurement.

A	155.80(6)	
x_0	3464.3(2)	μm
y_0	2554.4(3)	μm
σ_x	821.3(2)	μm
σ_y	1024.1(2)	μm
θ	24.65(4)	$^\circ$
f_0	0.638(3)	$^\circ$

4.4.1. The Loading Curve

When all laser, i.e. the MOT's cooling and repumping lasers as well as the Zeeman slower laser, and the MOT and Zeeman slower magnets are turned on and the valves blocking the hot atom beam is opened up, the MOT starts capturing atoms and shining brighter and brighter over time.

In first order, the flow of atoms reaching and being captured by the MOT is constant. As more atoms are captured, the MOT grows in size because more atoms equate to higher densities and higher pressures within the MOT. This is compensated by moving atoms to the edges of the MOT until this pressure equals the pressure applied by the laser beams. This increase in size is not only governed by the atom-atom collisions inside the MOT but in the case of ^6Li also by the fact, that fermions repel each other due to Pauli's exclusion principle. The MOT will grow so large that atoms on the outer edges aren't resonant to the applied laser light and thus cannot be trapped anymore.

Assuming the growth rate α to be constant and the loss rate to be dependent on the MOT's volume, the equation governing the number of atoms N inside the MOT can be inferred to be

$$\dot{N} = \alpha - \beta N, \quad (4.15)$$

with the loss parameter β . Higher-order loss mechanisms, such as two- or even three-body collisions, are not taken into account. This would add N^2 and N^3 dependencies to the above differential equation.

As the volume V of the MOT is proportional to N , a similar equation describes the behaviour of V . The emitted light is also assumed to be proportional to N , i.e. each atom deexcites by emitting a photon which is not absorbed by another atom. Consequently, the MOT's fluorence over time $F(t)$ is a direct measurement of its V or N . It is given by

$$F(t) = \begin{cases} 0 & t < 0, \\ F_{\text{max}} \cdot \left(1 - e^{-\frac{t}{\tau}}\right) & t \geq 0. \end{cases} \quad (4.16)$$

This solution assumes that the MOT is empty until at $t = 0$ the valve opens and atoms reach the MOT. The parameters α and β are incorporated into the rise time

parameter τ . From this value, the time $t_{99\%}$ which it takes the MOT to be filled by 99 % can be calculated using

$$t_{99\%} = \tau \cdot \ln \left(\frac{1}{1 - 0.99} \right). \quad (4.17)$$

The function which was used to fit the data shown in fig. 4.14 differs slightly from eq. (4.16):

$$f(t) = F_{\max} \cdot \left(1 - e^{-\frac{t-t_0}{\tau}} \right). \quad (4.18)$$

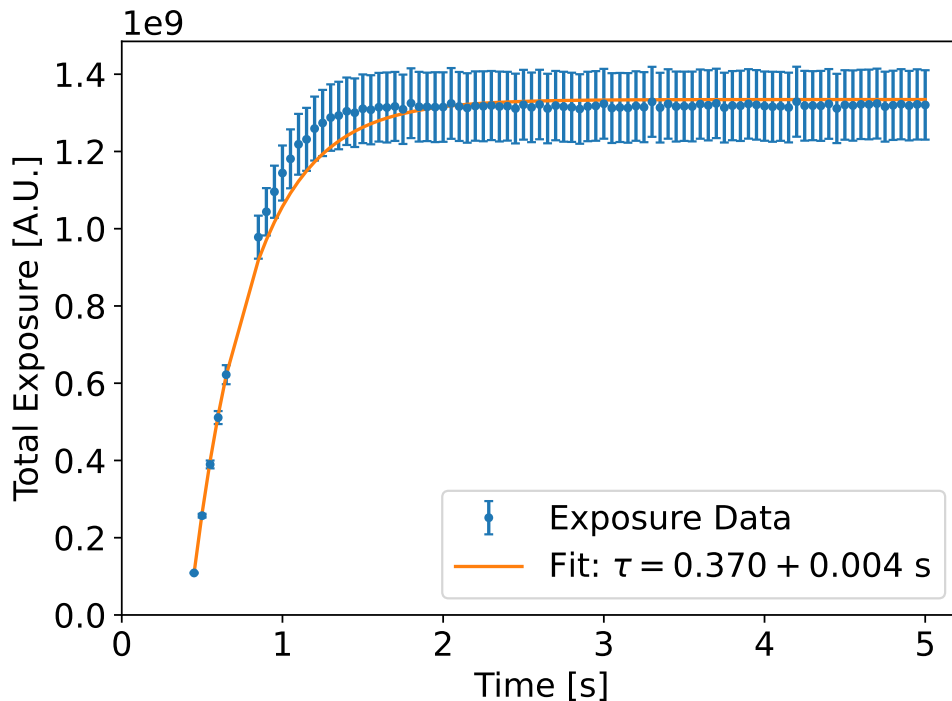


Figure 4.14: Data and fit of cumulative exposure over time. As the MOT is filled it becomes brighter until it cannot capture any more atoms. With 85 degrees of freedom the fit results in $\chi^2 = 18.7$.

Obviously, the function is not partially defined anymore. The measurement only starts after the valve has been opened, a constant part for $t < 0$ is not necessary. The second difference is the time offset t_0 . The exact start time of the measurement is unknown. The controlling software starts the measurement by sending a signal to open up the valve and allow the hot atoms to reach the MOT. Then, the camera is triggered every 50 ms. It takes a picture after an exposure time of 100 μ s which is then read out. A first fit contained a constant offset f_0 but it showed to be completely negligible and so it was dropped to reduce the number of fit parameters and thus increase the number of degrees of freedom to 85.

The fit procedure results are shown in table 4.4. Some data points seem to be missing. The fluorescences for times $t < 0.45$ s was too small for the fit algorithm to find a

stable solution. For $0.65 \text{ s} < t < 0.85 \text{ s}$, the data was unfortunately corrupted and could not be used. The corresponding χ^2 is $\chi^2 = 18.7$ and $t_{99\%} = 1.70(2) \text{ s}$. Adding the time between the opening signal of the valve and the beginning of the fluorescence t_0 the total time until the MOT is maximally filled becomes $T = t_{99\%} + t_0 = 2.12(2) \text{ s}$.

Table 4.4: Optimal parameters for fit shown in fig. 4.14. The individual errors were extracted from the fit algorithm.

F_{max}	1334(5)	$\cdot 10^6$
τ	370(4)	ms
t_0	418.7(4)	ms

It thus takes about 2.1 s to completely fill the MOT and create maximum fluorescence. After this period, the MOT can be used for spectroscopy.

4.4.2. The Loss Curve

As long as the MOT is being supplied with new cold atoms, it keeps its brightness. But once the respective valve closes, no more atoms reach the MOT and over time all the captured atoms are lost. As already explained in section 4.4, pictures of the MOT are taken by a CCD camera which are then analyzed by fitting a 2D Gaussian distribution to them. Plotting the resulting integrals over time reflect the darkening of the MOT. In contrast to the loading curve shown in fig. 4.14, the data was taken using pictures with ever increasing exposure times τ_i . To account for this, the calculated exposures are divided by their respective τ_i .

After the correction, the loss curve can be draw, as depicted in fig. 4.15. Although the decline in brightness seems to follow a simple exponential decay function, this is not the case. Especially the data points for low times t drop too sharply to be adequately described by a function, that must also fit the tail for higher t . A more complex loss mechanism was therefore assumed:

$$\dot{N} = -\frac{N}{\tau} - \beta N^2. \quad (4.19)$$

In addition to the regular linear loss with its lifetime τ , a quadratic effect governed by the value of β is taken into account³⁹. While the equation's linear part describes the MOT's interaction with the background gas, the N^2 part stems from atom-atom interactions [PRP⁺88].

³⁹A longer time frame, lower total exposure, and the absence of a loading atom beam make this higher-order loss effect more prominent.

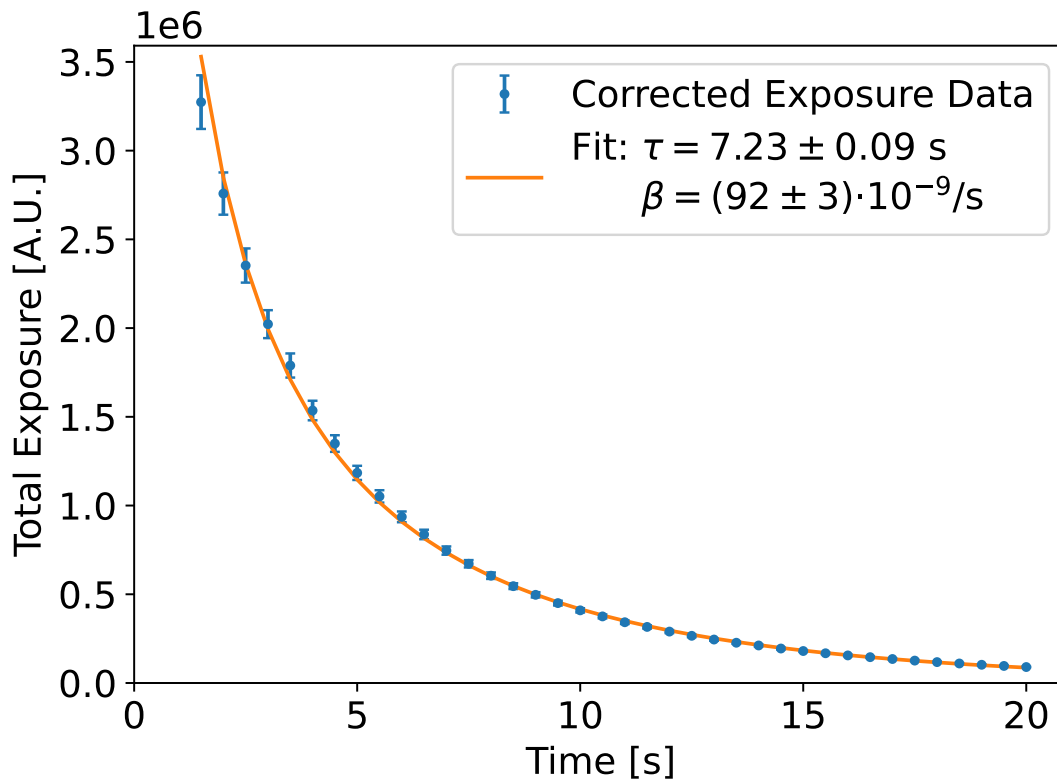


Figure 4.15: Corrected data and fit of cumulative exposure over time. As the MOT is depleting, it becomes darker and darker. With 34 degrees of freedom the fit results in $\chi^2 = 20.9$.

Assuming an internal time delay t_0 between the starting signal of the experimental procedure and the start of the MOT depletion, i.e. $N(t_0) = N_0$, as was done in section 4.4.1, a function solving this equation is

$$N(t) = N_0 \frac{e^{-\frac{t-t_0}{\tau}}}{1 + N_0 \beta \tau (1 - e^{-\frac{t-t_0}{\tau}})} \quad (4.20)$$

A similar function $f(t)$, in which N_0 was changed to F_0 , was used to fit the data depicted in fig. 4.15 but without the time offset. The resulting t_0 was highly dependent on its start value while exhibiting uncertainties many orders of magnitude larger than its actual value. Additionally, the inclusion of t_0 did not affect the outcome of the other parameters to a significant level. Therefore, it was omitted. These resulting parameters are listed in table 4.5. With 34 degrees of freedom, $\chi^2 = 20.9$.

Table 4.5: Optimal parameters for fit shown in fig. 4.15. The individual errors were extracted from the fit algorithm.

F_0	9.4(7)	$\cdot 10^6$
τ	7.23(9)	s
β	92(3)	$\cdot 10^{-9}/\text{s}$

Calculating a fall time $t_{1\%}$, i.e. the time until the MOT's brightness falls to 1% of its maximum value, is not as straightforward as calculating $t_{99\%}$ in section 4.4.1, because $t_{1\%}$ depends on F_0 :

$$t_{1\%} = \tau \ln \left(\frac{100 + F_0 \beta \tau}{1 + F_0 \beta \tau} \right). \quad (4.21)$$

A brighter MOT with larger F_0 therefore loses its relative brightness much faster than a darker MOT. For the shown values, the fall time was evaluated to be $t_{1\%} = 19.4(5)$ s. Spectroscopy on the MOT should be done when it exhibits maximum brightness, i.e. it's containing the maximum amount of ${}^6\text{Li}$ atoms. This means that after stopping the loading process, the spectroscopy procedure, be it fluorescence or absorption spectroscopy, should start as quickly as possible.

4.5. MOT Temperature

The following chapter covers the actual end goal of this thesis: the characterization of the MOT, its size and its temperature. Unfortunately, this was not possible during this work due to problems with the quenching of the magnetic field (see section 4.5.1). This section is therefore rather theoretical. Nonetheless, it might contain useful information for future progress on the experiment.

MOTs usually capture up to 10^{10} atoms (in this case $10(1) \cdot 10^9$, see section 4.3) and cool them down to temperatures in the order of the Doppler temperature [Foo05]

$$T_D = \frac{\hbar \Gamma}{2k_B}, \quad (4.22)$$

where \hbar is the reduced planck constant, Γ is the width of the chosen cooling transition (here $\Gamma = 2\pi \cdot 5.9$ MHz), k_B is the Boltzmann constant. For ${}^6\text{Li}$ and the chosen D_2 transitions, this limit is $T_D = 141$ μK . Standard Sisyphus cooling [DCT89], which could lead to temperatures down to the recoil limit of $T_r = 7.06$ μK , does not work for the D_2 lines because their respective excited states cannot be resolved [DHH⁺11, HKJ⁺14]. Therefore, typical temperatures for ${}^6\text{Li}$ MOTs which use these transitions, lie slightly below 300 μK [SEZ⁺98, Ger16].

The temperature can be measured by first preparing the MOT and then turning it off completely, i.e. stopping the trapping laser beams, ramping down the magnetic field, and closing the valve to stop the flow of hot atoms. Without the lasers and the B -field holding the atoms in space, they start to fall down while the MOT cloud expands. The hotter it is, the faster it spreads. After waiting and letting the cloud expand for a duration Δt , a collimated, low-intensity, resonant laser beam is shot through the cloud and onto a camera. Due to the absence of the trapping magnetic field, all atoms can absorb the light of the laser beam and the camera therefore sees the "shadow" of the atom cloud. This way, the cloud's size, i.e. its spatial size as

well as the amount of atoms it contains, can be deduced. Of course, the laser beam destroys the cloud and another MOT has to be prepared to redo this measurement procedure for a different Δt .

For each duration Δt , three measurements are done:

- a regular absorption measurement as described above,
- a measurement without a MOT to examine the intensity distribution of the laser beam and how the experimental setup itself absorbs it,
- a measurement with neither the MOT nor the laser beam to take any background light into account.

As an example, fig. 4.16 depicts the results for such measurements but for a rubidium ^{87}Rb MOT instead of the ^6Li MOT built during this thesis. The data was generously provided by M. Langbecker and Prof. Windpassinger. The difference between fig. 4.16a and fig. 4.16b is the presence or absence of the MOT, respectively. Both pictures show circular diffraction patterns, presumably from dust particles that stick to the mirrors, windows, or camera in the setup. The presence of the MOT leads to a reduction of the signal measured by the camera, visible as a darker spot on the left side of the picture. Lastly, fig. 4.16c contains information on the background light. An almost uniform signal across the whole picture reveals an almost uniform background. Only a larger variation on the lower edge of the picture stands out. In the following, p_{abso} , p_{ref} , p_{bkg} describe the signal measured by the camera, either pixel-wise or the complete signal, depending on the context.

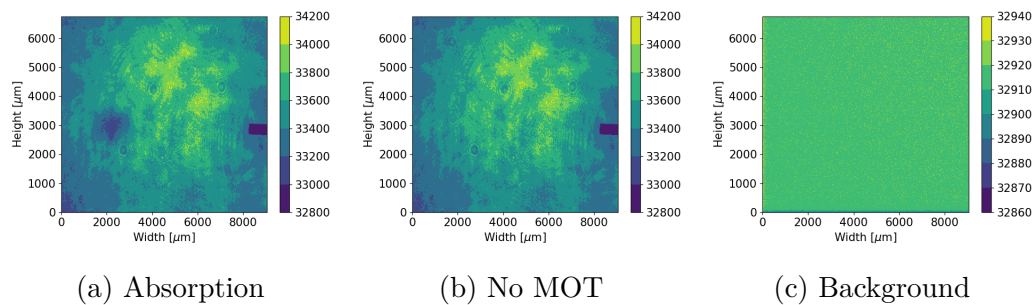


Figure 4.16: Exemplary measurement triplet for a shared wait time Δt . A laser passes an experimental setup which contains **(a)** a rubidium MOT (visible as a dark spot on the left side of the picture) or **(b)** no MOT. Then the light illuminates the sensor of a CCD camera. Picture **(c)** depicts a background measurement with neither a MOT nor the laser being present.

When radiation, such as the light of a laser, passes an absorbing medium, it loses some of its initial intensity I_0 according to Beer's law:

$$I(d) = I_0 e^{-\epsilon^* c d}. \quad (4.23)$$

After passing a depth d of a medium of concentration c which has an extinction coefficient ϵ^* only the intensity $I(d)$ is left. The light then hits a pixel of the camera which returns a signal of strength p . After correcting for the background signal by subtracting p_{bkg} from both p_{abso} and p_{ref} , the only difference in

$$p_{\text{abso, corr}} = p_{\text{abso}} - p_{\text{bkg}} \quad (4.24)$$

and

$$p_{\text{ref, corr}} = p_{\text{ref}} - p_{\text{bkg}} \quad (4.25)$$

is the difference in the composition of the medium that the light needed to pass through. Assuming a negligible effect of the vacuum inside the setup, the following proportionalities can be given:

$$p_{\text{abso, corr}} \propto I_0 e^{-\epsilon_{\text{Setup}}^* c_{\text{Setup}} d_{\text{Setup}}} e^{-\epsilon_{\text{MOT}}^* c_{\text{MOT}} d_{\text{MOT}}}, \quad (4.26)$$

$$p_{\text{abso, corr}} \propto I_0 e^{-\epsilon_{\text{Setup}}^* c_{\text{Setup}} d_{\text{Setup}}}. \quad (4.27)$$

As explained before, the only difference of interest is the presence of the MOT and it's obvious that its parameters can be extracted by dividing these expressions and taking the logarithm of the result:

$$\rho := \epsilon_{\text{MOT}}^* c_{\text{MOT}} d_{\text{MOT}} = -\ln \left(\frac{p_{\text{abso}} - p_{\text{bkg}}}{p_{\text{ref}} - p_{\text{bkg}} + t} \right). \quad (4.28)$$

For computing purposes, a small threshold parameter t was included to prevent division by 0. The optical density ρ for the above shown measurements is depicted in fig. 4.17, as a zoom-in on the region of interest. The signal strengths represented by p_{abso} , p_{ref} , and p_{bkg} are proportional to the number of photons that reach the pixel, therefore their respective errors are estimated conservatively by their square root $\Delta p = \sqrt{p}$. As a result, the error of the optical density is

$$\Delta \rho = \sqrt{\frac{p_{\text{abso}} + p_{\text{bkg}}}{(p_{\text{abso}} - p_{\text{bkg}})^2 + t} + \frac{p_{\text{ref}} + p_{\text{bkg}}}{(p_{\text{ref}} - p_{\text{bkg}})^2 + t}}, \quad (4.29)$$

which again includes a tiny threshold t to avoid division by 0.

Also shown in fig. 4.17 is a fit of a two-dimensional normal distribution as defined in eq. (4.13). For this and subsequently shown fits, the angle θ was assumed to be $\theta = 0$. In reality, θ should be adjusted but kept constant for all Δt .

With 98993 degrees of freedom, the fit procedure produces $\chi^2 = 67348$. The fit parameters and their respective errors are listed in table 4.6. By calculating the surface integral of the function, it's possible to gain insight on the amount of atoms within the cloud:

$$\int_A \rho dx dy = \epsilon_{\text{MOT}}^* \cdot N. \quad (4.30)$$

If the probability of an atom absorbing a photon ϵ^* is known, N can be computed easily.

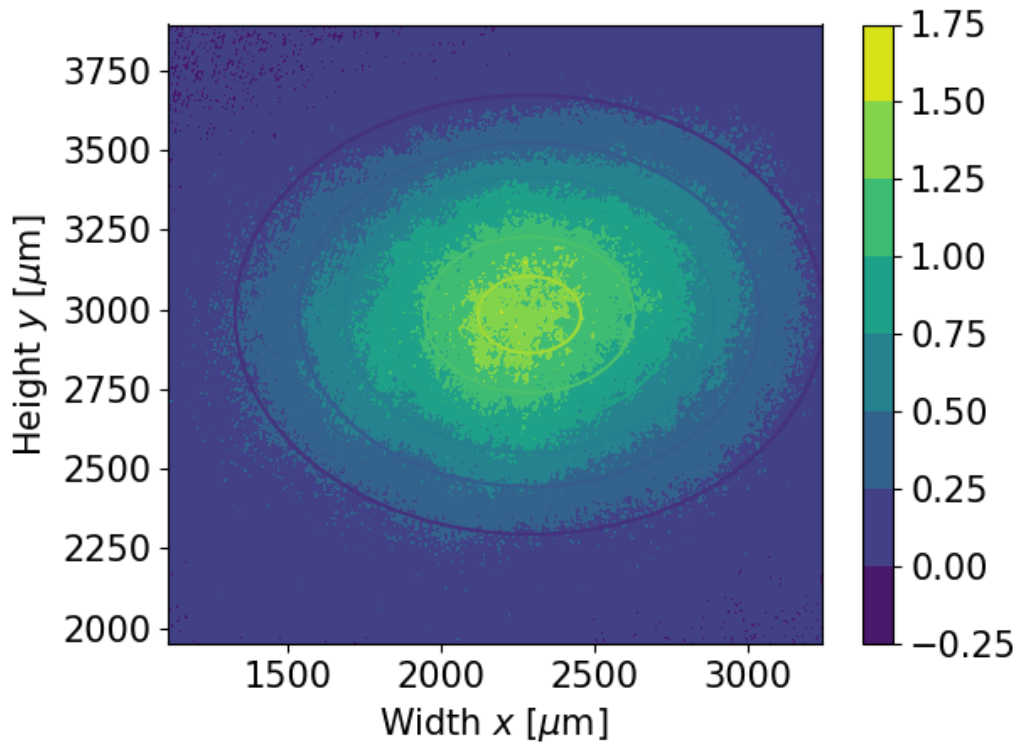


Figure 4.17: Zoom-in on MOT region as seen in fig. 4.16a. The data has been cleaned up by subtracting the general background and comparing it to a measurement without a MOT. This produced the optical density of the trap. Additionally, a 2D normal distribution which was fitted to this data is also depicted.

Table 4.6: Fit parameters of two-dimensional normal distribution as shown in fig. 4.17.

A	1.250(1)
x_0	2287.8(4) μm
y_0	2983.2(3) μm
σ_x	486.2(5) μm
σ_y	348.2(4) μm
f_0	0.0229(5)

This procedure can be done for multiple Δt . The extracted widths σ_x and σ_y are shown in fig. 4.18. The data points for both widths were fitted independently using

$$f(\Delta t) = \sqrt{v^2 \Delta t^2 + \sigma_0^2} \quad (4.31)$$

as a fit function which describes the expansion of a thermal gas in a vacuum [GOSDD98, VWB⁺05]. The parameters v and σ_0 can be interpreted as the root mean square velocity in one specific dimension and the width of the MOT in said dimension, respectively. Their values including errors are listed in table 4.7.

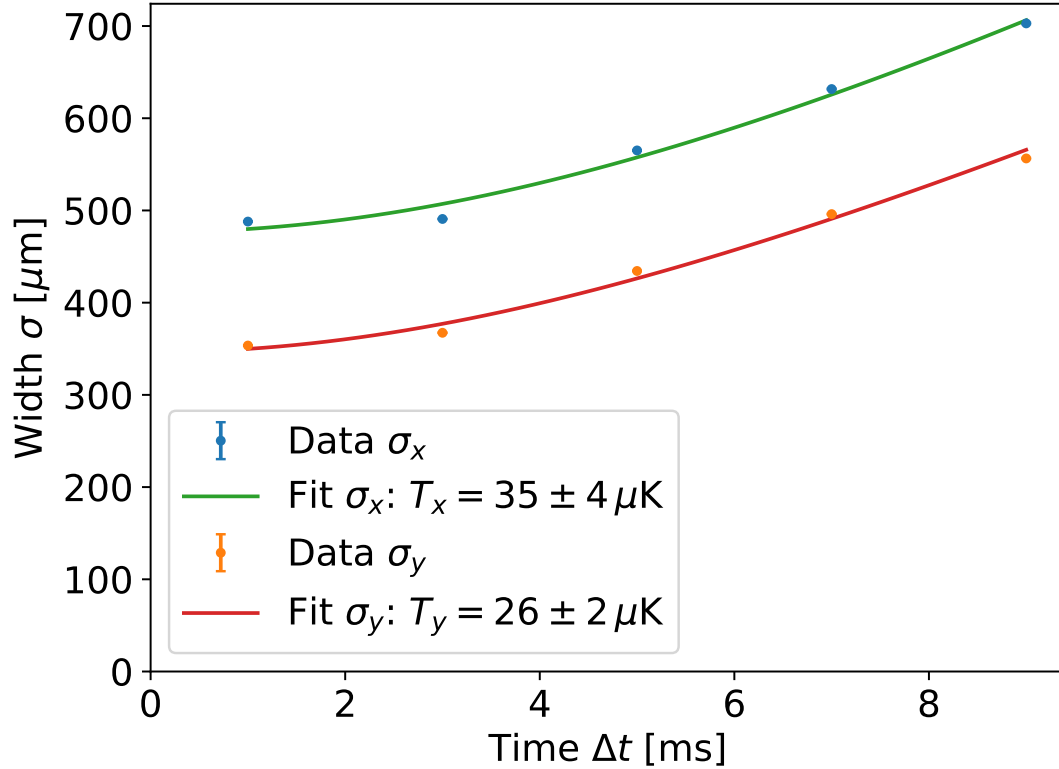


Figure 4.18: Expansion of an exemplary thermal ^{87}Rb cloud in a vacuum over time. Only the size in x - and y -direction are shown, as z describes the direction of the spectroscopy laser and therefore couldn't be examined. The cloud was created using a MOT and is not uniform. This led to different transverse temperatures T_x and T_y . The total temperature T most probably lies within the same order of magnitude.

Table 4.7: Parameters including error of fit functions as depicted in fig. 4.18.

	x -Direction	y -Direction
v [mm/s]	58(3)	50(2)
σ_0 [μm]	476(8)	346(5)

The MOT cloud is assumed to be thermal. The velocity distribution of the ^{87}Rb atoms follows the Maxwell-Boltzmann distribution. The MOT is also nonuniform in its size and its expansion, i.e. its projection on the x - y -plane is not circular but oval and σ_x grows faster than σ_y ($v_x > v_y$). Both dimensions are therefore analyzed

independently and two transverse temperatures T_x and T_y can be extracted from the data using

$$v = \sqrt{\frac{k_B T}{m}}, \quad (4.32)$$

where m is the atom mass. The fits shown in fig. 4.18 return $T_x = 35(4) \mu\text{K}$ and $T_y = 25(2) \mu\text{K}$. The transverse temperature in the direction of the spectroscopy beam T_z is assumed to be in the same order of magnitude but could not be measured using this procedure. The Doppler broadening

$$\Gamma_{\text{Doppler}} = \sqrt{\frac{8 \ln(2) k_B T_z}{m c^2}} \nu \quad (4.33)$$

for ^{87}Rb at the frequency of the D lines ($\nu \approx 384 \text{ THz}$) and $T_z = 30 \mu\text{K}$ would be $\Gamma \approx 162 \text{ kHz}$, which is well below the transition's natural line width (36 MHz or 38 MHz depending on the exact transition [Ste23]). To really determine T_z the measurement procedure could be repeated but with the spectroscopy beam coming from a different direction.

Up until now, this section has been largely an introduction on how to conduct a future analysis on the ^6Li (or a possible ^7Li) MOT. The problems with the current ^6Li MOT setup which prevented this analysis are explained in the following.

4.5.1. The Problem with the ^6Li MOT

As explained previously, a ^6Li MOT reaches typical temperatures of $T \approx 300 \mu\text{K}$, with the Doppler limit being the minimum. The corresponding Doppler broadening is $\Gamma_{\text{Doppler}} \approx 2.26 \text{ MHz}$ which is still below the natural linewidth of $\Gamma = 5.9 \text{ MHz}$. A well-tuned laser could therefore be absorbed by all atoms of the expanding cloud if the Zeeman splitting induced by the magnetic field is negligible. This negligibility is questionable, at least in the current setup.

The MOT field is produced by an anti-Helmholtz coil and driven by a current of 40 A. To allow the heat produced by the wires to dissipate effectively, they are wound around water-cooled brass bodies. Abruptly shutting down the magnetic field induces eddy currents within the brass and the steel of the vacuum chamber which impede and slow the fields decline. This was analyzed by [Len20] and some of the insights are presented in the following.

A single prototype coil built similar to the coils installed to the setup, as shown in fig. 4.19, served as a test object. In the coil's center, a Hall probe is visible. This probe is capable of measuring signals with a rise or fall time of $10 \mu\text{s}$ ⁴⁰.

For a lack of a better power source and access to water cooling, the prototype was only operated using a current of $I = 11.4 \text{ A}$. The real MOT coils use a higher

⁴⁰This was measured using a much smaller coil with much smaller currents

current of 40 A but because they are built in the same way, the only difference is their maximum field strength. It is assumed that the general behaviour of the coils is the same. A measurement of the coil's magnetic field after turning off the driving signal is depicted in fig. 4.20. The green signal shows this driving signal reaching the *off* state well below 1 ms. Compared to the decline of the red signal it can be treated as instantaneous. The red signal describes the output of the Hall probe. Its decline is much slower with an exponential decay time constant $\tau = 6.2$ ms. Again, it is assumed that the coils which currently create the magnetic field behave the same and the field's slope in the center of the MOT is therefore given by

$$B_0(\Delta t) = -2466 \frac{\text{mT}}{\text{m}} \cdot e^{-\frac{\Delta t}{\tau}}. \quad (4.34)$$

The amplitude value -2466 mT/m was determined in section 4.1.

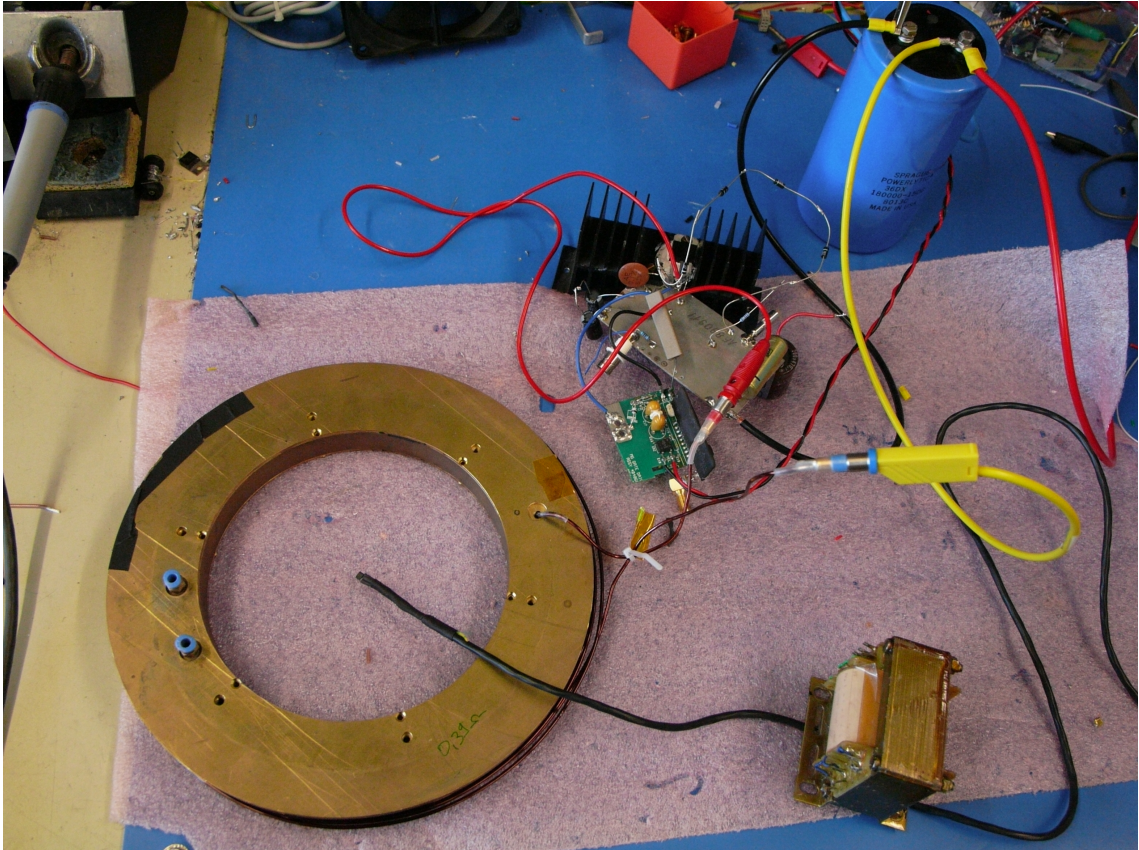
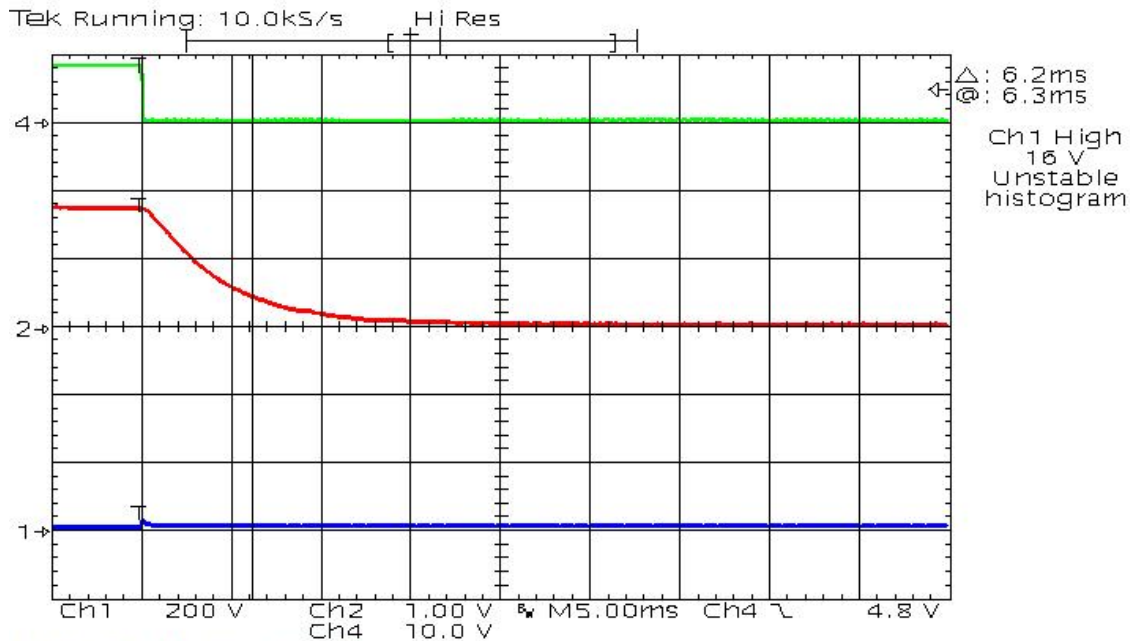


Figure 4.19: Picture of the setup used to test the shut down process of a magnetic field produced by a coil similar to the coils in the MOT setup. The coil is wound around a brass body/ bobbin. A Hall probe is placed at the center of the coil while additional electronics are placed outside the bobbin.

If the slope of the magnetic field is too high and the atoms move outward, the Zeeman effect shifts their resonance frequencies to higher or lower values, making them fall out of resonance with the spectroscopy laser and thus making measure-

ments of the atom cloud's size impossible. The estimated expansion of a ${}^6\text{Li}$ cloud of temperature $T = 300\ \mu\text{K}$ and a starting size $\sigma_0 = 500\ \mu\text{m}$ is shown in fig. 4.21. It expands much faster than the ${}^{87}\text{Rb}$ cloud depicted in fig. 4.18 because of its lower atomic mass and higher temperature. The expansion time Δt is limited to $\Delta t < 10\ \text{ms}$ because the cloud's size becomes too large to be analyzed effectively using the previously presented procedure with a regular sized CCD chip for longer durations.



MOT Coil with Brass-bobbin:
green: Gate driver control signal.
red: Magnetometer output for 11.4A Coil current.
Bobbin eddy current time constant = 6.2ms

Figure 4.20: Measurement of the delayed decline in magnetic field strength of a prototype coil similar to the coils which are used to create the MOT field. The green signal shows the turn-off signal of the power source. In the chosen resolution it can be considered instantaneous in comparison to the decline of the magnetic field signal in red. The magnetic field declines exponentially with a time constant $\tau = 6.2\ \text{ms}$. The real coils are assumed to show the same behaviour, although they run on 40 A of current while the prototype was driven by 11.4 A. Picture and data taken from [Len20].

Additionally, fig. 4.21 depicts the difference in magnetic fields ΔB when comparing both edges of the cloud:

$$\Delta B(\Delta t) = \sigma(\Delta t) \cdot e^{-\frac{\Delta t}{\tau}} \cdot 2.466 \frac{\text{T}}{\text{m}}. \quad (4.35)$$

In the beginning, the cloud is maximally compressed and it takes some time to expand. While its size stays approximately constant, the magnetic field declines

in strength. Hence, a small dip can be seen for low Δt . With time, the expansion becomes more and more linear and the difference in magnetic field strengths experienced by both sides of the cloud increases until $\Delta t \approx \tau$.

As mentioned above, the difference between the natural linewidth and the Doppler broadening gives an upper limit for the allowed Zeeman shift. This value is $\Gamma_{\max} = 3.64$ MHz. The splitting between the $2S_{1/2}$ $F = 3/2$ magnetic substates $m_F = -3/2$ and $m_F = 3/2$ is given by

$$\Delta\nu(\Delta B) = \Delta B \cdot 14.0098 \frac{\text{MHz}}{\text{mT}}, \quad (4.36)$$

which puts the maximum allowed ΔB to $\Delta B_{\max} = 0.26$ mT⁴¹. In the analyzed time frame, this value cannot be reached.

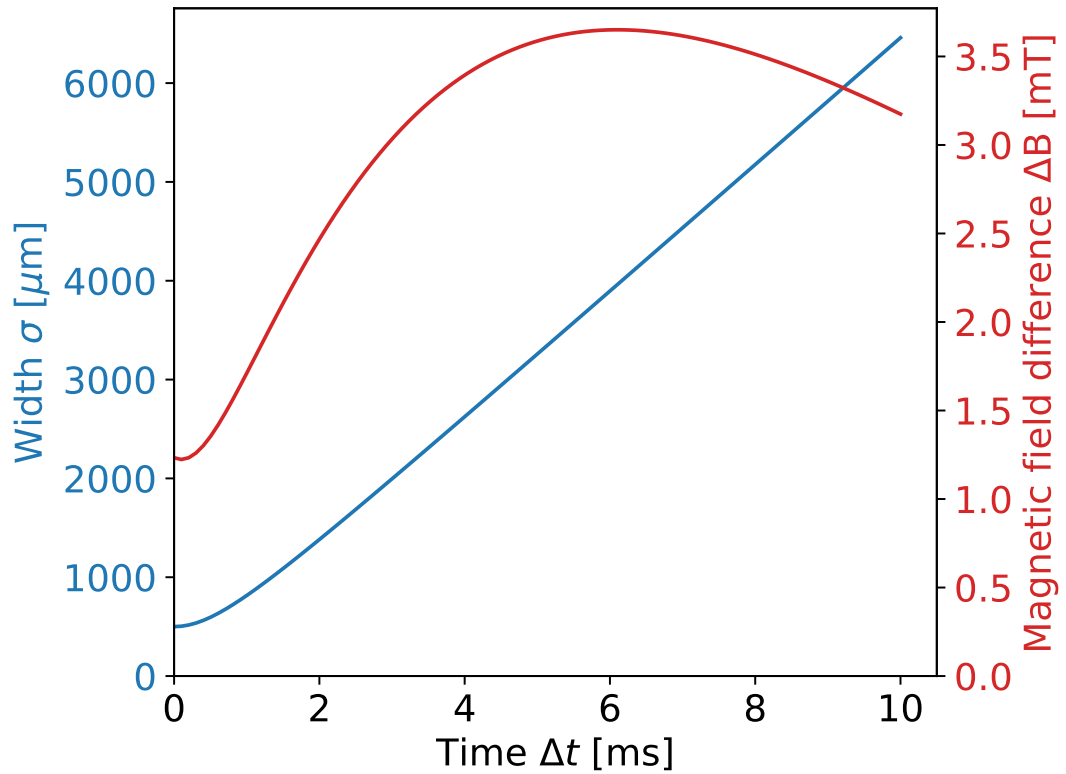


Figure 4.21: Width expansion of a ${}^6\text{Li}$ cloud with $T = 300$ μK (blue) and difference in magnetic field from cloud edge to cloud edge in the experimental B field (red) over time. To make atoms at both ends of the cloud resonant to the same light, a $\Delta B < 0.26$ mT is needed. This value cannot be reached in the analyzed time frame.

To make a proper analysis of the ${}^6\text{Li}$ MOT's temperature possible, the magnetic field has to be shut down significantly faster. This needs further research. The eddy

⁴¹A deeper analysis of how the quantum states of interest interact with magnetic fields can be found in section 3.2

currents could be counteracted by applying a second magnetic field using an additional pair of coils during the quenching process. The setup could be made smaller so that the coils could be placed closer to the MOT center and allow for lower currents, which would lead to cooler coil temperatures, and body materials other than brass could be considered. One could also replace the main stainless steel chamber of the setup with a small, non-conductive glass chamber, which would further reduce eddy currents.

Lastly, the ${}^6\text{Li}$ atoms could be brought to lower temperatures. While a MOT that works with 671 nm light is limited by a high natural linewidth and a low hyperfine splitting of the excited states and therefore can't be cooled below the Doppler limit $T_{\text{Doppler}} = 140 \mu\text{K}$, other trapping transitions are also possible. The $2S_{1/2} \rightarrow 3P_{3/2}$ transition at 323 nm has a linewidth of $\Gamma = 754 \text{ kHz}$ and therefore a lower Doppler temperature of $T_{\text{Doppler}} = 18 \mu\text{K}$ [DHH⁺11]. Of course, the recoil temperature is higher, compared to the D_2 -line MOT ($15 \mu\text{K}$ instead of $3.5 \mu\text{K}$). However, both versions are limited by T_{Doppler} anyway. This approach would require a completely new laser system and could potentially produce a MOT of temperature $T \approx 59 \mu\text{K}$. Another solution requires the use of a gray molasses [WEO⁺94]. By building upon the already existing laser system and leaving the MOT intact, but adding a second cooling stage in the form of a gray molasses, the atoms could be brought down to $T \approx 42 \mu\text{K}$ [Ger16].

5. Conclusion and Outlook

During this work, multiple laser systems were built⁴², most importantly the Zeeman slower laser and the MOT laser system. The former combines a home-built ECDL and a TA to provide approximately 160 mW at the wavelengths of the ${}^6\text{Li}$ D₂ and ${}^7\text{Li}$ D₁ lines. With a Fizeau interferometer-based wavelength meter, this laser could be stabilized to $\nu = 446\,799\,400(1)$ MHz and could thus produce the light beam which was necessary to slow down atoms in the Zeeman slower.⁴³

The second, commercial laser system can provide a Gaussian beam with a power of approximately 200 mW and can be tuned over a range of $446.79\text{ THz} < \nu < 446.81\text{ THz}$, spanning all ${}^6\text{Li}$ and ${}^7\text{Li}$ D lines. It could be shown that this laser could be stabilized to the ${}^7\text{Li}$ crossover resonance at $\nu = 446\,799\,818.0(6)$ MHz with a linewidth $\Gamma_{\text{Locked}} = 120(10)$ kHz, which is sufficient for its use as a MOT laser.

This work presented the implementation and (incomplete) optimization of a Zeeman slower with which a hot beam of ${}^6\text{Li}$ atoms can be partially cooled down to a velocity of $v_1 = 8.7(6)$ m/s and a transversal temperature $T_t = 255(1)$ mK. To simulate this and other potential Zeeman slower setups, a Monte Carlo simulation was developed. Therefore, the behavior of the ${}^6\text{Li}$ $2S_{1/2}$ ground state and $2P_{3/2}$ excited state in different magnetic fields has been described. By combining the Hamiltonians of the Zeeman effect and the hyperfine structure, these states' energies and their transition strengths were identified. This program was examined by comparing its results to measurements of the hot and slowed beams. In its current state, the simulation does not reproduce real data and severely underestimates the effectiveness of the slower. Only 1 % of the simulated atoms were slowed, instead of 18(1) %.

The slowed atoms were captured in a MOT which held up to $10(1) \cdot 10^9$ atoms, with loading and loss times determined to be 1.70(2) s and 19.4(5) s, respectively. The project's ultimate goal, performing high precision laser spectroscopy on a cold and dense target of lithium atoms, has not yet been reached because the MOT's magnetic field could not be quenched fast enough.

The following sections give an overview on the potential improvements and next steps for this experiment. Additionally, other promising projects that were started during this research are presented as they were highly influenced by the knowledge that was gained throughout the development of the MOT.

⁴²Additional lasers were, for example, other ECDLs at 671 nm for lithium spectroscopy and beat-offset locking, a Titanium-Sapphire laser, and an ECDL at 780 nm for the purpose of rubidium spectroscopy during a supervised master's thesis. These lasers are not presented because they were not used for the MOT or the Zeeman slower.

⁴³It has also been observed that the Zeeman slower is not necessary to load the MOT. Even without a slower, enough atoms are slow enough to be trapped by the MOT but the slower improves the loading significantly.

5.1. Potential Improvements

Although it has been shown that the MOT is fully functional and that many atoms can be trapped and cooled by it, there are still many challenges to be addressed. The final temperature of the atoms has not yet been measured and without knowing the temperature, the uncertainties of any resonance frequency measurement cannot be estimated adequately. The next logical step is therefore the determination of the MOT temperature T . It was shown that, with the setup in the current state, the magnetic field could not be quenched fast enough for the expected value of T .

The analysis was done only on a wire coiled around a brass housing being driven by a current of 11.4 A. This did not include the stainless steel vacuum chamber of the real experiment and was far below the final current of 40 A. To better understand the behaviour of the magnetic field, the analysis could be repeated inside the real setup. Even with this simplified system, the magnetic field strength did not drop fast enough to allow for an investigation of the atom cloud's T .

This test was also conducted on a plastic housing using a similar wire and the same current and as fig. 5.1 depicts, such a housing permits a much faster quenching of the magnetic field. Within roughly $60 \mu\text{s}$ the field strength drops to negligible values. Plastic is non-conductive and therefore no eddy currents can be created within the housing. This would be an acceptable time for an effective temperature determination. Even so, a plastic housing cannot be used.

When 40 A flow through the copper wire of the MOT coils, they heat up and the wire resistance increases. Additionally, a hot coil will damage nearby elements in the setup, such as a potential plastic housing. The brass housing's heat dissipation is necessary to keep the coil's temperature in a non-destructive range, provided that it is also cooled using the laboratory's water cooling system.

The Anti-Helmholtz coils themselves must be improved. If they could be kept at a lower temperature, a plastic housing would be possible. There exist hollow core conductors, copper wires through which a coolant can flow⁴⁴. Whether a usable coil can be built using such wires requires further research. The temperature could also be reduced by using smaller currents. This would lead to smaller field strengths at the MOT center as well, unless the coils are placed closer to the center, which would require a completely new MOT chamber.

When the central chamber is replaced, one might consider using glass instead of stainless steel. A regular steel chamber's viewport positions limit the solid angle from which fluorescence in the experiment can be observed. A fully transparent glass chamber would allow for a less restricted placement of any used measurement devices. Additionally, because the aspired precision of the spectroscopy should permit an examination of the effects of quantum interference [SSG⁺11, BWP⁺13] on

⁴⁴Such as but not limited to [Luv24]

the ${}^6\text{Li}$ resonance frequencies and the fluorescence spectrum, a larger solid angle is preferred as the fluorescence's polarization is expected to be strongly angle dependent [UMM⁺19]. One should keep in mind though, that the lithium atoms will most probably stick to the first surface they hit and over time the beam might sputter a thin layer of ${}^6\text{Li}$ on the glass, making it more opaque.

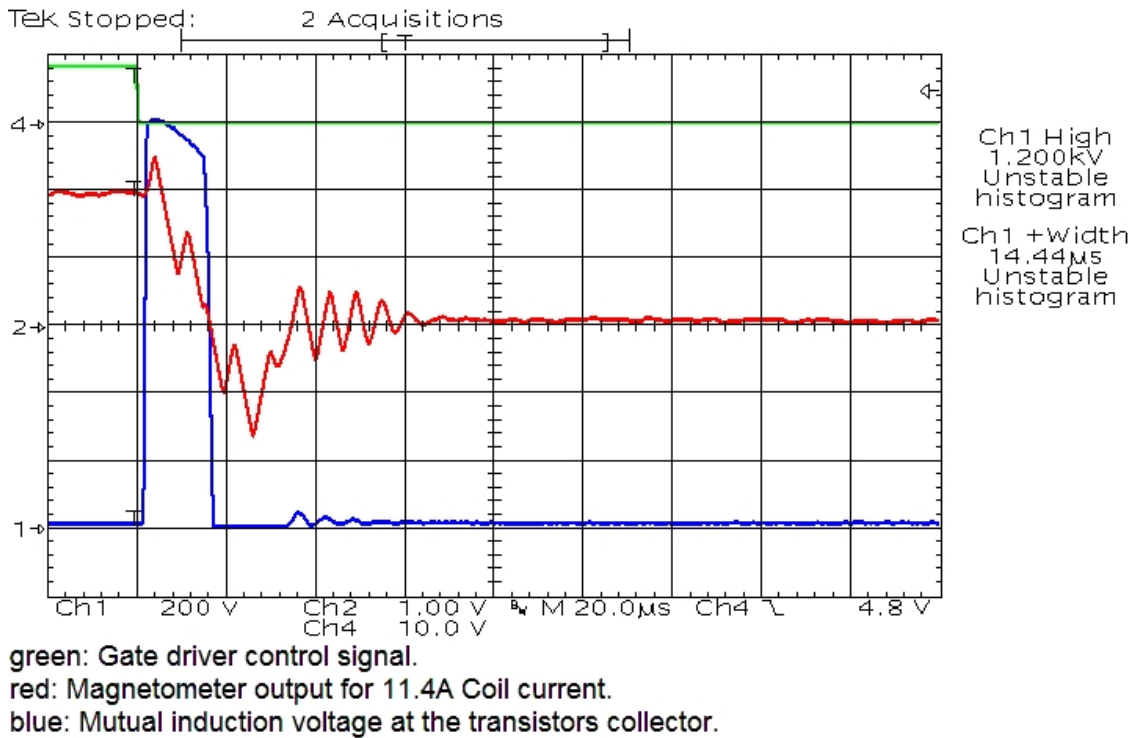


Figure 5.1: Measurement of the delayed decline in magnetic field strength of a prototype coil similar to the coils which are used to create the MOT field. In contrast to the real brass housing, a plastic housing was used and the current is 11.4 A rather than 40 A. The green signal shows the turn-off signal of the power source. In the chosen resolution it can be considered instantaneous in comparison to the decline of the magnetic field signal in red. The magnetic field declines with a superimposed ringing. It drops to zero after roughly 60 μs . Picture and data taken from [Len20].

Finally, the whole setup could be extended by adding a dipole trap. The MOT would capture and cool down many ${}^6\text{Li}$ atoms, the coldest of which could then be trapped within the electric field of a high power laser beam. There are several magic wavelengths available for both ${}^6\text{Li}$ and ${}^7\text{Li}$ [SSC12], especially 872.56(900) nm is easily reachable using an already present titanium-sapphire laser. While the atoms are kept in place by the dipole trap, the magnetic field can be shut off at any time and once the field strength is sufficiently low, the trapping laser can be blocked and the spectroscopy laser can illuminate the sample.

5.2. Offspring Projects

Many ideas that came up during the research on the 3D-MOT directly influenced another project in the laboratory: the 2D-MOT. By preparing a similar laser setup but omitting one spatial direction, ^6Li atoms that were emitted from a hot oven could be captured and cooled within the field of four permanent magnets. Several supervised students were involved during the development of this system ([Wes21, Sch22, Tsc23]).

The 3D-MOT setup contains a rather lengthy Zeeman slower to cool down atoms and make them catchable by the trap. To scale down the system, eliminate the need for a large magnetic field, and avoid an additional high-power laser which crossed the 3D-MOT center, replacing the slower with a 2D-MOT was considered. It could be shown that the two-dimensionally trapped atoms can be reliably pushed out of the 2D-MOT using a low-power, red-shifted laser beam. The resulting velocity distribution of the pushed-out atom beam is depicted in fig. 5.2. This beam itself could be examined using high-precision laser spectroscopy. A possible setup which utilizes an active fiber-based retroreflector based on [BMM⁺16] is currently under development. As its name suggests, the retroreflector reflects the spectroscopy laser beam back onto itself, thereby creating a symmetric fluorescence spectrum and suppressing the effects of higher-order Doppler shifts.

The laser system that drives all the necessary trapping and push beams is a titanium-sapphire laser⁴⁵. It generates a continuous wave beam with roughly 2 W at 671 nm and a linewidth in the range of 40 to 50 kHz. The beam is split into multiple other beams which are then manipulated further with the help of AOMs to get them to the desired wavelengths. The provided power is more than enough to create all MOT beams and the push beam while also being precise enough to target specific transitions.

The 2D-MOT is an effective source of low-velocity atoms. To effectively direct these atoms into a 3D-MOT or other setups, guides were built ([Hep19]) that utilize a field created by magnetic quadrupoles that follow a bent curve. In theory, slow atoms (low-field seekers) can follow the field minimum within these guides and thus a beam of slow atoms can be partially deflected. To date, this effect has not yet been observed in this working group. It is still searched for.

Of course, the flow of knowledge is bi-directional. What was learned during the work on the 2D-MOT, can be reapplied to the 3D-MOT. The TiSa laser with its high power and good precision can be used to drive the latter. More power in a wider beam might increase the number of trapped particles. This would free the TAPro diode laser for other usage. Together with other devices, it could be transformed into

⁴⁵The working principle of a titanium sapphire (TiSa) laser is not explained here, as it wasn't used during the 3D-MOT project. The interested reader is advised to take a look at the aforementioned theses.

a sub-kHz spectroscopy laser to examine the ${}^6\text{Li}$ transitions of interest. An ultra-low expansion cavity was installed to stabilize this laser and to minimize its linewidth. A frequency comb which is locked to a different laser [Wes24] can be used to determine its frequency. The fiber-based retroreflector can be used to improve the quality of future spectroscopy measurements and the quadrupole guide could be used to fill the MOT without the need for an additional Zeeman slower laser.

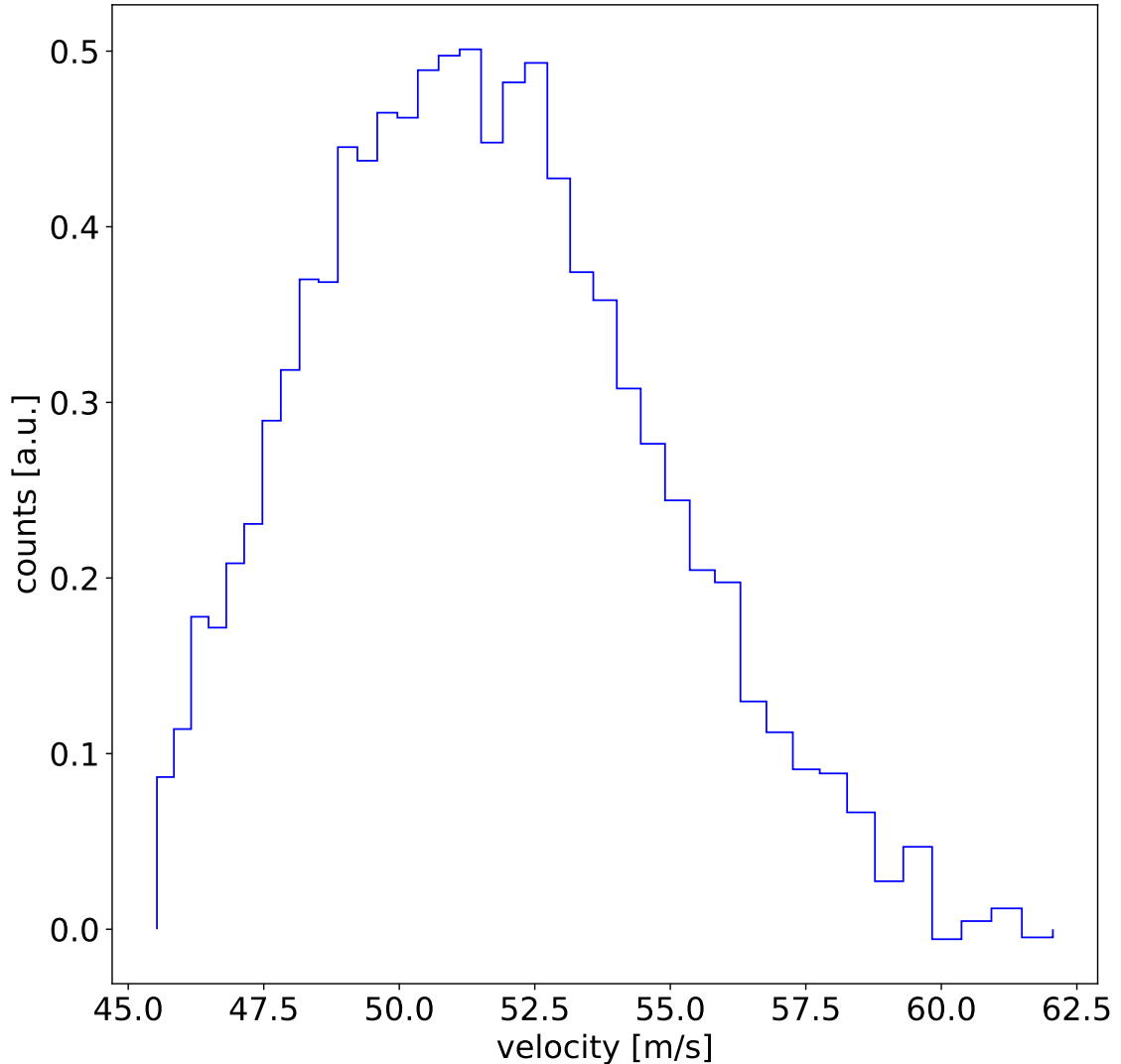


Figure 5.2: Velocity distribution of the ${}^6\text{Li}$ atom beam generated by applying a push laser beam to the 2D-MOT. Picture taken from [Tsc23].

5.3. Final Words

A magneto-optical trap can be a powerful tool to create a cold target for experimentation. As shown by [LWR⁺20], measurements on a cloud of ${}^6\text{Li}$ atoms captured by a MOT yielded more precise resonance frequencies than ever before. Although the thesis at hand could not provide a new high-precision spectroscopy for lithium, further development of the project promises new results. In addition to delivering a

target of cold ${}^6\text{Li}$, the setup can potentially be adjusted to switch to ${}^7\text{Li}$.

As is the case with ${}^6\text{Li}$, to trap ${}^7\text{Li}$ in a MOT a laser beam containing two frequencies is necessary to avoid the loss of atoms through an uninvolved dark state. While the former requires a frequency difference $\Delta\nu \approx 230$ MHz, the latter must be $\Delta\nu \approx 800$ MHz which may be accessed by a combination of multiple AOMs, by sideband-generating EOMs or by the usage of two independent laser systems which are stabilized to each other by means of beat-offset locking. Bosonic and fermionic lithium could be studied in a similar or even the same setup which would eliminate many systematic effects when measuring the isotope shift.

The 3D-MOT project is far from done and many exciting ideas are waiting for their implementation. Given time and manpower, it will create new and interesting insights on a variety of phenomena in atomic physics.

Bibliography

- [AH19] ADAMS, Charles S. ; HUGHES, Ifan: *Optics f2f: from Fourier to Fresnel*. First edition. Oxford, United Kingdom : Oxford University Press, 2019. – ISBN 978-0-19-878678-8 978-0-19-878679-5
- [AIV77] ARIMONDO, E. ; INGUSCIO, M. ; VIOLINO, P.: Experimental determinations of the hyperfine structure in the alkali atoms. In: *Rev. Mod. Phys.* 49 (1977), Januar, Nr. 1, 31–75. <http://dx.doi.org/10.1103/RevModPhys.49.31>. – DOI 10.1103/RevModPhys.49.31. – ISSN 0034–6861
- [Arm71] ARMSTRONG, Lloyd: *Theory of the hyperfine structure of free atoms*. New York : Wiley-Interscience, 1971. – ISBN 978-0-471-03335-6
- [Arm07] ARMTUK: *Periodic Table Armtuk3 - Periodic table of elements - Wikimedia Commons*. https://commons.wikimedia.org/wiki/Periodic_table_of_elements#/media/File:Periodic_Table_Armtuk3.svg. Version: April 2007
- [AWB98] ARNOLD, A. S. ; WILSON, J. S. ; BOSHIER, M. G.: A simple extended-cavity diode laser. In: *Review of Scientific Instruments* 69 (1998), März, Nr. 3, 1236–1239. <http://dx.doi.org/10.1063/1.1148756>. – DOI 10.1063/1.1148756. – ISSN 0034–6748, 1089–7623
- [Bar90] BARNES, J A.: Variances based on data with dead time between the measurements / National Bureau of Standards. Version: 1990. <http://dx.doi.org/10.6028/NIST.TN.1318>. Gaithersburg, MD, 1990 (NBS TN 1318). – Forschungsbericht. – NBS TN 1318 S. – Edition: 0
- [BD89] BOGGS, Paul T. ; DONALDSON, Janet R.: Orthogonal distance regression / National Institute of Standards and Technology. Version: 1989. <http://dx.doi.org/10.6028/NIST.IR.89-4197>. Gaithersburg, MD, 1989 (NIST IR 89-4197). – Forschungsbericht. – NIST IR 89-4197 S.
- [BGB⁺06] BAILLARD, X. ; GAUGUET, A. ; BIZE, S. ; LEMONDE, P. ; LAURENT, Ph ; CLAIRON, A. ; ROSENBUSCH, P.: Interference-filter-stabilized external-cavity diode lasers. In: *Optics Communications* 266 (2006), Nr. 2, 609–613. <http://dx.doi.org/https://doi.org/10.1016/j.optcom.2006.05.011>. – DOI <https://doi.org/10.1016/j.optcom.2006.05.011>. – ISSN 0030–4018
- [Bla98] BLACK, Eric D.: *Notes on the Pound-Drever-Hall technique*. <https://dcc.ligo.org/public/0028/T980045/000/T980045-00.pdf>. Version: April 1998
- [Bla01] BLACK, Eric D.: An introduction to Pound–Drever–Hall laser frequency stabilization. In: *American Journal of Physics* 69 (2001), Januar, Nr. 1, 79–87. <http://dx.doi.org/10.1119/1.1286663>. – DOI 10.1119/1.1286663. – ISSN 0002–9505, 1943–2909
- [BMM⁺16] BEYER, A. ; MAISENBACHER, L. ; MATVEEV, A. ; POHL, R. ; KHABAROVA, K. ; CHANG, Y. ; GRININ, A. ; LAMOUR, T. ; SHI, T.

- ; YOST, D. C. ; UDEM, Th. ; HÄNSCH, T. W. ; KOLACHEVSKY, N.: Active fiber-based retroreflector providing phase-retracing anti-parallel laser beams for precision spectroscopy. In: *Opt. Express* 24 (2016), Juli, Nr. 15, 17470. <http://dx.doi.org/10.1364/OE.24.017470>. – DOI 10.1364/OE.24.017470. – ISSN 1094–4087
- [BWP⁺13] BROWN, Roger C. ; WU, Saijun ; PORTO, J. V. ; SANSONETTI, Craig J. ; SIMIEN, C. E. ; BREWER, Samuel M. ; TAN, Joseph N. ; GILLASPY, J. D.: Quantum interference and light polarization effects in unresolvable atomic lines: application to a precise measurement of the ^{6,7}Li D₂ lines. In: *Phys. Rev. A* 87 (2013), März, Nr. 3, 032504. <http://dx.doi.org/10.1103/PhysRevA.87.032504>. – DOI 10.1103/PhysRevA.87.032504. – ISSN 1050–2947, 1094–1622. – arXiv:1212.2220 [physics, physics:quant-ph]
- [CLS⁺08] CHEN, N. C. ; LIN, C. M. ; SHEN, C. ; LIEN, W. C. ; LIN, T. Y.: Redshift of edge emission from AlGaInP light-emitting diodes and correlation with electron-hole recombination lifetime. In: *Opt. Express* 16 (2008), Dezember, Nr. 25, 20759. <http://dx.doi.org/10.1364/OE.16.020759>. – DOI 10.1364/OE.16.020759. – ISSN 1094–4087
- [CMM⁺14] CENTENO, R. ; MARCHENKO, D. ; MANDON, J. ; CRISTESCU, S. M. ; WULTERKENS, G. ; HARREN, F. J. M.: High power, widely tunable, mode-hop free, continuous wave external cavity quantum cascade laser for multi-species trace gas detection. In: *Appl. Phys. Lett.* 105 (2014), Dezember, Nr. 26, 261907. <http://dx.doi.org/10.1063/1.4905281>. – DOI 10.1063/1.4905281. – ISSN 0003–6951, 1077–3118
- [Dau20] DAUM, Julia J.: *Simulating and Designing a Zeeman Slower*. Mainz, Johannes Gutenberg-Universität, Masterarbeit, Juli 2020
- [DCT89] DALIBARD, J. ; COHEN-TANNOUJDI, C.: Laser cooling below the Doppler limit by polarization gradients: simple theoretical models. In: *J. Opt. Soc. Am. B* 6 (1989), November, Nr. 11, 2023. <http://dx.doi.org/10.1364/JOSAB.6.002023>. – DOI 10.1364/JOSAB.6.002023. – ISSN 0740–3224, 1520–8540
- [Dem11] DEMTRÖDER, Wolfgang: *Laserspektroskopie 1*. Berlin, Heidelberg : Springer Berlin Heidelberg, 2011. <http://dx.doi.org/10.1007/978-3-642-21306-9>. <http://dx.doi.org/10.1007/978-3-642-21306-9>. – ISBN 978–3–642–21305–2 978–3–642–21306–9
- [DH90] DUARTE, F. J. (Hrsg.) ; HILLMAN, Lloyd W. (Hrsg.): *Dye laser principles, with applications*. Boston : Academic Press, 1990 (Quantum electronics–principles and applications). – ISBN 978–0–12–222700–4
- [DHH⁺11] DUARTE, P. M. ; HART, R. A. ; HITCHCOCK, J. M. ; CORCOVILOS, T. A. ; YANG, T.-L. ; REED, A. ; HULET, R. G.: All-optical production of a lithium quantum gas using narrow-line laser cooling. In: *Phys. Rev. A* 84 (2011), Dezember, Nr. 6, 061406. <http://dx.doi.org/10.1103/PhysRevA.84.061406>. – DOI 10.1103/PhysRevA.84.061406. – ISSN 1050–2947, 1094–1622

- [DHK⁺83] DREVER, R. W. P. ; HALL, J. L. ; KOWALSKI, F. V. ; HOUGH, J. ; FORD, G. M. ; MUNLEY, A. J. ; WARD, H.: Laser phase and frequency stabilization using an optical resonator. In: *Appl. Phys. B* 31 (1983), Juni, Nr. 2, 97–105. <http://dx.doi.org/10.1007/BF00702605>. – DOI 10.1007/BF00702605. – ISSN 0721–7269, 1432–0649
- [DN07] DAS, Dipankar ; NATARAJAN, Vasant: Absolute frequency measurement of the lithium D lines: Precise determination of isotope shifts and fine-structure intervals. In: *Phys. Rev. A* 75 (2007), Mai, Nr. 5, 052508. <http://dx.doi.org/10.1103/PhysRevA.75.052508>. – DOI 10.1103/PhysRevA.75.052508. – ISSN 1050–2947, 1094–1622
- [EW07] ENDŌ, Masamori ; WALKER, Robert F.: *Gas lasers*. Boca Raton : CRC/Taylor & Francis, 2007. – ISBN 978–1–4200–1880–6. – OCLC: 83252040
- [FA18] FREUND, Henry P. ; ANTONSEN, Thomas M.: *Principles of Free Electron Lasers*. Third Edition. Cham, Switzerland : Springer, 2018 (Electrical Engineering). – ISBN 978–3–319–75106–1 978–3–319–75105–4
- [Fis23] FISCHER, Mathis S.: *Properties of Lithium-7*. <https://www.fdr.uni-hamburg.de/record/13790>. Version: November 2023. – Publisher: Universität Hamburg Version Number: 1.0
- [Foo05] FOOT, C. J.: *Atomic physics*. Oxford ; New York : Oxford University Press, 2005 (Oxford master series in physics 7. Atomic, Optical, and laser physics). – ISBN 978–0–19–850695–9 978–0–19–850696–6. – OCLC: ocm57478010
- [Fra21] FRANZ, Konrad: *Measurements in Trapped Atomic Lithium*. Mainz, Johannes Gutenberg-Universität, Masterarbeit, Juni 2021
- [Geh03] GEHM, Michael E.: *Properties of ⁶Li*. <https://jet.physics.ncsu.edu/techdocs/pdf/PropertiesOfLi.pdf>. Version: Februar 2003
- [Ger16] GERKEN, Manuel: *Gray Molasses Cooling of Lithium-6 Towards a Degenerate Fermi Gas*. Heidelberg, University of Heidelberg, Masterarbeit, 2016.
- [GM22] GROSS, Rudolf ; MARX, Achim: *Festkörperphysik*. De Gruyter, 2022. <http://dx.doi.org/10.1515/9783110782394>. <http://dx.doi.org/10.1515/9783110782394>. – ISBN 978–3–11–078239–4
- [GOSDD98] GUERY-ODELIN, D. ; SOEDING, J. ; DESBIOLLES, P. ; DALIBARD, Jean: Strong evaporative cooling of a trapped cesium gas. In: *Opt. Express* 2 (1998), April, Nr. 8, 323. <http://dx.doi.org/10.1364/OE.2.000323>. – DOI 10.1364/OE.2.000323. – ISSN 1094–4087
- [Hep19] HEPPENER, Merten: *Aufbau und Charakterisierung einer magnetischen Quadrupol-Transportstrecke für Atome*. Mainz, Johannes Gutenberg-Universität, Bachelorarbeit, Februar 2019

- [Her86] HERNANDEZ, G.: *Fabry-Perot interferometers*. Cambridge [Cambridgeshire] ; New York : Cambridge University Press, 1986 (Cambridge studies in modern optics 3). – ISBN 978-0-521-32238-6
- [Hig23] HIGHFINESSE: *Datasheet Wavelength Meter WS7-30 Series*. <https://www.highfinesse.com/en/wavelengthmeter/wavelengthmeter-further-information/technical-information-wavelengthmeter-ws7-30-series.pdf>. Version: 2023
- [HKJ+14] HAMILTON, Paul ; KIM, Geena ; JOSHI, Trinity ; MUKHERJEE, Biswaroop ; TIARKS, Daniel ; MÜLLER, Holger: Sisyphus Cooling of Lithium. In: *Physical Review A* 89 (2014), Februar, Nr. 2, 023409. <http://dx.doi.org/10.1103/PhysRevA.89.023409>. – DOI 10.1103/PhysRevA.89.023409
- [Hun09] HUNSPERGER, Robert G.: *Integrated optics: theory and technology*. 6th ed. New York ; London : Springer, 2009 (Advanced texts in physics). – ISBN 978-0-387-89774-5. – OCLC: ocn317252093
- [Jon41] JONES, R. C.: A New Calculus for the Treatment of Optical Systems I Description and Discussion of the Calculus. In: *J. Opt. Soc. Am.* 31 (1941), Juli, Nr. 7, 488. <http://dx.doi.org/10.1364/JOSA.31.000488>. – DOI 10.1364/JOSA.31.000488. – ISSN 0030-3941
- [JZT+16] JIANG, Zhaojie ; ZHOU, Qi ; TAO, Zhiming ; ZHANG, Xiaogang ; ZHANG, Shengnan ; ZHU, Chuanwen ; LIN, Pingwei ; CHEN, Jingbiao: Diode laser using narrow bandwidth interference filter at 852 nm and its application in Faraday anomalous dispersion optical filter. In: *Chinese Phys. B* 25 (2016), August, Nr. 8, 083201. <http://dx.doi.org/10.1088/1674-1056/25/8/083201>. – DOI 10.1088/1674-1056/25/8/083201. – ISSN 1674-1056
- [KHG+14] KANGARA, Jayampathi C. B. ; HACHTEL, Andrew J. ; GILLETTE, Matthew C. ; BARKELOO, Jason T. ; CLEMENTS, Ethan R. ; BALI, Samir ; UNKS, Brett E. ; PROITE, Nicholas A. ; YAVUZ, Deniz D. ; MARTIN, Paul J. ; THORN, Jeremy J. ; STECK, Daniel A.: Design and construction of cost-effective tapered amplifier systems for laser cooling and trapping experiments. In: *American Journal of Physics* 82 (2014), August, Nr. 8, 805-817. <http://dx.doi.org/10.1119/1.4867376>. – DOI 10.1119/1.4867376. – ISSN 0002-9505, 1943-2909
- [Koe96] KOECHNER, Walter: *Solid-state laser engineering*. 4th extensively rev. and updated ed. Berlin ; New York : Springer, 1996 (Springer series in optical sciences v. 1). – ISBN 978-3-540-60237-8
- [Koh16] KOHLERT, Thomas: *A Magneto-Optical Trap for Lithium Atoms*. München, Ludwig-Maximilians-Universität, Masterarbeit, September 2016
- [KSA+21] KRAUTH, Julian J. ; SCHUHMANN, Karsten ; AHMED, Marwan A. ; AMARO, Fernando D. ; AMARO, Pedro ; BIRABEN, François ; CHEN, Tzu-Ling ; COVITA, Daniel S. ; DAX, Andreas J. ; DIEPOLD, Marc ;

- FERNANDES, Luis M. P. ; FRANKE, Beatrice ; GALTIER, Sandrine ; GOUVEA, Andrea L. ; GÖTZFRIED, Johannes ; GRAF, Thomas ; HÄNSCH, Theodor W. ; HARTMANN, Jens ; HILDEBRANDT, Malte ; INDELICATO, Paul ; JULIEN, Lucile ; KIRCH, Klaus ; KNECHT, Andreas ; LIU, Yi-Wei ; MACHADO, Jorge ; MONTEIRO, Cristina M. B. ; MULHAUSER, Françoise ; NAAR, Boris ; NEBEL, Tobias ; NEZ, François ; DOS SANTOS, Joaquim M. F. ; SANTOS, José P. ; SZABO, Csilla I. ; TAQQU, David ; VELOSO, João F. C. A. ; VOGELANG, Jan ; VOSS, Andreas ; WEICHEL, Birgit ; POHL, Randolf ; ANTOGNINI, Aldo ; KOTTMANN, Franz: Measuring the α -particle charge radius with muonic helium-4 ions. In: *Nature* 589 (2021), Januar, Nr. 7843, 527–531. <http://dx.doi.org/10.1038/s41586-021-03183-1>. – DOI 10.1038/s41586-021-03183-1. – ISSN 0028-0836, 1476–4687
- [Len20] LENK, Heinz: *MOT Spulenabschaltung Machbarkeitstudie*. Juni 2020
- [Luv24] LUVATA: *Hollow Conductors*. <https://www.luvata.com/products/hollow-conductors>. Version: März 2024
- [LWR⁺20] LI, Rui ; WU, Yuelong ; RUI, Yang ; LI, Bo ; JIANG, Yanyi ; MA, Longsheng ; WU, Haibin: Absolute Frequency Measurement of ${}^6\text{Li}$ D Lines with khz-Level Uncertainty. In: *Phys. Rev. Lett.* 124 (2020), Februar, Nr. 6, 063002. <http://dx.doi.org/10.1103/PhysRevLett.124.063002>. – DOI 10.1103/PhysRevLett.124.063002. – ISSN 0031-9007, 1079–7114
- [LZG⁺15] LI, Kai ; ZHANG, Dongfang ; GAO, Tianyou ; PENG, Shi-Guo ; JIANG, Kaijun: Enhanced trapping of cold ${}^6\text{Li}$ using multiple-sideband cooling in a two-dimensional magneto-optical trap. In: *Phys. Rev. A* 92 (2015), Juli, Nr. 1, 013419. <http://dx.doi.org/10.1103/PhysRevA.92.013419>. – DOI 10.1103/PhysRevA.92.013419. – ISSN 1050-2947, 1094–1622
- [PAN⁺10] POHL, Randolf ; ANTOGNINI, Aldo ; NEZ, François ; AMARO, Fernando D. ; BIRABEN, François ; CARDOSO, João M. R. ; COVITA, Daniel S. ; DAX, Andreas ; DHAWAN, Satish ; FERNANDES, Luis M. P. ; GIESEN, Adolf ; GRAF, Thomas ; HÄNSCH, Theodor W. ; INDELICATO, Paul ; JULIEN, Lucile ; KAO, Cheng-Yang ; KNOWLES, Paul ; LE BIGOT, Eric-Olivier ; LIU, Yi-Wei ; LOPES, José A. M. ; LUDHOVA, Livia ; MONTEIRO, Cristina M. B. ; MULHAUSER, Françoise ; NEBEL, Tobias ; RABINOWITZ, Paul ; SANTOS, Joaquim M. F. ; SCHALLER, Lukas A. ; SCHUHMAN, Karsten ; SCHWOB, Catherine ; TAQQU, David ; VELOSO, João F. C. A. ; KOTTMANN, Franz: The size of the proton. In: *Nature* 466 (2010), Juli, Nr. 7303, 213–216. <http://dx.doi.org/10.1038/nature09250>. – DOI 10.1038/nature09250. – ISSN 0028-0836, 1476–4687
- [Phi10] PHILIPP, Simon: *Apparatus for the preparation of ultracold Fermi gases*. Heidelberg, Physikalisches Institut Heidelberg, Diplomarbeit, 2010. http://ultracold.physi.uni-heidelberg.de/files/diplomarbeit_philipp.pdf

- [PNF⁺16] POHL, Randolf ; NEZ, François ; FERNANDES, Luis M. P. ; AMARO, Fernando D. ; BIRABEN, François ; CARDOSO, João M. R. ; COVITA, Daniel S. ; DAX, Andreas ; DHAWAN, Satish ; DIEPOLD, Marc ; GIESEN, Adolf ; GOUVEA, Andrea L. ; GRAF, Thomas ; HÄNSCH, Theodor W. ; INDELICATO, Paul ; JULIEN, Lucile ; KNOWLES, Paul ; KOTTMANN, Franz ; LE BIGOT, Eric-Olivier ; LIU, Yi-Wei ; LOPES, José A. M. ; LUDHOVA, Livia ; MONTEIRO, Cristina M. B. ; MULHAUSER, Françoise ; NEBEL, Tobias ; RABINOWITZ, Paul ; DOS SANTOS, Joaquim M. F. ; SCHALLER, Lukas A. ; SCHUHMANN, Karsten ; SCHWOB, Catherine ; TAQQU, David ; VELOSO, João F. C. A. ; ANTOGNINI, Aldo ; THE CREMA COLLABORATION: Laser spectroscopy of muonic deuterium. In: *Science* 353 (2016), August, Nr. 6300, 669–673. <http://dx.doi.org/10.1126/science.aaf2468>. – DOI 10.1126/science.aaf2468. – ISSN 0036–8075, 1095–9203
- [PRP⁺88] PRENTISS, M. ; RAAB, E. L. ; PRITCHARD, D. E. ; CABLE, A. ; BJORKHOLM, J. E. ; CHU, Steven: Atomic-density-dependent losses in an optical trap. In: *Opt. Lett.* 13 (1988), Juni, Nr. 6, 452. <http://dx.doi.org/10.1364/OL.13.000452>. – DOI 10.1364/OL.13.000452. – ISSN 0146–9592, 1539–4794
- [PX14] PAM-XIAMEN: *AlGaInP Epi Wafer*. <https://www.powerwaywafer.com/de/AlGaInP-epi-wafer.html>. Version: Februar 2014. – Section: News
- [Ram86] RAMSEY, Norman: *Molecular Beams*. Oxford University Press, 1986. <http://dx.doi.org/10.1093/acprof:oso/9780198520214.001.0001>. <http://dx.doi.org/10.1093/acprof:oso/9780198520214.001.0001>. – ISBN 978–0–19–852021–4
- [RH08] RILEY, William ; HOWE, David: *Handbook of Frequency Stability Analysis*. https://tsapps.nist.gov/publication/get_pdf.cfm?pub_id=50505. Version: Juli 2008
- [RWE⁺95] RICCI, L. ; WEIDEMÜLLER, M. ; ESSLINGER, T. ; HEMMERICH, A. ; ZIMMERMANN, C. ; VULETIC, V. ; KÖNIG, W. ; HÄNSCH, T. W.: A compact grating-stabilized diode laser system for atomic physics. In: *Optics Communications* 117 (1995), Februar, 541–549. [http://dx.doi.org/10.1016/0030-4018\(95\)00146-Y](http://dx.doi.org/10.1016/0030-4018(95)00146-Y). – DOI 10.1016/0030–4018(95)00146–Y. – ISSN 0030–4018. – ADS Bibcode: 1995OptCo.117..541R
- [San05] SANDS, David: *Diode lasers*. Bristol : Institute of Physics Publ, 2005 (Series in optics and optoelectronics). – ISBN 978–0–7503–0726–0
- [Sch22] SCHUMACHER, Hendrik-Lukas: *Two-dimensional magneto-optical Trap for Lithium Atoms*. Mainz, Johannes Gutenberg-Universität, Masterarbeit, November 2022
- [SEZ⁺98] SCHÜNEMANN, U. ; ENGLER, H. ; ZIELONKOWSKI, M. ; WEIDEMÜLLER, M. ; GRIMM, R.: Magneto-optic trapping of lithium using semiconductor lasers. In: *Optics Communications* 158 (1998),

- Dezember, Nr. 1-6, 263–272. [http://dx.doi.org/10.1016/S0030-4018\(98\)00517-3](http://dx.doi.org/10.1016/S0030-4018(98)00517-3). – DOI 10.1016/S0030-4018(98)00517-3. – ISSN 00304018
- [SKJW96] SCHERF, W. ; KHAIT, O. ; JÄGER, H. ; WINDHOLZ, L.: Re-measurement of the transition frequencies, fine structure splitting and isotope shift of the resonance lines of lithium, sodium and potassium. In: *Z Phys D - Atoms, Molecules and Clusters* 36 (1996), März, Nr. 1, 31–33. <http://dx.doi.org/10.1007/BF01437417>. – DOI 10.1007/BF01437417. – ISSN 0178–7683, 1434–6079
- [SNL21] SZE, S. M. ; NG, Kwok K. ; LI, Yiming: *Physics of semiconductor devices*. Fourth edition. Hoboken, NJ, USA : Wiley, 2021. – ISBN 978-1-119-61800-3 978-1-119-42913-5
- [SSC12] SAFRONOVA, M. S. ; SAFRONOVA, U. I. ; CLARK, Charles W.: Magic wavelengths for optical cooling and trapping of lithium. In: *Phys. Rev. A* 86 (2012), Oktober, Nr. 4, 042505. <http://dx.doi.org/10.1103/PhysRevA.86.042505>. – DOI 10.1103/PhysRevA.86.042505. – American Physical Society
- [SSG⁺11] SANSONETTI, Craig J. ; SIMIEN, C. E. ; GILLASPY, J. D. ; TAN, Joseph N. ; BREWER, Samuel M. ; BROWN, Roger C. ; WU, Saijun ; PORTO, J. V.: Absolute Transition Frequencies and Quantum Interference in a Frequency Comb Based Measurement of the $^{6,7}\text{Li } D$ Lines. In: *Phys. Rev. Lett.* 107 (2011), Juli, Nr. 2, 023001. <http://dx.doi.org/10.1103/PhysRevLett.107.023001>. – DOI 10.1103/PhysRevLett.107.023001. – ISSN 0031–9007, 1079–7114
- [Ste23] STECK, Daniel A.: *Rubidium 87 D Line Data*. <http://steck.us/alkalidata>. Version: September 2023
- [Str97] STRINGFELLOW, Gerald B. (Hrsg.): *High brightness light emitting diodes*. San Diego : Acad. Press, 1997 (Semiconductors and semimetals 48). – ISBN 978-0-12-752156-5
- [Sun15] SUN, Haiyin: *A Practical Guide to Handling Laser Diode Beams*. 2nd ed. 2015. Dordrecht : Springer Netherlands : Imprint: Springer, 2015 (SpringerBriefs in Physics). <http://dx.doi.org/10.1007/978-94-017-9783-2>. <http://dx.doi.org/10.1007/978-94-017-9783-2>. – ISBN 978-94-017-9783-2
- [TGLW09] TIECKE, T. G. ; GENSEMER, S. D. ; LUDEWIG, A. ; WALRAVEN, J. T. M.: High-flux two-dimensional magneto-optical-trap source for cold lithium atoms. In: *Phys. Rev. A* 80 (2009), Juli, Nr. 1, 013409. <http://dx.doi.org/10.1103/PhysRevA.80.013409>. – DOI 10.1103/PhysRevA.80.013409. – ISSN 1050–2947, 1094–1622
- [Thoa] THORLABS: *Laser_Collimation_Tube_D1-780.gif* (GIF-Grafik, 780 × 250 Pixel). https://www.thorlabs.com/images/TabImages/Laser_Collimation_Tube_D1-780.gif

- [Thob] THORLABS: *Picture of Tapered Amplifier*. https://www.toptica.com/fileadmin/_processed_/9/6/csm_Geometry-of-a-tapered-amplifier-chip_317d1bccc5.jpg
- [Thoc] THORLABS: *Polarization-Maintaining FC/APC Fiber Optic Patch Cables*. https://www.thorlabs.com/newgrouppage9.cfm?objectgroup_id=3345&pn=P3-630PM-FC-2
- [Thod] THORLABS: *Thorlabs - DET36A2 Si Detector, 350 - 1100 nm, 14 ns Rise Time, 13 mm², Universal 8-32 / M₄ Mounting Holes*. <https://www.thorlabs.com/thorproduct.cfm?partnumber=DET36A2#ad-image-0>
- [Tho08] THORLABS: *Datasheet HL6756MG*. <https://www.thorlabs.com/drawings/2c52ee134c600e13-96BC6024-F32D-F8FD-062629D150B7F8C0/HL6756MG-SpecSheet.pdf>. Version: Februar 2008
- [Tsc23] TSCHARN, Benedikt: *A Cold Lithium Beam from a Two-Dimensional Magneto-Optical Trap*, Johannes Gutenberg-Universität, Masterarbeit, August 2023
- [TSF⁺23] THE CREMA COLLABORATION ; SCHUHMANN, Karsten ; FERNANDES, Luis M. P. ; NEZ, François ; AHMED, Marwan A. ; AMARO, Fernando D. ; AMARO, Pedro ; BIRABEN, François ; CHEN, Tzu-Ling ; COVITA, Daniel S. ; DAX, Andreas J. ; DIEPOLD, Marc ; FRANKE, Beatrice ; GALTIER, Sandrine ; GOUVEA, Andrea L. ; GÖTZFRIED, Johannes ; GRAF, Thomas ; HÄNSCH, Theodor W. ; HILDEBRANDT, Malte ; INDELICATO, Paul ; JULIEN, Lucile ; KIRCH, Klaus ; KNECHT, Andreas ; KOTTMANN, Franz ; KRAUTH, Julian J. ; LIU, Yi-Wei ; MACHADO, Jorge ; MONTEIRO, Cristina M. B. ; MULHAUSER, Françoise ; NAAR, Boris ; NEBEL, Tobias ; SANTOS, Joaquim M. F. d. ; SANTOS, José P. ; SZABO, Csilla I. ; TAQUU, David ; VELOSO, João F. C. A. ; VOSS, Andreas ; WEICHEL, Birgit ; ANTOGNINI, Aldo ; POHL, Randolf: The helion charge radius from laser spectroscopy of muonic helium-3 ions. (2023), Mai. <http://dx.doi.org/10.48550/ARXIV.2305.11679>. – DOI 10.48550/ARXIV.2305.11679
- [Ude94] UDEM, Thomas: *Linienprofile der kohärenten Vorwärtsstreuung (CFS) und der Atom-Absorptions-Spektroskopie (AAS) unter Berücksichtigung der Hyperfeinstruktur*. Gießen, Justus-Liebig Universität, Diplomarbeit, 1994. http://www2.mpq.mpg.de/~thu/home/udem_diplom.pdf
- [UMM⁺19] UDEM, Thomas ; MAISENBACHER, Lothar ; MATVEEV, Arthur ; ANDREEV, Vitaly ; GRININ, Alexey ; BEYER, Axel ; KOLACHEVSKY, Nikolai ; POHL, Randolf ; YOST, Dylan C. ; HÄNSCH, Theodor W.: Quantum Interference Line Shifts of Broad Dipole-Allowed Transitions. In: *Annalen der Physik* 531 (2019), Mai, Nr. 5, 1900044. <http://dx.doi.org/10.1002/andp.201900044>. – DOI 10.1002/andp.201900044. – ISSN 0003-3804, 1521-3889

- [VGO⁺20] VIRTANEN, Pauli ; GOMMERS, Ralf ; OLIPHANT, Travis E. ; HABERLAND, Matt ; REDDY, Tyler ; COURNAPEAU, David ; BUROVSKI, Evgeni ; PETERSON, Pearu ; WECKESSER, Warren ; BRIGHT, Jonathan ; WALT, Stéfan J. d. ; BRETT, Matthew ; WILSON, Joshua ; MILLMAN, K. J. ; MAYOROV, Nikolay ; NELSON, Andrew R. J. ; JONES, Eric ; KERN, Robert ; LARSON, Eric ; CAREY, C J. ; POLAT, İlhan ; FENG, Yu ; MOORE, Eric W. ; VANDERPLAS, Jake ; LAXALDE, Denis ; PERKTOLD, Josef ; CIMRMAN, Robert ; HENRIKSEN, Ian ; QUINTERO, E. A. ; HARRIS, Charles R. ; ARCHIBALD, Anne M. ; RIBEIRO, Antônio H. ; PEDREGOSA, Fabian ; MULBREGT, Paul van ; SCI-PY 1.0 CONTRIBUTORS ; VIJAYKUMAR, Aditya ; BARDELLI, Alessandro P. ; ROTHBERG, Alex ; HILBOLL, Andreas ; KLOECKNER, Andreas ; SCOPATZ, Anthony ; LEE, Antony ; ROKEM, Ariel ; WOODS, C. N. ; FULTON, Chad ; MASSON, Charles ; HÄGGSTRÖM, Christian ; FITZGERALD, Clark ; NICHOLSON, David A. ; HAGEN, David R. ; PASECHNIK, Dmitrii V. ; OLIVETTI, Emanuele ; MARTIN, Eric ; WIESER, Eric ; SILVA, Fabrice ; LENDERS, Felix ; WILHELM, Florian ; YOUNG, G. ; PRICE, Gavin A. ; INGOLD, Gert-Ludwig ; ALLEN, Gregory E. ; LEE, Gregory R. ; AUDREN, Hervé ; PROBST, Irvin ; DIETRICH, Jörg P. ; SILTERRA, Jacob ; WEBBER, James T. ; SLAVIČ, Janko ; NOTHMAN, Joel ; BUCHNER, Johannes ; KULICK, Johannes ; SCHÖNBERGER, Johannes L. ; MIRANDA CARDOSO, José V. ; REIMER, Joscha ; HARRINGTON, Joseph ; RODRÍGUEZ, Juan Luis C. ; NUNEZ-IGLESIAS, Juan ; KUCZYNSKI, Justin ; TRITZ, Kevin ; THOMA, Martin ; NEWVILLE, Matthew ; KÜMMERER, Matthias ; BOLINGBROKE, Maximilian ; TARTRE, Michael ; PAK, Mikhail ; SMITH, Nathaniel J. ; NOWACZYK, Nikolai ; SHEBANOV, Nikolay ; PAVLYK, Oleksandr ; BRODTKORB, Per A. ; LEE, Perry ; MCGIBBON, Robert T. ; FELDBAUER, Roman ; LEWIS, Sam ; TYGIER, Sam ; SIEVERT, Scott ; VIGNA, Sebastiano ; PETERSON, Stefan ; MORE, Surhud ; PUDLIK, Tadeusz ; OSHIMA, Takuya ; PINGEL, Thomas J. ; ROBITAILLE, Thomas P. ; SPURA, Thomas ; JONES, Thouis R. ; CERA, Tim ; LESLIE, Tim ; ZITO, Tiziano ; KRAUSS, Tom ; UPADHYAY, Utkarsh ; HALCHENKO, Yaroslav O. ; VÁZQUEZ-BAEZA, Yoshiki: SciPy 1.0: fundamental algorithms for scientific computing in Python. In: *Nat Methods* 17 (2020), März, Nr. 3, 261–272. <http://dx.doi.org/10.1038/s41592-019-0686-2>. – DOI 10.1038/s41592-019-0686-2. – ISSN 1548-7091, 1548-7105
- [Vis22] VISION, Allied: *Guppy F-038B NIR Datasheet*. https://cdn.alliedvision.com/fileadmin/pdf/de/Guppy_F-038B_NIR_DataSheet_de.pdf. Version: Juli 2022
- [VSSH01] VOIGT, D. ; SCHILDER, E. C. ; SPREEUW, R. J. C. ; HEUVELL, H. B. van Linden van d.: Characterization of a high-power tapered semiconductor amplifier system. In: *Applied Physics B* 72 (2001), Februar, Nr. 3, S. 279–284. <http://dx.doi.org/10.1007/s003400100513>. – DOI 10.1007/s003400100513
- [VWB⁺05] VOROZCOVS, Andrejs ; WEEL, Matthew ; BEATTIE, Scott ; CAUCHI, Saviour ; KUMARAKRISHNAN, A.: Measurements of temperature scal-

- ing laws in an optically dense magneto-optical trap. In: *J. Opt. Soc. Am. B* 22 (2005), Mai, Nr. 5, 943. <http://dx.doi.org/10.1364/JOSAB.22.000943>. – DOI 10.1364/JOSAB.22.000943. – ISSN 0740–3224, 1520–8540
- [WEO⁺94] WEIDEMÜLLER, M ; ESSLINGER, T ; OL'SHANII, M. A. ; HEMMERICH, A ; HÄNSCH, T. W.: A Novel Scheme for Efficient Cooling below the Photon Recoil Limit. In: *Europhys. Lett.* 27 (1994), Juli, Nr. 2, 109–114. <http://dx.doi.org/10.1209/0295-5075/27/2/006>. – DOI 10.1209/0295-5075/27/2/006. – ISSN 0295–5075, 1286–4854
- [Wes21] WESTERHOFF, Andreas: *Aufbau einer 2D MOT fuer Lithium*. Mainz, Johannes Gutenberg-Universität, Bachelorarbeit, Mai 2021
- [Wes24] WESTERHOFF, Andreas: *Building a fiber noise cancellation system for a 100 m fiber link*. Mainz, Johannes Gutenberg-Universität, Masterarbeit, Februar 2024
- [Wie19] WIELTSCH, Andreas: *Particle tracking simulation of atoms under magneto-optical influence*. Mainz, Johannes Gutenberg-Universität, Masterarbeit, April 2019
- [Zap04] ZAPPE, Hans: *Laser Diode Microsystems*. Berlin Heidelberg : Springer, 2004 <https://doi.org/10.1007/978-3-662-08249-2>. – ISBN 978–3–662–08249–2. – OCLC: 1184481095

A. Appendix: Diodes

Semiconductors [SNL21] are most commonly considered to be members of the fourth main group of the periodic table, as depicted in fig. A.1, such as $_{14}\text{Si}$ or $_{32}\text{Ge}$. By introducing impurities in the form of other elements, e.g. $_{5}\text{B}$ or $_{51}\text{Sb}$, the material can be doped to add holes (p-doped) or electrons (n-doped) as charge carriers. Another way to build a semiconductor is to combine elements of the third and fifth main group to form a so-called III-V-semiconductor whose valence and carrier bands depend on the specific mix of its constituents. There also exist II-VI-semiconductors or organic semiconductors which are not considered here as the described laser diode consists of aluminum gallium indium phosphide (AlGaInP) which is a III-V-semiconductor.

Period	I		II		Lanthanides, Actinides and Transition Metals												Group					
	III		IV		V		VI		VII		VIII											
1	1 H																		2 He			
2	3 Li	4 Be					5 B	6 C	7 N	8 O	9 F	10 Ne										
3	11 Na	12 Mg					13 Al	14 Si	15 P	16 S	17 Cl	18 Ar										
4	19 K	20 Ca					31 Ga	32 Ge	33 As	34 Se	35 Br	36 Kr										
5	37 Rb	38 Sr					49 In	50 Sn	51 Sb	52 Te	53 I	54 Xe										
6	55 Cs	56 Ba					81 Tl	82 Pb	83 Bi	84 Po	85 At	86 Rn										
7	87 Fr	88 Ra					113 Nh	114 Fl	115 Mc	116 Lv	117 Ts	118 Og										

Alkali metals	Alkaline earth metals	Halogens	Noble gases
Poor metals	Metalloids	Nonmetals	

Figure A.1: Excerpt of the periodic table. Note that the elements that comprise the used material AlGaInP are members of the third ($_{13}\text{Al}$, $_{31}\text{Ga}$, $_{49}\text{In}$) and fifth ($_{15}\text{P}$) main group. Picture taken from [Arm07].

Imagine a p-doped and an n-doped material joined together as depicted in fig. A.2. At their interface they form a p-n junction where their respective valence and conduction bands transition into each other. By applying a positive voltage to the p-side and a negative voltage to the n-side, electrons flow from the n- to p-doped

region⁴⁶. This corresponds to a flow from right to left in fig. A.2. The Fermi level E_F , i.e. the hypothetical energy level of an electron with a probability of being occupied of 50 % at thermal equilibrium, is just below the conduction band of the n-doped material. Therefore not much energy has to be added to lift an electron to it so that it can flow through the material to the p-doped material and subsequently to the anode.

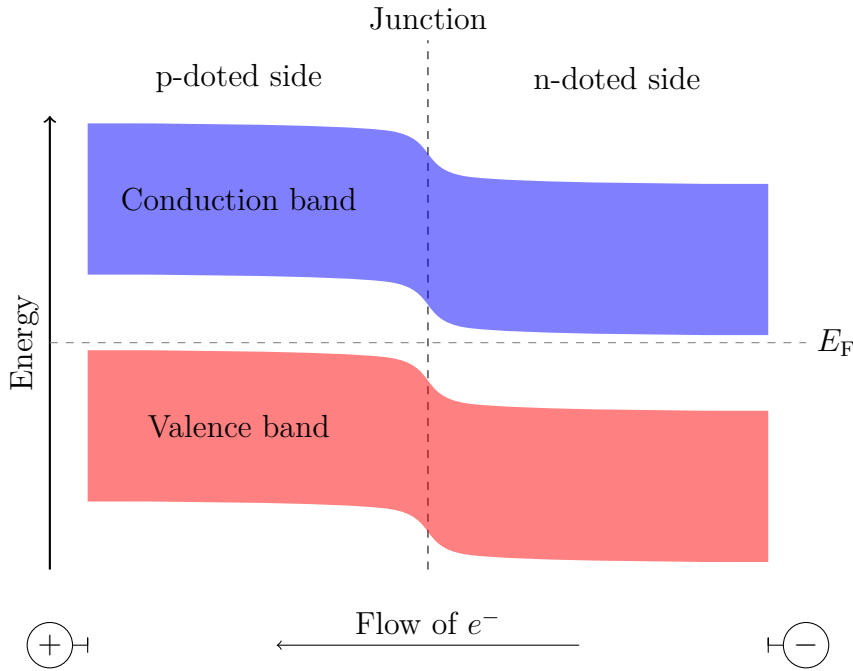


Figure A.2: A p-doped and an n-doped semiconductor joined together form a p-n junction. If a positive voltage is applied to the p-doped side and a negative to the n-doped site, electrons can flow through the material.

If the situation is reversed, i.e. the n-side is connected to the positive voltage and the p-side to the negative, the direction of current is from left to right in the above fig. A.2. However, it takes much more energy to lift an electron to the conduction band on the p-side and thus no current flows unless the voltage is sufficiently high. A component that allows current flow in one direction but forbids it in the other is called a diode. The relation between the applied voltage V and the current I is given by the Shockley equation:

$$I = I_0 \cdot \left(e^{\frac{qV}{k_B T}} - 1 \right), \quad (\text{A.1})$$

where

$$I_0 = \frac{qD_p n_i^2}{L_p N_D} + \frac{qD_n n_i^2}{L_n N_A}. \quad (\text{A.2})$$

The many coefficients of eq. (A.2) depend on the used semiconductor materials while eq. (A.1) describes the general relation which depends on the charge carrier

⁴⁶Remember that this is the physical current: electrons flow from a negative to a positive potential. The technical current flows from positive to negative.

q , i.e. electrons and holes in our case, and the applied voltage V , more specifically their product qV which is the energy of the charge carrier. Additionally, the thermal energy $k_B T$ with k_B being the Boltzmann constant and T being the temperature affect the current. The current's dependency of the applied voltage is plotted in fig. A.3. Some conclusions can be drawn from eq. (A.1):

- Obviously, if no voltage is applied ($V = 0$) no current will flow.
- A positive voltage leads to an exponentially increasing current.
- A negative voltage leads to a small constant current $-I_0$, the reverse-bias saturation current. A diode forbids current flow in reverse direction but a tiny drift is possible because electrons can tunnel from the p-side valence band to the n-side conduction band.
- An increase in temperature decreases the exponent $qV/k_B T$. This doesn't necessarily lead to smaller currents because I_0 is also temperature dependent and might compensate said decrease.

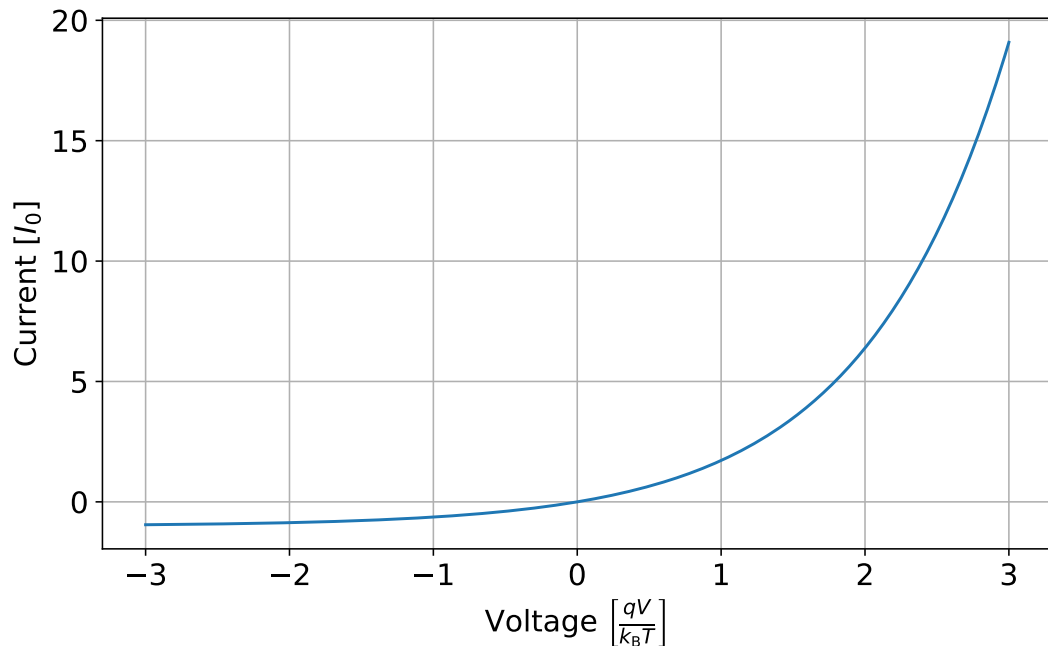


Figure A.3: Relation between current and voltage applied to a diode. The voltage corresponds to the electric potential on the p-doped side compared to the n-doped side's potential. Notice that the axes are normalized to make them dimensionless.

The current amplitude I_0 is given by eq. (A.2) and depends on the charge densities of electron donor and acceptors N_D and N_A of the depletion layer around the p-n junction, the Debye length L_x , the Einstein relation $D_x = (k_B T/q) \mu_x$ where

μ_x is the movability of the charge carriers (electrons and holes), and the product of minority charge carrier densities n_i^2 . These coefficients are solely dependent of the material's composition and its temperature.

B. Appendix: The Fabry-Pérot Cavity

In its most simple form, a Fabry-Pérot cavity consists of an etalon with two parallel facets of distance d as depicted in fig. B.1. This distance is to be understood as the optical path length, i.e. it is medium- and refraction index-independent. Although the laser beam is drawn at an angle, it is considered to be orthogonal to the facets. This is only done to better differentiate the order of reflection.

A laser beam enters the cavity and by passing the first facet with transmission coefficient $T < 1$ and reflection coefficient $R < 1$, the amplitude of its electric field changes by a factor of \sqrt{T} . The beam passes the etalon and gains a phase depending on d and its wavenumber k . The resulting transmitted electric field is then

$$E_1 = E_0 \cdot T \cdot e^{-ikd},$$

where E_0 describes the incoming electric field.

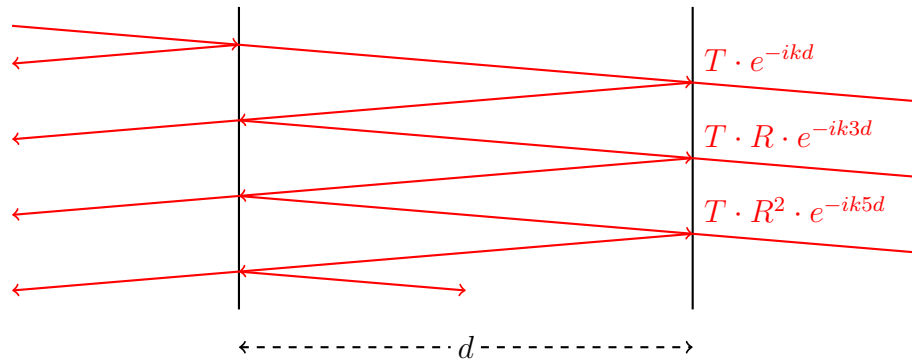


Figure B.1: Phase shift in a Fabry-Pérot cavity. Red light enters the cavity of length d from the left side and is emitted from the right side. The beam is only drawn at an angle to make differentiation between the reflections easier. As the light leaves the cavity, it has acquired a phase and an amplitude change depending on its path.

The reflected beam on the other hand returns to the first facet where it is again partly transmitted or reflected. This repeats again and again and every pass through the cavity leads to an additional component of the electric field at the output facet:

$$\begin{aligned} E_2 &= E_0 \cdot T \cdot R \cdot e^{-ik3d}, \\ E_3 &= E_0 \cdot T \cdot R^2 \cdot e^{-ik5d}, \\ E_4 &= E_0 \cdot T \cdot R^3 \cdot e^{-ik7d}, \\ &\dots \\ E_n &= E_0 \cdot T \cdot R^{n-1} \cdot e^{-ik(2n-1)d}. \end{aligned}$$

These field components evolve like a geometric series and the total electric field is therefore quickly evaluated to

$$E_{\text{total}} = \frac{T e^{-ikd}}{1 - R \cdot e^{-ik2d}}$$

and the outgoing intensity becomes

$$I_{\text{out}} = \frac{cn\epsilon_0}{2} E_{\text{total}} E_{\text{total}}^* = \frac{cn\epsilon_0}{2} \frac{T^2}{1 + R^2 - 2R \cos(k2d)},$$

with the speed of light c , the refractive index of the outside medium n (not to be confused with the counting index n in the equation further above), and the vacuum permittivity ϵ_0 . It's easy to see, that the intensity becomes maximum for $\cos(k2d) = 1$. With $k = \frac{2\pi}{\lambda}$, this results in the condition

$$\frac{2d}{\lambda} = m. \quad (\text{B.1})$$

The intensity is maximum if the etalon's size is a multiple ($m \in \mathbb{N}^+$) of half the wavelength. Translated to frequency, the m -th resonance frequency becomes

$$\nu_m = \frac{mc}{2d}. \quad (\text{B.2})$$

The free spectral range (FSR), i.e. the difference between the m -th and the $m + 1$ -th resonance, and the full width at half maximum (FWHM) of the resonances are constants that depend solely on the size of the cavity and the reflectivity of its facets:

$$\text{FSR} = \frac{c}{2d}, \quad (\text{B.3})$$

$$\text{FWHM} = \frac{c}{\pi d} \arccos \left(2 - \frac{1 + R^2}{2R} \right). \quad (\text{B.4})$$

The shorter the cavity, the further the resonances are from each other and the higher the reflectivity, the narrower and the better defined are they.

These equations are true for all cavities and are not specific for the Fabry-Pérot cavity. Without curved facets, which focus the laser within the cavity, the beam becomes larger with every transit. After the first transit, the electrical field of a gaussian beam that already traveled a distance z_0 from its waist position outside the cavity is given by

$$E_1(r) = E_0 \cdot T \cdot \frac{w_0}{w(z_0 + d)} \cdot e^{-\left(\frac{r}{w(z_0 + d)}\right)^2} e^{-ik \frac{r^2}{R(z_0 + d)}} e^{-i(kz_0 + kd - \zeta(z_0 + d))} \quad (\text{B.5})$$

with

$$w(z) = w_0 \sqrt{1 + \left(\frac{z}{z_R}\right)^2}, \quad (\text{B.6})$$

$$R(z) = z \left(1 + \left(\frac{z_R}{z}\right)^2\right), \quad (\text{B.7})$$

$$\zeta(z) = \arctan\left(\frac{z}{z_R}\right). \quad (\text{B.8})$$

Here, w_0 is the beam's waist and z_R is its Rayleigh length. Each additional double-transition through the cavity adds another electric field

$$E_n(r) = E_0 \cdot T \cdot R^{n-1} \cdot \frac{w_0}{w(z_0 + (2n-1)d)} \cdot e^{-\left(\frac{r}{w(z_0 + (2n-1)d)}\right)^2} \cdot e^{-ik\frac{r^2}{R(z_0 + (2n-1)d)}} \cdot e^{-i(kz_0 + k(2n-1)d - \zeta(z_0 + (2n-1)d))} \quad (\text{B.9})$$

and the total electrical field becomes too complicated to be expressed by a geometric series. The real laser beam which is emitted by a Fabry-Pérot cavity is therefore not a simple gaussian beam but can show a diffraction pattern as depicted in fig. B.2.

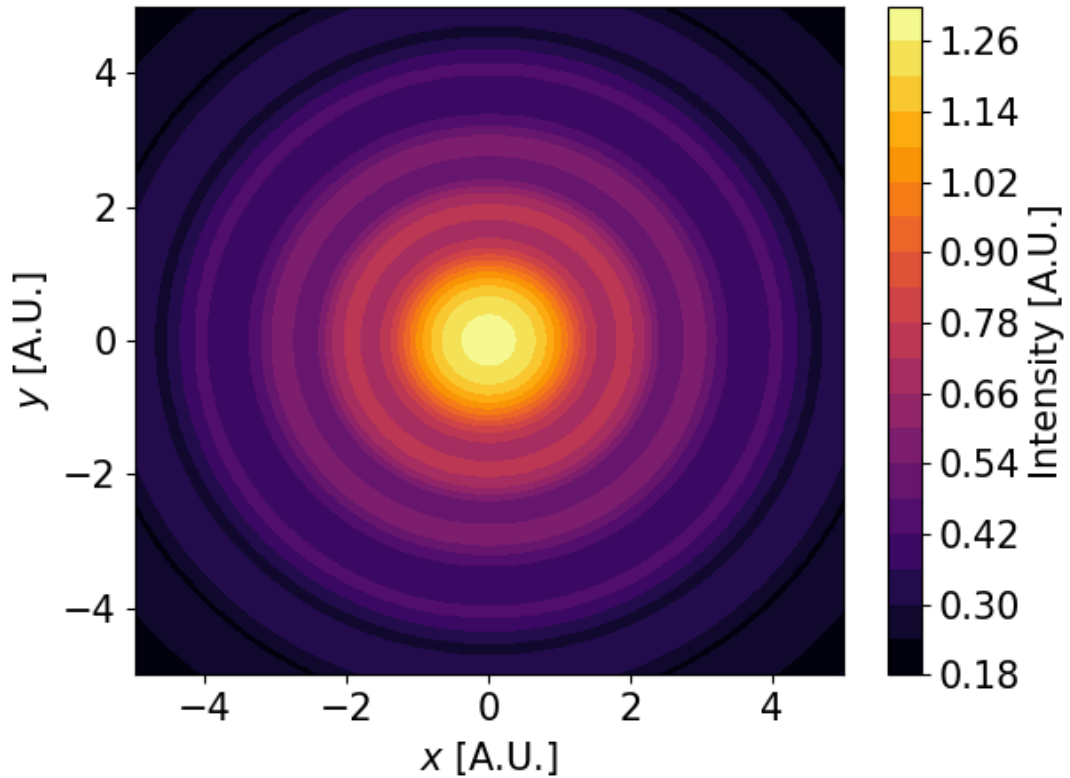


Figure B.2: Simulated Fabry-Pérot cavity transmitted intensity.

C. Appendix: Optical Elements

Many different elements are used in the various optical setup of this thesis. Some of the more interesting ones are discussed in the following section. Any reader who wants to learn more about optics, the nature of electro-magnetic waves, and their behavior is highly advised to take a look at [AH19].

C.1. Beam Splitter

Beam splitters that, as their name suggests, split a beam that enters the element into two parts that are emitted from two separate output port. Although one might plainly use a simple semi-transparent plate with transparency T and reflectivity R , the splitters that were used during this work were beam splitter cubes as depicted in fig. C.1. In this thesis,

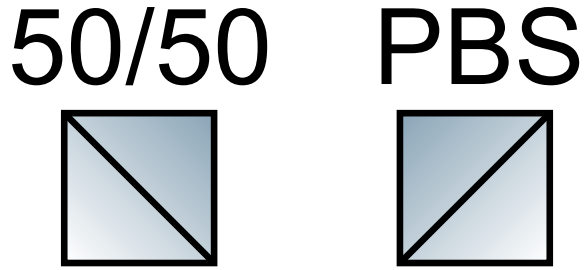


Figure C.1: 50/50 and polarizing beam splitter cubes.

both are represented by the same symbol, their type is specified by annotations.

Both kinds essentially consist of two prisms that are glued together at their bases with a resin which forms a very thin layer between the prisms. On one hand, this resin fills up all the space between the prisms, leaves no gaps and form a layer of constant refractive index n_L . On the other hand, its refractive index is slightly smaller than the one of the prisms' substrate n_S . On the first interface from n_S to n_L , total reflection can occur. The incoming beam is reflected in a 90° angle.

An electric field \vec{E} , such as the electric field of the laser beam, cannot abruptly drop to zero because

$$\vec{\nabla} \cdot \vec{E} = \frac{\rho}{\epsilon_0}.$$

A small fraction of the light, the so-called evanescent wave, enters the resin where its amplitude decreases the further it propagates into the medium. As the resin layer is very thin, the field can reach the second prism and a fraction of the intensity is effectively transmitted: a phenomenon called frustrated total internal reflection.

By adjusting the thickness of the resin layer as well as its composition, the ratio between transmitted and reflected intensity can be adjusted. Most often, it is 50/50. The polarizing beam splitter cube contains multiple layers of alternating resins with refractive indices $n_{L,1}$ and $n_{L,2}$. At the interface of these materials, the laser beam with angle of incident θ_i is partially reflected ($\theta_r = -\theta_i$) and partially transmitted following Snell's law

$$n_{L,1} \cdot \sin(\theta_i) = n_{L,2} \cdot \sin(\theta_t).$$

If $\theta_i + \theta_t = 90^\circ$, i.e. the beam hits the interface at Brewster's angle,

$$\theta_B = \arctan\left(\frac{n_{L,2}}{n_{L,1}}\right),$$

the reflected beam is purely s-polarized, while the transmitted beam contains more p-polarized than s-polarized light. By adjusting the materials' refractive indices it is possible to get θ_B close to 45° . Many of these layers will thus filter out all s-polarized components of the transmitted beam and all p-polarized parts of the reflected beam. This is the working principle of the polarizing beam splitter (PBS).

C.2. Retarder Plates

Imagine a retarder plate made out of birefringent material with two refractive indices n_{fast} and n_{slow} , corresponding to two orthogonal main axes: a slow and a fast axis. In the following, the x -axis is treated as the fast axis, where the speed of light is

$$c_{\text{fast}} = \frac{c}{n_{\text{fast}}} > c_{\text{slow}} = \frac{c}{n_{\text{slow}}}.$$

When light of wavelength λ and polarization

$$\frac{\vec{E}_0}{|\vec{E}_0|} = \frac{1}{\sqrt{2}} \begin{pmatrix} 1 \\ \pm 1 \end{pmatrix}$$

passes such a material of thickness d , both components gain a phase

$$\begin{pmatrix} e^{-2\pi i \frac{n_{\text{fast}} \cdot d}{\lambda}} \\ e^{-2\pi i \frac{n_{\text{slow}} \cdot d}{\lambda}} \end{pmatrix} \hat{=} \begin{pmatrix} 1 \\ e^{-2\pi i \frac{(n_{\text{slow}} - n_{\text{fast}}) \cdot d}{\lambda}} \end{pmatrix}.$$

By adjusting d , the relative phase

$$\Delta\phi(d) = 2\pi \frac{(n_{\text{slow}} - n_{\text{fast}}) \cdot d}{\lambda}$$

can be set. Different polarization vectors are listed in table C.1, shown below. These special polarization vectors reveal two special $\Delta\phi$:

$$\Delta\phi|_{d=(2m+1) \cdot \frac{\lambda}{2(n_{\text{slow}} - n_{\text{fast}})}} = (2m + 1) \cdot \pi, \quad (\text{C.1})$$

$$\Delta\phi|_{d=(2m+1) \cdot \frac{\lambda}{4(n_{\text{slow}} - n_{\text{fast}})}} = (2m + 1) \cdot \frac{\pi}{2}, \quad (\text{C.2})$$

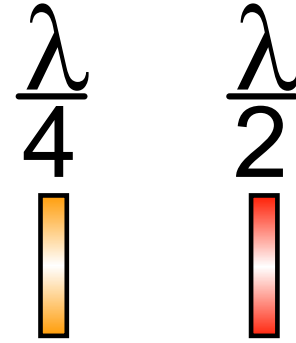


Figure C.2: Quarter-wave plate and half-wave plate.

with $m \in \mathbb{N}$. Retarder plates that satisfy the first condition are called $\frac{\lambda}{2}$ - or half-wave plates, while those that fulfill the second one are $\frac{\lambda}{4}$ - or quarter-wave plates, both depicted in fig. C.2. For $m = 0$, these plates are zero-order plates. They are usually more temperature and wavelength independent than multi-order plates with higher m . A half-wave plate turns one linear polarization into a different one by mirroring the Jones vector on the fast axis. With the correct angle of the retarder plate, horizontal polarization can be turned into vertical and vice versa. Combining a half-wave plate with a PBS makes a very simple setup for controlling a laser beam's power and polarization. The quarter-wave plate will turn linear polarization to elliptical polarization (even circular polarization for the correct angle). The handedness depends on the exact order m .

Circular polarized light that passes a $\frac{\lambda}{2}$ -plate changes its handedness independent on the plates angle. A $\frac{\lambda}{4}$ -plate turns any handedness into linear polarization. Again, here the specific resulting polarization depends on the plates angle and order.

Table C.1: Special light polarizations and their corresponding polarization vectors.

Linear horizontal	$v_{\text{H}} = \begin{pmatrix} 1 \\ 0 \end{pmatrix}$
Linear vertical	$v_{\text{V}} = \begin{pmatrix} 0 \\ 1 \end{pmatrix}$
Circular right-handed	$v_{\text{R}} = \frac{1}{\sqrt{2}} \begin{pmatrix} 1 \\ -i \end{pmatrix}$
Circular left-handed	$v_{\text{L}} = \frac{1}{\sqrt{2}} \begin{pmatrix} 1 \\ i \end{pmatrix}$

C.3. Optical Isolator

Some materials, e.g. many crystal, exhibit birefringence behavior. Linear light that passes lithium niobate (or calcite or rutile or many others) gains a phase which depends on the angle of its polarization. But there are also many materials, such as sugars or terbium gallium garnet crystals within a magnetic field, which show optical activity and are circular birefringence. Circular left- and right-handed light that pass such media experience different refractive indices n_L and n_R . The occurrence of optical activity in a magnetic field is the so-called Faraday effect.

An optical isolator, as it is shown in fig. C.3, comprises at least two polarization filters (here, polarizing beam splitter cubes) and a material in a strong magnetic field which exhibits the Faraday effect. Only linear polarized light passes the first filter. It is therefore assumed, that the light's polarization is given by

$$\begin{aligned} \frac{\vec{E}_0}{|\vec{E}_0|} &= \begin{pmatrix} 1 \\ 0 \end{pmatrix} \\ &= \frac{1}{2} \left(\begin{pmatrix} 1 \\ i \end{pmatrix} + \begin{pmatrix} 1 \\ -i \end{pmatrix} \right) \\ &= \frac{1}{\sqrt{2}} (v_L + v_R), \end{aligned}$$

where v_L and v_R are the Jones vectors of circular left- and right-handed polarization as listed in table D.1. Every wave can be understood as the superposition of at least two other waves and so linear polarized light can be expressed as a superposition of v_L and v_R . Both polarizations experience a phase shift when they pass a medium of length d depending on the light's wavelength λ :

$$\begin{aligned} \frac{\vec{E}'_0}{|\vec{E}'_0|} &= \frac{1}{\sqrt{2}} \left(v_L \cdot e^{-2\pi i \frac{n_L \cdot d}{\lambda}} + v_R \cdot e^{-2\pi i \frac{n_R \cdot d}{\lambda}} \right) \\ &= \frac{e^{-2\pi i \frac{(v_L + v_R) \cdot d}{2\lambda}}}{2} \left(e^{-2\pi i \frac{(v_L - v_R) \cdot d}{2\lambda}} + e^{2\pi i \frac{(v_L - v_R) \cdot d}{2\lambda}} \right) \\ &\hat{=} \begin{pmatrix} \cos \left(2\pi \frac{(v_L - v_R) \cdot d}{2\lambda} \right) \\ \sin \left(2\pi \frac{(v_L - v_R) \cdot d}{2\lambda} \right) \end{pmatrix} \end{aligned}$$

The polarization of the incoming light is rotated, hence the component's name being Faraday rotator. This rotation is independent of the light beam's direction and by

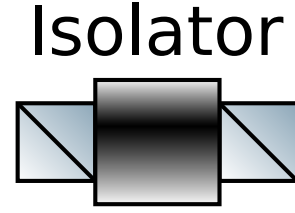


Figure C.3: Optical Isolator.

adjusting d a rotation of 45° for a specific λ can be generated⁴⁷.

After the light passed the first filter and the Faraday rotator, it reaches the second filter. Ideally, this filter is turned by 45° compared to the first filter. Light that travels in this forward direction can also pass the second filter and is hence transmitted by the optical isolator.

Light that travels backwards through the setup is first polarized by the second filter. The optically active material rotates the light by 45° . This results in a polarization which is not transmitted by the first filter, but reflected, e.g. into a beam dump. In the backward direction, the light cannot pass the setup. This way, an optical isolator can protect sensitive elements such as a laser diode or tapered amplifier from back reflections. It also prevents the formation of unwanted cavities within a setup.

⁴⁷ 45° is only the ideal case. Often the polarization filters have to be adjusted to minimize transmission in backwards direction.

D. Appendix: MOT Laser Polarization and Jones Calculus

A MOT can only trap atoms if its laser beams are polarized correctly. A setup as depicted in fig. 4.4 ensures this via multiple quarter-wave plates. This can be explained best by using the formalism of Jones calculus [Jon41].

In vacuum, light can be described as a purely transversal electromagnetic wave and in this specific and most other experiments the longitudinal component is negligible. Its polarization can therefore be described using a two-dimensional vector containing the information of the horizontal and vertical polarization components, i.e. their amplitudes and their relative phases.

The electromagnetic field is usually completely characterized by

$$\vec{E}(t, \vec{r}) = E_0 \begin{pmatrix} a \\ be^{i\phi} \end{pmatrix} e^{i(\omega t - \vec{k} \cdot \vec{r})}. \quad (\text{D.1})$$

Many of these parameters are not important to describe the polarization of the light. They are either constant amplitudes E_0 or phases that change with time or position $\omega t - \vec{k} \cdot \vec{r}$. Only the relative phase ϕ and the coefficients $a^2 + b^2 = 1$ between the horizontal and the vertical polarization matter and four special cases can be identified that are listed in table D.1: horizontal, vertical, right-handed, and left-handed polarization.

Table D.1: Special light polarizations and their corresponding Jones vectors.

Linear horizontal	$v_{\text{H}} = \begin{pmatrix} 1 \\ 0 \end{pmatrix}$
Linear vertical	$v_{\text{V}} = \begin{pmatrix} 0 \\ 1 \end{pmatrix}$
Circular right-handed	$v_{\text{R}} = \frac{1}{\sqrt{2}} \begin{pmatrix} 1 \\ -i \end{pmatrix}$
Circular left-handed	$v_{\text{L}} = \frac{1}{\sqrt{2}} \begin{pmatrix} 1 \\ i \end{pmatrix}$

Different optical elements, such as polarization filters, quarter-wave plates, and mirrors, can change the polarization of light. Mathematically this is expressed by element-dependent matrices that act on the light's Jones vector. Some exemplary matrices are listed in table D.2.

Table D.2: Special polarization shifting optical elements and their corresponding Jones matrices.

Horizontal Polarizer	$M_{H,P} =$	$\begin{pmatrix} 1 & 0 \\ 0 & 0 \end{pmatrix}$
Polarizer (any angle θ)	$M_P(\theta) =$	$\begin{pmatrix} \cos^2(\theta) & \cos(\theta)\sin(\theta) \\ \cos(\theta)\sin(\theta) & \sin^2(\theta) \end{pmatrix}$
$\frac{\lambda}{4}$ -plate (fast axis = horizontal)	$M_{H,\frac{\lambda}{4}} =$	$e^{-i\frac{\pi}{4}} \begin{pmatrix} 1 & 0 \\ 0 & i \end{pmatrix}$
$\frac{\lambda}{4}$ -plate (any angle θ)	$M_{\frac{\lambda}{4}}(\theta) =$	$e^{-i\frac{\pi}{4}} \begin{pmatrix} \cos^2(\theta) + i\sin^2(\theta) & (1-i)\cos(\theta)\sin(\theta) \\ (1-i)\cos(\theta)\sin(\theta) & \sin^2(\theta) + i\cos^2(\theta) \end{pmatrix}$
$\frac{\lambda}{2}$ -plate (any angle θ)	$M_{\frac{\lambda}{2}}(\theta) =$	$\begin{pmatrix} \cos(2\theta) & \sin(2\theta) \\ \sin(2\theta) & -\cos(2\theta) \end{pmatrix}$
Mirror	$M_M =$	$\begin{pmatrix} 1 & 0 \\ 0 & -1 \end{pmatrix}$

Some consequences for the setup can be deduced quite simply. An arbitrarily linear polarized beam (angle α) enters the corresponding first quarter-wave plate which changes the polarization according to

$$M_{\frac{\lambda}{4}}(\theta) \begin{pmatrix} \cos(\alpha) \\ \sin(\alpha) \end{pmatrix} = \frac{1}{\sqrt{2}} \begin{pmatrix} \cos(\alpha) - i\cos(\alpha - 2\theta) \\ \sin(\alpha) + i\sin(\alpha - 2\theta) \end{pmatrix}.$$

To generate circular polarized light with the correct handedness, the angle θ has to be set carefully to $\alpha \pm \frac{\pi}{4}$ to allow for maximum trapping efficiency. The circular polarized light then passes a second quarter-wave plate. Assuming right-handed light and an arbitrary angle θ'

$$M_{\frac{\lambda}{4}}(\theta') v_R = \frac{e^{-i(\theta' + \frac{\pi}{4})}}{\sqrt{2}} \begin{pmatrix} \cos(\theta') - \sin(\theta') \\ \cos(\theta') + \sin(\theta') \end{pmatrix}$$

the resulting polarization is always linear. Its exact composition might depend on θ' and a negligible phase is added but these facts don't matter. Therefore, the exact adjustment of the second quarter-wave plate also doesn't matter. The same holds true if left-handed light is assumed.

Because the value of the second quarter-wave plate's angle θ' is not important, it can be assumed to be $\theta' = 0$ without changing the physical outcome. Right-handed light passes the second quarter-wave plate, is reflected by a mirror and passes the same quarter-wave plate again or in the language of Jones calculus:

$$M_{H,P} M_M M_{H,P} v_R = v_R e^{-i\frac{\pi}{2}}.$$

This specific setup only adds a negligible phase to the light but keeps the handedness. Again, assuming left-handed light results in an equivalent outcome. The quarter-wave plates are absolutely necessary for a functioning MOT setup.

E. Appendix: ${}^6\text{Li } 2P_{3/2}$ excited state

As explained in section 3.2, the anomalous Zeeman effect can be considered as a perturbation on an atom's hyperfine structure or vice versa, depending on the value of the applied magnetic field. It is therefore better to treat both of them as a perturbation on the fine structure.

The $2P_{3/2}$ state comprises 12 substates, twice the amount of the $2S_{1/2}$ ground state and consequently the interaction Hamiltonian \hat{H}_{int} (shown below in eq. (E.1)) contains four times as many entries. It is calculated according to eq. (3.12) with the following parameters:

$$\begin{aligned} I &= 1, \\ J &= \frac{3}{2}, \\ A_{2P_{3/2}} &= -1.15 \text{ MHz}, \\ B_{2P_{3/2}} &= -0.1 \text{ MHz}, \\ g_J &= 1.335. \end{aligned}$$

The single parameters A_i are

$$A_1 = -0.08 \text{ MHz} \cdot h, \quad (\text{E.2})$$

$$A_2 = -14.01 \text{ MHz} \cdot h, \quad (\text{E.3})$$

$$A_3 = 0.06 \text{ MHz} \cdot h \quad (\text{E.4})$$

$$A_4 = -9341.89 \frac{\text{MHz}}{\text{mT}} \cdot h, \quad (\text{E.5})$$

$$A_5 = -0.58 \text{ MHz} \cdot h, \quad (\text{E.6})$$

$$A_6 = 0.03 \text{ MHz} \cdot h \quad (\text{E.7})$$

$$A_7 = -28\,070.94 \frac{\text{MHz}}{\text{mT}} \cdot h, \quad (\text{E.8})$$

$$A_8 = 1.72 \text{ MHz} \cdot h, \quad (\text{E.9})$$

$$A_9 = 0.05 \text{ MHz} \cdot h \quad (\text{E.10})$$

$$A_{10} = -1.63 \text{ MHz} \cdot h. \quad (\text{E.11})$$

Due to the larger number of potentially interacting states, the eigenvalues of \hat{H}_{int} , i.e. the energy levels depending on B , aren't derived as straightforward for $2P_{3/2}$ compared to $2S_{1/2}$. The states that can be expressed easily have the eigenvalues

$$\langle 11 | \hat{H}_{\text{int}} | 11 \rangle (B) = -A_6 - A_8 - A_7 \cdot B, \quad (\text{E.12})$$

$$\langle 10 | \hat{H}_{\text{int}} | 10 \rangle (B) = -A_6 - A_8 + A_7 \cdot B, \quad (\text{E.13})$$

$$\langle 0 | \hat{H}_{\text{int}} | 0 \rangle (B) = \frac{1}{2}(A_5 + A_6 + A_9 - (A_4 + A_7) \cdot B - \sqrt{4(A_2 - A_3)^2 + (A_5 + A_6 - A_9 - A_4 \cdot B + A_7 \cdot B)^2}), \quad (\text{E.14})$$

$$\langle 1 | \hat{H}_{\text{int}} | 1 \rangle (B) = \frac{1}{2}(A_5 + A_6 + A_9 - (A_4 + A_7) \cdot B + \sqrt{4(A_2 - A_3)^2 + (A_5 + A_6 - A_9 - A_4 \cdot B + A_7 \cdot B)^2}), \quad (\text{E.15})$$

$$\langle 5 | \hat{H}_{\text{int}} | 5 \rangle (B) = \frac{1}{2}(A_5 + A_6 + A_9 + (A_4 + A_7) \cdot B - \sqrt{4(A_2 - A_3)^2 + (A_5 + A_6 - A_9 + A_4 \cdot B - A_7 \cdot B)^2}), \quad (\text{E.16})$$

$$\langle 6 | \hat{H}_{\text{int}} | 6 \rangle (B) = \frac{1}{2}(A_5 + A_6 + A_9 + (A_4 + A_7) \cdot B + \sqrt{4(A_2 - A_3)^2 + (A_5 + A_6 - A_9 + A_4 \cdot B - A_7 \cdot B)^2}). \quad (\text{E.17})$$

The numbering of the states $|i\rangle$ is the same as listed in table 3.7. As a reminder, they are also listed below. The other half of the eigenvalues are more complex and require the determination of the zero-crossings of two cubic equations. These equations and their solutions are not listed here.

By solving these equations for various fields B and determining the eigenstates EV , the transition strengths could be calculated according to eq. (3.23). They are

depicted in fig. E.1, fig. E.2, fig. E.3, fig. E.4, fig. E.5, and fig. E.6. Note that the closed circle transitions $5 \rightarrow 11$ and $4 \rightarrow 10$ are not depending on B .

Table E.1: Reminder: $2P_{3/2}$ eigenstates of ${}^6\text{Li}$ and the corresponding $|F, m_F\rangle$ states for small magnetic fields B .

State Number	Corresponding $ F, m_F\rangle$
0	$ \frac{5}{2}, \frac{3}{2}\rangle$
1	$ \frac{3}{2}, \frac{3}{2}\rangle$
2	$ \frac{5}{2}, -\frac{1}{2}\rangle$
3	$ \frac{1}{2}, -\frac{1}{2}\rangle$
4	$ \frac{3}{2}, -\frac{1}{2}\rangle$
5	$ \frac{5}{2}, -\frac{3}{2}\rangle$
6	$ \frac{3}{2}, -\frac{3}{2}\rangle$
7	$ \frac{1}{2}, \frac{1}{2}\rangle$
8	$ \frac{5}{2}, \frac{1}{2}\rangle$
9	$ \frac{3}{2}, \frac{1}{2}\rangle$
10	$ \frac{5}{2}, -\frac{5}{2}\rangle$
11	$ \frac{5}{2}, \frac{5}{2}\rangle$

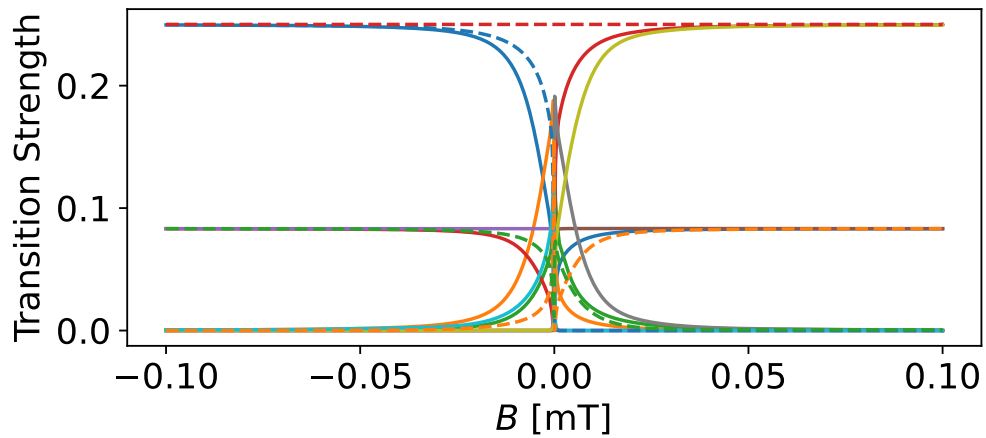


Figure E.1: Strength of allowed transitions driven by σ^+ -polarized light for different magnetic field strengths. Same picture as fig. 3.7.

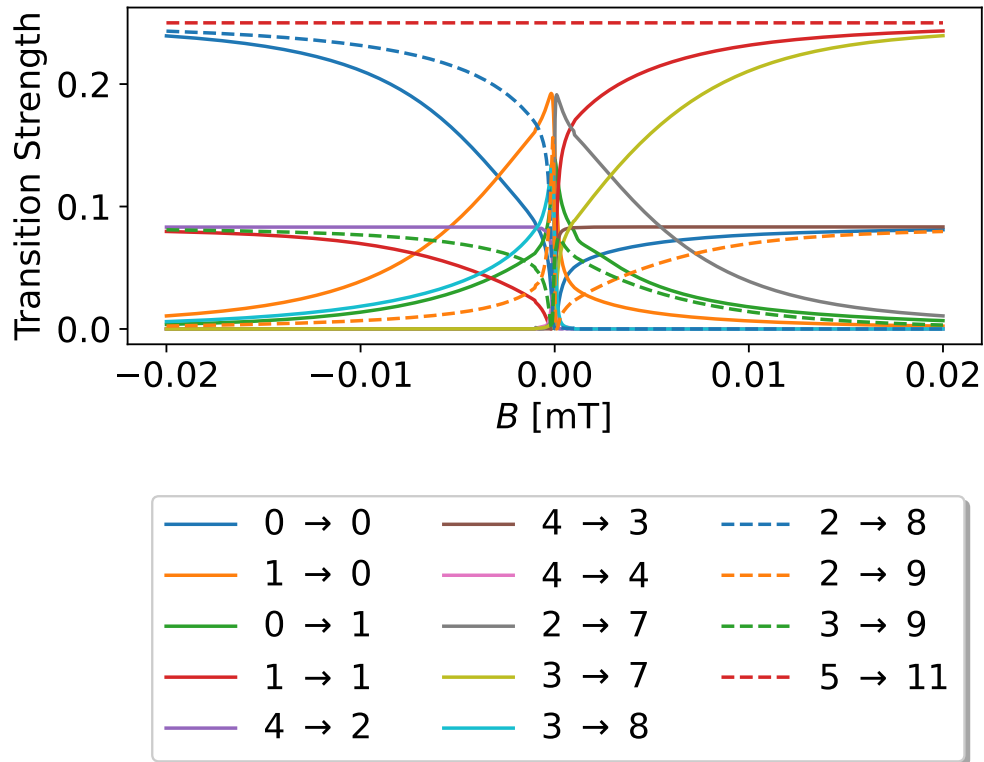


Figure E.2: Strength of allowed transitions driven by σ^+ -polarized light for different magnetic field strengths. Zoomed in version of fig. E.1.

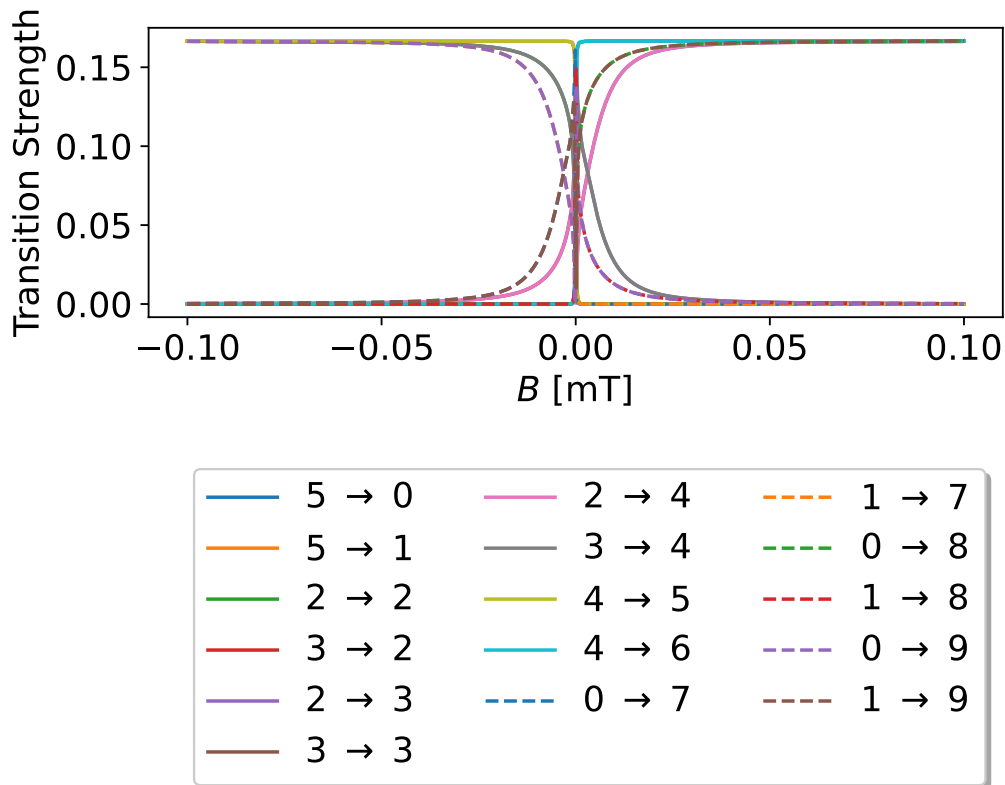


Figure E.3: Strength of allowed transitions driven by π -polarized light for different magnetic field strengths.

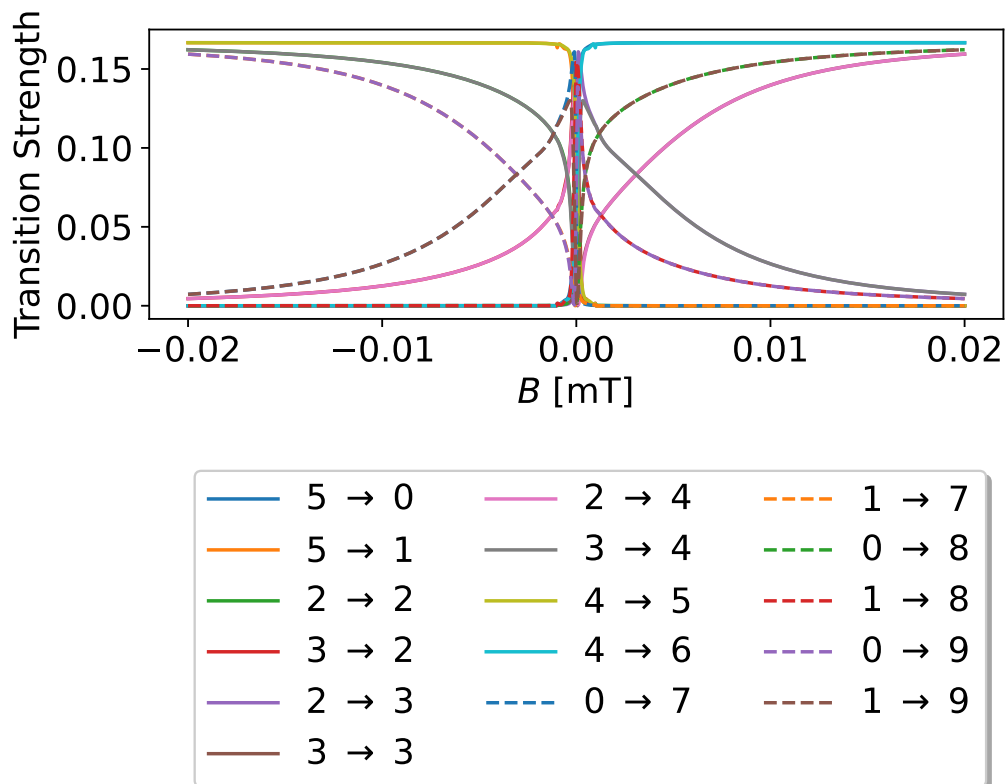


Figure E.4: Strength of allowed transitions driven by π -polarized light for different magnetic field strengths. Zoomed in version of fig. E.3.

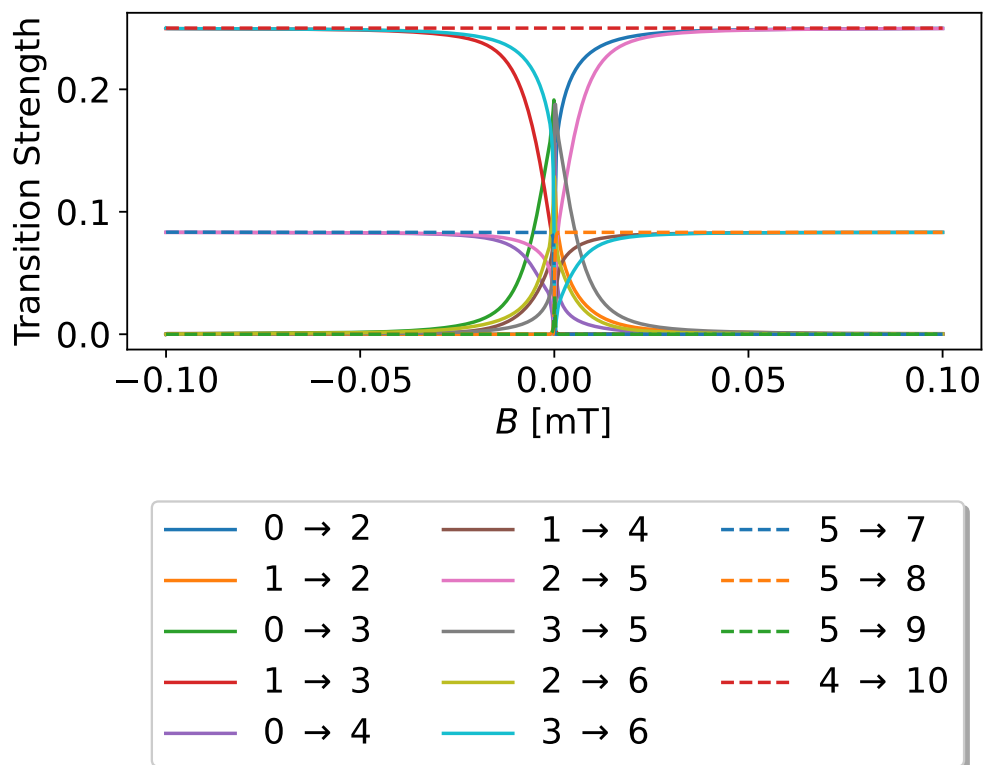


Figure E.5: Strength of allowed transitions driven by σ^- -polarized light for different magnetic field strengths.

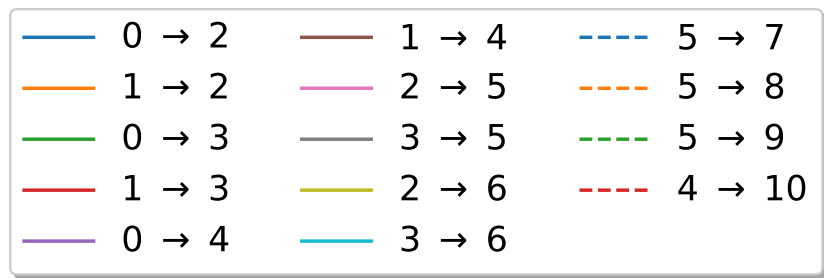
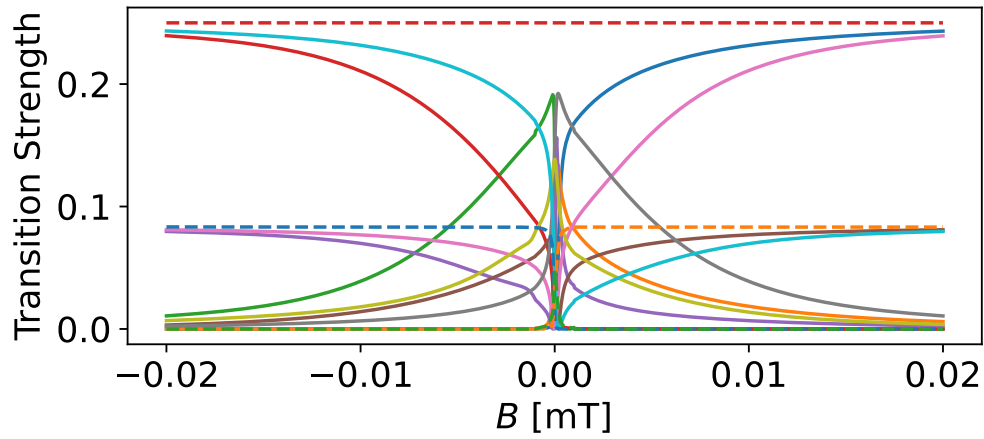


Figure E.6: Strength of allowed transitions driven by σ^- -polarized light for different magnetic field strengths. Zoomed in version of fig. E.5.

F. Appendix: Generating Random Velocities

A computer can generate pseudo-random number, i.e. numbers that seem random but are in reality calculated deterministically. Usually, a start or *seed* value is chosen and from it, the following value is calculated using an algorithm. The second value is then taken to generate the third and so on. By default, Numpy, the python module for numerical calculations, uses a permuted congruential generator (PCG) to produce samples of uniformly distributed "random" numbers r in the range $[0, 1)$. In the following, the reader is assumed to know how such algorithms work or to just accept that they do.

In the simulation which was presented in this thesis, multiple random numbers are needed. Whether an atom is excited and to which excited state specifically and to which ground state it would then deexcite can be determined quite easily. As with the starting position x_0 and y_0 , several uniformly distributed numbers can be generated to sufficiently set these values. But one attribute needs non-uniformly distributed values: the starting velocity v .

As explained in section 3.1, the starting velocity follows a modified Maxwell-Boltzmann distribution

$$\rho_{\text{mMB}}(v) = \frac{m^2}{2k_{\text{B}}^2 T^2} v^3 e^{-\frac{mv^2}{2k_{\text{B}}T}}.$$

Corresponding values can be easily generated using an acceptance-rejection method. With this method, random v below a select maximum value v_{max} can be generated. Two random numbers r_1 and r_2 are created and used to calculate

$$v_r = v_{\text{max}} \cdot r_1, \tag{F.1}$$

$$\rho_r = \rho_{\text{max}} \cdot r_2, \tag{F.2}$$

where ρ_{max} is the maximum of $\rho_{\text{mMB}}(v)$ in the range $v \in [0, v_{\text{max}}]$. This value pair defines a point as depicted in fig. F.1. If

$$\rho_r < \rho_{\text{mMB}}(v_r),$$

the velocity v_r is accepted, else it is rejected and a new value pair is generated. This is repeated until an acceptable v_r occurs.

This method is easily implemented but has some drawbacks. Firstly, it necessitates an upper limit v_{max} . Values above this limit are not taken into account in the simulation. Depending on the assumed probability distribution, the occurrence of such values might be so rare that they can be ignored altogether. But some distributions

have a long tail and throwing away so many potential values could affect the result of the simulation. Secondly, the chance of generating an accepted value is

$$\frac{\int_0^{v_{\max}} \rho_{\text{mMB}}(v) dv}{\rho_{\max} \cdot v_{\max}} < 1. \quad (\text{F.3})$$

Just like the generated number, the amount of pairs (v_r, ρ_r) needed until an acceptable velocity is produced is quasi-random. On average it takes the inverse of the above expression of pairs and each pair requires two random numbers and a check for acceptance. Another method might be computationally superior.

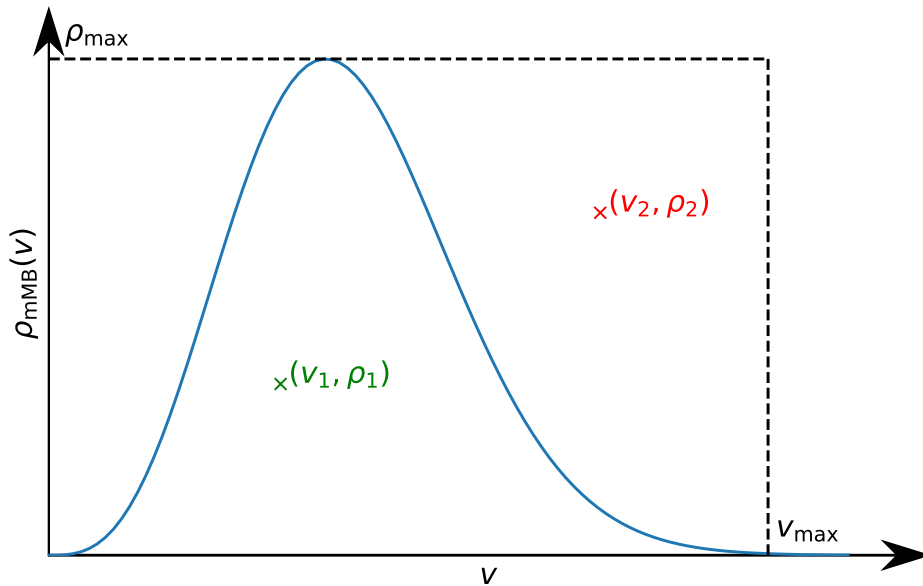


Figure F.1: Exemplary value generation using the acceptance-rejection method. Value pairs (v_r, ρ_r) are generated and if they are below the curve described by the probability density function $\rho(v)$, such as (v_1, ρ_1) , v_r is accepted. If they are above the curve, such as (v_2, ρ_2) , v_r is rejected and a new pair is generated until an acceptable v_r occurs.

Many probability density functions (PDFs) in physics, such as the one presented here, possess a corresponding cumulative distribution function (CDF)

$$F(x) = \int_{x_{\min}}^x f(x') dx'$$

which is strictly monotonic increasing. Here, the lower limit x_{\min} is the smallest physically reasonable value. For normal and Breit-Wigner distributions it is $-\infty$.

For ρ_{mMB} it is 0 because there are no absolute velocities $v < 0$ and the CDF is therefore

$$F(v) = \int_0^v \rho_{\text{mMB}}(v') dv' = 1 - \left(1 + \frac{mv^2}{2k_{\text{B}}T}\right) e^{-\frac{mv^2}{2k_{\text{B}}T}} \quad (\text{F.4})$$

which is depicted in fig. F.2.

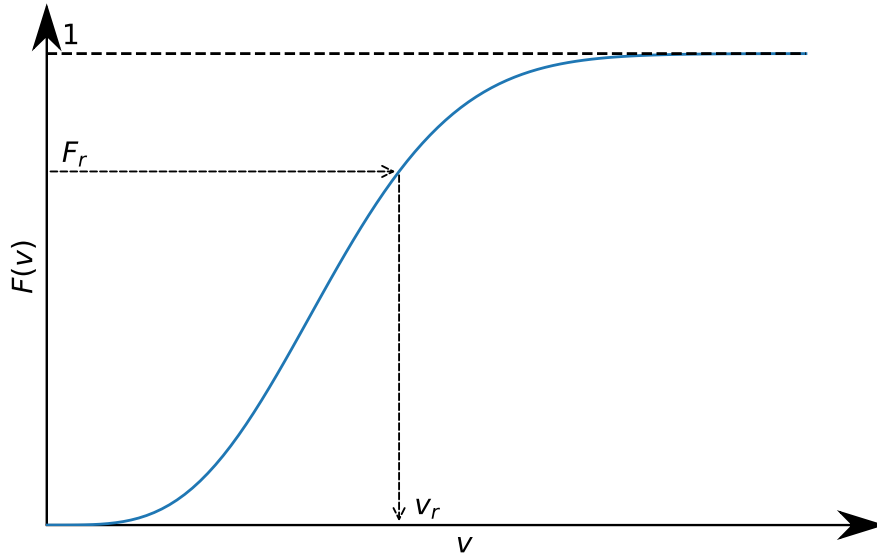


Figure F.2: Cumulative distribution function for the modified Maxwell-Boltzman velocity distribution. The function takes on values between 0 and 1 and because of its bijectivity, an inverse function exists which translates any $x \in [0, 1)$ to exactly one velocity v . This way, v that follow the aforementioned distribution can be easily generated.

Every PDF is normalized so that the resulting CDF produces values between 0 and 1, just like a regular uniform random number generator. Due to the $F(v)$'s strict monotonic behaviour, it is bijective and an inverse function $F^{-1}(x)$ exists which links any number x between 0 and 1 to exactly one value of v . This inverse function is

$$F^{-1}(x) = \sqrt{\frac{2k_{\text{B}}T}{m}} \sqrt{-W_{-1}\left(\frac{x-1}{e}\right) - 1}, \quad (\text{F.5})$$

with W_{-1} being the Lambert W function, specifically the -1 st branch. With a single random number F_r , one can use $F^{-1}(F_r) = v_r$ to directly generate a velocity value which follows the aforementioned PDF. This procedure does not exhibit the disadvantages of the acceptance-rejection method. A direct translation from a set of randomly generated numbers to a sample of random velocities without the need of a lower or upper limit for v in constant time is highly parallelizable and might thus produce more velocities in less time.

This technique is only applicable if an analytical (or at least numerically calculable) solution for F^{-1} exists and is implementable. For many of the PDFs used in physics research, it does. Some prominent PDFs and their respective CDFs' inverse functions are listed in table F.1.

Table F.1: Prominent PDFs and their respective CDFs' inverse functions F^{-1} . y is to be understood as a random number between 0 and 1. While the normal, Cauchy, and logistic distribution are all used for $x \in \mathbb{R}$, the exponential distribution, which can be used to describe exponential decay, is most often only used for $x \geq 0$, while a point on a circle with radius R has a distance to the center r in the range $0 < r < R$.

	PDF	F^{-1}
Normal	$\frac{1}{\sqrt{2\pi}\sigma} e^{-\frac{(x-\mu)^2}{2\sigma^2}}$	$\mu - \sqrt{2}\sigma \cdot \text{InverseErfc}(2y)$
Cauchy	$\frac{2\Gamma}{\pi(\Gamma^2+(x-x_0)^2)}$	$x_0 + \frac{\Gamma}{2} \tan\left(\frac{\pi}{2}(2y-1)\right)$
Exponential	$\alpha e^{-\alpha x}$	$\frac{1}{\alpha} \ln\left(\frac{1}{1-y}\right)$
Logistic	$\frac{1}{2\beta(1+\cosh(\frac{x-\mu}{\beta}))}$	$\mu + \beta \ln\left(\frac{y}{1-y}\right)$
Radius (uniform circle)	$\frac{2r}{R^2}$	$R \cdot \sqrt{y}$

This thesis has been a yearslong journey that has cost me blood, sweat, tears and many sleepless nights. Many things, including myself, broke down and had to be put together again. I couldn't have taken this road without the people by my side. I want to acknowledge and thank them on this very page.

First and foremost I want to thank Randolph Pohl for giving me the chance to work on this project. I was his first PhD student in Mainz and I'm grateful for the experience of building a completely new working group together. His knowledge, his inspiration, his helpful input, and his endless patience made this thesis possible. Thank you for the many free drinks. Also, thank you Julian and Stefan: the best postdocs I could imagine.

I want to thank Prof. Dr. Maas, Prof. Dr. Vanderhaeghen, and Prof. Dr. Elmers for not only being my examiners but also for their wonderful lectures that I had the honor to hear. Their teaching prepared me for this thesis and gave me an outlook on all the other interesting areas of physics that I'm usually not involved in.

I want to thank my colleagues. First, Hendrik, because he wanted to be the first one. Thank you for your calmness and your help. I appreciate your deep knowledge. Thank you Merten for your instructions on coding better programs and better theses. Thank you Ahmed for the stimulating discussions. Thank you Siddharth for caring. Thank you Gregor for taking over the lab. You fill any hole that I could have left there. I know that you and the people you lead will do great research. Thank you all for reading this sorry effort of a thesis and giving me advice on this work.

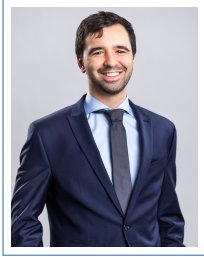
I want to thank my former students. Thank you Konrad and Julia. Without your effort and work I never would have gotten the 3D-MOT to shine. Thank you Ruben and Lukas (plural) for your work on the lasers, magnets and the 2D-MOT. Thank you Andreas (plural) for your great software (number one) and for your work on the 2D-MOT (number two). Thank you Benedikt for not only making the 2D-MOT brighter but also helping me find a new life in Mainz.

I want to thank my former study group. Without Eric, Stephan, Sascha, Eduard, Alexander, Dave, Roman, and Stanislav I wouldn't even have finished my bachelor. Ihr seid ein großartiger Trupp.

Ich möchte *K* danken, dass sie es so lange mit mir ausgehalten hat. Ich weiß, ich konnte schrecklich sein. Ich möchte *C* danken, für ihr großes Herz. Es war ein Glück, dich kennengelernt zu haben.

Ich möchte meiner Familie danken. Diese Thesis ist die Kulmination von 32 Jahren Ausbildung und harter Arbeit und ohne die Fürsorge und Unterstützung von Mutter, Vater, Brüdern, Großeltern, Tanten, Onkeln, Cousins und Cousinen wäre ich nicht an der Stelle, an der ich jetzt bin.

Zuletzt danke ich auch Kevin, David und Dennis. Vor allem in der Abschlussphase der Arbeit musste ich einige Rückschläge hinnehmen und ihr habt mir nach jedem Sturz wieder aufgeholfen. Ich danke euch von Herzen.



Marcel Willig

Lebenslauf

Arbeitserfahrung

- 2024–2025 **Berater im Bereich Energiewirtschaft**, *Hochfrequenz Unternehmensberatung*.
- 2023–2024 **Fertigstellung der Doktorarbeit**.
- 2017–2023 **Wissenschaftlicher Mitarbeiter**, *Johannes Gutenberg Universität, Mainz*.
Doktorand im Fachbereich Physik: Forschung an ultrakalten Atomen mithilfe von Lasern.

Ausbildung

- 2017–2025 **Doktorarbeit Physik**, *Johannes Gutenberg-Universität, Mainz*.
Abschlussnote: *magna cum laude*
- 2014–2016 **Master of Science Physik**, *Johannes Gutenberg-Universität, Mainz*.
Abschlussnote: 1,4
- 2011–2014 **Bachelor of Science Physik**, *Johannes Gutenberg-Universität, Mainz*.
Abschlussnote: 1,6
- 2001–2011 **Abitur**, *Eleonoren-Gymnasium, Worms*.
Abschlussnote: 2,1

Computer-Skills

- Grundkenntnisse C, C#, MySQL, ABAP
- Fortgeschritten Word, Excel, PowerPoint, PYTHON, JAVA, C++, L^AT_EX, Linux

Sprachen

- Deutsch **Muttersprache**
- Englisch **Fließend**
- Französisch **Grundkenntnisse**

Sonstiges

- Führerschein **Klasse B**
- Zertifikate **Scrum Master I & II, Scrum Product Owner I**

Wallstraße 56 – 55122 Mainz

☎ (+49) 157 58379000 • ✉ marcel.willig.arbeit@gmail.com